Signal Processing Issues Related to Deterministic Sea Wave Prediction

Submitted by
Lamia Fathi Abusedra
to the University of Exeter as a thesis for the degree of
Doctor of Philosophy in Engineering, February 2009

I certify that all the material in this thesis which is not my own work has been identified and that no material has previously been submitted and approved for the award of a degree by this or any other University

……..

Abstract

The bulk of the research work in wave related areas considers sea waves as stochastic objects leading to wave forecasting techniques based on statistical approaches. Due to the complex dynamics of the sea waves' behaviour, statistical techniques are probably the only viable approach when forecasting over substantial spatial and temporal intervals. However this view changes when limiting the forecasting time to a few seconds or when the goal is to estimate the quiescent periods that occur due to the beating interaction of the wave components, especially in narrow band seas.

This work considers the multi disciplinary research field of deterministic sea wave prediction (DSWP), exploring different aspects of DSWP associated with shallow angle LIDAR systems. The main goal of this project is to study and develop techniques to reduce the prediction error. The first part deals with issues related to shallow angle LIDAR systems data problems, while the remaining part of this work concentrates on the prediction system and propagation models regardless of the source of the data.

The two main LIDAR data problems addressed in this work are the non-uniform distribution and the shadow region problems. An empirical approach is used to identify the characteristics of shadow regions associated with different wave conditions and different laser position. A new reconstruction method is developed to address the non-uniformed sampling problem, it is shown that including more information about the geometry and the dynamics of the problem improves the reconstruction error considerably.

The frequency domain approach to the wave propagation model is examined. The effect of energy leakage on the prediction error is illustrated. Two approaches are explored to reduce this error. First a modification of the simple dispersive phase shifting filter is tested and shown to improve the prediction. The second approach is to reduce the energy leakage with an iterative Window-Expansion method. Significant improvement of the prediction error is achieved using this method in comparison to the End-Matching method typically used in DSWP systems. The final part in examining the frequency domain approach is to define the prediction region boundaries associated with a given prediction accuracy.

The second propagation model approach is the Time/Space domain approach. In this method the convolution of the measured data and the propagation filter impulse response is used in the prediction system. In this part of the research work properties of these impulse responses are identified. These are found to be quite complicated representations. The relation between the impulse response (duration and shift) with prediction time and distance are studied. Quantification of these impulse responses properties are obtained by polynomial approximation and non-symmetric filter analysis. A new method is shown to associate the impulse response properties to the prediction region of both the Fixed Time and Fixed Point mode.

Acknowledgments

Firstly, I would like to thank my supervisor, Mike Belmont. Your advice, encouragement, and enthusiasm for this research have been invaluable, and indeed I am sure that without your support I wouldn't have had the progress that I had. I would also like to thank Richard Thurley and Mike Horwoord for your thoughtfulness, and understanding.

I would also like to express my gratitude to the people in Engineering and Computer Science, and to my Friends in Exeter I would like to say thank you for being like a little family in my home away from home.

Mai: I am grateful for the chance I got to be your friend, thanks for all your support.

I would like to thank Samina and Janetka for giving me a place in their hart and in their home.

Finally I would like to thank my Family, I never would have started this work if it was not for your support and guidance. To mom I say: I know it wasn't easy for you having me away for that long, I thank you for you patient and support. To my dad I would like to say you're my rock, thanks for being there for me. To my sister Rehab I say: I am gratefully for having you in my life.

A special thanks to my sister Hanan, for your major help in the printing of this thesis. I am grateful for your support and for giving up your holiday to be by my side.

Contents

Chapter 1

Introduction

1.1What is DSWP?

Deterministic Sea Wave Prediction **(DSWP)** is the ability to predict the actual detailed shape of the sea surface, sufficiently far a head in time to have practical marine applications. This type of prediction is totally different from sea state based techniques typically associated with marine operations, which are entirely statistical in nature.

The main question asked in this field is “Is deterministic sea wave prediction possible?”. Considering the enormous complexity of the sea wave systems, which is mainly due to the nonlinearity effects and significant directional evolution in all sea waves it was the common believe that only statistical prediction methods were possible. This became the main stream in oceanographic research since Pierson and Neumman presented their stochastic system approach for sea wave analysis in [1]

However this view has changed after the findings of a series of research programs by the Exeter Marine Dynamic Group [2] [3] [4] ,where they concluded that sea wave surface prediction is possible if the prediction objectives are narrowed down to swell dominated seas over small time and space scales. Sea surface prediction was shown to be possible up to 60 s in some situations. They also showed that for large swells and non-local wind waves prediction errors in the range of (5-10) % could be achieved[5].

Although the prediction range considered in DSWP is very limited compared with the traditional time and space ranges considered in sea wave forecasting, which try to forecast wave movements for hours and days ahead, this is adequate for certain applications and many marine operations would benefit considerably from such

predictions. This is particularly true in short-term critical state maritime tasks, where the critical time windows have scales of a few tens of seconds.

A major factor in the importance of such predictions come from the presence of relatively calm periods better known as quiescent periods of tens of seconds between large waves, as shown in *Figure 1.1*. Quiescent periods are observed more with large well developed seas, and as the average wave height increases the duration of quiescent intervals increase.

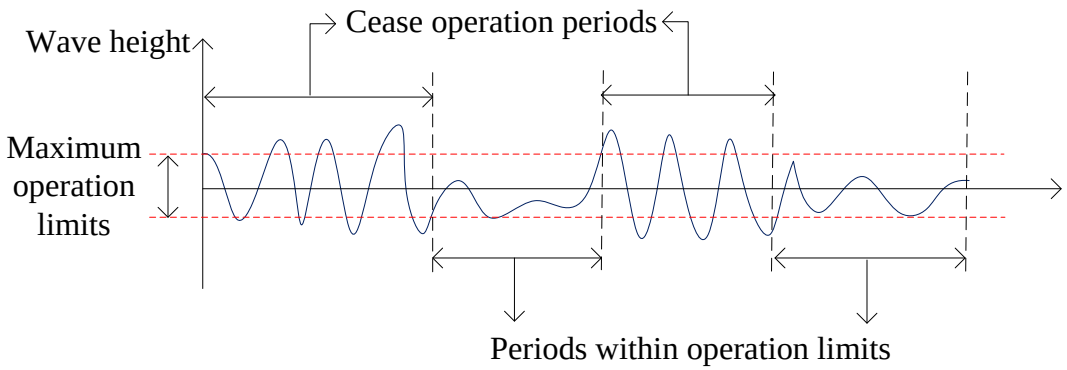

Figure 1. 1: Quiescent periods in rough seas

The main technique of DSWP involves first measuring the shape of the sea surface at some distance from the site where prediction is required and then using this data to build a model capable of estimating the shape of the sea surface when it has propagated to the prediction site.

The main types of waves that are of interest in this field are moderate to large long wavelength swells (> 1m). That is mainly because moderate to large sized vessels are relatively unresponsive to the period and size of most wind waves, unless local storm conditions are extreme, in this case wind conditions themselves would prevent the undertaking of those operations of interest. On the computational level, the weakly nonlinear aspects of the swells make short term real time prediction achievable, while wind waves are highly nonlinear and almost certainly non-computable in the few seconds available for building a DSWP prediction model.

1.2 Motivation of DSWP

Many marine related operations would benefit considerably from the ability to predict waves approaching a vessel or around an installation site. Sufficiently predicting the surface elevation allows the extension of marine operating envelopes, while increasing safety and lowering environmental risks. The following list is a general category of activities that benefits from DSWP:

1. **Serving offshore installations**

A common marine operation that benefits from the ability to predict the sea elevation is the transfer of cargo and personnel between vessels and offshore installations. This operation is typically limited to suitable sea states, which is set according to safety programs.

Cargo transfer operations benefit from predicting the heave (vertical motion) and pitch (side rotation) by reducing the impacting chances of transferred items, as shown in *Figure 1. 2(a)*. Although many crane cargo transfer already enjoy automated systems that have telemetry links to the service vessels, the incorporation of DSWP systems is a natural development.

Many personnel transfer from and to marine vessels using small types of fixed winged crafts or helicopters. The safe landing of those crafts depends on the wind and sea state conditions, as shown in *Figure 1. 2(b)*. These types of operations are a very good candidate for the implementation of DSWP, since the period of the critical stage landing and take off are in the range of the few seconds provided by DSWP systems.

(a)

(b)

Figure 1. 2: serving offshore installation
a-Offshore cargo transfer
b- Offshore helicopter landing

Another advance in the personnel transfer might be realized by synchronizing the power driven gangways with the motion of the service vessels.

2. Single point Mooring

Offshore loading and discharging locations are becoming now a days wildly spread with the advances in the so-called single-point mooring (SPM) systems. However, the operating sea state range remains relatively modest due to the limitation imposed by the connecting stage. Small service craft that are usually needed in the connecting up stage may have their operation envelope extended by introducing new working strategies that adopt the DSWP system.

Another situation that may be considerably improved with DSWP technology involves predicting the peak loads in the mooring hawser to reduce the possibility of line breakage. This problem is of practical importance specially when considering super tankers, and the frightening environmental implications of a tanker accident.

3. Offshore construction

Improving the station keeping that is possible using DSWP techniques, would add considerable benefits to most offshore construction operation and maintenance work by extending their operational time envelope. Another important role for this technology in the field of offshore construction and salvage operations is associated with certain critical phases such as topside mating, where different surfaces are joined. These are very high cost penalty operations that actually only take a few tens of seconds.

4. Deep water Mooring and Harbours

Large vessel manoeuvring and many other marine operations would be improved by providing the existing deep water mooring systems and harbours with the knowledge of coming waves. It should be noted that the benefit of the DSWP technology is limited in shallow waters due to the strong nonlinear affects that might invalidate the type of real time algorithms used in the prediction process.

5. Wave Energy Farms

Marine renewable energy systems are part of the modern, very highly supported exploration for alternative energy sources. Although relatively new compared to wind energy for example, a large body of research on wave energy is available, putting it on the edge of practical implementation. Fundamental research projects are in progress to investigate the enhancement of average energy production delivered by a range of Wave

Energy Converters systems (WECs), when coupled with the DSWP techniques. The advantages of Linking DSWP technology to WECs systems is addressed in [6].

It is clear that the greatest wave energy potential are in stormy conditions, unfortunately this presents problems to WECs that must survive such conditions without damage to them selves or their mooring systems. This is overcome by having a disconnection mechanism that decouples the WEC devices in potentially damaging seas. When using average statistical methods and standard sea state information as shutting down criteria a great opportunity is missed by not taking advantage of quiescent periods that occur between larger wave conditions. Using DSWP would provide the chance to operate WECs during these periods thus increasing the energy production and improving the economic feasibility of the farm.

On a separate front, the DSWP technology would be valuable to those marine devices that incorporate tunable dynamics. Typically tunable parameters in such devices are set using the prevailing sea properties such as wave spectrum bandwidth and maximum wave heights. However, as the sea properties aren't strictly stationary, each incoming group of waves has different properties. The DSWP allows the prospective of optimized real time tuning based on the instantaneous sea surface profile at the device's location.

1.3 Basic concepts in oceanography

Ocean waves occur as a result of many forces acting on the ocean surface. Most recognized natural force sources are the winds, earthquakes, the Earth gravity, gravity of celestial bodies and surface tension. These complicated systems of forces produce a complicated system of waves. The type and strength of these forces creating the waves are responsible for their period, hence it is common to categorize ocean waves by their *period*, this is illustrated in *Figure 1. 3*.

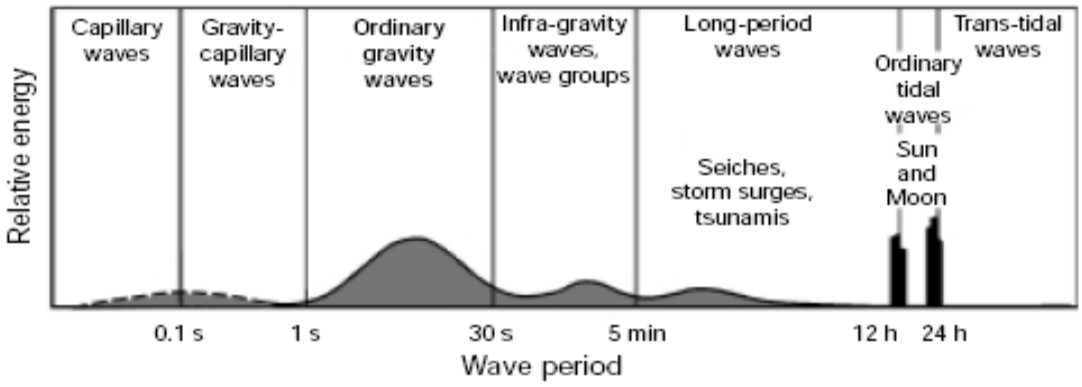

Figure 1. 3: Classification of ocean waves by wave period ([WMO 1998][7])

This work concentrates on the wind-generated gravity waves, which are almost always present at sea. As the name suggests these waves are generated by winds forces and they affect a wide range of coastal and offshore activities. There are two types of wind waves, seas and swells. Seas are short-period waves still being created by winds in the storm area, while swells are waves that have moved out of the generating area, and hence, are more regular waves with well defined long crests and long periods.

At the growth stage of wind-generated oceanic waves wind energy is imparted to the water; however this growth is not indefinite. The point when waves stop growing is termed a fully developed sea condition, well defined crests and troughs appear when they are no longer under the influence of winds. Swells appear to be almost unidirectional and have distinctly separated crests. Surface waves can travel hundreds or thousands of kilometres without much loss of energy.

Although waves of different periods existed originally together in the generation area, in time the various wave components in the sea separate from one another, this happens because of differences in the speed of waves with different wave periods. Longer period waves are faster, so shorter period components may reach certain site several days after the longer period waves. However, short-period components lose their energy more readily than long-period components. Which results in swells having somewhat longer periods than seas, this is typically greater than 10 sec.

Figure 1. 4 shows a one-dimensional, simple progressive wave propagating in the positive x direction. Wave parameters are defined below with the symbols used through out the thesis.

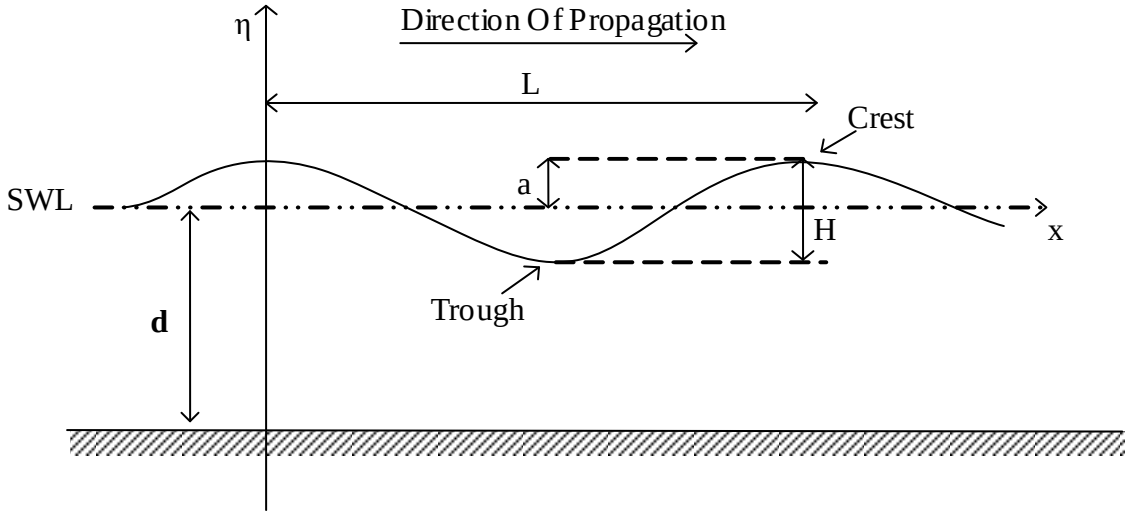

Figure 1. 4: One-dimensional simple propagating wave

η :	Displacement of the water surface relative to the still-water level (SWL)		
a :	Wave amplitude maximum wave displacement from (SWL).		
H :	Wave height	T :	wave period
L :	wavelength	d :	water depth

Before any attempt to understand complex water motion, basic understanding of the physical processes in generation and propagation of surface waves is fundamental. There is a great body of work toward developing theories to help understand the waves behaviour, and waves models that are needed to analyze waves. In this introduction we will touch on the most important wave theories, highlighting the wave elevation estimation given by each of them. Detailed descriptions of the basic equations for water mechanics are available in several textbooks [8] [9] [10] .

1.3.1 Wave theories

1.3.1.a Linear wave theory

The linear theory, also known as the first-order and small-amplitude, developed by Airy [11], is the simplest wave theory. This theory provides a reasonable approximation of the waves characteristics and waves parameters. This theory develops the wave model based on a few assumptions:

• Incompressibility: When deriving the continuity equation, the density is constant and conservation of fluid within a small cell of water or particle.

• Inviscid.: Forces acting on a water particle (gravity and pressure) are perpendicular to the surface of the water , and friction is ignored.

• Irrotational: The individual water particles do not rotate. They may move around each other, but there is no twisting action.

The derivation can be found in many textbooks on waves, for example [12]. The wave motion is found to be represented by a sinusoidal, long-crested, progressive wave. The wave profile has the form given by:

$$\eta(x,t) = A\cos(kx - \omega t + \theta) \qquad \textbf{1. 1}$$

where ω,k are the angular frequency and the wave number, and θ the phase shift.

Although the simple sinusoidal wave represent the basic solutions of the physical equations, which govern waves on the sea surface, these simple waves are never found

at sea; only swell, passing through an area with no wind, may come close. Never the less these simple waves are used as "building blocks" for more complicated waves occurring at sea. The simple concept of sinusoidal waves is frequently used to describe and understand waves on the sea surface, and in spite of this simplified description, the definitions and formulae derived from it are extensively used in practice and have proved their worth.

1.3.1.b Nonlinear wave theories

Properties of an ocean surface wave are driven in the linear wave theory under the assumption of infinitely small wave amplitude. For the linear theory to hold, the small amplitude assumption must be valid. The wave steepness ($\varepsilon = a/L$) is a measure of how large a wave is relative to its height and whether the linear wave assumption is valid. For large values of the wave steepness the linear wave theory fails to describe the water waves and nonlinear wave theories are needed[13]. Higher power series of *(ka)* as in *Equation 1.2* are used in the case of large steepness. [14]

$$\eta = a\cos(kx-\omega t)+\frac{1}{2}ka^2\cos 2(kx-\omega t)+\frac{3}{8}k^2a^3\cos 3(kx-\omega t)+\ldots\ldots \qquad \textbf{1. 2}$$

Such nonlinear waves have sharpened crests and flattened troughs and are called Stokes waves, as shown in *Figure 1. 5*.

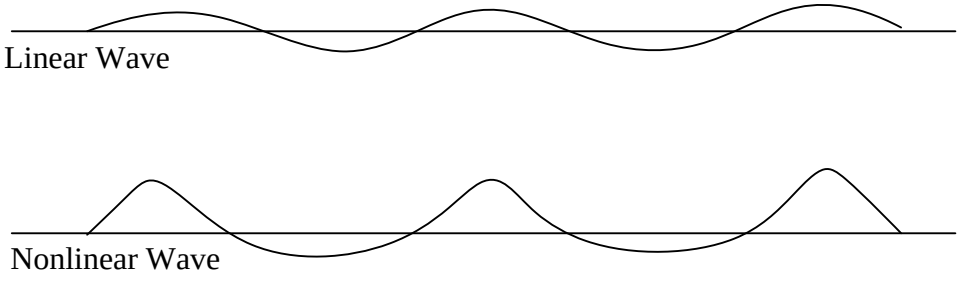

Figure 1. 5 : Linear and nonlinear waves

Many nonlinear wave theories evolved to give a better description of surface gravity waves, these include cnoidal, solitar, Stokes theories and Fenton's theory, an extensive description of these theories is presented in [14] . These higher-order or extended solutions of gravity waves result often in a better agreement between theoretical and observed waves, and can also describe phenomena such as mass transport where there is a small net forward movement of the water during the passage of a wave, however this comes with the down side of tedious mathematical requirements.

1.3.1.c Validity of wave theories

Validation of the different wave theories is important to ensure their proper use. Very high-order Stokes theories are used as a reference against which the accuracy of other theories are tested. Nonlinear wave theories better describe mass transport, wave reflection, transmission, and other nonlinear characteristics. On the other hand the additional effort necessary for using nonlinear theories may not be justified in certain applications.

In addition to steepness, many dimensionless parameters were developed over the years to assess the relevance of different wave theories, like Ursell number (U_R) and Stokes number. There are a number of studies to show the limiting value of wave heights and wave steepness at different water depths to establish range of validity of wave theories [14]. An important product of these studies is that for low steepness waves in transitional and deep water, linear theory is adequate to describe the wave dynamics. Since work in this thesis concentrates on long wavelength deep water swells, these waves are generally treated in the literature [10] to be adequately described by linear theory. This is important to achieve real time operation algorithms, since the mathematical demands for a nonlinear solution will eat into the limited prediction time available.

1.3.2 Wave propagation

A disturbance on the water surface will travel away from the point at which it was generated. *Figure 1. 4* shows a one-dimensional, simple progressive wave propagating in the positive x direction, the speed at which a waveform propagates is defined by the phase velocity or wave speed ($c_p = \frac{L}{T}$). An important relation in water wave mechanics is the dispersion relation, relating wave speed to wavelength and water depth.

$$c_p = \sqrt{\frac{gL}{2\pi}\tanh\left(\frac{2\pi d}{L}\right)} \qquad \textbf{1. 3}$$

Where g is gravitational acceleration.

The dispersion relation indicates that waves with different periods travel at different speeds, where the longer period wave will travel faster. An interesting result of the

dispersion relation is the relation between wave number *(k)* and angular frequency *(ω)* given by

$$\omega = \sqrt{g \cdot k \cdot \tanh\left(k \cdot d\right)} \qquad \textbf{1. 4}$$

These relations also incorporate the effect of water depth on the wave propagation. As the wave propagates, both the surface and the deeper water under a wave are in motion. The water particle's vertical circles motions become progressively smaller with increasing depth. The influence of the bottom on the movement of water particles changes with the depth of the wave. Gravity waves are classified by the water depth in which they travel according to the ratio between depth (d) and wavelength (L) :

- Deep water $d > L/4$
- Transitional depth $L/25 < d < L/4$
- Shallow water $d < L/25$

In deep water the term *[tanh(k.d)]* approaches unity, and wave characteristics are virtually independent of depth, resulting in the deep water dispersion relation $\omega = \sqrt{gk}$ or $k = \frac{\omega^2}{g}$. As the waves of interest in this work are deep water swells, the deep water dispersion relationship are used to govern the relation between the wave number and angular frequency in the remaining of this thesis, and consequently these deep water relations have major importance in the building of the propagation models.

Another wave propagation parameter found in the literature is the group velocity (c_g). This is the rate by which wave energy travels, where in general the speed by which the energy travels is different than that of the speed of the wave, for example in the case of deep water waves the group velocity (c_g) is only half of the phase velocity. The group velocity is typically used in traditional wave forecasting, where there is more interest in the over all statistical properties of the waves, unlike in the field of DSWP where the interest is in the actual change in the shape of the wave surface.

For any one location the energy is actually spread over a spectrum of waves at different frequencies. These frequencies will propagate at different speeds. Long waves and their energy travel faster than short waves and their energy. This is the main reason that waves evolve over the water surface as they are moving from one location to another. When predicting the shape of a wave in a certain location, it is not enough to simply measure the speed of the group of waves at a remote location. As seen in Chapter *2* the prediction model needs to consider the relations between the speed of the

different wave components, and the effect that has on changing the shape of the wave as it propagates from one location to another. In DSWP the wave speed considered is that for individual components of the wave not the speed of the wave group as a whole.

Main causes of decay for wind waves are dispersion and spreading. Energy is also lost through internal friction and air resistance. This acts on all components of the wave spectrum, but is strongest on the shorter waves, contributing to the lengthening of swell further away from the storm source. This dissipation is often small enough that swell can survive over large distances, and certainly doesn't affect the waves on the relatively limited space scale considered in this work.

1.3.3 Wave spectrum

Single components are not adequate to model the random appearance of sea surface waves. The sea surfaces with a random appearance are better described as the sum of many simple wave trains. Wave spectrum is the formal description of this concept. The surface wave is decomposed usually by means of Fourier analysis into a large number of sinusoidal wave components, of different frequencies, directions, amplitudes and phases.

There are many types of spectral descriptions in the literature [9], the most general type uses the two spatial domains *(x_1,x_2)* and the time dimension*(t)*, resulting in a three dimensional spectrum defined by :

$$B_3(k_1,k_2,\omega)=\int_{x_1}\int_{x_2}\int_{t}\eta(x_1,x_2,t)e^{-i(k_1x_1+k_2x_2-\omega t)}dx_1dx_2dt \qquad \textbf{1. 5}$$

Assuming the sea wave to be stationary, we can represent the sea surface elevation by

$$\eta(x_1,x_2,t)=\iiint B_3(k_1,k_2,\omega)e^{i(k_1x_1+k_2x_2-\omega t)}dk_1dk_2d\omega \qquad \textbf{1. 6}$$

One and two dimensional spectra are special cases of $B_3(k_1,k_2,\omega)$, these simpler spectra are more common in wave studies [15]. In Chapter *4* we introduce a two dimensional spectrum considering the frequency and only one of the wave number dimensions.

In general, sea surface spectra does not follow any specific mathematical form, however it is found that under certain conditions the spectrum does have a specific shape. A series of empirical expressions called parametric spectrum models are found to fit the spectrum of the sea surface elevation. These are usually defined in terms of frequency, *S(f)*, however this can easily be changed to a wave number representation ,

S(k), since the wave number and frequency are related by the dispersion relation. The frequency and wave number forms can be transformed from one to the other.

There are many forms of wave energy spectra used in practice, which are based on one or more parameters such as wind speed, significant wave height, wave period, shape factors[8] [9]. A single-parameter spectrum termed the Pierson-Moskowitz (P.M.) spectrum is often used as a model spectrum for a fully developed sea, (an idealized equilibrium state reached when duration and fetch are unlimited). The power spectral density function $S(\omega)$ for P.M has the form given in *Equation* 1. 7

$$S(\omega) = \frac{\alpha g^2}{\omega^5} \exp\left\{-\beta\left(\frac{g}{U\omega}\right)^4\right\} \qquad \textbf{1. 7}$$

Where g is the gravitational constant and U the wind velocity in $m.\sec^{-1}$ at a height of $19.5m$ above the sea surface, $\alpha = 8.1\times10^{-3}$ and $\beta = 0.74$.

It can be shown that the peak frequency or the dominant frequency of the Pierson-Moskowitz spectrum is:

$$\omega_D = \frac{g}{U}\sqrt[4]{\frac{4}{5}\beta} \qquad \textbf{1. 8}$$

The spectrum bandwidth is defined by the two frequencies ω_1 and ω_2 where the first boundary is the frequency below which r_1 % of the total sea power is present while the second boundary is the frequency above which r_2 % of the power is present then:

$$\omega_1 = \left\{\frac{0.74}{|\ln(r_1)|}\right\}^{\frac{1}{4}}\left\{\frac{g}{U}\right\} \qquad \textbf{1. 9}$$

$$\omega_2 = \left\{\frac{0.74}{|\ln(1-r_2)|}\right\}^{\frac{1}{4}}\left\{\frac{g}{U}\right\} \qquad \textbf{1. 10}$$

Another important coefficient of the wave spectrum is the significant wave height (SWH) usually denoted in the literature as H_{m0}. For a fully-grown P.M sea the (SWH) is defined as :

$$H_{m0} = (0.0246)U^2 \qquad \textbf{1. 11}$$

The Pierson-Moskowitz spectrum is used to model the sea waves for all the practical work presented in this thesis. A full description of the wave model used in this work is given in *Section 2.7*.

1.4 This Thesis: Aims and structure

The main research objective is to introduce and study different methods to improve the quality of wave prediction based on a deterministic signal processing approach.

- Investigate problems associated with the LIDAR data specially the shadow region and spatial non-uniformity in the data distribution.
- Examine the performance of spectrum domain prediction methods.
- Explore the Time/Space domain approach of wave prediction.

This Chapter has given an introduction to DSWP. Some general marine activities that benefit from DSWP was listed. The remaining part of this chapter represented some basic principles in the field of ocean waves, concentrating on the surface elevation and wave propagation given by the linear wave theory.

Chapter 2 describes the different stages in the DSWP process, discussing the developments in each of these stages. The shallow angle LIDAR system is introduced, highlighting the data problems associated with such a wave measurement device. The main focus of this chapter is to introduce the propagation stage and the prediction region boundaries.

Chapter 3 investigates the shadow region problem association with the shallow angle LIDAR system. Statistical properties of these regions are found for different wave models. The second part of this chapter looks into the reconstruction of the wave from non-uniformly distributed snapshot data. Iterative and non-iterative reconstruction algorithms are implemented. Special modification of these algorithms to better suit the reconstruction objectives is introduced.

Chapter 4 investigates the DSWP from the spectral domain point of view. Prediction algorithms for different types of wave data are discussed and the two dimensional wave spectrum of the unidirectional deep water wave is introduced. This chapter also looks into the effects of energy leakage on prediction, investigates existing

prediction algorithms to deal with this problem, and introduces new methods to help reduce the prediction error.

Chapter 5 A numerical approach is used to estimate the prediction error surface for different wave models and different prediction algorithms, providing an important tool in comparing prediction results for different conditions. The second part of this chapter parameterizes the error surface and estimates the prediction region for different prediction accuracy requirements.

Chapter 6 investigates the prediction process using Time/Spatial domain approaches. Two methods are developed to determine the impulse response properties (polynomial approximation) (non-symmetrical filter). The next part of this chapter is to illustrate a method to determine the prediction region from the response properties, and an investigation of the prediction accuracy relation to the impulse response truncation is performed.

Chapter 7 consists of a summary and direction for future work.

Chapter 2

The Basis for DSWP

2.1 Introduction

This chapter identifies the main elements of DSWP, mainly based upon the existing literature. This provides the jumping off point for the developments to DSWP presented in this thesis which constitutes the bulk of Chapters 3 to 7.

It is standard practice in the marine world to depend heavily on statistical forecasting of the sea-state to indicate conditions in which it is possible to undertake certain types of marine operations. Sea state critical operations include transfer of materials and personnel between ships and offshore installations, helicopter operations from ships and underwater and surface operations managed from ships.

It was recently recognized that for short duration of time it is realistic to predict the actual shape of the sea surface, rather than merely its statistics[16] [17] [18]. The relatively narrow band spectrum of large waves indicates the presence of statistical dependence in sea surface behaviour[19]. This offers the prospective to change marine operation strategies to exploit the short calm periods of a few tens of seconds that exist in heavy sea conditions. This gives the chance of safely undertaking operations in sea conditions that were previously considered too hazardous.

DSWP includes first measuring waves at a remote location from the prediction site, then analyzing the waves into their components. As mentioned in *Section 1.4* different frequency components have different speeds, which causes the waves to evolve over the

water surface as they are moving from one location to another, this is illustrated in *Figure 2. 1.*

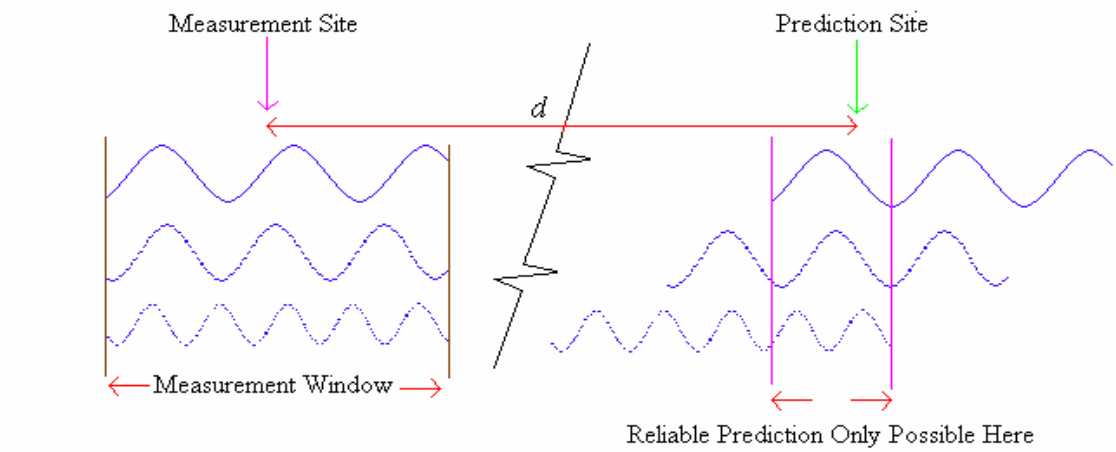

Figure 2. 1: Wave component propagation and reliable prediction window

Prediction times of the actual surface shape of large swells have the potential to reach up to 60 seconds into the future, with surface level prediction errors as low as 10% of the significant wave height [4].

DSWP is a multi-disciplinary research field including different theoretical, computational and instrumentational aspects. The block diagram shown in Figure 2. 2 illustrates the main elements of a DSWP system each of which will be explored in this thesis.

There are three approaches to implementing DSWP which are categorized by the type of wave data acquired, [20] [21]. The FIXED POINT technique employs time series data measured at one or more fixed locations remote from the prediction site which might typically use heave pitch roll buoys as sensors.

The FIXED TIME technique requires data samples taken over a large number of spatial locations in a negligibly small time during which the sea surface shape can be considered fixed. This data effectively comprises snapshots of the sea surface profile. The collection of such data requires some form of scanning remote sensing system such as the LIDAR device described subsequently.

The final technique is the MIXED SPACE TIME technique which again uses data from multiple spatial locations but this time allows the measurements to be made over an interval during which the sea surface shape may change somewhat. Again this information would normally require a remote sensing system. Of the three techniques as

might be expected the MIXED SPACE TIME mode is by far the most demanding to exploit, it does however offer certain advantages to the FIXED TIME mode in terms of confidence in the wave data due to improved signal to noise ratios.

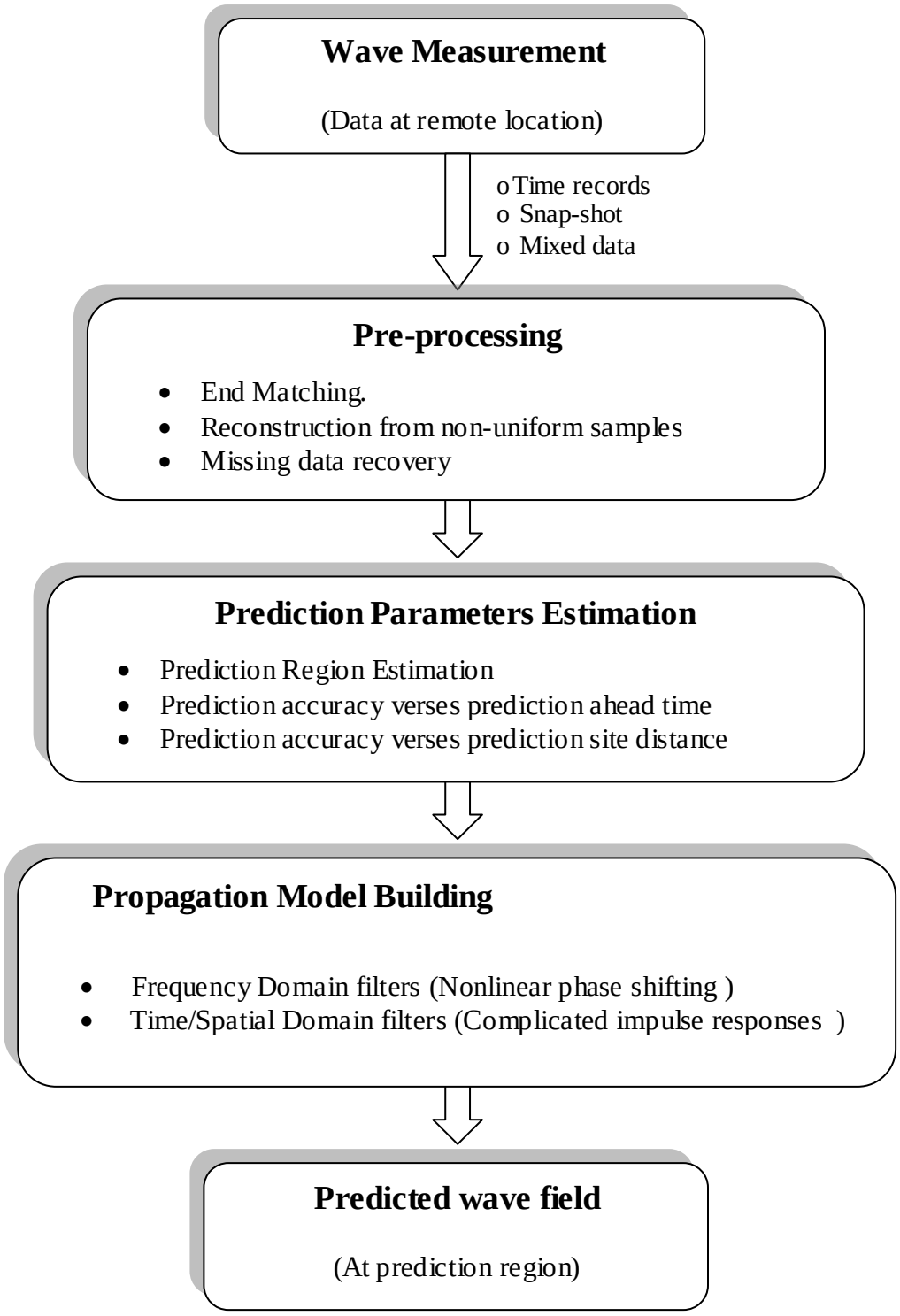

Figure 2. 2: Block diagram of the DSWP system

2.2 Wave measurement (Shallow angle LIDAR system)

From the implementation point of view, there are two distinct approaches for DSWP. The FIXED POINT approach, this uses simple wave sensors like wave buoys and might be used by stationary vessels, salvage and construction craft, and offshore installations. The second approach is the FIXED TIME method which is more suited for moving vessels. This covers many types of marine operations on moving vessels including aircraft landing. Sophisticated remote sensors are required for this approach. Measurement techniques developed to meet the needs of this approach are found in[22].

The traditional approach to measuring the elevation of the sea surface is via heave, pitch roll buoys [9] [23] and wave staffs. More recently some promise has been shown by acoustic doppler devices (ADCPs), but only in depths of less than 50m. Sensors such as Buoys, ADCPs, etc., provide point measurements and as such are only of practical value in the Fixed Point mode prediction technique. Even then a significant number of devices must be deployed in order to model a useful number of different wave directions. Such wave sensors and their associated telemetry systems are expensive and notoriously vulnerable.

Some form of remote sensing is much cheaper and more practical, as it allows the use of all the different prediction modes. At present satellite based sensors do not have the required resolution and also do not provide 24 hour coverage of specific locations. Bragg scattering radars [24], can only provide statistical wave data and as yet attempts to exploit micro-wave radars using developments of image processing techniques such as WaMoS (The Wave and Surface Current Monitoring System), developed by the company Ocean Waves, have yet to be proven. In contrast shallow angle optical radar, LIDAR, has been shown to offer an effective solution to the data collection technique [25] [26] [27], although as yet there are no commercial systems available.

LIDARs (optical radars) were first developed as airborne surveying systems for coastal bathymetry and later for underwater obstacle detection [28] [29] [30] [31] [32]. They were based around the green 532 nm wavelength laser which was chosen for bottom echo generation because this spectral region corresponds to minimum absorption in particle free sea water. In order to accurately determine the sea surface location bathymetry LIDARs typically also employ a red beam which is why such instruments are also capable of providing sea surface profile data[33] [34]. Despite being minimally absorbed by bulk sea water green wavelengths are significantly

scattered by components of calcareous plankton in the surface layers of the sea [35] [36].

The probe beams employed in airborne LIDAR systems typically operate at or near normal incidence where plankton scattering constitutes an unwanted return signal. However for vessel mounted or portable shore based system operating close to grazing incidence this light scattering process will constitute an important data source. Other sources of backscatter are capillary waves, small local trochoidal wavelets, suspensions and foam. As foam is a strong scattering agent it means that the amplitude data can be used to identify those regions of the wave profile where the wave is breaking.

The signal returns from airborne LIDARs, at approximately normal incidence, are strong compared to the very weak returns available from the shallow angle LIDARs needed for coastal or ship born operations. This problem is aggravated by the legal requirements for LIDARS to be eye safe which obviates the use of the giant pulse lasers that have been employed in wide field of view work wave roughness studies, [35] , and more recently using Raman scattering, [37]. The consequential signal to noise ratio problem is one of the main reasons why such instruments have not been developed up until very recently.

The shallow angle technique is in principle extremely simple, it involves scanning a laser beam along a set of scan directions as illustrated in *Figure 2.* 3 for the case of a vessel mounted LIDAR, The general properties of waves profiles measured using shallow angle LIDAR are discussed in [38] [39] .

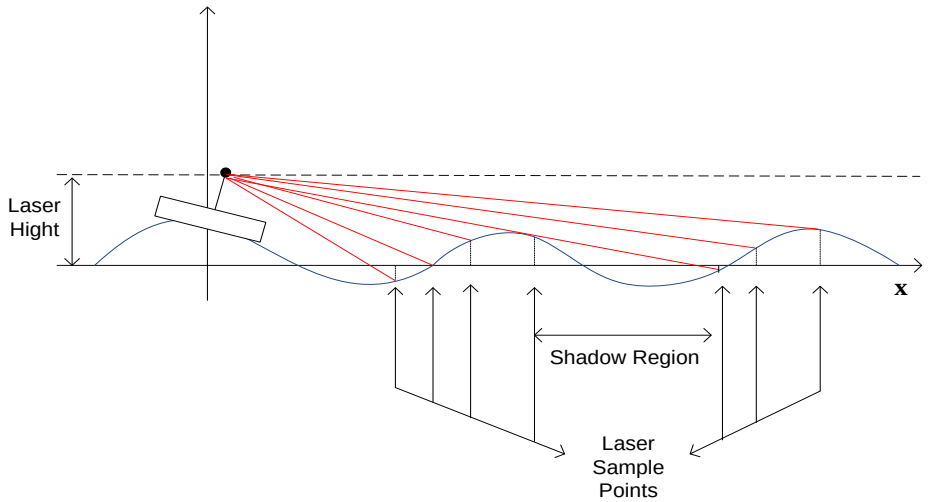

Figure 2. 3: Shallow angle LIDAR system

Examining *Figure 2.* 3 immediately reveal two features of the measurement process. Firstly the geometry of the situation means that the spatial locations of the measurements are inevitable non-uniformly distributed along the space axis. The only

way to choose scan angles to avoid this would be if the shape of the sea surface were known in advance. In particular samples are clustered closely together at the front of waves and spread out on their rear faces. Secondly, in the limit of non-uniform sampling the rear face of the wave is actually obscured, so called wave shadowing.

Both the non-uniform sampling and the wave shadowing have profound effects on the signal processing strategies required to extract useful data for the prediction process. The sequence of experimental wave profiles presented in *Figure 2.* 4, taken from [26] , obtained using a shallow angle LIDAR system show these two features very clearly.

The properties of the wave shadow regions associated with different wave models and different laser position are the subject of *Section 3.2* of this research. The nonuniform sampling problem is also addressed in *Chapter 3* where different methods for signal reconstruction are implemented.

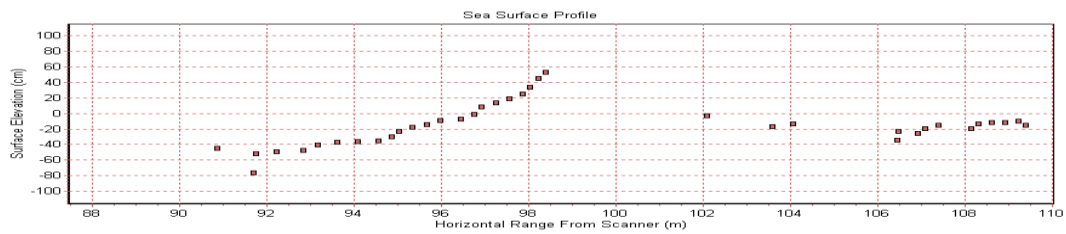

0.0 sec.

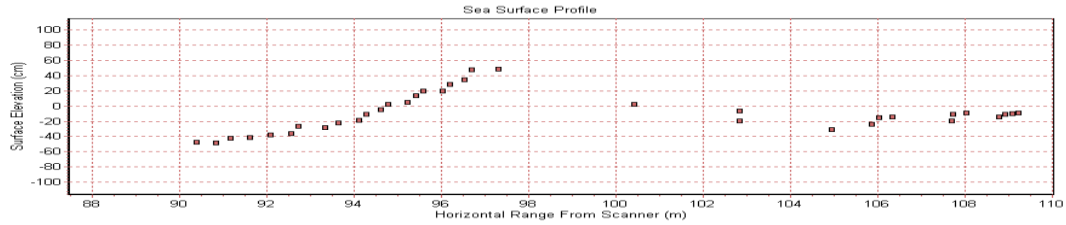

0.4 sec.

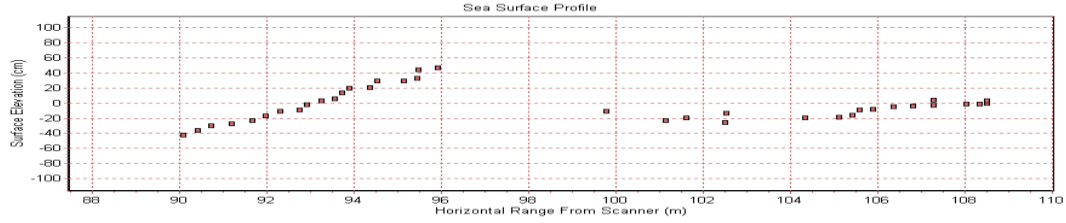

0.8 sec.

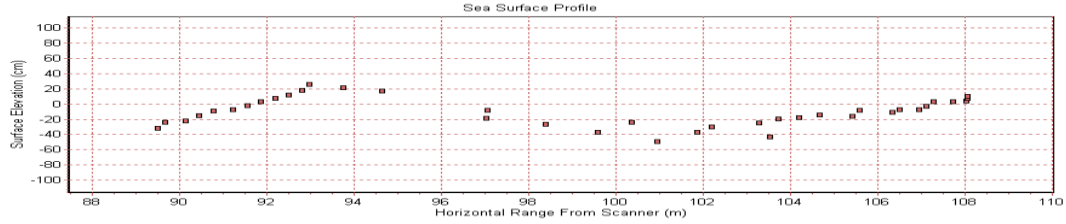

1.2 sec.

Figure 2. 4: Four successive frames taken from a 'spatial wave movie' of a low amplitude wave propagating in shallow water, taken from [26].

2.3 Pre-Processing of Raw Wave Data

In the FIXED POINT technique using heave pitch roll buoy measurements the raw wave data can be used directly in building the prediction models providing the buoys do not wander too far off their nominal locations during wave induced motions. In contrast data from shallow angle LIDAR or similar ship mounted sensors will contain the effects of wave shadowing and non-uniform spatial sampling. The removal of these effects will require certain types of pre-processing as discussed in *Chapter 3*.

2.4 Prediction Model Parameter Estimation

This is the first stage in the DSWP process, where the main parameters are set and the requirements of the prediction process are determined. The main assumption made in DSWP is that the surface waves are stationary for time duration longer than the actual prediction period. This allows the use of traditional power spectrum parameters to determine the average properties of the sea, which are required in order to make initial estimates of key parameters such as the upper and lower frequencies, required in the prediction process. The spectrum can be derived from the accumulated measured wave data used in prediction.

The main part of this stage in the prediction process is to locate the prediction region associated with the prevailing sea power spectrum. The approach uses upper and lower band limits of the sea spectrum and the measurement region dimension to determine the time period at each location where wave prediction is possible. As stated previously, two distinctive cases are considered based on the type of wave measurement used. First is the FIXED POINT method, as the name suggests this method deals with time records measured at a fixed location in space. The second method deals with snapshots of the sea taken at a particular instant in time, hence its called, the FIXED TIME method.

The discussion is dedicated to a wave train arriving at the prediction site from a single direction. This can be extended to a multi dimensional wave system by using the superposition concept. Also this prediction region estimation technique is concerned with linear wave systems, hence the nonlinear wave interaction effects –mentioned previously in *Section 1.3.1.b*- are being neglected.

2.4.1 Prediction region estimation for FIXED POINT method

Consider a train of small amplitude dispersive waves with a finite frequency range $f_1 < f < f_2$. For simplicity we assume all wave components have the same direction, resulting in a unidirectional wave travelling in the positive x -direction. The propagation paths of the individual wave components are represented by a line on the (x,t) plane, see *Figure 2. 5* where the slope is equal to the phase velocity $c_p(f)$ of that component.

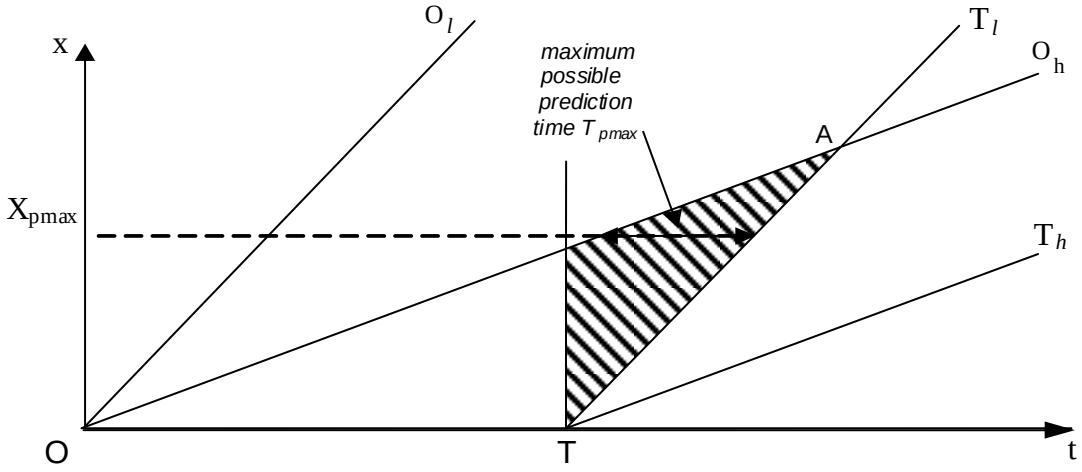

Figure 2. 5: Prediction region for the Fixed-Point mode

The relation between the phase velocity and frequency in the case of linear waves is given in *Equation* 1. 3. It is clear that higher frequency components have larger velocity than lower frequency components. This relation results in lower frequency components being represented by steeper line slop on the (x,t) plane. The diagram of wave propagation on the *(x,t)* plane define the region where prediction is possible[40] [2], as shown in *Figure 2. 5* .

The wave surface is measured at the fixed point $x = 0$ over the time interval $0 < t < T$, this is represented in *Figure 2. 5* by the line OT. The path of propagation of the lowest and the highest frequency wave which pass the measurement point at the beginning of the measurement period are represented by the two lines (O_l, O_h) shown on the figure staring from point O. Similarly the two lines (T_l, T_h) that originate at point T, represent the lowest and the highest frequency wave which pass the measurement point $x = 0$ at end of the measurement interval.

All waves present in the region defined by the triangle (OTA) have passed the measurement point during the measurement interval, therefore the time record OT can be used to determine the wave propagation in this region. However, practically we need

the time record to build the prediction model, which reduces the actual prediction region to the shadowed region shown in *Figure 2. 5*.

The maximum prediction period T_{pmax}, and the distance from the measurement site to the maximum prediction period location is X_{pmax} ,are also shown. For the fixed-point method this is the optimum distance between measurement and prediction point. Notice that the optimum distance and the maximum prediction period depend on the time record length and also on the wave spectrum limits.

For distances larger that the optimum distance it is clear that the prediction window starts shifting in location and shifting in time. This results in a delay period between the measurement ending and the prediction time. This concept will be analyzed in more details in *Chapter 5* and *Chapter 6*.

It is important to notice the relationship between the prediction region and the sea bandwidth. When the spectra become narrower the slopes of the two lines representing the spectrum lower and higher limits become closer. This results in the increase in the prediction region. The effect of water depth, wave spectrum properties and the distance to the prediction site on the maximum prediction period are studied in [2] [40] .

2.4.2 Prediction region estimation for FIXED TIME method

The Fixed Time case is shown in *Figure 2. 6*. A snapshot of the wave is measured at a fixed time $t = 0$ over the region $L < x < O$. By applying the same concept of the propagation path of the lower and higher limits of the wave spectrum passing the two ends of the measured location, we obtain the prediction region estimation as the triangle (OLA). In this case the optimal prediction location is at the origin (O), and hence the maximum prediction period is (OT), as shown in Figure 2. 6. As in the previous method, the prediction window becomes smaller in size and shifts location for distances larger that the optimum distance, an elaborated discussion on this concept is presented in *Chapter 5*

The relation between the prediction region dimensions and the various parameters is very similar to that of the previous method. The effect of spectrum width, measurement location and distance from the prediction site to the beginning of the measurement location, on the prediction time is demonstrated in [2].

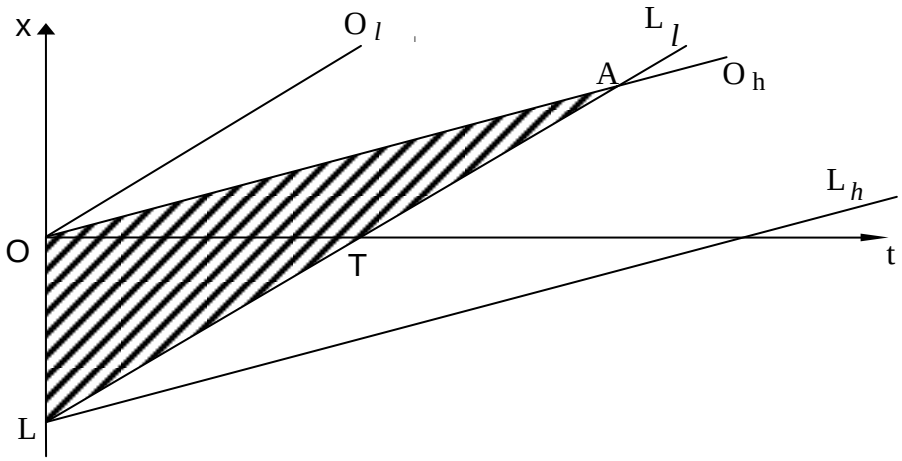

Figure 2. 6: Prediction region for the fixed-time mode

The *(x,t)* plots showing the prediction region in *Figure 2. 5* and *Figure 2. 6* introduce the optimal situation. However, in practice a number of factors need to be considered to get the region where prediction is achievable. For example the time required to process the prediction model will cut into the proposed region shown. Another factor is the effect of ship waves *Figure2.7* on the prediction process, where introducing a ship wave model into the prediction model not only adds to the calculation requirements, it also might change the prediction region dimension. The simplest way to avoid these complications is to set the distance between the measuring site and the prediction site so the ship waves would fade away and their affect could be neglected.

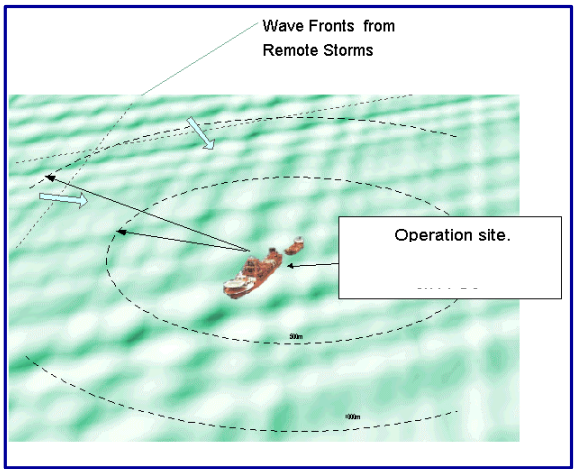

Figure2.7: Effect of ship waves on incoming waves

The prediction region introduced in this section doesn't give any information on the prediction error associated with different part of this region. *Chapter 5* shows the change in the prediction accuracy along the (x-t) plan for different wave models. It will be shown that the prediction region can be defined as a function of the required prediction accuracy.

2.5 Spectrum based wave prediction model

The standard approach found in the literature used to build the prediction model for DSWP systems is frequency (or wave-number) domain based [4] [18]. There are usually two steps in this method, first is the decomposition where the wave components are computed, secondly a nonlinear phase shifting all pass filter is used to propagate the wave components to the prediction site.

To date attempts at incorporating nonlinear affects into DSWP [41] [42] [43] has involved iteratively computing a combination of free and bound waves which match the empirical data. This technique is computationally intensive and unrealistic for real time DSWP.

2.5.1 Linear wave prediction for the Fixed Point mode

The linear wave theory represents the surface elevation of a propagating unidirectional deep water waves using the single sided one dimensional spectrum A(ω) :

$$\eta(x,t)=\int_0^{\infty} A(\omega)\cos\left(\frac{\omega^2}{g}x-\omega t+\theta(\omega)\right)d\omega \qquad \textbf{2. 1}$$

Assuming that the sea surface is totally stationary and one had an infinitely long time record $\eta(0,t)$ taken at a point in space $x=0$, the spectrum is defined as

$$A(\omega)e^{j\theta(\omega)}=\int_{-\infty}^{\infty}\eta(0,t)e^{-j\omega t}dt \qquad \textbf{2. 2}$$

In this ideal case the wave elevation at any point would be defined using *Equation 2.* 1. The prediction process in the Fixed Point mode can be represented as an all pass filter with a nonlinear phase derived from the dispersion relation. The distance (x) is considered a filter parameter, where the original phase *θ(ω)* is adjusted by the factor $\left(\frac{\omega^2}{g}x\right)$, as demonstrated in *Figure 2. 8.*

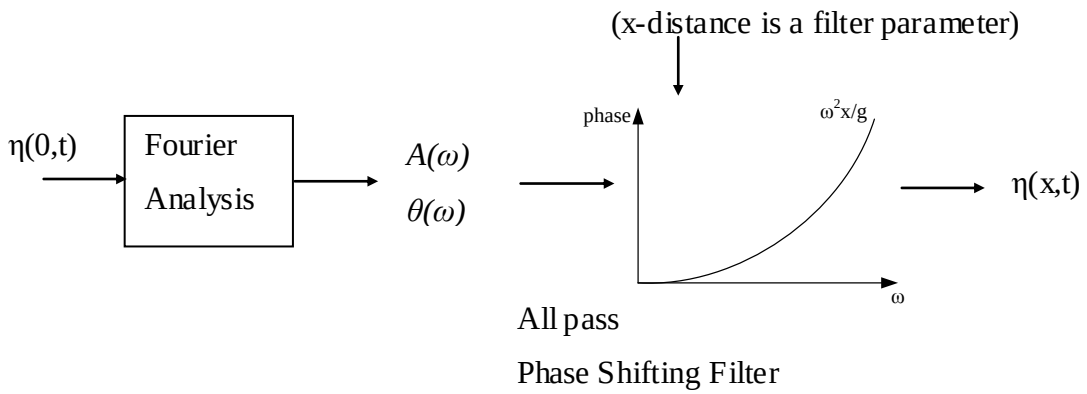

Figure 2. 8 Linear wave prediction for Fixed Point mode

The practical Fixed Point DSWP process measures the wave at $x = 0$ for a period of $0 < t < N\tau$, where we assume the time record combines N points with a sampling interval τ . The DFT is used to estimate the spectrum of this piece of sea.

$$A'\left(\frac{n}{N\tau}\right) = \sum_{m=0}^{N-1} \eta(0, mT) e^{-j2\pi\frac{nm}{N}} \qquad n = 0,1,2\ldots\ldots N-1 \qquad \textbf{2. 3}$$

The Fourier coefficients obtained are incorporated in a wave train prediction model given by :

$$\eta'(x,t) = \frac{1}{N}\sum_{no0}^{N-1} A_n \cos(k_n x - \omega_n t - \theta_n(\omega_n)) \qquad \textbf{2. 4}$$

Where $\omega_n = \frac{2\pi}{NT} n$ and $k_n = \frac{4\pi^2 n^2}{N^2 T^2 g}$

$$A_n = \left|A'\left(\frac{n}{N\tau}\right)\right| \text{ and } \theta_n = \angle A'\left(\frac{n}{NT}\right)$$

A key objective in DSWP research is to find the relation between the estimated wave elevation *η′(x,t)* and original wave height *η(x,t)*. Also an important issue is to identify the region on the *(x,t)* plan where the error between the estimated wave elevation is sufficiently small to be practically useful.

2.5.2 Linear wave prediction for the fixed time mode

The development of the prediction model for fixed time mode is similar to the fixed point case, however, the linear wave elevation is represented using the wave number spectrum *B(k)*:

$$\eta(x,t)=\int_0^{\infty} B(k)\cos\left(kx-\sqrt{gk}+\phi(k)\right)dk \qquad \textbf{2. 5}$$

The spectrum in this case is defined using an infinitely long snapshot of the wave at time *t=0*

$$B(k)e^{j\phi(k)}=\int_{-\infty}^{\infty}\eta(x,0)e^{-jkx}dx \qquad \textbf{2. 6}$$

As was the case with the Fixed-Point mode the prediction in this mode can also be represented using an all pass filter with a nonlinear phase $\left(\sqrt{kg}\,t\right)$. The prediction time *(t)* is a parameter to the propagation filter as shown in *Figure 2. 9.*

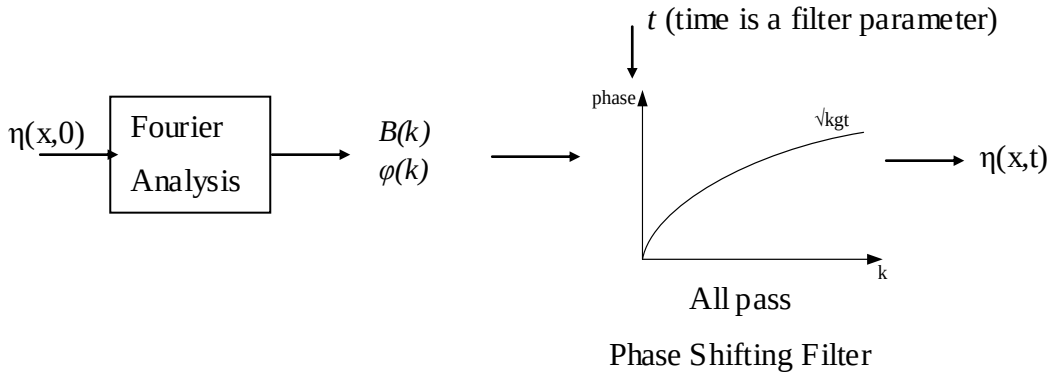

Figure 2. 9: Linear wave prediction for Fixed Time mode

In this mode the DSWP process assumes *N* instantaneous measurements of the wave surface are taken at *t= 0* over the distance *0<x<Nα* where *α* is the sampling interval. The spectrum is estimated using DFT

$$B'\left(\frac{n}{N\alpha}\right)=\sum_{m=0}^{N-1}\eta(m\alpha,0)e^{-j2\pi\frac{nm}{N}} \qquad n=0,1,2\ldots\ldots N-1 \qquad \textbf{2. 7}$$

These coefficients are then used in building the prediction model for the Fixed Time mode as:

$$\eta'(x,t)=\frac{1}{N}\sum_{no0}^{N-1}B_n\cos\left(k_n x-\omega_n t-\phi_n\right) \qquad \textbf{2. 8}$$

Where $k_n=\dfrac{2\pi n}{N\alpha}$ and $\omega_n=\sqrt{gk_n}$

$B_n=\left|B'\left(\dfrac{n}{N\alpha}\right)\right|$ and $\phi_n=\angle B'\left(\dfrac{n}{N\alpha}\right)$

2.5.3 Prediction improvement using End Matching

The continuous forms given in *Equation* 2. 1 and *Equation* 2. 5 can't be used in real practice due to the fact that infinitely long records of the sea waves are not realistically available, and even if they were for the sake of argument, the sea wave are only stationary over limited time and space. Limiting the size of the wave records introduces various windowing problems, however the DSWP doesn't aim to estimate the full spectrum of the sea (if such a thing exists), instead the aim is to use the spectrum of a small piece of the sea where stationary and linearity conditions hold, to estimate the wave's elevation in the other part of the wave field. A major issue in DSWP is finding out to what extent information in this small piece of the sea, can be used to describe other pieces of the wave surface.

The use of discrete Fourier Transform to estimate the wave's spectrum forces unnatural periodicity on the sea surface wave's model. The quality of prediction is found to depend on the alignment of the two ends of the wave's measurements records. Accordingly the less the difference between the value and all derivatives of the records two ends, the better continuity is achieved, and hence the better the prediction becomes. The End Matching algorithm suggested in [2] reduces prediction errors by minimizing the difference in both the elevation and slope at the edges of the data record.

The algorithm includes searching the data record for the part of the record where the two ends satisfy certain restrictions put on the difference in elevation and slope. While this part of the data record is passed to the prediction model, the rest of the data record is discarded. The end matching algorithm also should include a restriction to avoid over-reduction of the data record. A slightly modified version of this algorithm is suggested in *Section 4.3* and a comparison of the prediction results using end matching to the results using classical windowing methods is presented in *Section 4.4*.

2.6 Time \ Spatial Domain based prediction model

The periodic nature of the models produced by the spectrum based techniques, and the inadequacy of traditional windowing techniques in solving the energy leakage problem without deforming the time/spatial information, also the time requirements for the alternative end matching method, all drove the research in DSWP systems to

investigate the use of finite impulse response filters to provide the required dispersive phase shifting.

Finding the impulse response of the prediction filters would allow the prediction of waves using the convolution method. In [44] it is found that in the two operation modes (Fixed Time mode, Fixed Point mode) the impulse response and its respective spectrum both have infinite support in each of their respective domains. This appears to be a breach of the uncertainty principle, which states that the width in one domain is inversely related to the width in the conjugate domain. However, this issue was dealt with by truncation of the spectrum band width of the propagation filters

In the Fixed Point mode the spectrum is limited to $\omega_{\min} < \omega < \omega_{\max}$ resulting in the impulse response $\lambda(x,t)$ given by :

$$\lambda(x,t) = \sqrt{\frac{2\pi g}{x}}\left\{ cos\left(\frac{g}{4x}t^2\right)\left[C\left(\frac{1}{\sqrt{2\pi g x}}\left(2\omega_{\max}x - gt\right)\right) - C\left(\frac{1}{\sqrt{2\pi g x}}\left(2\omega_{\min}x - gt\right)\right)\right]\right.$$

$$\left. + sin\left(\frac{g}{4x}t^2\right)\left[S\left(\frac{1}{\sqrt{2\pi g x}}\left(2\omega_{\max}x - gt\right)\right) - S\left(\frac{1}{\sqrt{2\pi g x}}\left(2\omega_{\min}x - gt\right)\right)\right]\right\} \qquad \textbf{2. 9}$$

Where C, S are the Fresnel integrals.

While in the Fixed Time mode the spectrum is limited to $k_{\min} < k < k_{\max}$ resulting in the impulse response $\zeta(x,t)$ given by

$$\zeta(x,t) = \frac{1}{x}\left(sin\left(k_{max}x - \sqrt{k_{max}g}t\right) - sin\left(k_{min}x - \sqrt{k_{min}g}t\right)\right)$$

$$+ \sqrt{\frac{\pi g}{2}}\,\frac{t}{x^{3/2}}\left\{ tcos\left(\frac{g}{4x}t^2\right)\left[C\left(\frac{1}{\sqrt{2\pi g x}}\left(2\sqrt{k_{max}g}\,x - gt\right)\right) - C\left(\frac{1}{\sqrt{2\pi g x}}\left(2\sqrt{k_{min}g}\,x - gt\right)\right)\right]\right.$$

$$\left. + \left[S\left(\frac{1}{\sqrt{2\pi g x}}\left(2\sqrt{k_{max}g}\,x - gt\right)\right) - S\left(\frac{1}{\sqrt{2\pi g x}}\left(2\sqrt{k_{min}g}\,x - gt\right)\right)\right]\right\} \qquad \textbf{2. 10}$$

Prediction filter responses in [44] are derived using the one dimensional transfer function of all-pass filters demonstrated in *Figure 2. 8* and *Figure 2. 9* . A similar result is achieved using the two dimensional spectrum introduced in *Chapter 4*. Properties of these filters responses are investigated in *Chapter 6*, explaining the unusual behavior of these filters. *Chapter 6* also demonstrates the result of prediction using this approach.

2.7 Wave model

The experimental wave data records available to date for marine research are not suitable for the purposes of this work, since to test the different prediction algorithms on real sea waves would require both spatial and temporal information. For the Fixed Point mode , time records would be needed for at least two stations separated by a few hundred metres. As for the Fixed Time mode in addition to photogrammetric shots of up to 1000m of sea wave, data from down stream sites are also required. Thus artificial sea models must be used.

The earlier DSWP work model the sea using wave spectrum models with the same characteristics as the Nonweiler [45] spectrum. These models had very coarse frequency resolution using modest number of components as low as five components in some cases. Although these components were widely separated in the frequency domain, they are not from a harmonic series, instead they belong to the more general class of Almost Periodic Functions[46] [47]. In more recent work in DSWP a much smaller frequency resolution is used allowing a large number of very closely compact components resulting in a more effective sea wave simulation.

A collection of methods for numerical simulation of irregular sea waves is found in[48] [49], including the wave superposition method used in this work. The typical linear dispersive sea surface generating function given by *Equation* 2. 11 is used for simulation purpose throughout this work where η(x,t) is the wave elevation at point x and time *(t)* .

$$\eta(x,t) = \sum_{i=1}^{N} A_i \cos\left(\frac{\omega_i^2}{g}x - \omega_i t + \theta_i\right) \qquad \textbf{2. 11}$$

Where θ_i phase is randomly distributed $\left(\frac{-\pi}{2} < \theta_i < \frac{\pi}{2}\right)$

While the components $A_i = \sqrt{2 \,.\, S(\omega_i).\delta\omega}$ are defined using the wave spectrum model $S(\omega)$ defined in *Equation 1.7,* and sampled with a frequency resolution $\delta\omega$.

The Pierson Moskowitz spectrum introduced in *Section 1.3.3* provides the simulation of all sea like waves used in testing the algorithms studied in this work. The Pierson Moskwitz spectra for different wind speed are shown in *Figure 2. 10*. The lower boundary of the spectrum is set at the frequency below which 5% of the total sea power

is present. This frequency is calculated from *Equation*1. 9. where (r_1=0.05). The upper boundary is set at the frequency above which 5% of the total power is present, using *Equation1. 10* where (r_2=0.05). The lower and the upper spectrum limits for different wind speeds are given in *Table 2.1 and Table 2.2.* The same tables contain other spectrum parameters of the Pierson Moskowitz sea with different conditions.

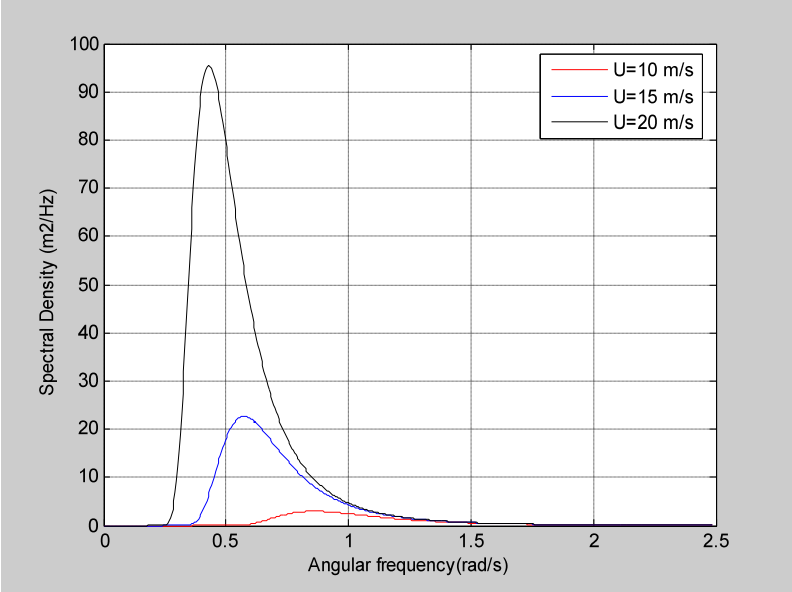

Figure 2. 10 Pierson Moskowitz sea with different wind conditions

Table 2.1 Pierson Moskowitz Parameters for different wave conditions ((frequency)

U m/s	*SWH m*	*ω_max rad/s*	*ω_min rad/s*	*Δω rad/s*	*ωo rad/s*	*ω_dominant rad/s*	*T_ dominant S*
5	*0.6150*	*3.8199*	*1.3818*	*1.2190*	*2.6008*	*1.3748*	*4.5704*
10	*2.4600*	*1.9099*	*0.6909*	*0.6095*	*1.3004*	*0.6874*	*9.1407*
15	*5.5350*	*1.2733*	*0.4606*	*0.4063*	*0.8669*	*0.4583*	*13.7111*
20	*9.8400*	*0.9550*	*0.3454*	*0.3048*	*0.6502*	*0.3437*	*18.2814*
25	*15.3750*	*0.7640*	*0.2764*	*0.2438*	*0.5202*	*0.2750*	*22.8518*
30	*22.1400*	*0.6366*	*0.2303*	*0.2032*	*0.4335*	*0.2291*	*27.4222*

Table 2.2 Pierson Moskowitz Parameters for different wave conditions (wave number)

U m/s	*SWH m*	*k_max rad²/m*	*k_min rad²/m*	*Δk rad²/m*	*ko rad²/m*	*k dominant rad²/m*	*L dominant m*
5	*0.6150*	*1.4889*	*0.1948*	*0.6470*	*0.8419*	*0.1929*	*32.5797*
10	*2.4600*	*0.3722*	*0.0487*	*0.1618*	*0.2105*	*0.0482*	*130.3188*
15	*5.5350*	*0.1654*	*0.0216*	*0.0719*	*0.0935*	*0.0214*	*293.2174*
20	*9.8400*	*0.0931*	*0.0122*	*0.0404*	*0.0526*	*0.0121*	*521.2753*
25	*15.3750*	*0.0596*	*0.0078*	*0.0259*	*0.0337*	*0.0077*	*814.4927*
30	*22.1400*	*0.0414*	*0.0054*	*0.0180*	*0.0234*	*0.0054*	*1172.9*

The next step in the wave simulation is to define (N=100) uniformly distributed spectral sampling points (ω_i) given by:

$$\omega_i = i\left(\frac{\omega_{max} - \omega_{min}}{N}\right) + \omega_{min} \qquad \text{Where } i=1,2,3\ldots\ldots N \qquad \textbf{2. 12}$$

The angular frequency (ω_i) form a regular harmonic sequence, which in turn results in an unnatural periodicity in the simulation. This is adjusted by adding a random factor (r) which shifts the frequency sampling points from their original locations. The adjusted spectrum sampling points are given by :

$$\omega_i = i\left(\frac{\omega_{max} - \omega_{min}}{N}\right) r + \omega_{min} \qquad -0.2 < r < 0.2 \qquad \textbf{2. 13}$$

The wave components required for the wave model defined by *Equation*2. 11 are found by sampling the Pierson Moskowitz spectrum at the point ω_i given by *Equation* 2. 13.

Chapter 3

Wave Shadowing and Nonuniform sampling

3.1 Introduction

As explained in the previous chapters, DSWP requires measurements of the shape of the sea surface remote from the prediction site; the results are then used to build a short term prediction model. For fixed locations applications such as offshore oil/gas rigs, support vessels deploying submersibles and shuttle tankers, it is possible to utilize the Fixed Point DSWP operating mode, where measurements are made at a set of fixed spatial locations. This allows the use of traditional wave-slope buoys. However the sea data demands for the wider solution for both fixed sites and free moving vessels are beyond the scope of existing wave measurement systems[20].

Enabling the use of different implementation modes such as Fixed Time requires some kind of particle remote sensing. At present satellite based sensors do not have the required resolution and also do not provide 24 hour coverage of specific locations. Also attempts to exploit micro-wave radars using developments of image processing techniques such as WAMOS system have yet to be proven. This prompted the growing interest in the use of scanning LIDAR as an alternative to RADAR in sea surface profiling applications. These systems are typically near normal incidence LIDAR systems where air craft are used. For general purpose real time operations these air craft based system are not cost effective, which raises the need for vessel mounted LIDAR systems which in order to have an effective horizontal range operate at very shallow angle, hence gaining there name (shallow angle LIDAR systems).

The key difference between shallow angle systems and the traditional systems is that the spatial location of the samples are non- uniformly distributed, and part of the sea profile is missing as a result of wave shadowing, as illustrated in *Figure 3. 1*. The shadowing happens when the rear wave slope exceeds the angle of the sensing beam. Signal processing strategies required for the prediction process are significantly affected by both the non-uniform sampling and the wave shadowing problem. The main consequence of these differences is that traditional signal processing techniques- like discrete Fourier Transform and digital filters- can't be directly used on the collected data.

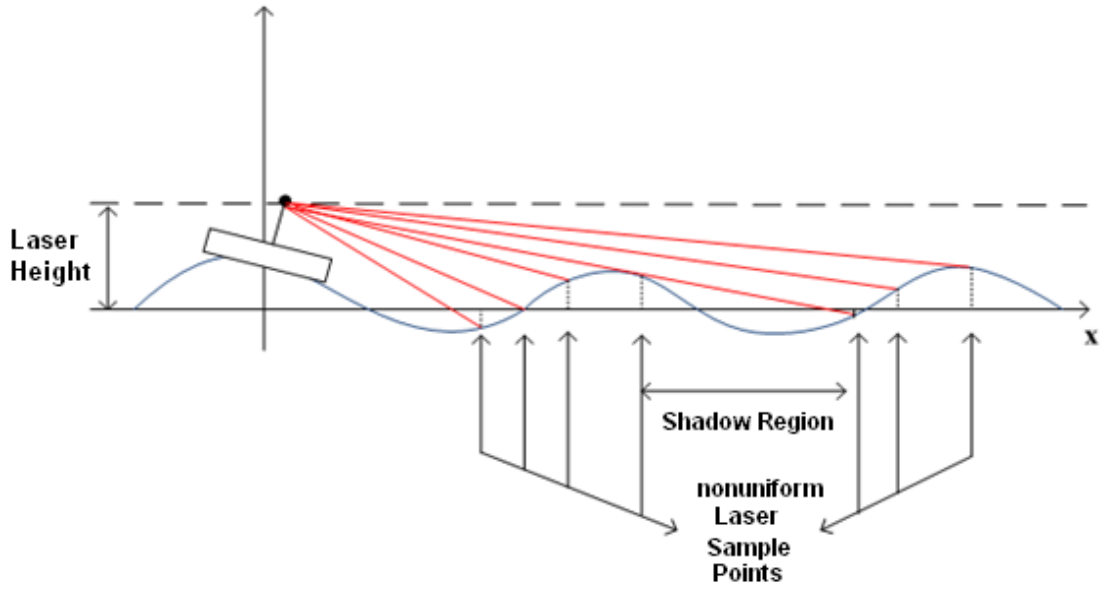

Figure 3. 1: Shallow angle LIDAR system

The properties of the wave shadow regions associated with different wave models and different laser position are the subject of *Section 3.2* of this research. The nonuniform sampling problem is addressed in the remaining of this chapter. Different methods for signal reconstruction are implemented.

3.2 Wave Shadowing

Wave shadowing is the most extreme form of Non-uniform sampling. These gaps in the wave profile have profound effects on the utilization of data from shallow angle LIDAR. The wave shadow effect is superficially obvious in so far as it reflects the absence of data, although as will be shown it is possible to compensate somewhat for this. The main problem associated with the non-uniform sampling is that most signal processing algorithms used in data manipulation require a uniform sample distribution.

Thus it is necessary to transform the sea surface elevation data onto a uniform sampling grid. This later problem has been explored in relation to shallow angle LIDAR[50] [51] [52], and thus the emphasis here will be on wave shadowing.

The prediction time associated with Deterministic Sea Wave Prediction derives from the time taken for the fastest wave component to travel from the measurement location to the prediction site. Clearly all computation associated with signal processing or prediction model building directly subtracts from the potential prediction time. Using wave shadowed data is associated with significant computational costs and thus a user wishing to plan an operation involving a DSWP system must have a good understanding of the significance of wave shadowing under the prevailing conditions. Such information can be obtained by simulating the shallow angle LIDAR measurement process as in the following section.

3.2.1 Shallow Angle LIDAR Simulations

The model of the LIDAR measurement situation explored here is based upon a variant of *Figure 3. 1* in which the vessel mounted sensor is replaced with a fixed device at an elevation *(Laser-height)* above the (SWL). On the scale of the problem the beam width can be neglected even at shallow angles and thus the probe beam is represented by a line which intersects the sea surface.

In the study of the shadow region of a Pierson-Moskowitz sea using this simulation, five wind speeds were chosen to cover different sea conditions (5,10,15, 20,25,35)m/s. In each case 100 samples are taken from the corresponding spectrum band width. Instead of using equally spaced samples it was chosen to use a random variation factor of 0.2 to alter the frequency sampling values, this is done to avoid generating periodic seas in our model, full details on the simulation are given in *Section 2.7*.

Using this basic model sea wave elevation is calculated over the space range (0-1000)m with a resolution of one metre. To obtain statistics which depend on wave time records, many successive snap-shots are required, covering a time interval of two minutes with a time step of one second. This gives a total of (120)*s* long time record for each point in space. Figure 3. 2 shows the simulation grid used in this study.

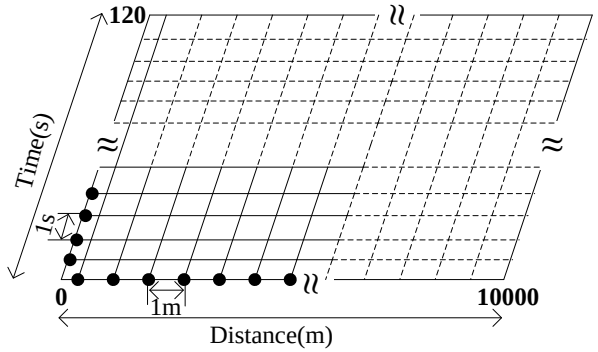

Figure 3. 2: Wave simulation grid

The next step is to find the shadow region of each point on this grid. The shadow region is calculated using the function:

$$shadow\_region(x,t) = \begin{cases} 1, & LH(\gamma,t) > \eta(\gamma,t) \quad for \quad Ld < \gamma < x \\ 0, & otherwise \end{cases} \qquad \textbf{3. 1}$$

Where

LH is the laser height

Ld is the laser distance to the measurement region

The shadow region characteristics don't only depend on the wave properties but also on the laser point position (laser height, laser distance). In this study the shadow regions were found for eight different laser heights (10,20,30,40,50,60,70,75) m above SWL, see Figure 3. 3. As for the laser distance from the measurement region, 500m was chosen, this distance is sufficient to avoid the affect of ship wave on the original wave system.

The user panel described in Appendix B- provides a useful tool in exploring the properties of the shadow region under the conditions described above. This panel displays individual snapshots, and gives a powerful visual indication of the shadow region properties. However, for an extended study the property of a more comprehensive set is required, which is the subject of the coming section.

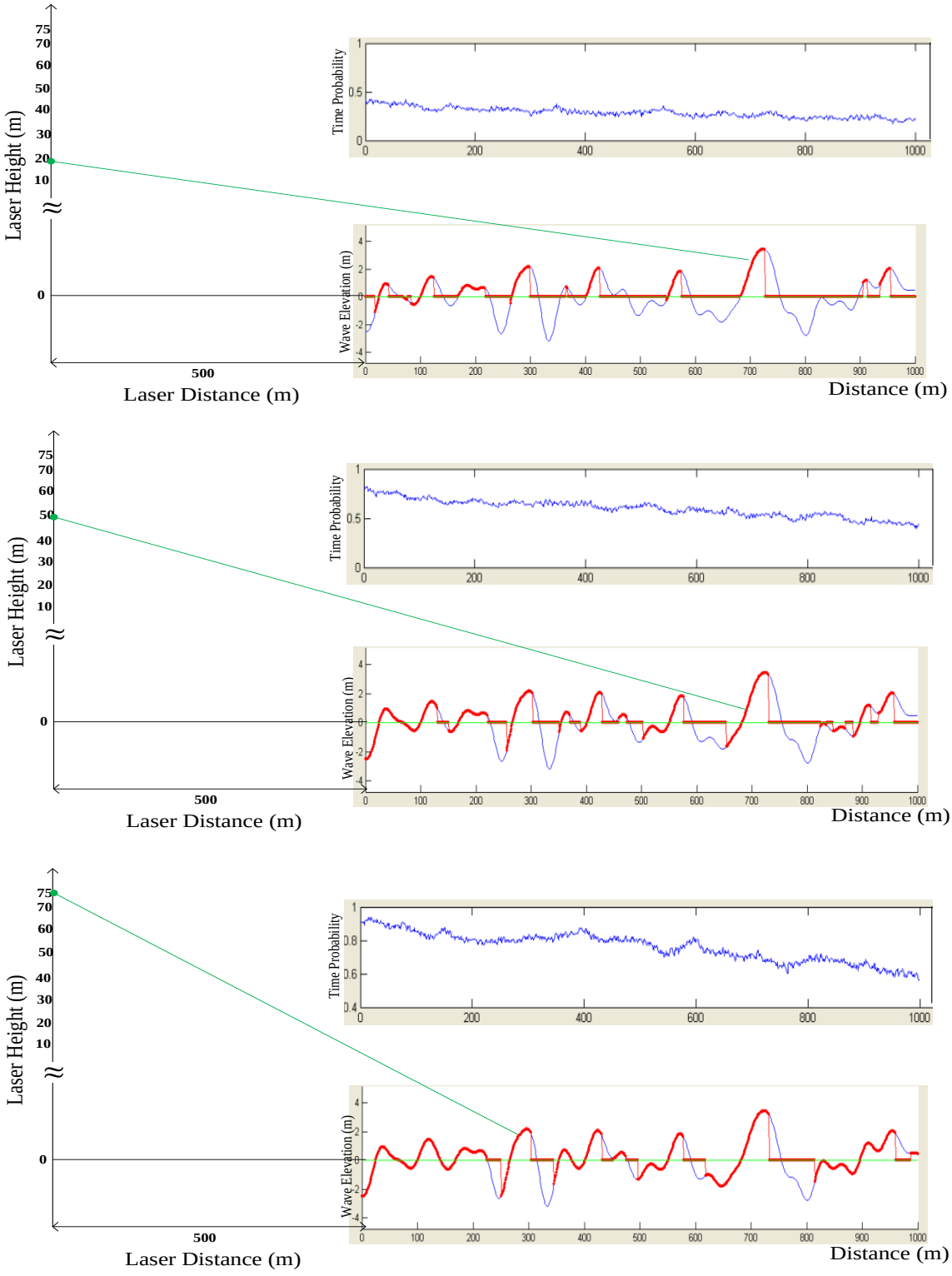

Figure 3. 3: Shallow angle LIDAR system Simulation

3.2.2 Shadow region Parameters

Four shadow region parameters are defined to help find the empirical relations between the shadow region properties for different wave models resulting from scanning with different laser positions. The first two parameters describe the shadow region in the spatial domain, while the other two are the equivalent in the time domain.

The First parameter is the (Non-shadow space). This indicates the percentage of the available regions of each snap-shot. For example if 60% of the(1000 m) snap-shot is a non shadow region, this means that 400 m are found to be shadow region points while the laser beam has a clear path to the remaining 600 m.

The second parameter (Space shadow length) gives more detailed information than the first parameter, since this parameter considers the actual length of the individual shadow region. This length is an indication of the best possible separation between the collected data, which in turn is an important factor in the reconstruction procedure. An important practical implementation of this parameter is to indicate the suitability of a certain reconstruction algorithm, given that many reconstruction algorithms from non uniform data are associated with a necessary condition that is usually in terms of the average sampling rate and the maximum separation of the data points.

Third is the (Non-shadow time period) parameter. This is the equivalent to the first parameter but in the time domain. Hence if 60% of the time record at a certain point is available, this indicates that for 72s from the total 120s the laser beam can get a hit at that certain point in space.

The fourth parameter (Time shadow length) considers the actual length of the individual shadow region in the time dimension. As with the second parameter this is an indication of the best possible separation between the collected data, representing an important factor in the reconstruction procedure, and indicating the suitability of reconstruction algorithms.

These four parameters were calculated for a set of one thousand different wave fields. The final step is to find the distribution of these four main parameters. A kernel smoothing method [53] is used to estimate the probability density function of these four parameters. Figure 3. 4 is an illustration of these probability distributions. The full set of these distributions are given in Appendix A.

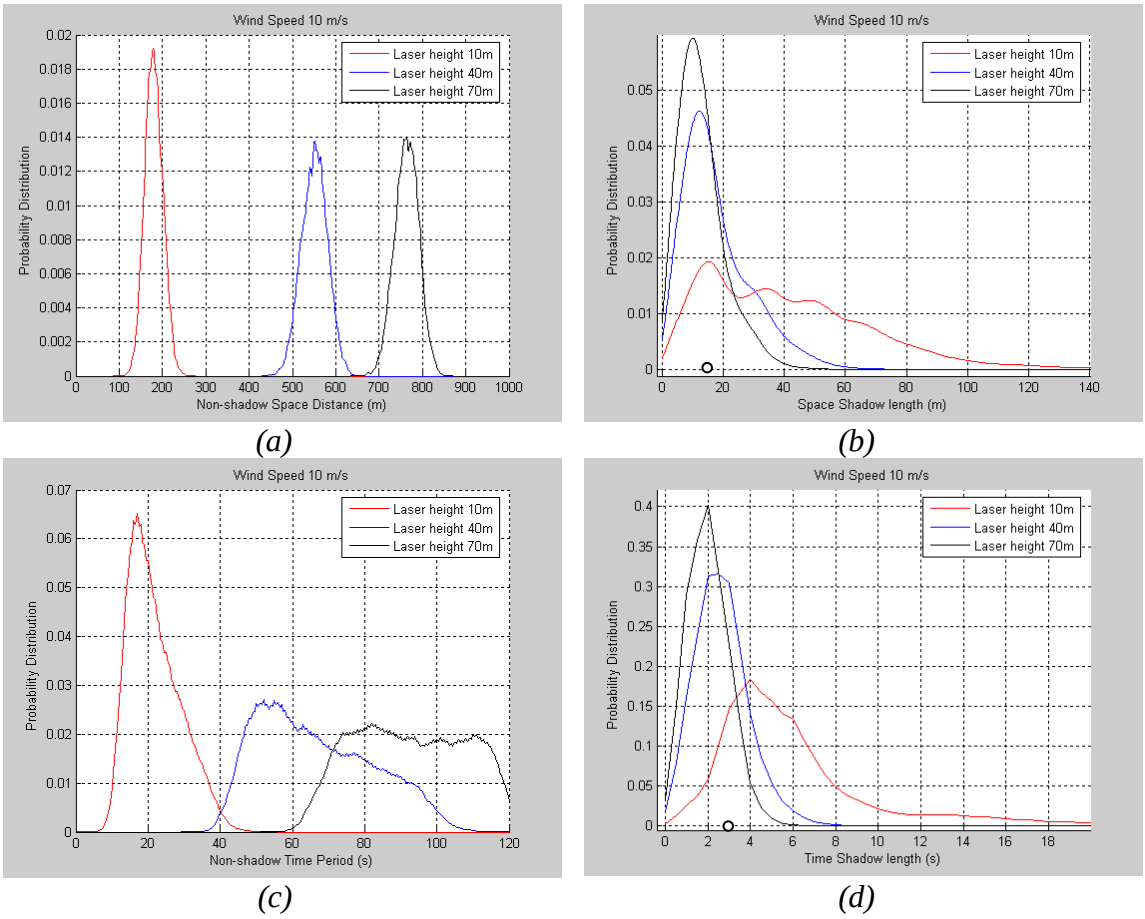

Figure 3. 4 Shadow region parameters distribution

The most important finding of the simulation study is that it provides measures of the fraction of the time for which wave shadowing is insignificant under given conditions (sensor elevation, scan distance, wind strength etc). This in turn indicates the fraction of the time for which it is possible to employ DSWP in a marine operation without the additional time penalty (reduced prediction time) introduced by the wave shadow effects. Such information is critical in planning any type of marine operation for which DSWP plays a central role. For example the plot in Figure 3. 4-a shows that in case of a 70 metre high laser on average 75% of the region can be scanned, this percentage dropes to less than 20% when the laser height is only 10 metres. The shadow length distribution plotted in Figure 3. 4-b indicate that in the case of 70 metre high laser most of the shadow region length are between 5 and 20 metres, while in the case of a 10 metre laser height the most of the shadow region length are between 10 and 60 metres .

Given the practical value of this information it is useful to look for ways of reducing the large number of figures needed to display such information. After some exploration it transpires that the probability data can be conveniently compacted by

recognizing that by simply normalizing the shadow length by the dominant wavelength. The probabilities of this normalized quantity appear to solely depend on laser height. The same applies to the shadow duration when normalized by the dominant wave period. This is a purely empirical finding but certainly applies to all the cases explored. The results of such normalization are shown in *Figure 3. 5* . The value of such normalization is that for a PM sea at any wind speed the mean shadow length depends solely on laser elevation.

The above has even further ramifications for the work described in the remainder of this chapter which deals with methods of reconstructing the data in shadowed regions. The dependence of the normalized data solely on laser elevation suggests that the errors in such reconstruction processes should also depend only on laser height. This suggestion is actually confirmed in the results presented in *Section 3.6*

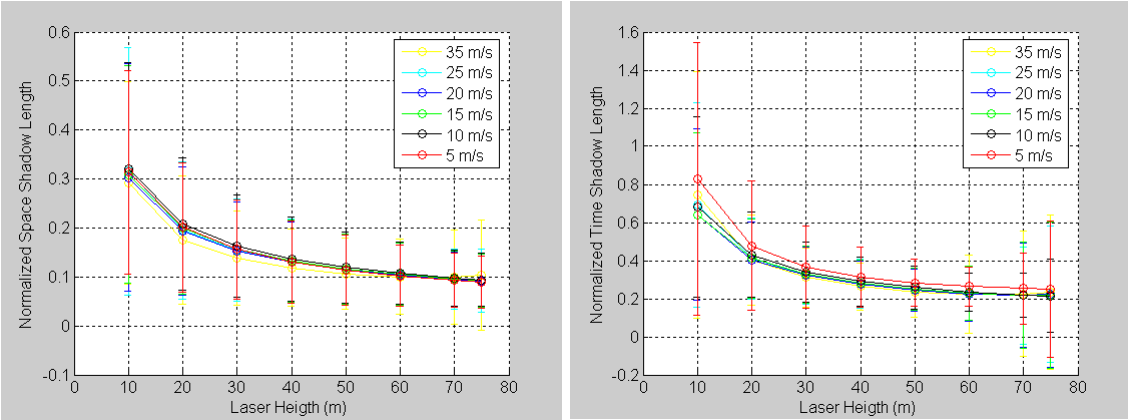

(a) *(b)*

Figure 3. 5 normalized shadow region parameter distributions

3.3 Wave Reconstruction

If DSWP is required on an occasional basis then the sensible strategy is to repeatedly acquire LIDAR sea profile scans retaining only those for prediction purposes that do not contain significant wave shadowing. However if continuous DSWP is critical to the task at hand, e.g., during committed aircraft recovery onto a vessel, then it is necessary to explore what information can be recovered from wave shadowed data.

A very simple application of the sampling theorem [54] [55] shows that provided a spatial profile of the wave is a band limited function with finite support it is possible to generate a set of trigonometric polynomial equations that in principle can be inverted to provide a uniformly sampled set of profile values. Furthermore provided there are enough samples so that the data on average satisfies the Nyquist sampling condition and also the distances to the samples form a monotonically increasing set then it is again in

principle possible to have very large gaps in the data, i.e., shadowed regions. As is well known simple inversion of the sampling theorem is highly ill-conditioned, [56]and as a consequence numerous techniques have been explored for achieving this reconstruction.

Some of these techniques are actually non-uniform to uniform sample mappings with a very restricted deviation from uniformity while others are able to reconstruct significant length shadowed regions.

3.4 Nonuniform Sampling

In many applications nonuniform sampling is more efficient than uniform sampling. However, the implementation nonuniform sampling remains limited. This type of sampling is still not totally understood, mainly because of the technical problems involved in the time and frequency domain analysis. Furthermore from a practical point of view, the nonuniform sampling does not have a simple reconstructed method like low pass filtering used in the case of uniform sampling, a complicated nonlinear form of time varying filter is required for signal recovery, as will be discussed in the coming section. For a comprehensive theoretical and practical background a tutorial exposition and a review of papers on the non uniform sampling is found in [57] [58] .

To appreciate the difficulty of analyzing a nonuniformly sampled signal, we need to illustrate the uniform case. The key factor in analyzing the uniform sampled signal comes from the fact that Fourier transform of an impulse train is also an impulse train, this is demonstrated by:

$$s(t) = \sum_{n=-\infty}^{\infty} \delta(t - nT) \Leftrightarrow \sum_{n=-\infty}^{\infty} e^{j\omega nT} = \frac{1}{T} \sum_{n=-\infty}^{\infty} \delta\left(f - \frac{n}{T}\right)$$

$$for\ n = -\infty \dots \dots -2, -1, 0, 1, 2, \dots \dots \infty$$

3. 2

Where $f = \frac{\omega}{2\pi}$

The sampled signal $\eta_s(t)$ results from multiplying the original signal $\eta(t)$ with the sampling function $s(t)$. The multiplication in the time domain results in convolution of the two spectra in the frequency domain, and since the uniform sampling function is an impulse train given *Equation 3. 2*. The original spectrum will be simply repeated in the frequency domain. As long as the sampling frequency is above the Nyquist rate there will be no aliasing and the original spectrum can be obtained by a simple low frequency filter.

Unfortunately, the spectrum analysis is not as simple in the case of irregular sampling, this is mainly because the spectrum of a set of nonuniform impulses is not another set of nonuniform impulses, this is given by:

$$\delta(t) = \sum_{n=-\infty}^{\infty} \delta(t - t_n) \Leftrightarrow \sum_{n=-\infty}^{\infty} e^{j\omega t_n} = S(f) \qquad \textbf{3. 3}$$

There is no general form of *S(f)* and typically it is not a simple impulse train. This results in the spectrum of nonuniformly sampled signal being smeared. Methods required to deal with irregular samples are more demanding [59] [60] and complicated filters are required to recover the original signal. [61] [62]

The next *Sections 3.5 to 3.7* deal with various methods of addressing the problem of reconstructing wave shadowed region by treating shadow as an extreme case of non-uniform sampling.

3.5 The Time Variant method

Also known as the nonlinear method, this technique was outlined in [63] [64] and implemented in [65]. It is based on the spectrum analysis of non-uniform samples that deviate from the uniform position by a finite amount. For the one dimension case, we assume that γ is the distance between the uniform positions, and x_i is the nonuniform sampling points. The sampled signal is given by:

$$\eta_s(x) = \eta(x) \cdot g_s(x) \qquad \textbf{3. 4}$$

Where

$$g_s(x) = \sum_i \delta(x - x_i)$$

If we define the function $g(x) = x - i\gamma - \theta(x)$, where $\theta(x)$ defines the deviation of the non-uniform samples from the uniform position, such that :

$$\theta(x_i) = x_i - i\gamma$$

From the theory of generalized functions, the sampling function can be written in the form of:

$$g_p(x) = \sum_i |g'(x)| \; \delta[g(x)]$$

Providing that $g(x_i) = 0$ and $g'(x_i) \neq 0$

Using this definition the Fourier expansion of the sampling function is given by:

$$g_s(x) = \frac{[1-\theta'(x)]}{\gamma}\left[1+2\sum_{i=1}^{\infty}\cos\left(\frac{2\pi.i.x}{\gamma}-\frac{2\pi.i.\theta(x)}{\gamma}\right)\right] \quad \textbf{3. 5}$$

This shows that the sampling function $g_s(x)$ has a DC component $\left(\frac{1-\theta'(x)}{\gamma}\right)$, plus phase modulated harmonics, this function is sketched in Figure 3. 6.a. From Equation 3. 4 and Equation 3. 5 the sampled signal is given by:

$$\eta_s(x) = \eta(x).\frac{[1-\theta'(x)]}{\gamma}\left[1+2\sum_{i=1}^{\infty}\cos\left(\frac{2\pi.i.x}{\gamma}-\frac{2\pi.i.\theta(x)}{\gamma}\right)\right] \quad \textbf{3. 6}$$

The spectrum of the non-uniformly sampled function is obtained by convolving the original spectrum $\eta(x)$ with the spectrum of $g_s(x)$ this is shown in Figure 3. 6-b. If the band width ω_θ of $\theta(x)$ is small where $\left(\omega_\theta << \frac{1}{2\gamma}\right)$ the narrow band phase modulated signals are removed by low pass filtering $g_s(x)$ resulting in

$$g_{slp}(x) = \frac{[1-\theta'(x)]}{\gamma} \quad \textbf{3. 7}$$

As long as there is no overlap between the narrow band phase modulated signal and the rest of the spectrum, low pass filtering the sampled signal $\eta_s(x)$ results in

$$\eta_{slp}(x) = \eta(x).\frac{[1-\theta'(x)]}{\gamma} \quad \textbf{3. 8}$$

From Equation3. 7 and Equation3. 8 the original signal can be recovered by

$$\hat{\eta}(x) = \frac{\eta_{slp}(x)}{g_{slp}(x)} \quad \textbf{3. 9}$$

In [58] it was shown that a sufficient condition for this method to converge is that $|\theta(x)| < \frac{\gamma}{\pi}$ for all x.

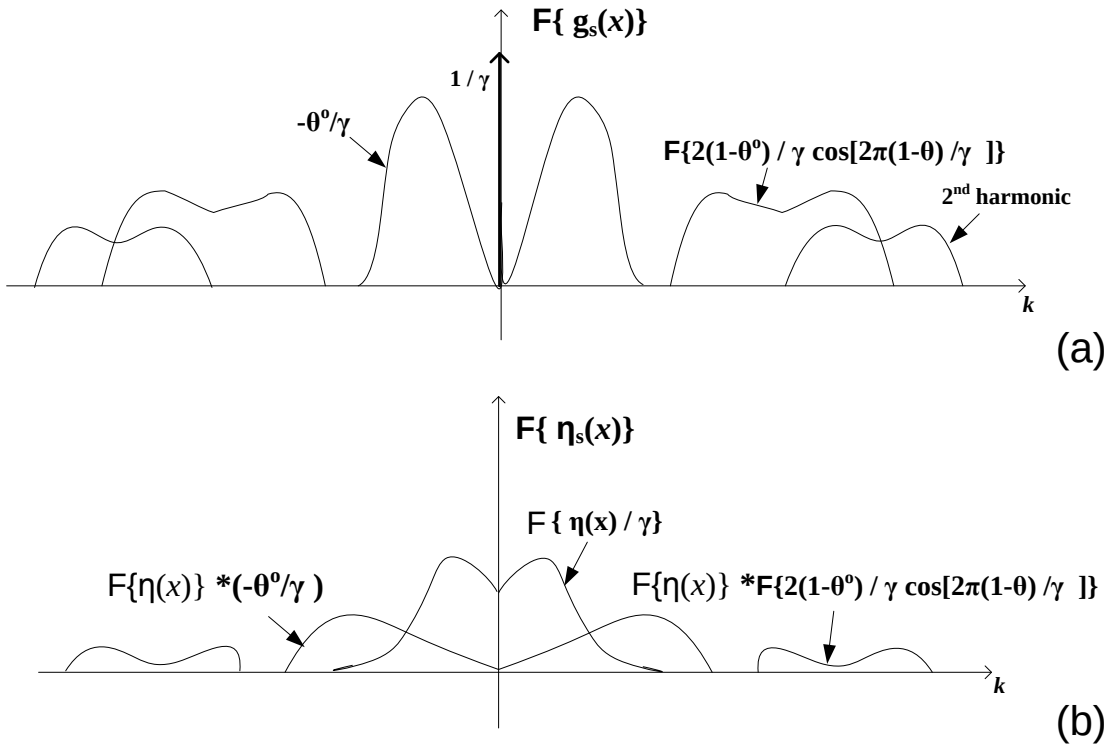

Figure 3. 6 spectrum analysis of non uniformly distributed samples

The wave simulation introduced in the previous section of different wave conditions and different laser height wave, was used to test the time varying method to reconstruct the shadow regions from nonshadow region data. The shadow region being treated as large non-uniformity. The algorithm consists of the following steps:

1. Start with N points of sea data $\eta(x_n)$
2. Determine the shadow region points from Equation 3. 1 where the sampling function g_s is defined by selecting *Ns* randomly from the non-shadow region points, where *Ns* is the number of sampling points

$$g_s(x) = \begin{cases} 1 & x \text{ is a sampling point} \\ 0 & \text{otherwise} \end{cases}$$

3. The available part of the wave is given by : $\eta_s(x_n) = \eta(x_n) \cdot g_s(x_n)$
4. Compute the Discrete Fourier Transform of the sampled signal $\mathcal{F}\{\eta_s(x)\}$ and the sampling function $\mathcal{F}\{g_s(x)\}$.
5. Truncate the spectrum of $\mathcal{F}\{\eta_s(x)\}$ at k_{max} and the spectrum of $\mathcal{F}\{g_s(x)\}$ at $\frac{k_{\max}}{2}$ to obtain the low pass spectra $\mathcal{F}\{\eta_s(x)\}_{lp}$ and $\mathcal{F}\{g_s(x)\}_{lp}$ respectively .

6. The low pass signals $\eta_{slp}(x)$ and $g_{slp}(x)$ are the result of the Inverse Fourier Transform of $F\{\eta_s(x)\}_{lp}$ *and* $F\{g_s(x)\}_{lp}$ respectively.
7. The wave is estimated by dividing the two low pass signals

$$\eta(x) \approx \frac{\eta_{slp}(x)}{g_{slp}(x)}$$

Figure 3. 7shows the shadow region reconstruction using the Time Variant method. The original wave is from a Pierson Moskowitz with wind speed $20ms^{-1}$. The laser height is set at 70m above SWL. Different sample number points are taken in each case (30,50,100,200), as expected the reconstruction improves with the increase in the number of samples.

By examining the reconstruction of the different wave forms under different scanning conditions, it is clear from the results that this construction method can not overcome the difficulty of having such large gaps. The average reconstruction error is not calculated for this method because of regular discontinuity observed in the reconstruction.

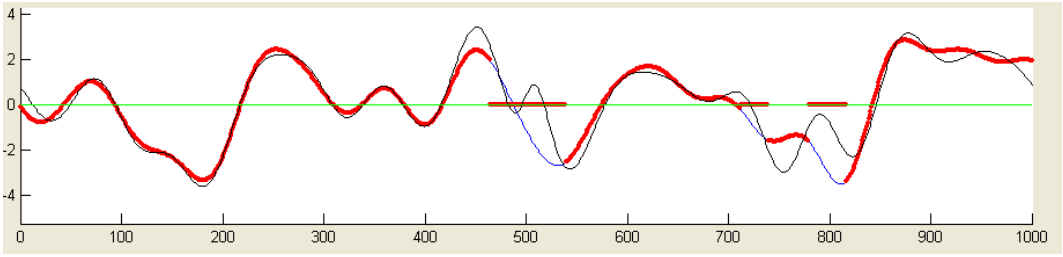

a)Extensive scanning

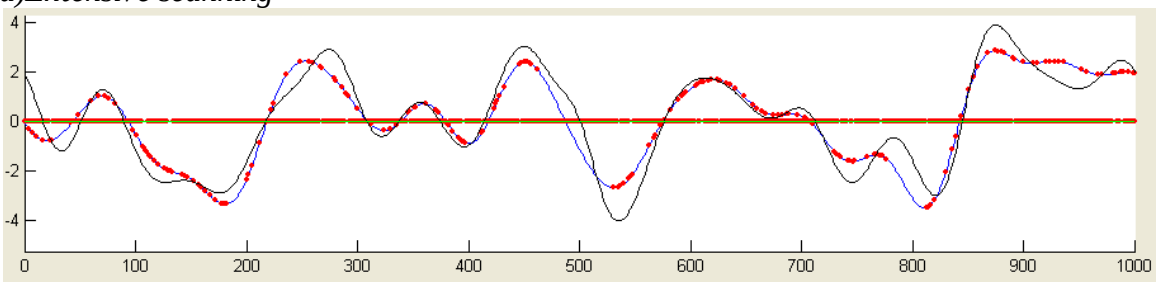

b) sample Numbers Ns=200

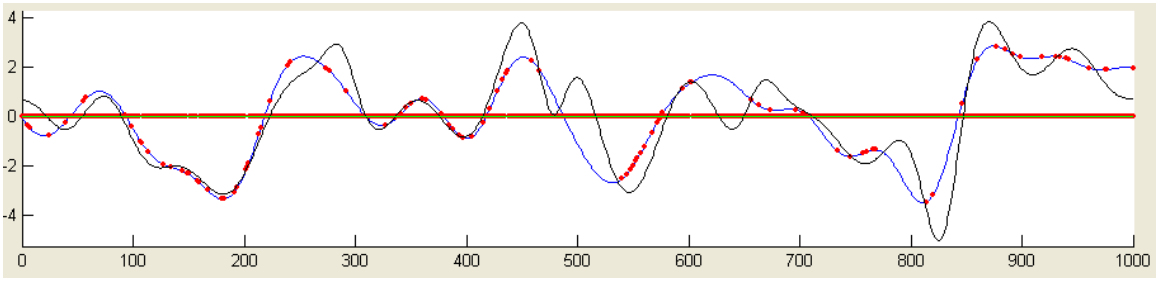

c) sample Numbers Ns=100

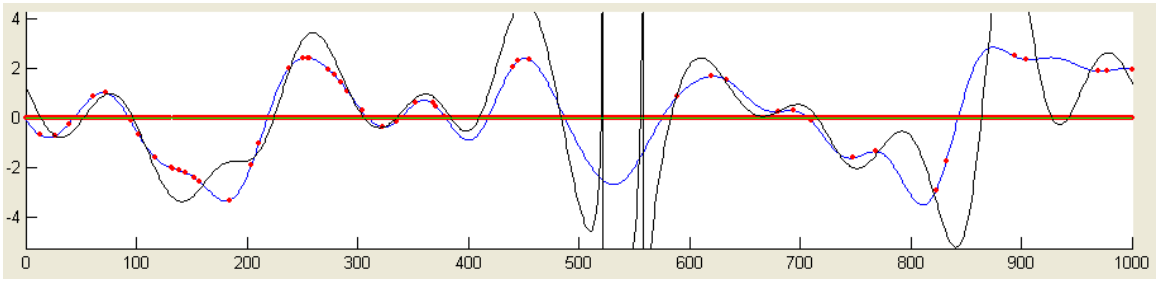

d) sample Numbers Ns=50

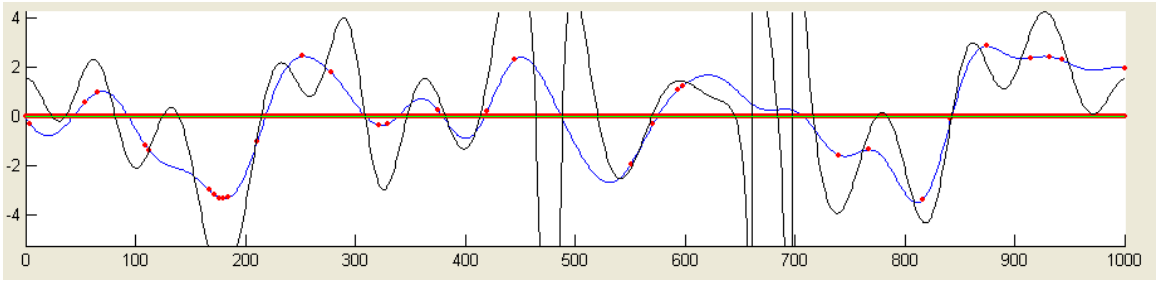

e) sample Numbers Ns=30

---- Wave snapshot ----- Wave Reconstruction ---- Sampling points

Figure 3. 7 Wave reconstruction using Time Variant Method with different sample number

3.6 Papoulis and Gerchberg method

This method of reconstruction from irregularly distributed data is based on the work done independently by Papoulis[66] and Gerchberg [67]. While Gerchberg introduced a method to perform signal reconstruction given the diffraction limit of the signal and a part of the spectrum, Papoulis' work concentrated on extrapolation of a bandlimited signal from only a part of the original signal. The signal reconstruction is carried out by the method of alternate projections [6], iterating alternately between the two conjugate domains, the space domain and wave-number spectral domain. Efficient methods for implementing this technique of signal reconstruction is found in [68] [69] .

The algorithm for implementing the alternating projection method for reconstructing the shadow region is given in the following steps:

1. Start with N points of sea data $\eta(x_n)$
2. Determine the shadow region points from Equation 3. 1 where the sampling function g_p is defined by selecting Ns randomly from the non-shadow region points, where Ns is the number of sampling points

$$g_s(x)=\begin{cases}1 & x \text{ is a sampling point}\\ 0 & \text{otherwise}\end{cases}$$

3. The available part of the wave is given by : $\eta_s^1(x_n)=\eta(x_n)\cdot g_s(x_n)$
4. Compute the Discreate Fourier Transform $F^i = DFT\left(\eta_s^i(x_n)\right)$
5. Form F_{lp}^i by truncating F^i outside k_{max}
6. Return to the conjagate domain $\eta_{lp}^i(x_n)=IDFT\left(F_{lp}^i\right)$.
7. Replace the known data parts while keeping the data at the shadow regions. $\eta_s^{i-+1}=\eta_s^1(x_n)+\eta_{lp}^i(x_n)\cdot \bar{g}_s(x_n)$ where $\bar{g}_s(x_n)$ is the inverse of the sampling function $g_s(x_n)$.

Figure 3. 8 illustrates the basic iterative method. The example shown is from Pierson Moskowitz wave with wind speed 15 ms^{-1} and laser height 40m. Figure 3. 8-a shows the non shadow region in red with the original wave plotted in blue. The first part of the iterative algorithm -shown in Figure 3. 8-b- shows the result of the low filtering stage plotted in black. The next stage is the resampling shown in Figure 3. 8-c where the known data are put back while the shadow region parts of the low pass filter output are kept. The discontinuity caused by the resampling step is adjusted by the low pass

filtering. This process is repeated until a certain criterion is obtained, this could be a given error factor or the number of iterations. The final Figure 3. 8-d shows the reconstruction result after 20 iterations.

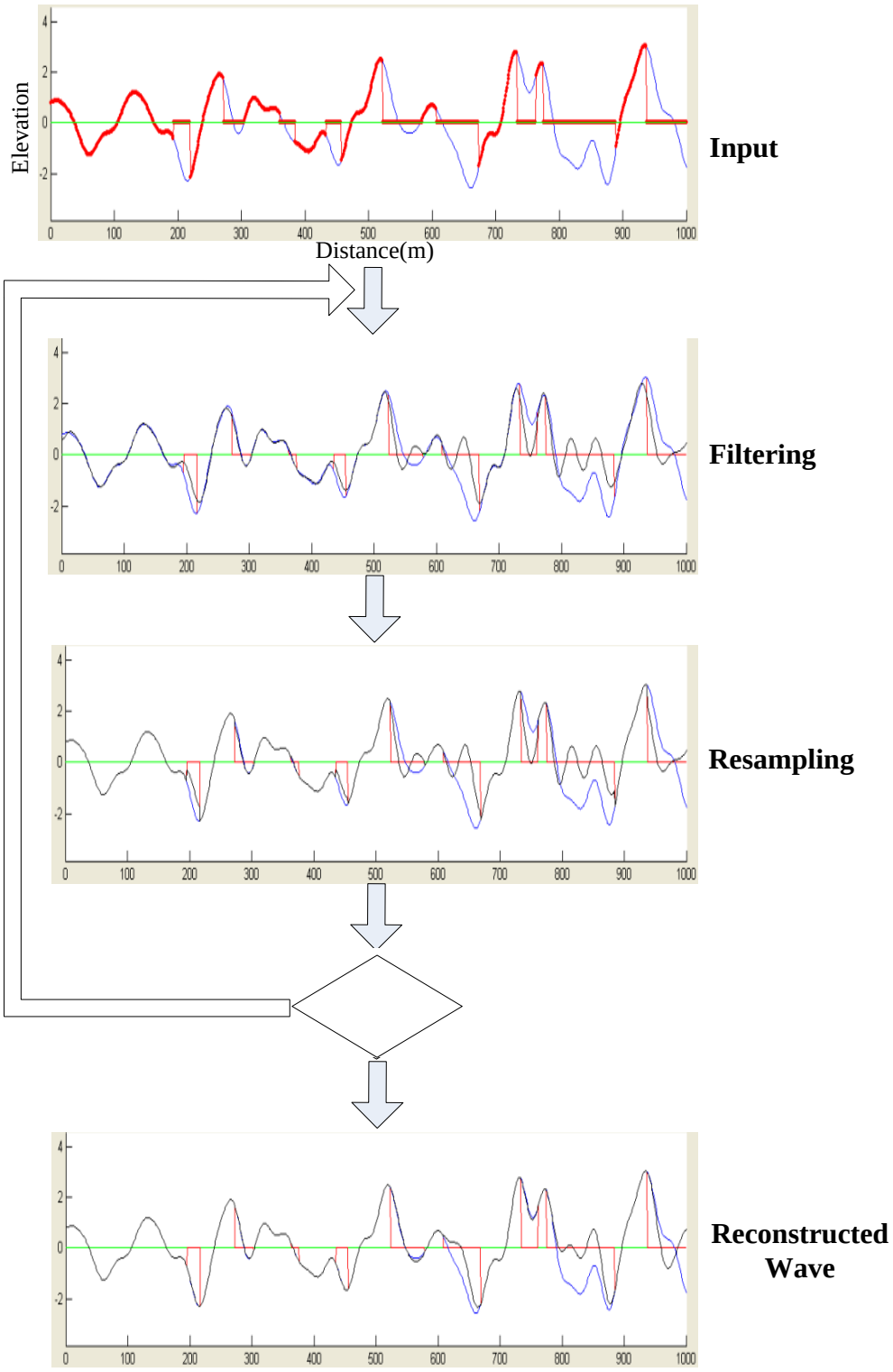

Figure 3. 8: Papoulis and Gerchberg method reconstructing method

Figure 3. 9 illustrates the reconstruction of the wave using different data point numbers. As expected the more data points available the better the performance of the reconstruction method. A comprehensive comparison is given in *Section 3.6*

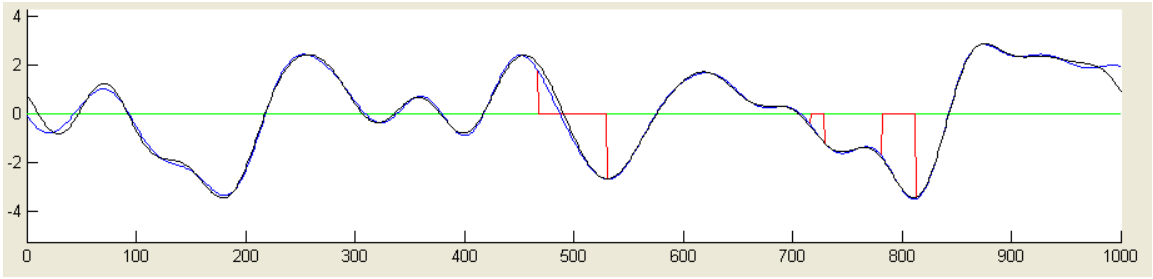

a)Extensive scanning

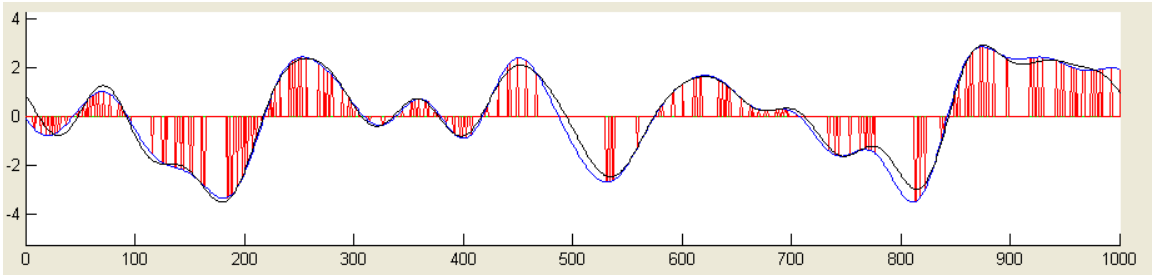

b) sample numbers Ns=200

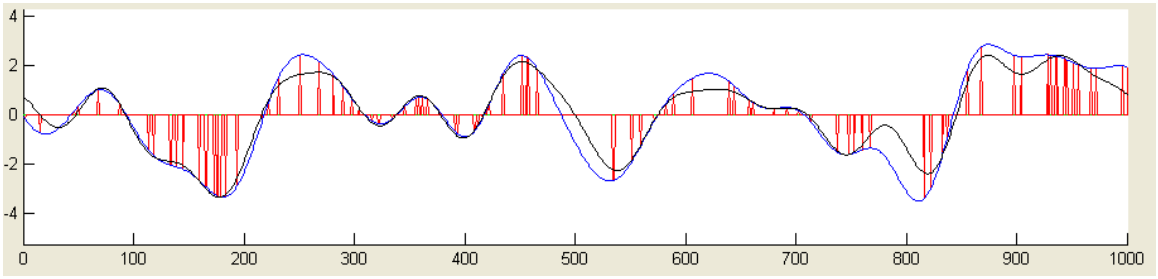

c) sample numbers Ns=100

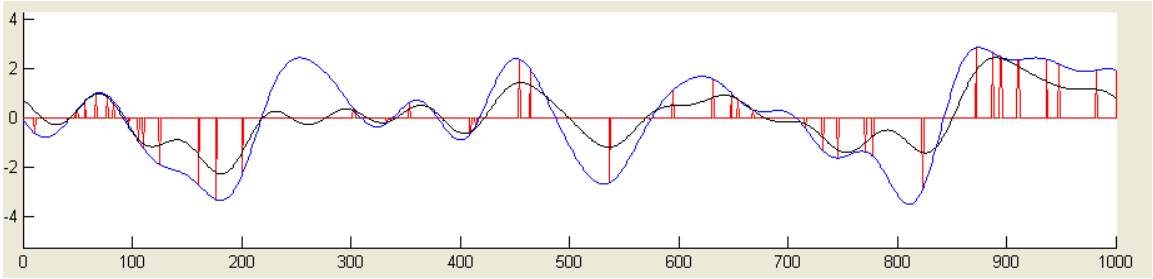

d) sample numbers Ns=50

---- ***Wave snapshot*** ----- ***Wave Reconstruction***
---- ***Sampling Points*** ----- ***Non Shadow region part of the wave***

Figure 3. 9: Wave reconstruction with Papoulis and Gerchberg method reconstructing method using different data numbers

3.6.1. Iteration algorithm with added spatial domain restriction

The iterative method explained in the previous section is modified to include more information about the missing parts of the wave. Although the laser beam can not indicate the wave's elevation within the shadow regions, an important observation is given by the laser height in these regions. The wave height at a certain location can't exceed the laser beam height for the beams that hit the wave beyond this location.

A new stage is included in the iterative method where the reconstructed shadow region is checked for any data that exceeds the laser beam height. If an incidence is found the reconstructed wave is adjusted to match the laser beam height. *Figure 3.10* shows the modified iterative method with an added stage to include this restriction.

In the given example two segments of the filtered wave are found to exceed the laser height. The adjustment can be seen clearly as a start line in the region x=(600,700) m and x=(800,900) m replacing these segments of the snapshot by straight lines adds discontinuity to the reconstructed wave, which in turn introduces higher frequency contents in the spectrum, which is adjusted in the next iteration.

The out put of the 20^{th} iteration is shown in Figure 3. 10 – e Comparing to the result of the basic iterative method, it is clear that this method improves wave reconstruction results.

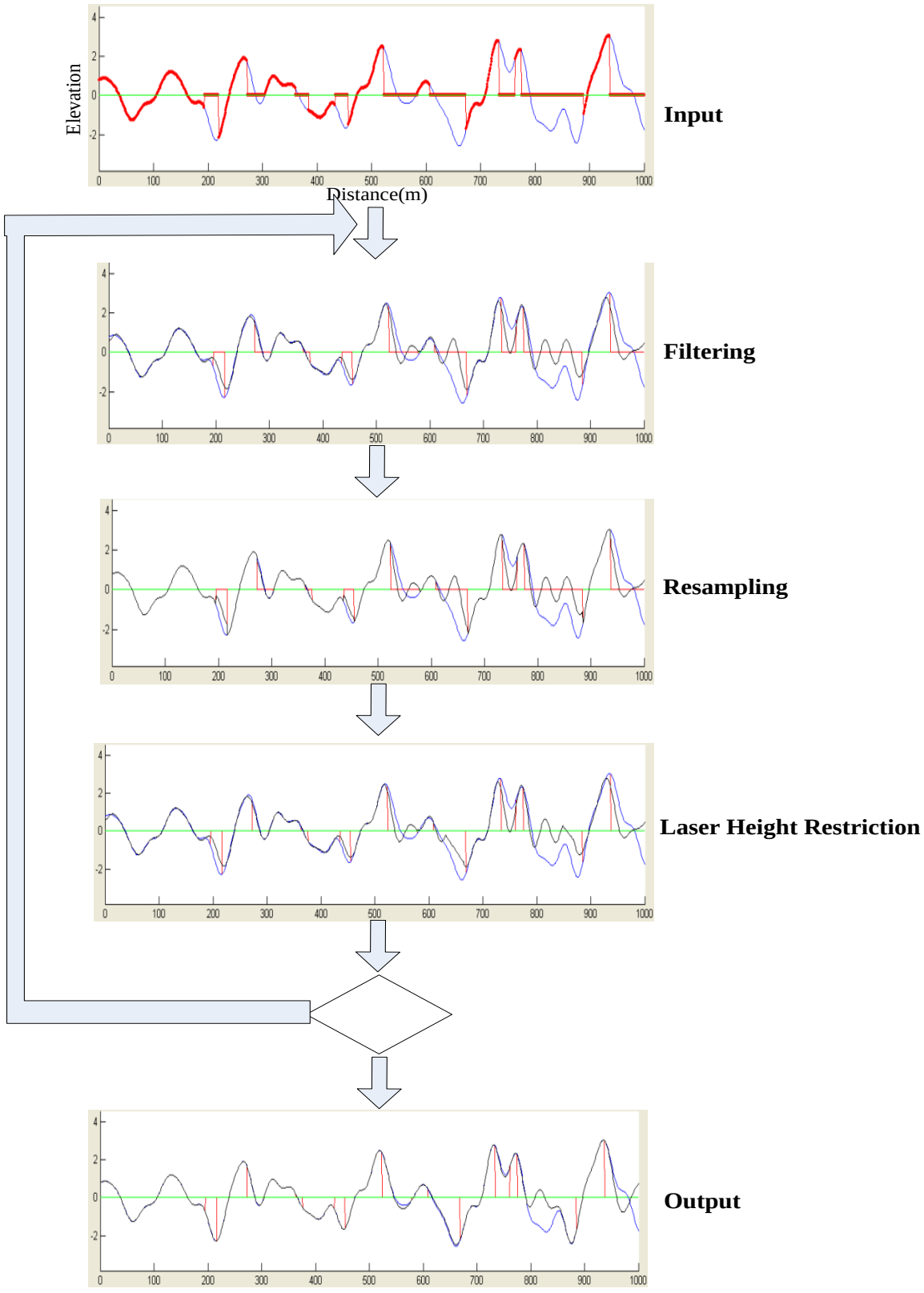

----*Wave snapshot* ----- *Wave Reconstruction*
---- *Shadow region Boundaries* ----- *Non Shadow region part of the wave*

Figure 3. 10: Modified reconstructing method

The reconstruction using different number of samples are illustrated in Figure 3. 11. As expected the reconstruction accuracy improves with the increase in the sample numbers. *Section 3.7* compares the average rms error of the 20th iteration for different sea conditions and different laser heights. Compared to the results of the basic iterative method it is clear that adding the laser height restriction improves the reconstruction.

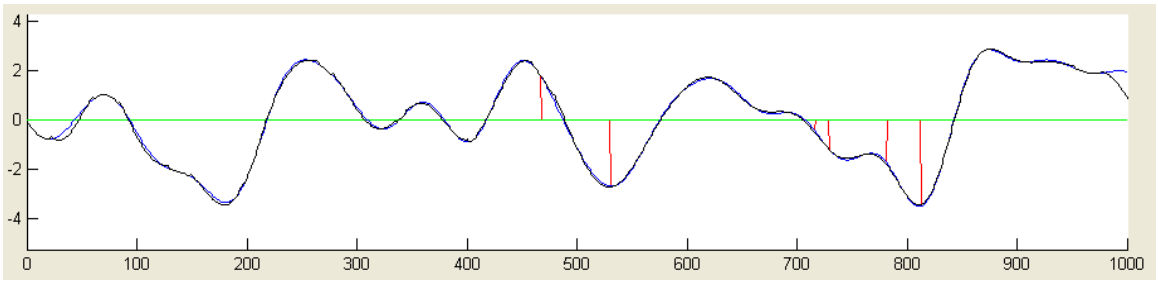

a)Extensive scanning

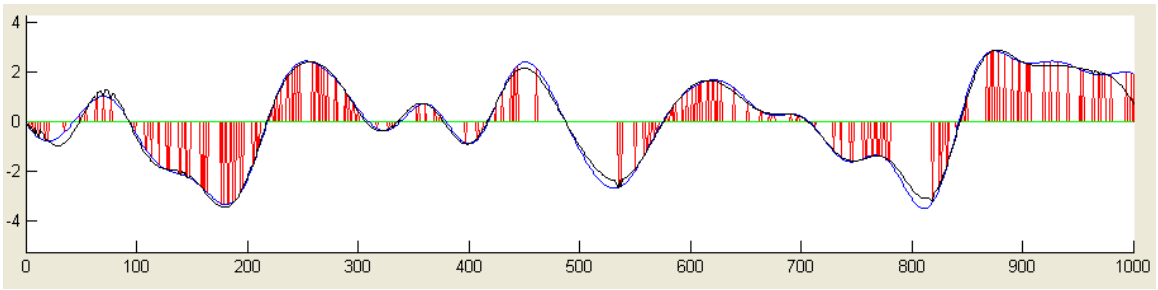

b) sample numbers Ns=200

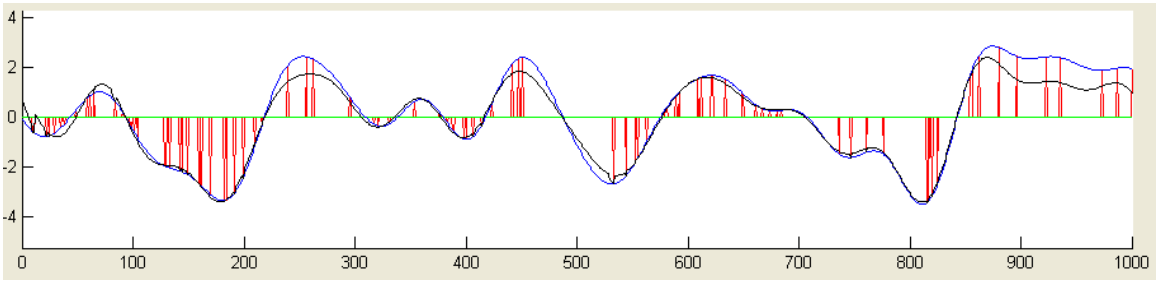

c) sample numbers Ns=100

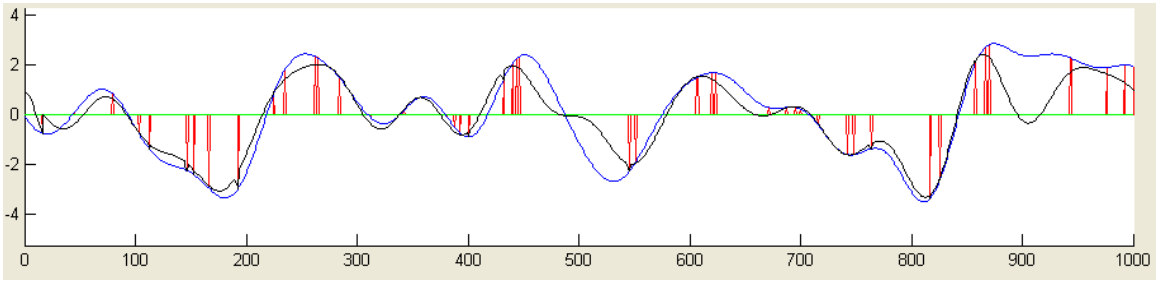

d) sample numbers Ns=50

---- ***Wave snapshot*** ----- ***Wave Reconstruction***
---- ***Sampling Points*** ----- ***Non Shadow region part of the wave***

Figure 3. 11: Wave reconstruction with modifide reconstructing method using different data numbers

3.6.2 Iteration algorithm with added dynamic information

Both iterative methods explained in the previous two sections reconstruct the wave from samples taken from a single snap-shot. In this section an algorithm is described that allows the use of samples taken from more that one snapshot. This is achieved by introducing the dynamic information into the algorithm, since one snapshot is the result of the evolvement of the previous snapshot, governed by the dispersion relation.

In this technique two iterative cycles are joined to include successive snapshots taken at $t=t_1$ and $t=t_2$.

The non-shadowed part of these snapshots are given by

$$\eta_s^1(x_n,t_1)=\eta(x_n,t_1)\cdot g_{1s}(x_n)$$

$$\eta_s^1(x_n,t_1)=\eta(x_n,t_2)\cdot g_{2s}(x_n)$$

Figure 3.12 shows the different stages of this method as explained in the following steps

1. the snapshot $\eta_s^i(x_n,t_1)$ at time $t=t_1$ is filtered resulting in the low pass signal given by $F_{1lp}^i = lowpass\left[DFT\left(\eta_s^i(x_n,t_1)\right)\right]$
2. the propagation filter is used to back propagate the filtered wave to time $t=t_2$ $F_{2lp}^i = F_{1lp}^i \cdot e^{-j\sqrt{kg}(t_2-t_1)}$
3. using the Inverse Fourier Transform we get the wave estimation of $t=t_2$ $\eta_{lp}^i(x_n,t_2)=IDFT\left(F_{2lp}^i\right)$
4. the resampling at $t=t_2$ is achieved by reinstating the nonshadow region parts of the wave at $t=t_2$ $\eta_s^i(x_n,t_2)=\eta_s^1(x_n,t_2)+\eta_{lp}^i(x_n,t_2)\cdot \bar{g}_{2s}(x_n)$
5. the snapshot at $t=t_2$ is filtered to obtain the low pass wave given by $F_{2lp}^i = lowpass\left[DFT\left(\eta_s^i(x_n,t_2)\right)\right]$
6. the propagation filter is used to forward propagate the wave to $t=t_1$ $F_{1lp}^i = F_{2lp}^i \cdot e^{j\sqrt{kg}(t_2-t_1)}$
7. using the Inverse Fourier Transform to get the low pass wave at $t=t_1$ $\eta_{lp}^i(x_n,t_1)=IDFT\left(F_{1lp}^i\right)$
8. the final stage in this iterative method is to reinstate the nonshadow data of $t=t_1$

$$\eta_s^i(x_n,t_1)=\eta_s^1(x_n,t_1)+\eta_{lp}^i(x_n,t_1)\cdot \bar{g}_{2s}(x_n)$$

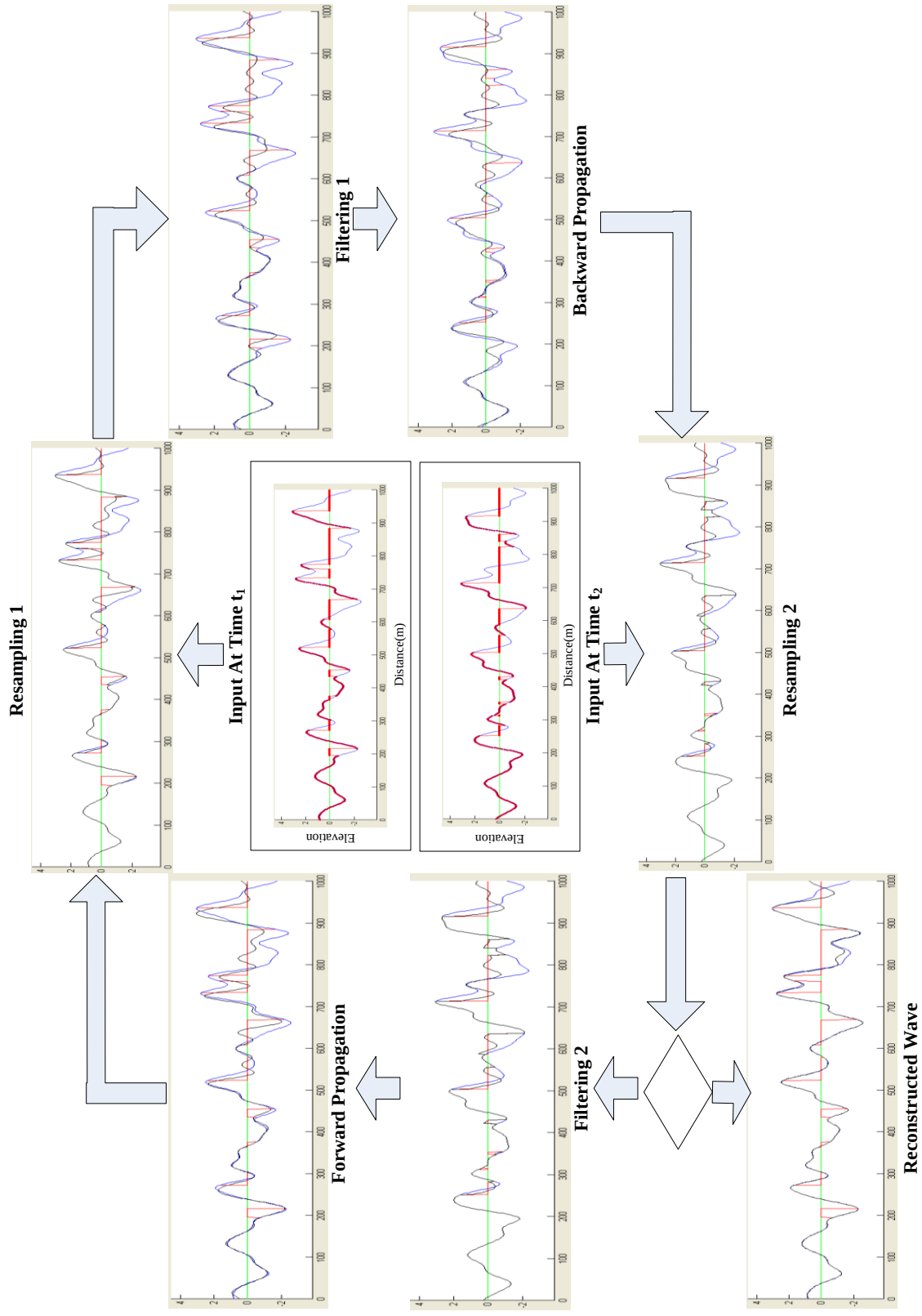

Figure 3. 12 Iteration algorithm with added dynamic information

The reconstruction using different number of samples are illustrated in Figure 3. 13 . As expected the reconstruction accuracy improves with the increase in the sample numbers *Section 3.7* compares the average rms error of the 20th iteration for different sea conditions and different laser heights. It will be shown that this method provides much better results.

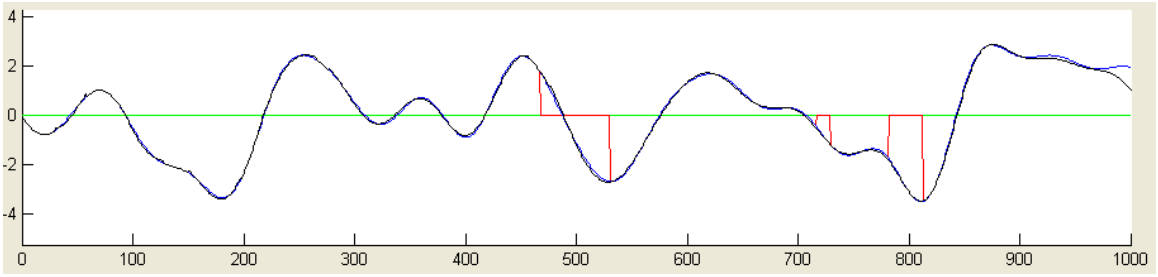

a)Extensive scanning

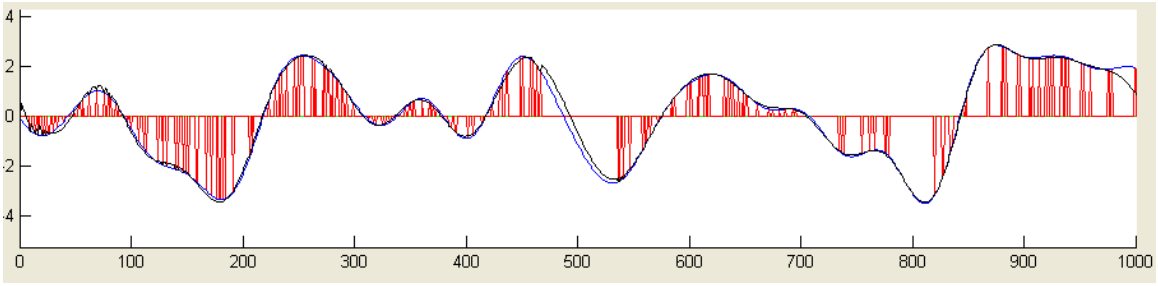

b) sample numbers Ns=200

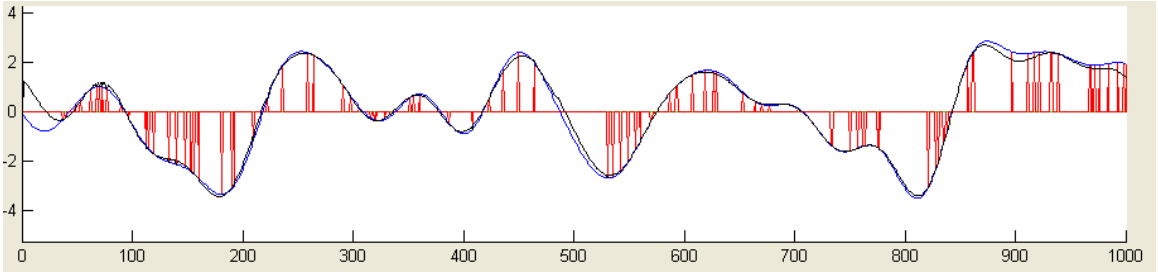

c) sample numbers Ns=100

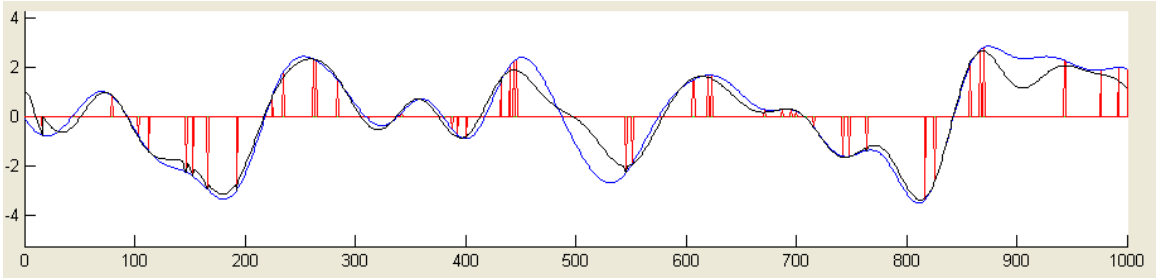

d) sample numbers Ns=50

----Wave snapshot ----- Wave Reconstruction
---- Sampling Points ----- Non Shadow region part of the wave

Figure 3. 13: Wave reconstruction with with added dynamic information reconstructing method using different data numbers

3.7 Wave Reconstruction results using iterative methods

The average Reconstruction error for each case was calculated for 1000 example. Reconstruction evaluation is achieved using ratio reconstruction error measured as :

$$Reconstruction \quad error = \frac{\sum_n \eta^2(x_n)}{\sum_n \left(\eta(x_n) - \hat{\eta}(x_n) \right)^2}$$

Where $\eta(x_n)$ is the nth wave model elevation value

$\hat{\eta}(x_n)$ is the nth wave elevation reconstruction

3.7.1 Wave Reconstruction for extensive scanning

Results illustrating the shadow region data reconstruction are shown in Figure 3. 14. The various graphs describe the variation of reconstruction error with laser height and wind speed for the three different techniques described in *Section 3.3*. The trends bear out all the anticipated behaviours, i.e. improvement in reconstruction error with laser elevation and improvement with number of iterations. Of considerable practical interest is the almost complete independence of error on wind speed for a given laser height. This finding bears out the expectations of the results in *Section 3.2.1* concerning the effects of normalizing the shadow length to the appropriate dominant length or time or time scale of the wave system.

In addition a general finding is that the technique employing added dynamic information produces considerably better results.

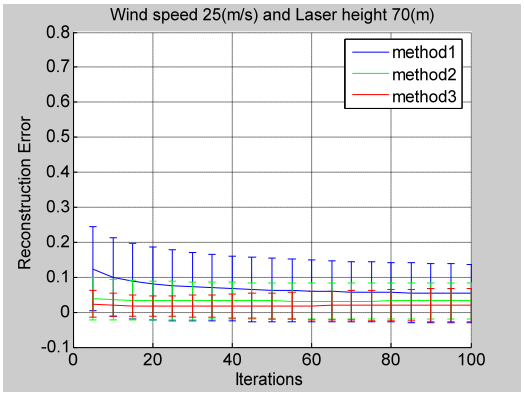

(a-1)

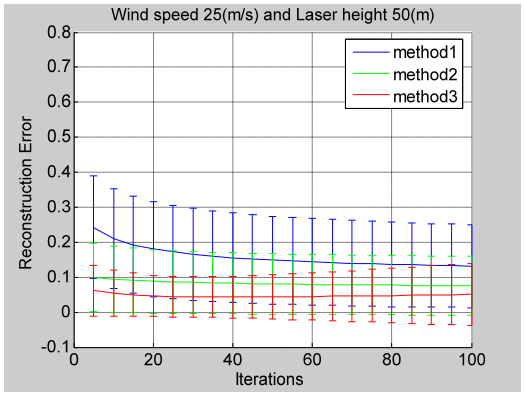

(a-2)

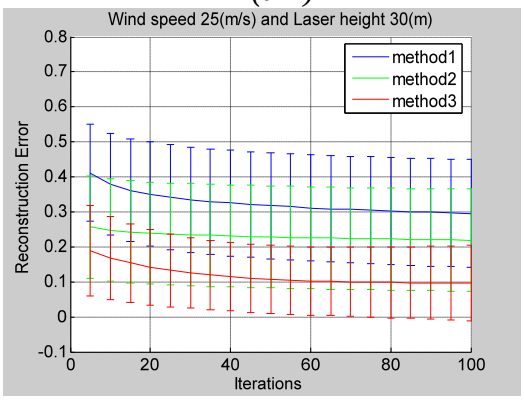

(a-3)

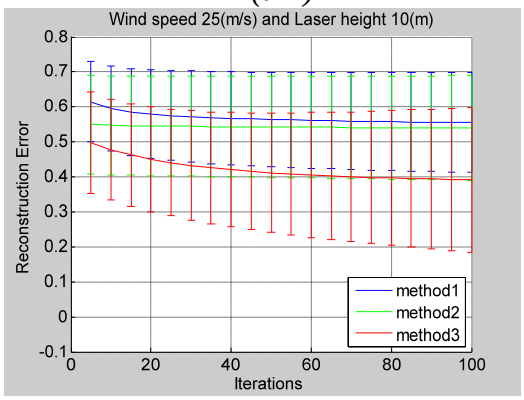

(a-4)

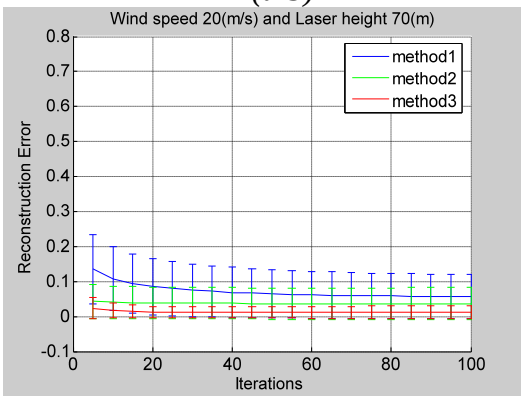

(b-1)

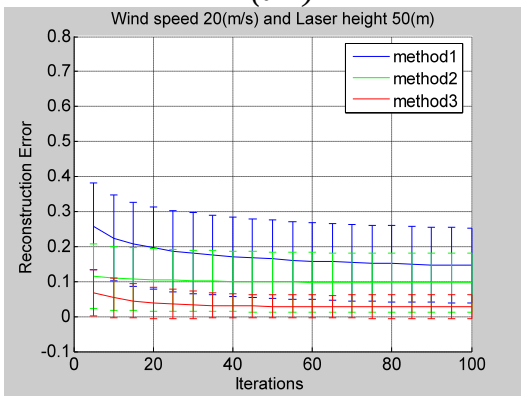

(b-2)

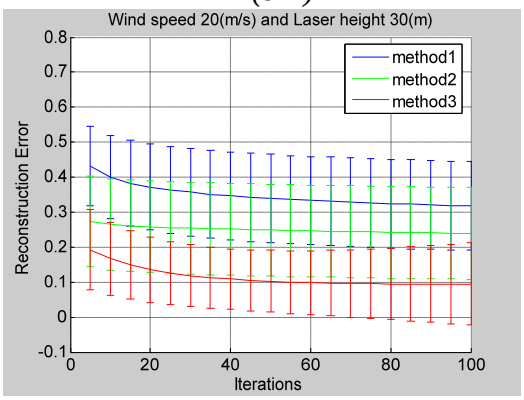

(b-3)

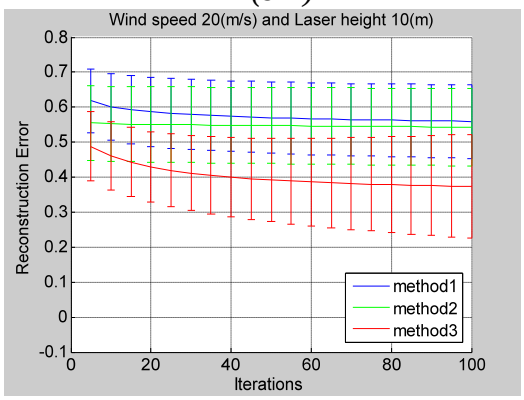

(b-4)

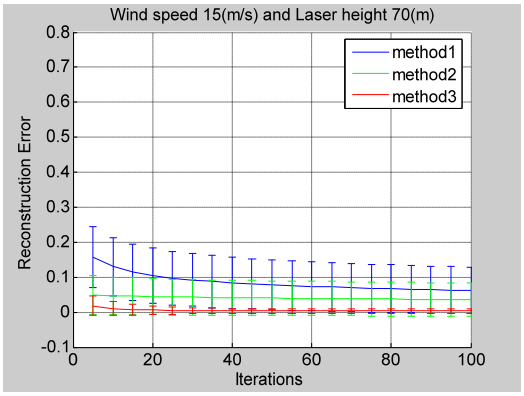

(c-1)

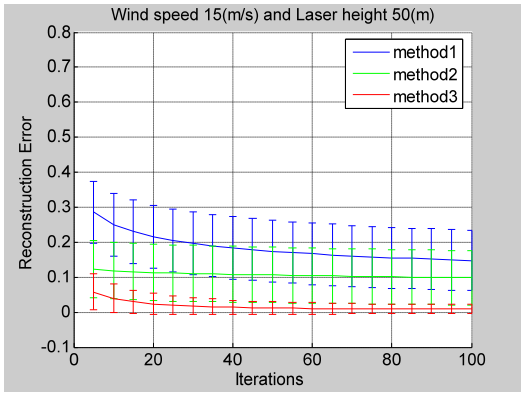

(c-2)

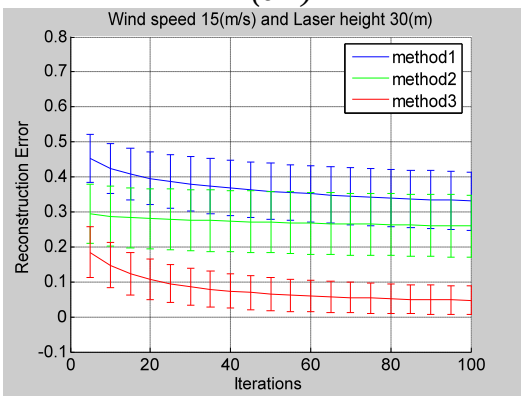

(c-3)

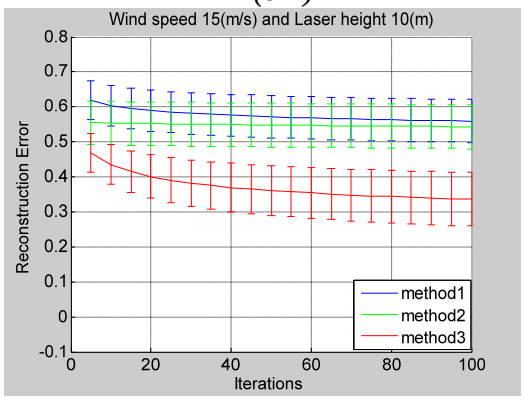

(c-4)

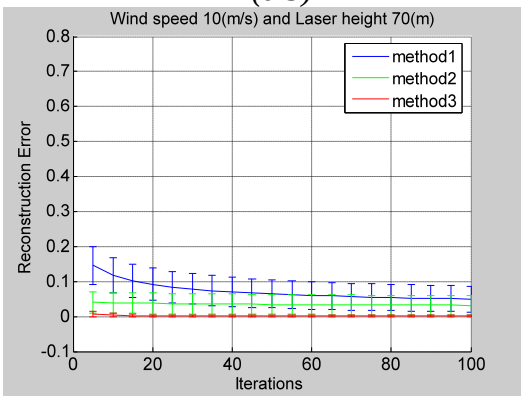

(d-1)

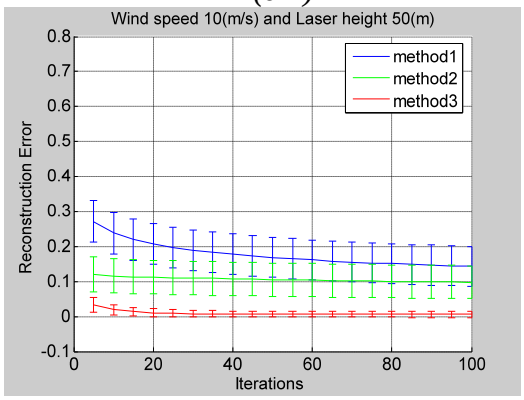

(d-2)

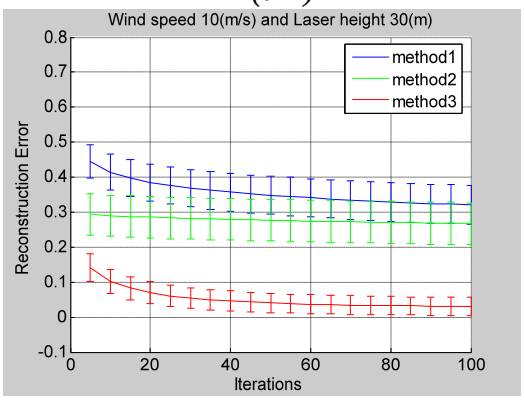

(d-3)

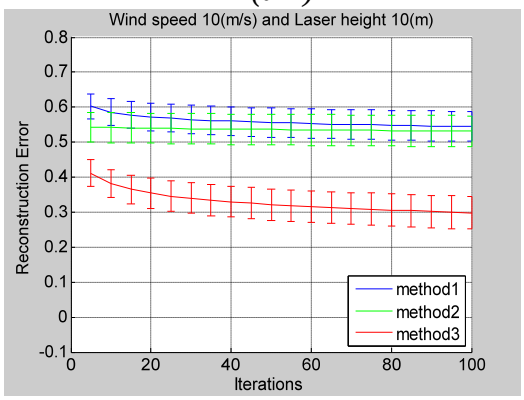

(d-4)

------*method 1(Papoulis and Gerchberg method)*

------*method 2(Iteration algorithm with added spatial domain restriction)*

------*method 3 (Iteration algorithm with added dynamic information)*

Wind speed (a)-25m/s (b)-20m/s (c)-15m/s (d)-10m/s

Figure 3. 14:Reconstruction Error for different iteration methods

3.7.2 The Effect on Wave Reconstruction of the number of data points

The reconstruction methods introduced in the previous sections considered reconstruction of the shadow regions from extensive data sets of 1000 points scans of which clearly only those scan points in the non-shadow regions were used. For practical LIDARs. data signal to noise ratio is related to the number of samples taken and thus it is important to asses the effects of using reduced data sets for reconstruction. In this section the result of reconstruction using limited data numbers (30 ,50,100.150 ,200), randomly selected from the non-shadowed regions of the full 1000 point scans.

The results are presented *Figure 3.15* and exhibit the same trends as found with the full 1000 points scans and as expected the reconstruction errors reduce smoothly with increasing number of data points.

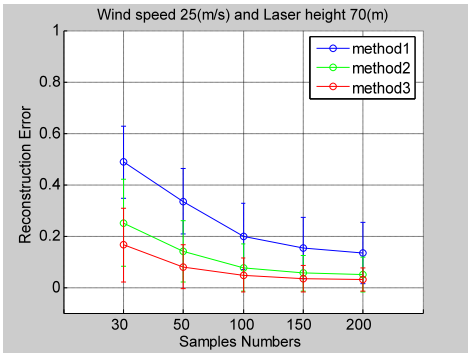

(a-1)

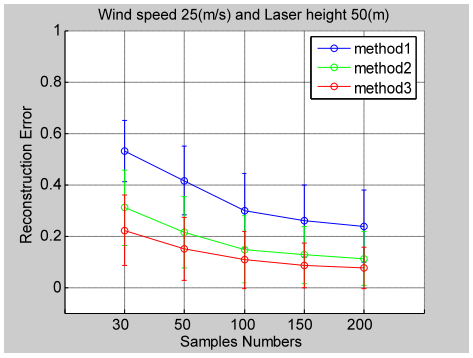

(a-2)

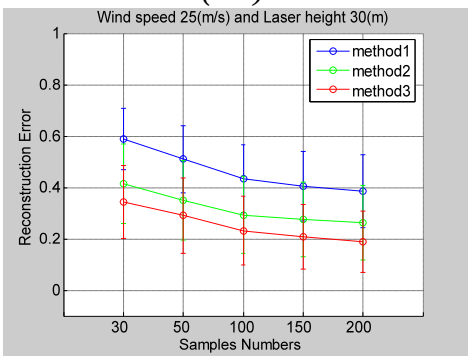

(a-3)

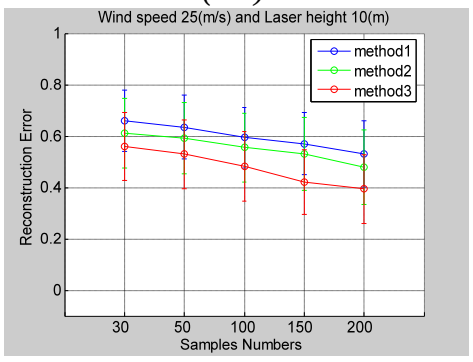

(a-4)

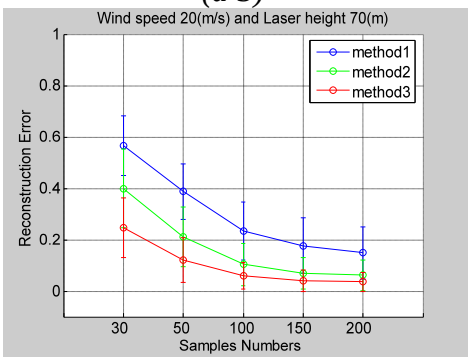

(b-1)

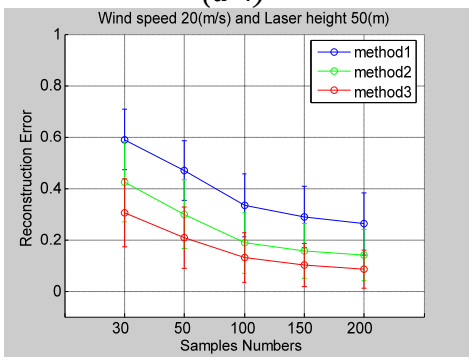

(b-2)

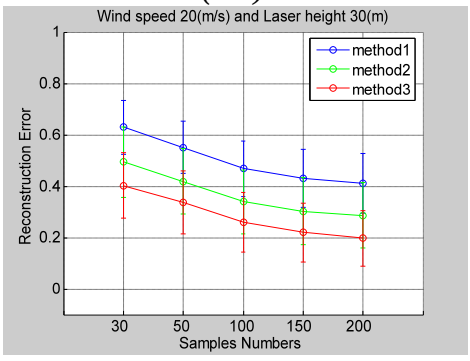

(b-3)

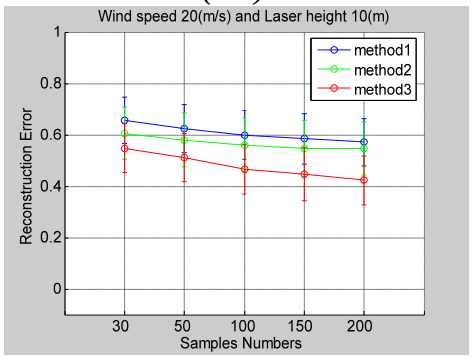

(b-4)

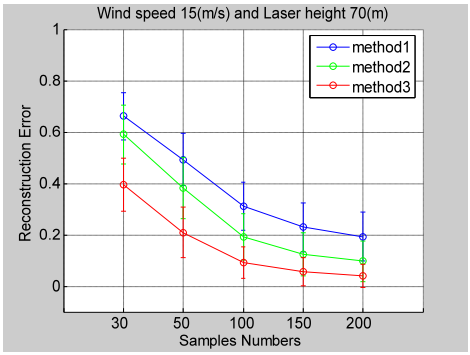

(c-1)

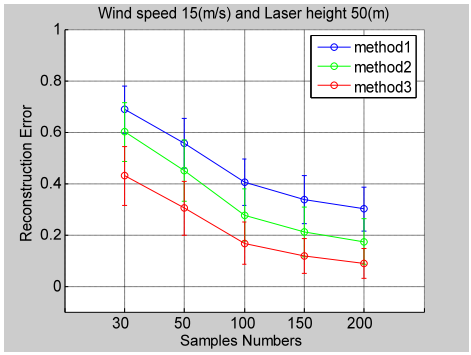

(c-2)

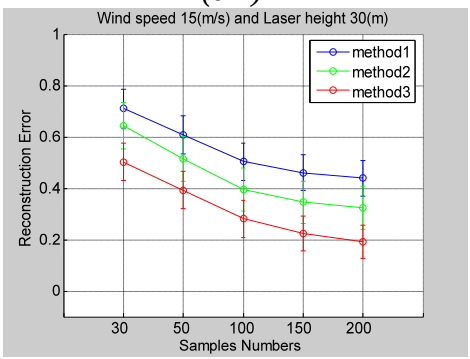

(c-3)

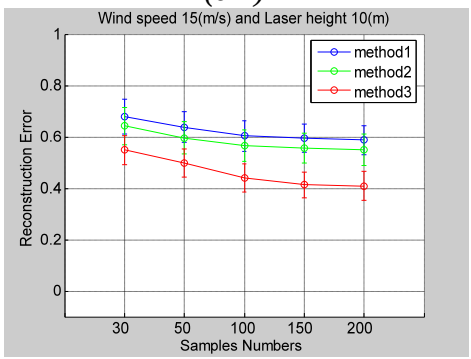

(c-4)

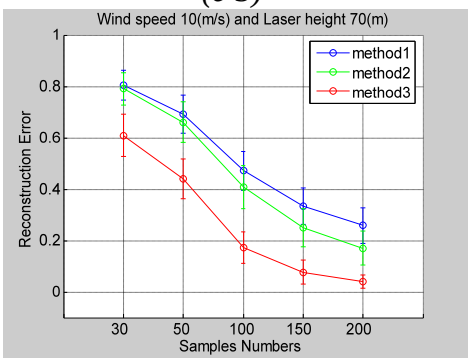

(d-1)

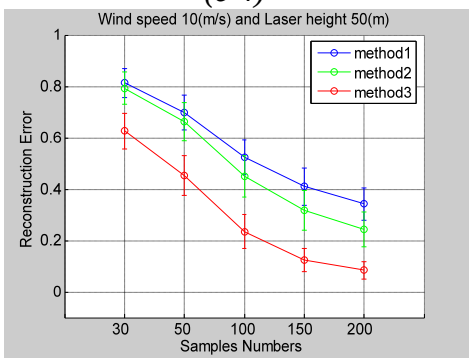

(d-2)

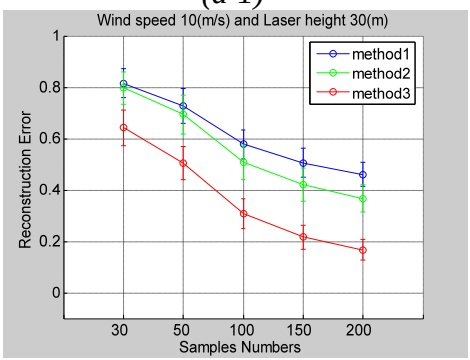

(d-3)

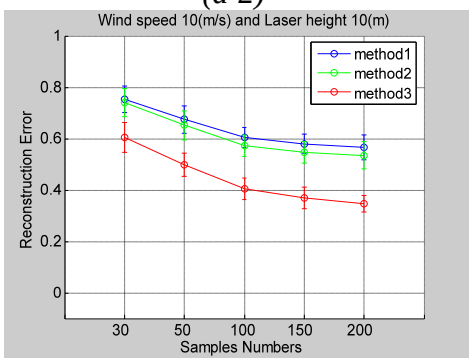

(d-4)

------method 1(Papoulis and Gerchberg method)
------method 2(Iteration algorithm with added spatial domain restriction)
------method 3 (Iteration algorithm with added dynamic information)
Wind speed (a)-25m/s (b)-20m/s (c)-15m/s (d)-10m/s

Figure3. 15: Reconstruction error for different sample numbers after 20 iterations

Chapter 4

Spectrum analysis of DSWP

This chapter discusses different aspects of the DSWP process from the spectrum domain point of view. The first part finds the relation between the one dimensional spectra of the wave's time record (or snapshot) to the more general two dimensional spectrum of the unidirectional deep water wave. The goal of introducing this type of spectrum is to derive the prediction model for mixed data. The second part of this chapter deals with problem of energy leakage and its effect on prediction. Four methods (Partial Filter Linearization, Classical windowing, End matching and Window Expansion) are discussed, and the relative prediction ability for each method is illustrated.

4.1 Two dimensional spectrum of unidirectional deep water waves

Since this research is concerned mainly with unidirectional waves, a special case of the spectrum given in *Equation*1. 5 can be used, where only one wave number dimension is considered. The linear wave elevation $\eta(t,x)$ can be represented by a two dimensional spectrum $H(\omega,k)$:

$$\eta(t,x)=\int_{-\infty}^{\infty}\int_{-\infty}^{\infty}H(\omega,k)e^{j(\omega t+kx)}\,d\omega\,dk \qquad \textbf{4. 1}$$

The dispersion relation between the wave number and the frequency for deep water sea $k = \frac{\omega^2}{g}$ defines only the positive part of the spectrum. This part of the spectrum exists on the curved plane defined by this relation, as shown in *Figure 4. 1*. On the other hand considering that this is the spectrum of a real function, it should satisfy:

$$H(\omega,k) = H^*(-\omega,-k) \qquad \textbf{4. 2}$$

This restriction is forced by extending the spectrum to the negative part of the spectrum using the relation given by *Equation*4. 3. The full sea wave spectrum is demonstrated in *Figure 4.1*

$$k = \begin{cases} \frac{\omega^2}{g} & \omega \geq 0 \\ \frac{-\omega^2}{g} & \omega < 0 \end{cases} \qquad \textbf{4. 3}$$

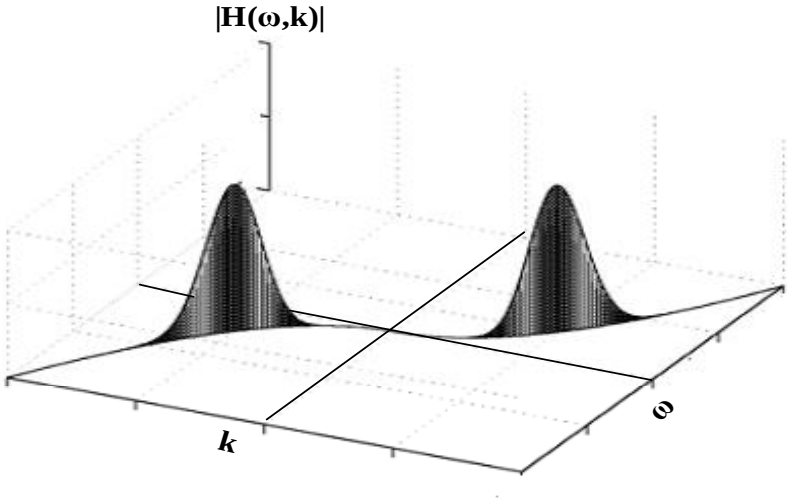

Figure 4. 1: Two dimensional spectrum of deep water wave

Implementing this restriction on *Equation*4. 1 the double integration is reduced to:

$$\eta(t,x) = \int_0^{\infty} H\left(\omega, \frac{\omega^2}{g}\right) e^{j\left(\omega t + \frac{\omega^2}{g}x\right)} d\omega + \int_{-\infty}^{0} H\left(\omega, \frac{-\omega^2}{g}\right) e^{j\left(\omega t - \frac{\omega^2}{g}x\right)} d\omega$$

This can be simplified to the form:

$$\eta(t,x) = \int_{-\infty}^{\infty} H\left(\omega, sign(\omega)\frac{\omega^2}{g}\right) e^{j\left(\omega t + sign(\omega)\frac{\omega^2}{g}x\right)} d\omega \qquad \textbf{4. 4}$$

4.1.1 Prediction using infinite time records

The plane $x = x_o$ is defined by the delta function $\delta_x(x-x_o)$ shown in *Figure 4. 2.a.*, The Fourier transform of $\delta_x(x-x_o)$ is given by $P_{xo}(\omega,k)$ where:

$$\delta_x(x-x_0) \Leftrightarrow P_{x0}(\omega,k) \qquad \textbf{4. 5}$$

With direct implementation of the two dimensional Fourier transform we get

$$P_{x_o}(\omega,k) = e^{-j(kx_o)} \cdot \delta_\omega(\omega) \qquad \textbf{4. 6}$$

Where $\delta_\omega(\omega)$ is the plane $\omega = 0$, shown in *Figure 4. 2.b.*

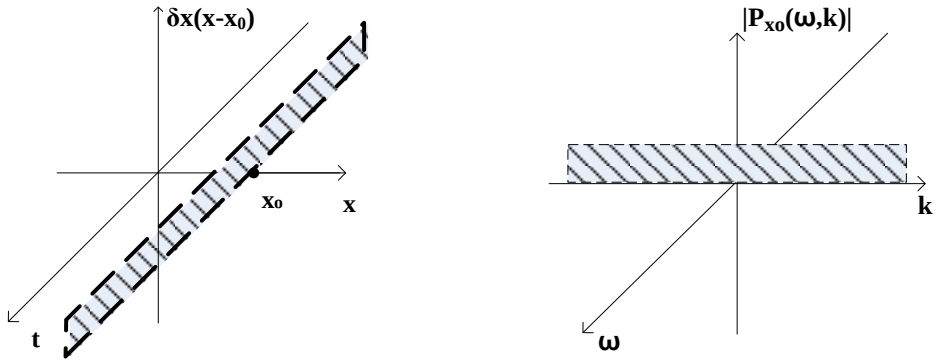

(a) *(b)*

Figure 4. 2: (a) $\delta_x(x-x_o)$ & (b) Its Fourier Transform

Now we define the time record taken at point $x = x_o$ as $g_{xo}(t,x)$ where:

$$g_{x0}(t,x) = \eta(t,x) \cdot \delta_x(x-x_0) = \begin{cases} \eta(t,x) & x = x_o \\ 0 & otherwise \end{cases} \qquad \textbf{4. 7}$$

If $G_{xo}(\omega,k)$ is the Fourier transform of the time record $g_{xo}(t,x)$ where:

$$g_{x0}(t,x) \Leftrightarrow G_{x0}(\omega,k) \qquad \textbf{4. 8}$$

By taking the Fourier transform of this time record $g_{xo}(t,x)$, we get

$$G_{x0}(\omega,k) = e^{-j(kx_o)} \int_{-\infty}^{\infty} \eta(t,x_o) \cdot e^{-j(\omega t)} dt \qquad \textbf{4. 9}$$

Using the convolution relationship we can also define $G_{xo}(\omega,k)$ as

$$G_{xo}(\omega,k) = H(\omega,k) * P_{x_o}(\omega,k) = \int_{-\infty}^{\infty}\int_{-\infty}^{\infty} H(\tau_\omega,\tau_k) \cdot e^{-j(k-\tau_k)x_o} \delta_\omega(\omega-\tau_\omega) d\tau_\omega d\tau_k \qquad \textbf{4. 10}$$

Since $H(\omega,k)$ exists only on the curve defined by Equation 4. 3

$$G_{x_o}(\omega,k) = \int_{-\infty}^{0} H\left(\tau_\omega, \frac{-\tau_\omega^{\,2}}{g}\right) e^{-j\left(k+\frac{\tau_\omega^{\,2}}{g}\right)x_o} \delta(\omega-\tau_\omega) d\tau_\omega + \int_{0}^{\infty} H\left(\tau_\omega, \frac{\tau_\omega^{\,2}}{g}\right) e^{-j\left(k-\frac{\tau_\omega^{\,2}}{g}\right)x_o} \delta(\omega-\tau_\omega) d\tau_\omega$$

Because of the impulse response function this integration exist only at $\tau_\omega = \omega$, resulting in :

$$G_{xo}(\omega,k)=\begin{cases} H\left(\omega,\dfrac{\omega^2}{g}\right)e^{-j\left(k-\frac{\omega^2}{g}\right)x_o} & \omega\geq 0 \\ H\left(\omega,\dfrac{-\omega^2}{g}\right)e^{-j\left(k+\frac{\omega^2}{g}\right)x_o} & \omega<0 \end{cases} \qquad \textbf{4. 11}$$

This is the relation between Fourier transform of the time record and the Fourier transform of the sea wave as illustrated in
Figure 4. 3.

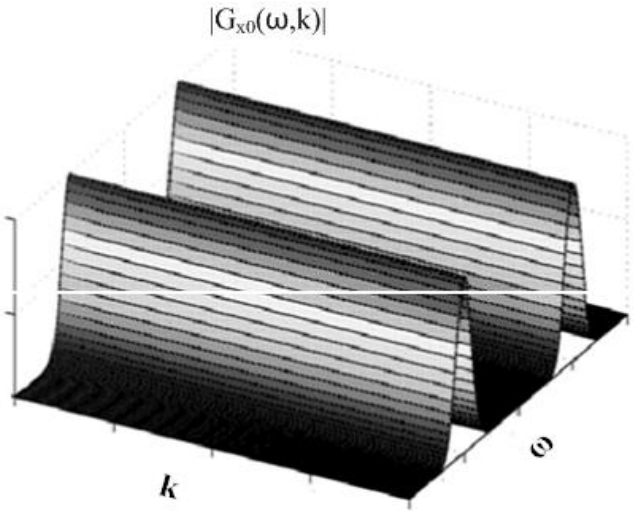

Figure 4. 3: Two dimensional spectrum of time record

This relation can be simply inverted to define the spectrum of the original sea wave H(ω,k) from the time record spectrum $G_{xo}(\omega,k)$

$$H\left(\omega,\frac{\omega^2}{g}\right)=G_{x_o}(\omega,k)e^{j\left(k-\frac{\omega^2}{g}\right)x_o}=e^{-j\left(\frac{\omega^2}{g}\right)x_o}\left[\int_{-\infty}^{\infty}\eta(t,x_o)\cdot e^{-j(\omega t)}dt\right] \quad \text{for } \omega\geq 0 \qquad \textbf{4. 12}$$

$$H\left(\omega,\frac{-\omega^2}{g}\right)=G_{x_o}(\omega,k)e^{j\left(k+\frac{\omega^2}{g}\right)x_o}=e^{j\left(\frac{\omega^2}{g}\right)x_o}\left[\int_{-\infty}^{\infty}\eta(t,x_o)\cdot e^{-j(\omega t)}dt\right] \quad \text{for } \omega<0 \qquad \textbf{4. 13}$$

Putting *Equation* 4. 12 and *Equation* 4. 13 together we get

$$H\left(\omega,\frac{sign(\omega)\omega^2}{g}\right)=e^{j(-sign(\omega))\left(\frac{\omega^2}{g}\right)x_o}\int_{-\infty}^{\infty}\eta(t,x_o)\cdot e^{-j(\omega t)}dt \qquad \textbf{4. 14}$$

From *Equation* 4. 4 and *Equation* 4. 14 the wave elevation is defined by:

$$\eta(t,x)=\int_{-\infty}^{\infty} e^{j(-sign(\omega))\left(\frac{\omega^2}{g}\right)x_o}\cdot\left[\int_{-\infty}^{\infty}\eta(\tau,x_o)\cdot e^{-j(\omega\tau)}d\tau\right]\cdot e^{j(\omega t+sign(\omega))\left(\frac{\omega^2}{g}\right)x}d\omega \qquad \textbf{4. 15}$$

Given that the one dimensional Fourier transform of the time record taken at point x_o is defined as:

$$A_{xo}(\omega)=\int_{-\infty}^{\infty}\eta(t,x_o)\cdot e^{-j(\omega t)}dt \qquad \textbf{4. 16}$$

Combining *Equation 4.15* and *Equation 4.16* gives a very important result which states that the wave elevation $\eta(t,x)$ at any time *(t)* and point in space *(x)* is fully defined from a single infinite time record. To put *Equation 4.15* in the convolution form we change the integration order as:

$$\eta(t,x)=\int_{-\infty}^{\infty}\eta(\tau,x_o)\cdot\lambda(t-\tau,x-x_o)d\tau \qquad \textbf{4. 17}$$

Where

$$\lambda(t,x-x_o)=\int_{-\infty}^{\infty}e^{j\omega t}\cdot e^{j\left(sign(\omega)\frac{\omega^2}{g}(x-x_o)\right)}d\omega \qquad \textbf{4. 18}$$

This is the impulse response of the Fixed Point mode filter which will be studied in Chapter 6.

4.1.2 Prediction using infinite snap shot

Using a similar argument to the one used in the time record case; here we try to show the relation between the spectrum of the snapshot and the spectrum of the deep water sea wave. We start by defining the snapshot $g_{to}(t,x)$

$$g_{to}(t,x)=\eta(t,x)\cdot\delta_t(t-t_o)=\begin{cases}\eta(t,x) & t=t_o\\ 0 & otherwise\end{cases} \qquad \textbf{4. 19}$$

Where $\delta_t(t-t_o)$ defines the plain $t=t_o$ shown in *Figure 4. 4.a* . Using straight forward Fourier transform it can be shown that

$$\delta_t(t-t_o)\Leftrightarrow P_{to}(\omega,t)=e^{j(kt_o)}\cdot\delta_k(k) \qquad \textbf{4. 20}$$

Where $\delta_k(k)$ is the plane defined by k=0 shown in *Figure 4. 4.b*

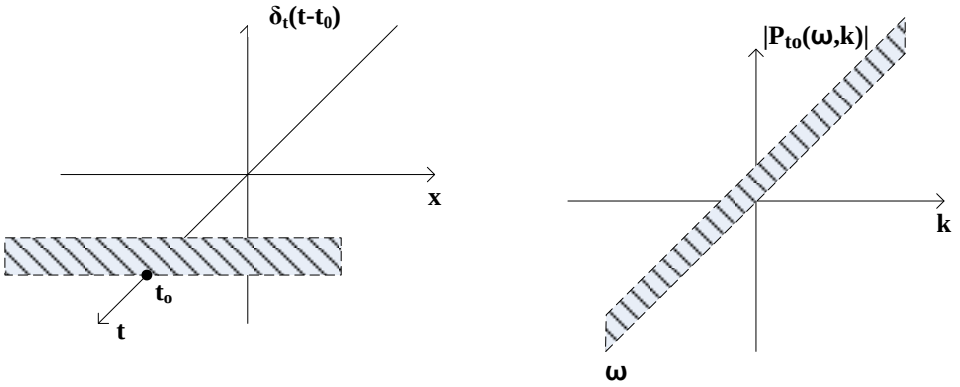

(a) *(b)*

Figure 4. 4: (a) Impulse function $\delta_t(t-t_o)$, (b) Its Fourier Transform

If we define $G_{to}(\omega,k)$ as the Fourier transform of the snap shot $g_{to}(t,x)$,by implementing the two dimensional Fourier transform we can simply define $G_{to}(\omega k)$ as:

$$G_{to}(\omega,k) = e^{-j(\omega t_o)} \int_{-\infty}^{\infty} \eta(t_o,x)\cdot e^{-j(kx)} dx \qquad \textbf{4. 21}$$

The next step in finding the relation between the original spectrum and the spectrum of the snapshot taken at $(t=t_o)$ is to use the convolution between the $H(\omega,k)$ and $P_{to}(\omega,k)$, where $G_{to}(\omega,k)$ is defined as:

$$G_{to}(\omega,k) = H(\omega,k) * P_{t_o}(\omega,k) = \int_{-\infty}^{\infty}\int_{-\infty}^{\infty} H(\tau_\omega,\tau_k)\cdot e^{-j(\omega-\tau_\omega)t_o}\delta_k(k-\tau_k)\,d\tau_\omega\, d\tau_k \qquad \textbf{4. 22}$$

since $H(\omega,k)$ exist only on the curve define by *Equation4. 3*

$$G_{to}(\omega,k) = \int_{-\infty}^{0} H\left(-\sqrt{-g\tau_k},\tau_k\right) e^{-j\left(\omega+\sqrt{-g\tau_k}\right)t_o}\delta_k(k-\tau_k)\,d\tau_k + \int_{0}^{\infty} H\left(\sqrt{g\tau_k},\tau_k\right) e^{-j\left(\omega-\sqrt{g\tau_k}\right)t_o}\delta_k(k-\tau_k)\,d\tau_k \qquad \textbf{4. 23}$$

The function $\delta_k(k-\tau_k)$ reduce this integration to:

$$G_{to}(\omega,k) = \begin{cases} H\left(\sqrt{gk},k\right)e^{-j\left(\omega-\sqrt{gk}\right)t_o} & k \geq 0 \\ H\left(-\sqrt{-gk},k\right)e^{-j\left(\omega+\sqrt{-gk}\right)t_o} & k < 0 \end{cases} \qquad \textbf{4. 24}$$

The amplitude of this spectrum is shown in *Figure 4. 5*. This relation is inverted to define the two dimensional spectrum of the wave *H(ω,k)* from the spectrum of an infinite snapshot $G_{to}(\omega,k)$ taken at $t = t_o$.

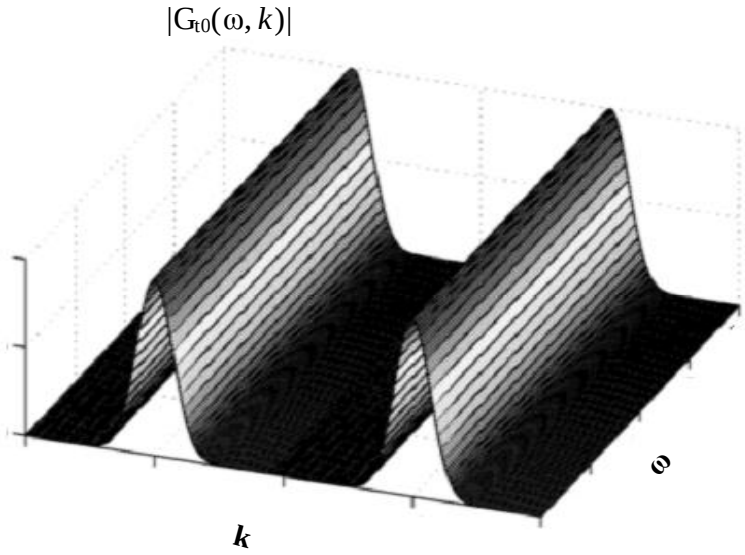

Figure 4. 5: Two dimensional spectrum of infinite snap shot

For $k \geq 0$

$$H\left(\sqrt{gk},k\right)=G(\omega,k)e^{j\left(\omega-\sqrt{gk}\right)t_o}=e^{-j\left(\sqrt{gk}t_o\right)}\left[\int_{-\infty}^{\infty}\eta(t_o,x)\cdot e^{-j(kx)}dx\right] \quad \textbf{4. 25}$$

for $k < 0$

$$H\left(-\sqrt{-gk},k\right)=G(\omega,k)e^{j\left(\omega+\sqrt{-gk}\right)t_o}=e^{j\left(\sqrt{-gk}t_o\right)}\left[\int_{-\infty}^{\infty}\eta(t_o,x)\cdot e^{-j(kx)}dx\right] \quad \textbf{4. 26}$$

Putting *Equation* 4. 25 together we can represent the wave spectrum as :

$$H\left(sign(k)\sqrt{sign(k)gk},k\right)=e^{j(-sign(k))\left(\sqrt{(sign(k)gk}t_o\right)}\left[\int_{-\infty}^{\infty}\eta(t_o,x)\cdot e^{-j(kx)}dx\right] \quad \textbf{4. 27}$$

Substituting Equation4. 27 in *Equation* 4. 4 the wave elevation is defined as:.

$$\eta(t,x)=\int_{-\infty}^{\infty}e^{j(-sign(k))\left(\sqrt{(sign(k)gk}t_o\right)}\cdot\left[\int_{-\infty}^{\infty}\eta(t_o,v)\cdot e^{-j(kv)}dv\right]\cdot e^{j(sign(k))\left(\sqrt{(sign(k)gk}t+kx\right)}dk \quad \textbf{4.28}$$

The one dimensional Fourier transform of the infinite snap shop $\eta(t_o,x)$ taken at time t_o is defined as:

$$B_{to}(k)=\int_{-\infty}^{\infty}\eta(t_o,x)\cdot e^{-j(kx)}dx \quad \textbf{4.29}$$

As was shown in the case of the infinite time record, *Equation*4.28 indicates that the wave elevation at any instance of time and point in space is total defined by an infinite snapshot at the $t=t_o$. The convolution form of this equation is obtained by the change of integrals order

$$\eta(t,x)=\int_{-\infty}^{\infty}\eta(t_o,v)\cdot\zeta(t,x-v)dv \qquad \textbf{4.30}$$

Where

$$\zeta(t,x)=\int_{-\infty}^{\infty}e^{jkx}e^{j(sign(k))\left(\sqrt{(sign(k)gk}\right)t}dk \qquad \textbf{4.31}$$

This is the impulse response of the Fixed Time prediction filter mentioned in *section 2.6.2*. The properties of $\zeta(t,x)$ are studied in Chapter 6.

4.1.3 Prediction using Mixed data

When using a LIDAR system in FIXED POINT mode the continuously varying amplitude and slope of the waves means that simply operating at a fixed scan angle results in variation of the beam interception point on the surface. Without knowing in advance the sea surface profile it is not actually possible to correct the scan angle for this effect. In FIXED TIME mode the data is also non-uniformly distributed in space and in addition each wave height measurement must be completed in a very short time to ensure negligible evolution of the sea surface shape during the entire scan duration. This results in low signal to noise ratios as only a small number of scattered photons are captured during each measurement. The above indicates that the optimum LIDAR operating mode in terms of data quality is where both space and time are allowed to vary during the measurement process.

Unfortunately, it is very complicated to determine the sea spectrum from such data and hence implementing the prediction process is extremely difficult. This section considers a type of mixed data where there is a linear relation between the location of the measured data and the measuring time. This eases the mathematical difficulties and offers reasonable scope for implementation as it only requires control of the LIDAR scan system. Using the two dimensional spectrum it will be shown that the wave elevation of the unidirectional deep water wave is fully defined by this type of mixed data. The special case of mixed data considered in this section is defined by *g(t,x)* where

$$g(t,x)=\eta(t,x)\cdot\delta(x-at-b)=\begin{cases}\eta(t,x) & x=at+b\\ 0 & otherwise\end{cases} \qquad \textbf{4.32}$$

Where a, b are constants defining the data line location in the (t,x) plane.

The Fourier transform of $\delta(x-at-b)$ is *P(ω,k)* where

$$P(\omega,k)=\int_{-\infty}^{\infty}\int_{-\infty}^{\infty}\delta(x-at-b)e^{-j(\omega t+kx)}\,dtdx=\int_{-\infty}^{\infty}e^{-j(\omega t_o+k(at+b))}\,dt$$

$$=e^{(-jkb)}\delta(\omega+ak)=\begin{cases}e^{(-jkb)} & k=-\dfrac{\omega}{a}\\ 0 & otherwise\end{cases} \qquad \textbf{4.33}$$

The two dimensional Fourier Transform of the mixed data *g(t,x)* is given by

$$G(\omega,k)=\int_{-\infty}^{\infty}\int_{-\infty}^{\infty}g(t,x)e^{-j(\omega t+kx)}\,dtdx=\int_{-\infty}^{\infty}\eta(t,at+b)\cdot e^{-j(\omega t+k(at+b))}dt$$

$$G(\omega,k)=e^{(-jkb)}\int_{-\infty}^{\infty}\eta(t,at+b)\cdot e^{-j(\omega+ak)}dt \qquad \textbf{4.34}$$

As was the case with the time record and the snap shot we find the relation between the two dimensional spectrum $G(\omega,k)$ of the mixed data record g(t,x)to that of the original sea wave spectrum H(ω,k) by using the convolution relation ship.

$$G(\omega,k)=H(\omega,k)*P(\omega,k)==\int_{-\infty}^{\infty}\int_{-\infty}^{\infty}H(\tau_\omega,\tau_k)\cdot e^{-jb(k-\tau_k)t_o}\delta(\omega-\tau_\omega)+a(k-\tau_k)d\tau_\omega d\tau_k$$

By implementing the dispersion relation between the frequency and wave number we get :

$$G(\omega,k)=\int_{-\infty}^{0}H\left(\tau_\omega,\frac{-\tau_\omega^2}{g}\right)e^{-jb\left(k+\frac{\tau_\omega^2}{g}\right)x_o}\delta(\omega-\tau_\omega)+a\left(k+\frac{\tau_\omega^2}{g}\right)d\tau_\omega$$

$$+\int_{0}^{\infty}H\left(\tau_\omega,\frac{\tau_\omega^2}{g}\right)e^{-jb\left(k-\frac{\tau_\omega^2}{g}\right)x_o}\delta(\omega-\tau_\omega)+a\left(k-\frac{\tau_\omega^2}{g}\right)d\tau_\omega$$

The integration is reduced to the value determined by the impulse function $\delta(\omega-\tau_\omega)$, since the plane defined by $\delta(\omega-\tau_\omega)$ intersects the original spectrum at a single point.

$$G(\omega,k)=\begin{cases}H\left(C,\dfrac{C^2}{g}\right)e^{-jb\left(k-\frac{C^2}{g}\right)} & \omega<-ak\\ H\left(D,\dfrac{-D^2}{g}\right)e^{-jb\left(k+\frac{D^2}{g}\right)} & \omega\geq-ak\end{cases} \qquad \textbf{4.35}$$

Where

$$C(\omega,k)=\frac{-g}{2a}+\frac{1}{2a}\cdot\sqrt{g^2+4g(a\omega+a^2k)}$$

$$D(\omega,k)=\frac{g}{2a}-\frac{1}{2a}\cdot\sqrt{g^2-4g(a\omega+a^2k)}$$

From *Equation* 4.35 and *Equation* 4.34 the relation is reversed to define the original spectrum.

$$H\left(\omega, sign(\omega)\frac{-\omega^2}{g}\right) = e^{-j(sign(\omega))\frac{\omega^2}{g}b_o}\int_{-\infty}^{\infty}\eta(t, at+b)\cdot e^{-j\left(\omega+\frac{sign(\omega)a}{g}\cdot\omega^2\right)t}dt \qquad \textbf{4.36}$$

Substituting Equation 4.36 in Equation 4. 4 we get the wave elevation defined by mixed data as :

$$\eta(t,x) = \int_{-\infty}^{\infty} e^{-j(sign(\omega))\left(\frac{\omega^2}{g}\right)b}\cdot\left[\int_{-\infty}^{\infty}\eta(\tau, a\tau+b)\cdot e^{-j\left(\omega+\frac{sign(\omega)a}{g}\cdot\omega^2\right)\tau}d\tau\right]\cdot e^{j\left(\omega t+\frac{sign(\omega)\omega^2}{g}x\right)}d\omega \qquad \textbf{4.37}$$

This relation states that the wave elevation of the unidirectional deep water wave is totally determined from an infinite record of mixed data, where the position of the data points and the time of measurement have a linear relation.

To implement the mixed data prediction method given by *Equation* 4.37 we use the wave model described in *Section 2.7*. The Pierson Moskowitz wind speed parameter is set to U=15m/s to generate the wave data along the line AB shown in Figure 4. 6 where the slope of the line is (a = -100) and since the line passes through the origin(*b=0*). and the data region is [0,10]s. The implementation is carried out by converting the integrals of *Equation* 4.37to a summation with a time step (Δt=0.01)sec. The discrete version of mixed data prediction algorithm is given in two steps.

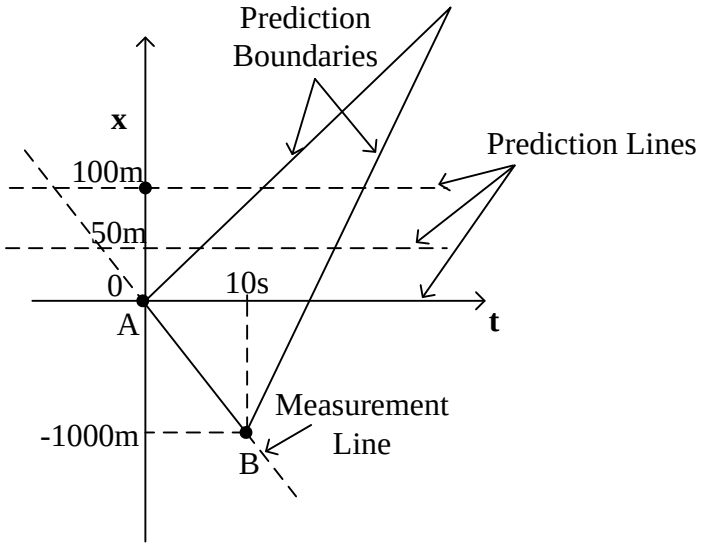

Figure 4. 6: Experiment diagram for testing mixed data prediction model

First calculate the discrete mixed data spectrum

$$A_m = \sum_{n=0}^{N-1} \eta\left(n\Delta t, -100(n\Delta t)\right) \cdot e^{-j\,(n\Delta t).\left(m\ \Delta\omega + \frac{a(m\ \Delta\omega)^2}{g}\right)}$$

$$\text{for} \quad \mathrm{m} = 0,1,2 \ldots \ldots \frac{\mathrm{N}-1}{2} \qquad \textbf{4. 38}$$

Where $\Delta\omega = \frac{2\pi}{t_2} = \frac{2\pi}{10} rad\ s^{-1}$ and N is the length of the data record.

Notice that the spectrum has an odd symmetry and hence only the positive half of the spectrum is calculated. The second step is to calculate the wave elevation $\eta'(x,t_i)$ using the discrete version of *Equation* 4.37, given by:

$$\eta'(t,x) = 2 \sum_{m=1}^{(N-1)/2} \left(A_m \cdot e^{j\left(\omega_m t + \frac{\omega_m^{\ 2}}{g} x\right)} \right) \qquad \textbf{4. 39}$$

The predicted wave form is calculated for the three snapshots *x=[0,50,100]m* over the range $t_i = i(0.1)\ s$ i=0,1,2……140 .The simulated data and prediction from the mixed data is shown in Figure 4. 7*(a,b,c)* respectively. This example illustrates the prediction algorithm for this type of mixed data, the prediction clearly follows the expected trends, as the prediction distance increases the prediction accuracy decreases and the prediction region shifts to the direction of the propagated wave.

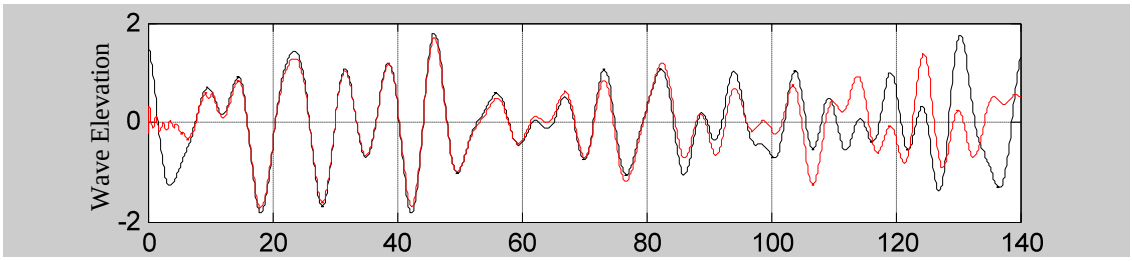

(a) Prediction at x = 0m

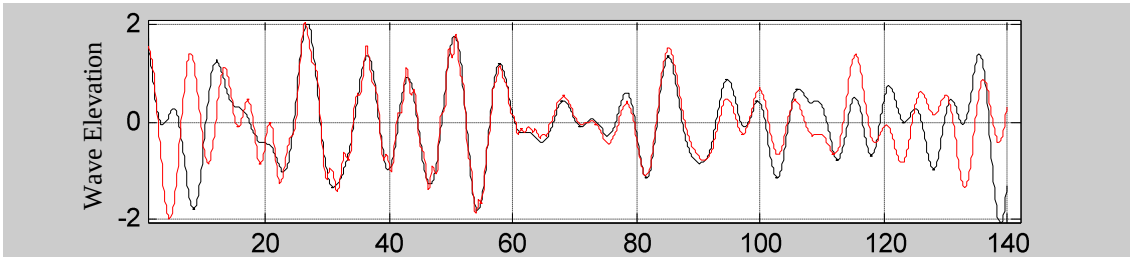

(b) Prediction at x = 50m

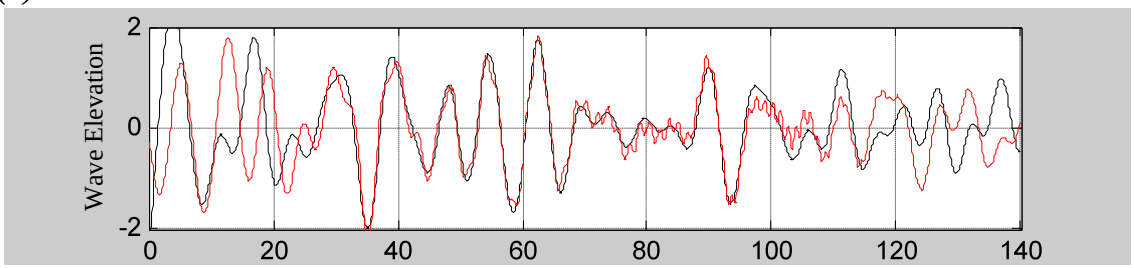

(c) Prediction at x = 100m

----- *Propagating wave* , ----- *wave prediction*

Figure 4. 7: Prediction using mixed data (Horizontal axis are data index value)

4.2 The Energy leakage problem

The first part of this chapter considered infinite data records of deep water waves, however practically these infinite records are not available and limited data records are used for the prediction process. As is the case in many signal-processing applications, energy leakage is a direct result of the windowing of the data records. The remaining part of this chapter discusses the effect of energy leakage on prediction in the Fixed Time mode.

The example shown in Figure 4. 8.*a* represents a Pierson-Moskowitz wave with a speed $(U = 20\ m/s)$ which has an upper limit of the wave number spectrum at $(k = 0.1\ m^{-1})$. The simulation wave is plotted using the blue line, while the two vertical lines illustrate the measurement window's edges which in the demonstrated case have the dimensions (893,1832)*m*.

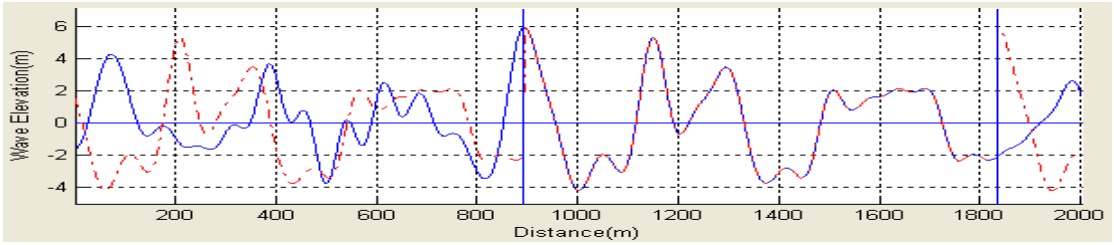

a) wave prediction model at t =0s

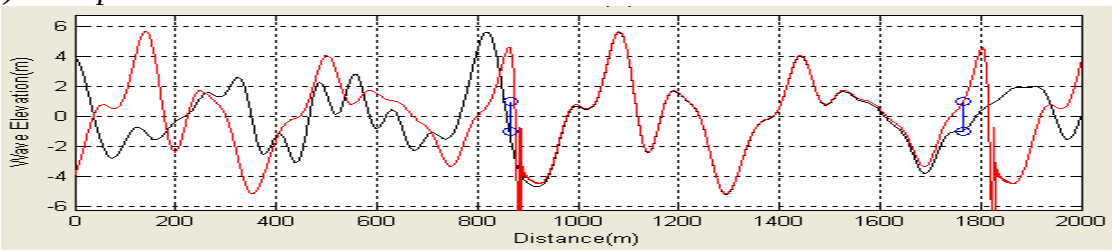

b) wave prediction model at t =5s

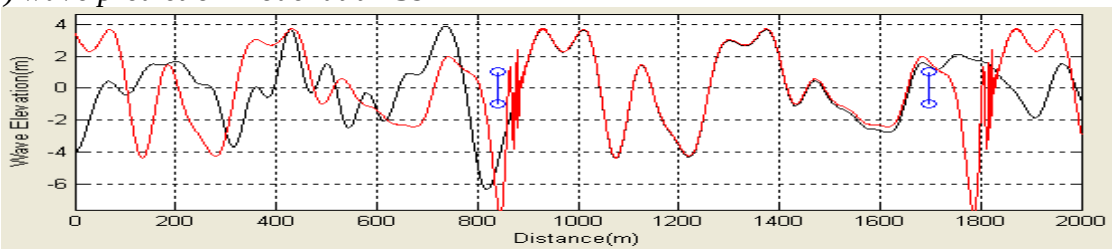

c) wave prediction model at t =10s

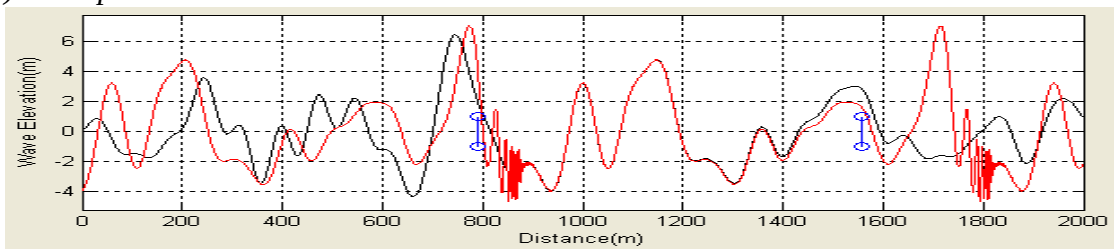

d) wave prediction at t =20s

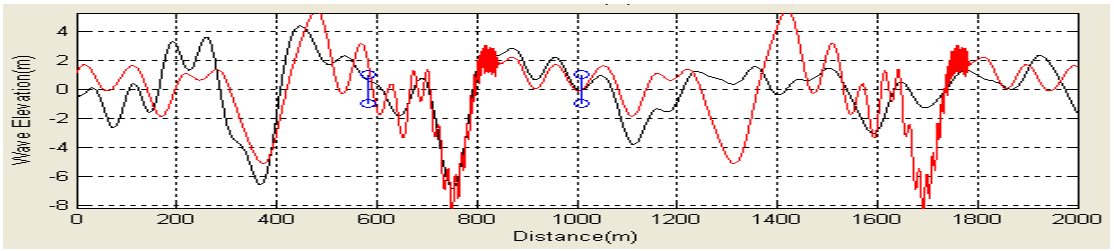

e) wave prediction at t =60s

-------Propagating wave U=15ms^{-1},-------- Prediction wave, -------- Prediction boundary

Figure 4. 8: Wave prediction using square window

This particular window is chosen to have a large discontinuity at the two ends and causing large energy leakage outside the waves spectrum band (k_{min}=0.01 , k_{max}=0.1)m^{-1}. The windowing effect is clear in the prediction model spectrum shown in Figure 4. 9.

The predicted wave is plotted using the red line in *Figure 4.* 8 *(a,b,c,d,e)* for different instance in time (*t=[0,5,10,20,60]sec*). High frequency ripples appearing in the predicted wave associated with the energy leakage and resulting is poor prediction results.

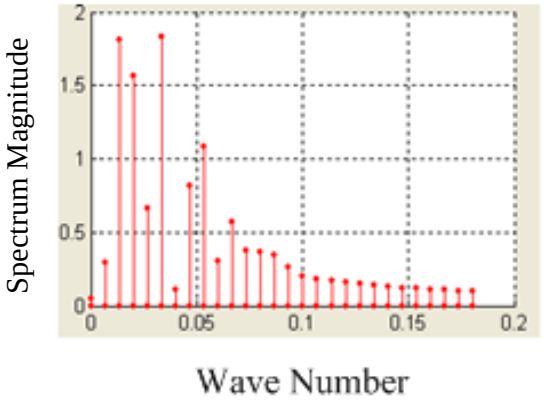

Figure 4. 9: Energy leakage using square window

4.2.1 Effect of energy leakage on Fixed Time mode wave prediction

In this section we find the difference between the spectrum of the propagated wave and the spectrum of the propagation model derived from a limited snap shot in the Fixed Time mode. The linear wave elevation given by *Equation* 4.28 can be rewritten as:

$$\eta(x,t)=\int_{-\infty}^{\infty} B_0(k)e^{j\,sign(k)\sqrt{g|k|}\cdot t}\cdot e^{-jkx}dk \qquad \textbf{4. 40}$$

Where B_o is the one-dimensional spectrum of the snap-shot $\eta(0,x)$. Notice that the wave number amplitude spectrum of the sea wave snap shot at a given $t=t_0$ $\eta(x,t_o)$ is given by

$$\eta(x,t_0)\Leftrightarrow B_{t0}(k)=B_0(k)e^{j\,sign(k)\sqrt{g|k|}\cdot t_0} \qquad \textbf{4. 41}$$

Having the spectrum representation of the sea surface, we will investigate the errors in the predicted spectrum. Consider that the sea surface was measured at an instance *t=0* for $-\Delta x<x<\Delta x$. This is represented by multiplying the wave with a rectangular window $w(x)$ with spectrum $W(k)$ is the well known *sinc( )* function shown in Figure 4. 10.b

$$w(x)=\begin{cases}1 & -\Delta x<x<\Delta x\\ 0 & otherwize\end{cases}\Leftrightarrow W(k)=\frac{sin(k\cdot\Delta x)}{k\cdot\Delta x} \qquad \textbf{4. 42}$$

The measured snapshot is given by :

$$\eta_w(x)\big|_{t=0} = \eta(x,0)\cdot w(x)$$

4. 43

Multiplication in the time domain is equivalent to convolution of the two spectra. The spectrum $H_w(k)$of the measured part of the snapshot is defined by using the convolution theory.

$$H_w(k) = \int_{-\infty}^{\infty} B(\tau)\cdot \frac{\sin[(k-\tau)\Delta x]}{(k-\tau)\Delta x} d\tau$$

4. 44

The next stage in the prediction process is to use the nonlinear phase shifting filter to propagate the wave by the parameter $t=t_0$, resulting in the propagated windowed spectrum $H_{wp}(k)$. This procedure is shown in *Figure 4. 10*

$$H_{wp}(k) = H_w(k)e^{-j\,sign(k)\sqrt{g|k|}\cdot t_0}$$

$$H_{wp}(k) = \int_{-\infty}^{\infty} B(\tau)\cdot \frac{\sin[(k-\tau)\Delta x]}{(k-\tau)\Delta x} d\tau \cdot e^{-j\,sign(k)\sqrt{g|k|}\cdot t_0}$$

4. 45

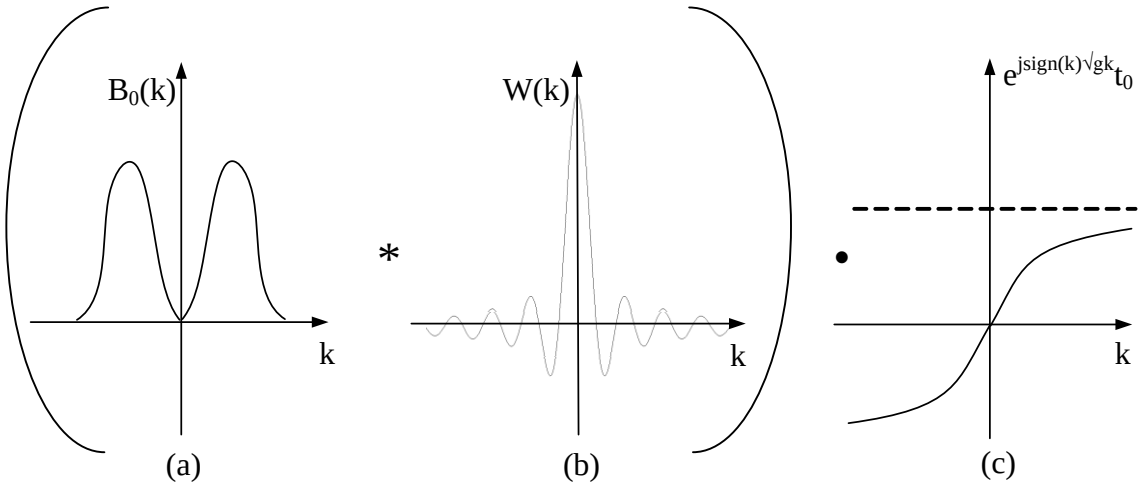

Figure 4. 10: Propagation of windowed snapshot

Now consider the actual propagated wave at $t=t_0$ .The wave number spectrum of sea wave at $t=t_0$ is given by *Equation 4. 41*. To simplify the comparison between the measured spectrum and actual spectrum, we will limit the propagated wave to the same size window that was used in the measurement stage. The only difference in this window is that it is shifted in space by x_0. The spectrum of this shifted window is shown in *Figure 4. 11*.c

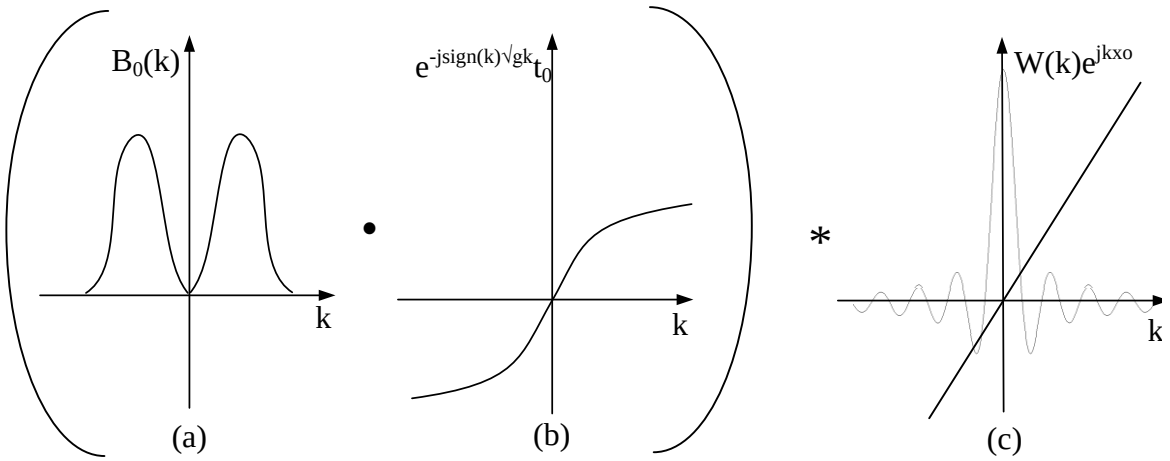

Figure 4. 11: Windowing the Propagation wave at t=t_0

As in the previous case the multiplication in space domain is represented as convolution of the two spectra resulting in the spectrum of the propagated wave given as :

$$H_{pw}(k) = \left[B(k)\big|_{t=0} \cdot e^{-j\,sign(k)\sqrt{g|k|}\cdot t_0} \right] * \left[\frac{sin(k\Delta x)}{k\Delta x} \cdot e^{-jk\,x_0} \right]$$

$$H_{pw}(k) = \int_{-\infty}^{\infty} B_0(\tau) \cdot e^{-j\,sign(\tau)\sqrt{g|\tau|}\cdot t_0} \cdot \frac{sin[(k-\tau)\Delta x]}{(k-\tau)\Delta x} \cdot e^{-jx_0(k-\tau)} d\tau \cdot \qquad \textbf{4. 46}$$

Comparing between *Equation*4. 45 and *Equation* 4. 46 we notice that the difference between the spectrum of the predicted wave $H_{wp}(k)$ and the actual windowed wave $H_{pw}(k)$ is caused by the difference in the phase factor in the two integrations. The prediction error is given by:

$$e_p = \left[H_{wp}(k) - H_{pw}(k) \right] = \int_{-\infty}^{\infty} B(\tau) \cdot \frac{sin[(k-\tau)\Delta x]}{(k-\tau)\Delta x} \cdot \left[e^{-j\,sign(k)\sqrt{g|k|}\cdot t_0} - e^{-j\left(sign(\tau)\sqrt{g|\tau|}\cdot t_0 + x_0(k-\tau)\right)} \right] d\tau$$

4. 47

The prediction error e_p is a function of the prediction window shift x_o. The optimal prediction position minimizes *Equation 4. 47* over the entire band width. Where the optimum x_o is defined by :

$$\frac{\int_{k\,min}^{k\,max} e_p \, dk}{dx_o} = 0$$

Where k_{man} , k_{max} are the higher and the lower limits of the wave number spectrum. This analytical solution to find the optimum prediction window position requires the full knowledge of the wave spectrum *B(k)*

An alternative and easier way to define the prediction window position is given by the prediction region described in *Section 2.2.2* and shown in *Figure 4. 12* .The prediction window mid point is defined by the line a_m in the middle of the prediction region, with the line slope relation to phase speeds and some geometric manipulation a_l, a_H and a_m are given by:

$$a_l : x = \sqrt{\frac{g}{k_{\max}}}t + \Delta x$$

$$a_H : x = \sqrt{\frac{g}{k_{\min}}}t - \Delta x$$

$$a_m : x_0 = \frac{\sqrt{g}}{2}\left(\frac{1}{\sqrt{k_{\min}}} + \frac{1}{\sqrt{k_{\max}}}\right)t$$

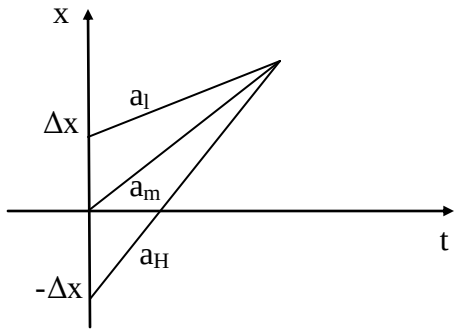

Figure 4. 12: Prediction Window Shift

Notice that the line a_l slope is equal to the dispersive curve slope at k_{max} , and line a_H slope is equal to the dispersive relation curve slope at k_{min}. The slope of line a_m that describes the prediction window shift in space has a value between the two previous slopes and hence the point k_m on the dispersive curve which has the same slope as a_m is within the wave band between (k_{man}, k_{max}).

Now we can look closer to the three phase factors in *Equation 4. 47* defined for positive values of *k* shown in *Figure 4. 13*

$$\theta_1(\tau) = \sqrt{gk}\,t_0$$
$$\theta_2(\tau) = \sqrt{g\tau}\,t_0$$
$$\theta_3(\tau) = x_0(k - \tau)$$

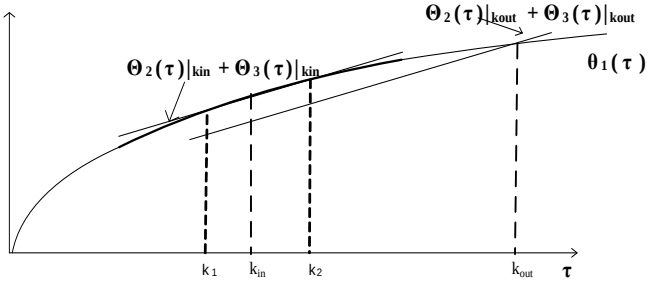

Figure 4. 13: Phase coefficient of prediction error

For simplicity we will consider the positive values of *k*.. The error in the predicted spectrum is equal to the distance between H_{wp} H_{pw}.This error is minimum when $\theta_2(\tau) + \theta_3(\tau)$ is closer to the value of $\theta_1(\tau)$. Consider the case where k_{in} is within the wave's band (k_{man}, k_{max}) and hence close to k_m described earlier, from *Figure 4. 13*

notice that the result of $(\theta_2(\tau)+\theta_3(\tau))$in this case is very close to $\theta_1(\tau)$. Next consider k_{out} outside band, notice that phase difference between θ_2, θ_3 and θ_1 is very large within the waves band. This indicates that the further away the spectrum components from k_m the larger the error (e_p), and since energy leakage results in the presence of spectrum components outside the spectrum band the errors caused by these components are expected to be larger that the components within the spectrum band.

From the previous discussion it is obvious that the prediction error in is not caused solely as a result of the energy leakage, but also by the nonlinearity of the phase shifting propagation filter. In fact if the propagation had a linear dispersion relation it would have been possible to find a value x_o that cancels the prediction error entirely even with the presence of large leakage factors. However in the case of the nonlinear dispersion relation it seems there are two approaches to reduce this error, either to reduce the energy leakage it self or to linearize the propagation phase outside the wave band. These solutions to the prediction error are the subject of the remaining of this chapter.

4.3 Partial linearization of propagation filter

As discussed in the previous section, the prediction error associated with energy leakage is mainly due to the nonlinear phase of the propagation filter. In this section we will attempt to linearize the propagation phase outside the wave band. This is demonstrated in *Figure 4. 14* for the single sided spectrum since keeps its nonlinear phase relation based on the dispersion relation ship within the wave band while outside the band the propagation filter phase is modified to equal the slope at k_m that is within the band .

The propagation filter is modified to

$$F(k)=e^{j\alpha(k)t_0}$$

Where

$$\alpha(k)=\begin{cases}\sqrt{\dfrac{k_1+k_2}{2}} & k<k_1 \;\&\; k>k_2\\ \sqrt{gk} & k_1<k<k_2\end{cases}$$

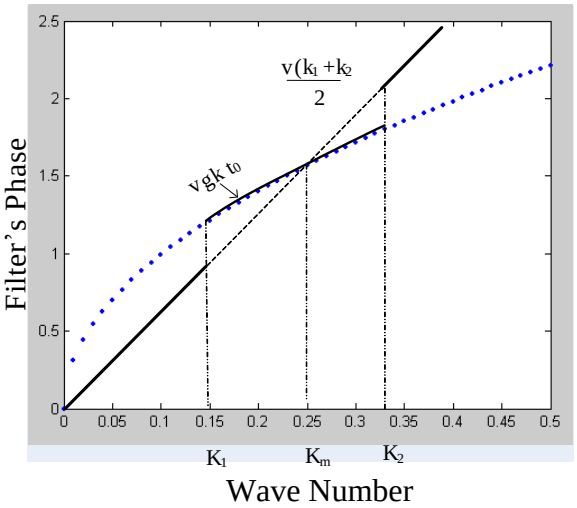

Figure 4. 14: Partial filter linearization

To test this method the same wave form described in *Section 4.2* and shown in Figure 4. 8.a was used.

Figure 4. 15 shows the prediction result for time (5,10,20,60)s using a partial linearized prediction filter. The results of this method compared to the result of the original propagation filter wave form shown in Figure 4. 8(b,c,d,e) it is clear that linearizing the propagation filter outside the signal's band improves the prediction errors associated with energy leakage considerably. However, The problem in this method is the discontinuity in the filter phase which introduces clear spikes in the predicted wave form.

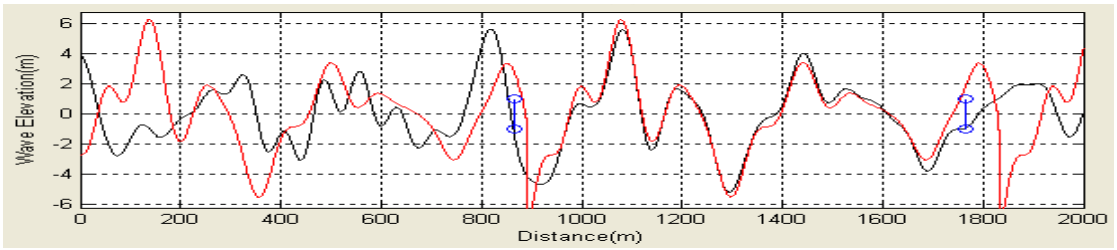

a) wave prediction at t =5s

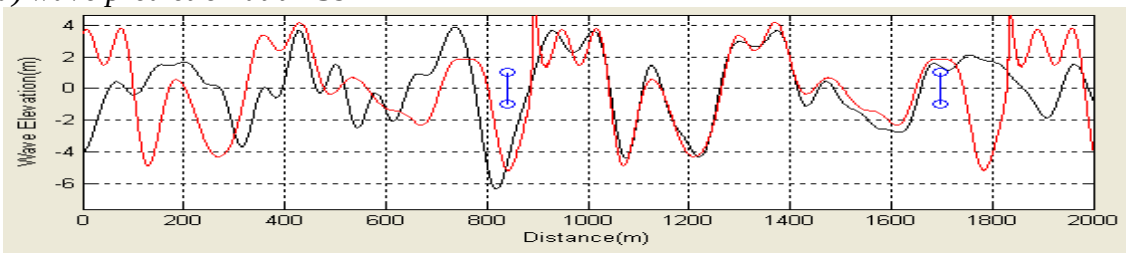

b) wave prediction at t =10s

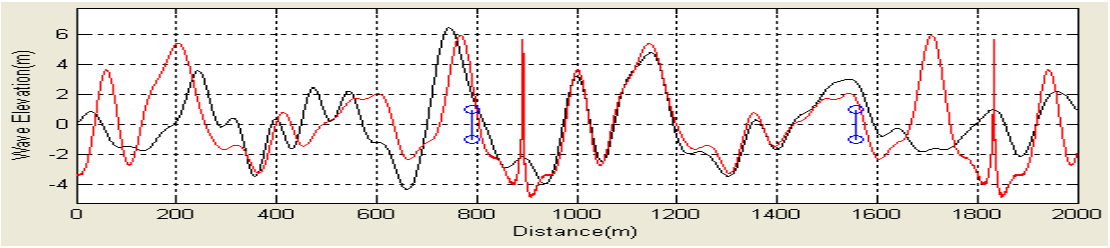

c) wave prediction at t =20s

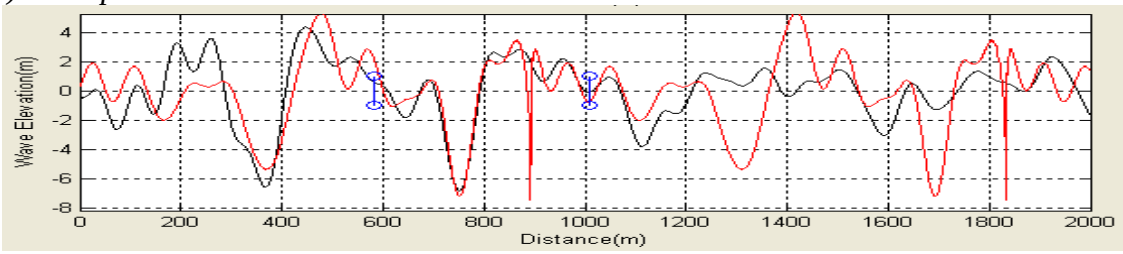

d) wave prediction at t =60s

----- *Propagated wave* , ----- *Prediction wave* , ------ *Prediction boundary*

Figure 4. 15:Wave prediction using square window with partial linearization prediction filter

4.4 Weighting windows

Truncation or weighting windows are widely studied in the literature [70] as a method to reduce energy leakage in many scientific fields. Several popular windowing functions and their corresponding frequency response functions are illustrated in [71] [72] . All weighting windows have spectral side lobes of lower amplitude than those of the rectangular function, which is the main reason for improving the energy leakage problem. On the other hand all of these weighting windows also have a broader main spectral lobe and hence the more smeared the spectrum components would be. That is the broader the main lobe, the less distinguishable the spectrum components become resulting in worst spectrum resolution. This results in a trade of between leakage (side lobe level) and spectrum resolution (main lobe width).

The Hanning window is chosen to study the affect of weighting function on wave prediction. *Figure 4. 16.a* shows the same example given in *Figure 4. 8.a*. The scanned region of the wave is chosen to maximize the energy leakage. The wave is multiplied by the Hanning weighting function before passed through the prediction filter.

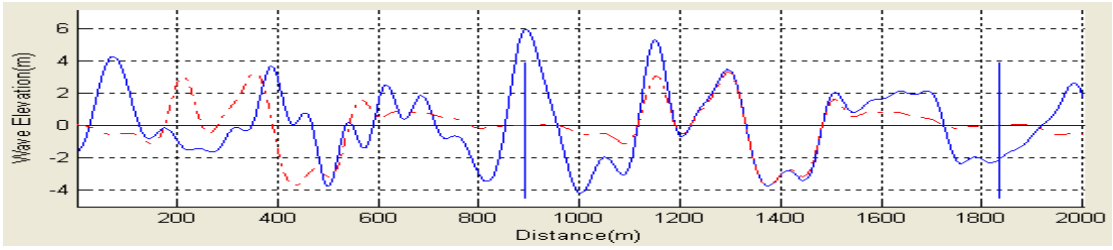

a) wave prediction at t =0s

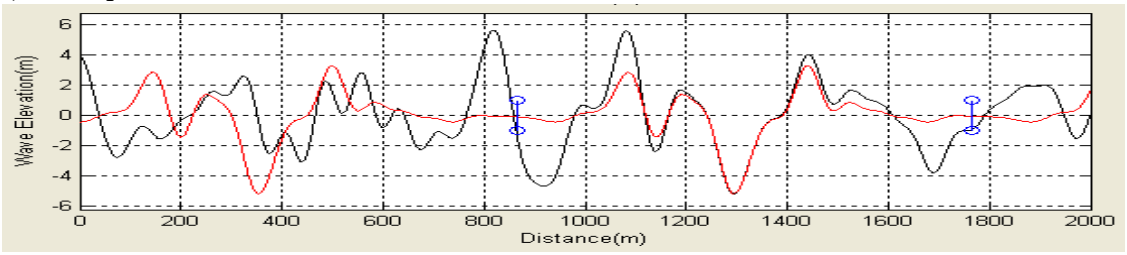

b) wave prediction at t =5s

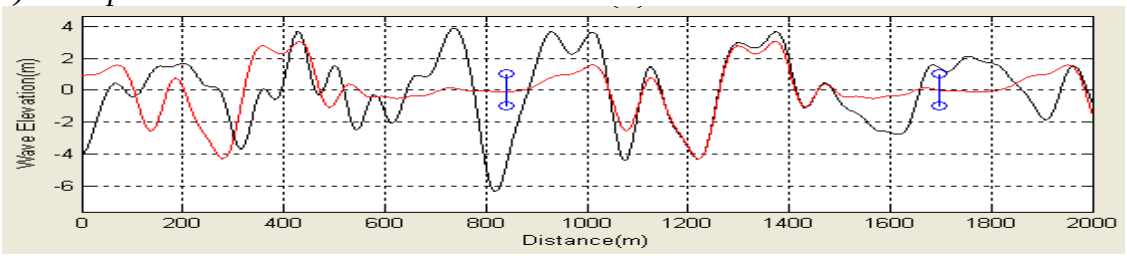

c) wave prediction at t =10s

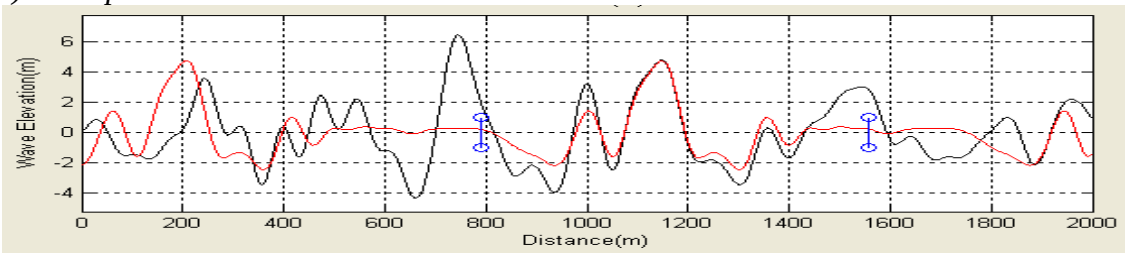

d) wave prediction at t =20s

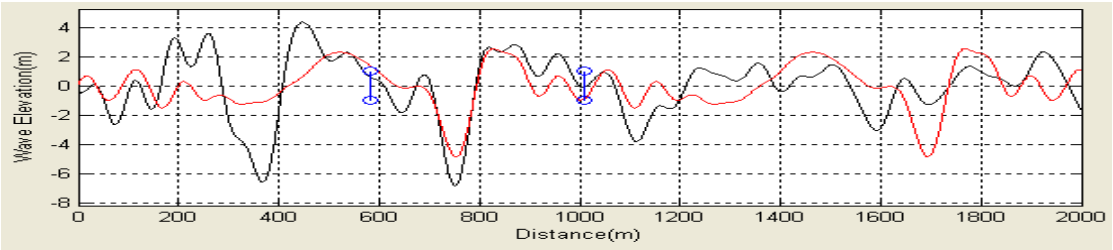

e) wave prediction at t =60s

------ *Original wave* , ------- *Prediction wave model* , ------- *Prediction boundary*

Figure 4. 16: Wave propagation using Hanning window

The prediction results using this window are illustrated in *Figure 4. 17-b,c,d,e* for $t_0 = (5,10,20,60)s$. The spectrum of the windowed wave is shown in Figure 4. 17. Compared to the spectrum of the square windowed wave shown in Figure 4. 9, the spectrum leakage outside the wave's pectrum band *[kmin=.01 kmin=0.1]* is reduced considerably and as a result the high frequency ripples that appear in the prediction using a square window are eliminated. However it is clear that the deformation of the measured part of the wave results in poor prediction results within the prediction window compared to the square window prediction and the prediction using linearized filters.

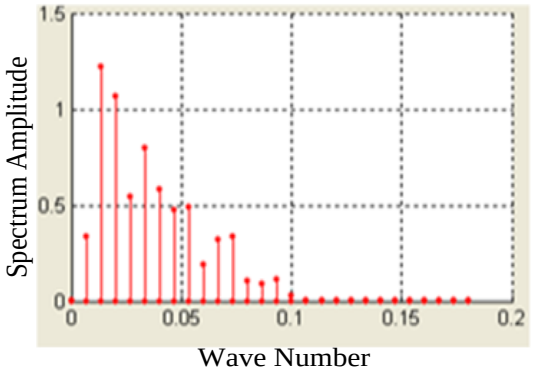

Figure 4. 17: Wave number spectrum using Hann window

4.5 End matching

The End-matching method was suggested in[2] as a technique to improve the prediction error in DSWP system , see *Section 2.4.3*. This was based on the forced periodicity associated with the DFT. In this section some changes are introduced to the original algorithm; however the main goal remains to find two matching points in the data record. End-matching is used to reduce the difference in wave elevation between the first point and the last point of the data record to an acceptable level. Also in End-matching the difference between the first and the last derivatives of the data record are considered.

The first step is to determine the two parameters used in this technique (maximum first deviation D_{max},and maximum second deviation D^2_{max}), which are defined as

- D_{max} is the maximum slope of the line joining the scanned points of the wave
- D^2_{max} is the maximum difference between two successive slopes.

For simplicity we assume our wave model is the single harmonic wave given by:

$$h(x) = A \cdot cos(kx) \qquad \textbf{4. 48}$$

If the wave is sampled at a resolution of Δx ,the maximum derivative is at $x = \frac{\pi}{2k}$ which is the slope of the line between the two points($x = \frac{\pi}{2k} - \frac{\Delta x}{2}$, $x = \frac{\pi}{2k} + \frac{\Delta x}{2}$). The

maximum first derivative is the slope of the line between two points shown in Figure 4.18.a, where

$$D_{\max} = \frac{2A\sin\left(k\frac{\Delta x}{2}\right)}{\Delta x} \qquad \textbf{4. 49}$$

The maximum second derivative is at $x = 0$,which is the difference between the slope of the two lines shown in Figure 4.18.b

$$D^2_{\max} = 2A(1 - \cos k\Delta x) \qquad \textbf{4. 50}$$

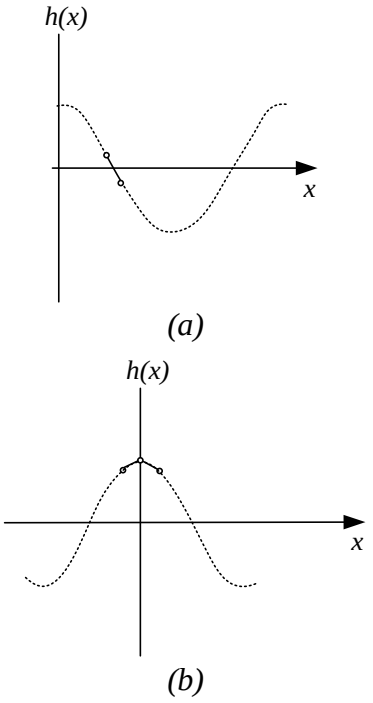

Figure 4. 18: Maximum first and second derivates

Using super position these parameters are be evaluated for a more complex wave form

$$D_{\max} = \frac{2}{\Delta x}\sum_{h=1}^{N} A_n \sin\left(k_n\frac{\Delta x}{2}\right) \qquad \textbf{4. 51}$$

$$D^2_{\max} = 2\sum_{h=1}^{N} A_n\left(1 - \cos\left(k_n\Delta x\right)\right) \qquad \textbf{4. 52}$$

Where A_n is the nth wave component amplitude. Table 4.1 shows the values of (D_{max},D^2_{max})for the Pierson-Moskowitz model with a one meter resolution. These values are used in the implementation of the End-matching method.

Table 4. 1: Maximum first and second derivatives of the Pierson Moskowitz Sea

Wind speed m/s	D_{max},	D^2_{max}
5	*0.2792*	*0.2290*
10	*0.3164*	*0.0626*
15	*0.3025*	*0.0338*
20	*0.2848*	*0.0159*
25	*0.3131*	*0.0127*
35	*0.3041*	*0.0053*

When matching two points ,the point at the beginning of the data record is denoted P_b ,the point at the end of the record is denoted P_e. The slope of P_b is $D_b = P_{b+1} - P_b$ and the slope of P_e is $D_e = P_e - P_{e-1}$, as shown in *Figure 4. 19*. The third slope shown in this figure is $D_{eb} = P_b - P_e$.

For the two points (P_b&P_e) to match:

1. The slope between the point should be less or equal the maximum slope $D_{eb} \le D_{\max}$

2. The deference between each successive slopes should be less than or equal to maximum second deviation

$$\left|D_{eb} - D_e\right| \le D^2_{\max} \quad ,$$

$$\left|D_{eb} - D_b\right| \le D^2_{\max}$$

3. The distance between P_b&P_e should not be less than $N_{\min}$ which is specified to prevent over reduction of window length

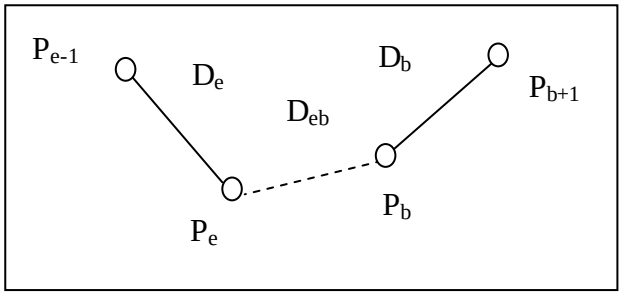

Figure 4. 19: Matching two edge points

Figure 4. 20.*a* shows the End-matching result of the wave form a given in Figure 4. 8.*a* .The measurement window was reduced in length, since a match was found between the two points $(x=1047)m$ and $(x=1832)m$, this reduces the window length from the original length of *940 meters* to *758 meters* , the new window boundaries are illustrated by the green vertical lines in Figure 4. 20-a. In this example the reduction in the window size is reasonable. The prediction model produced using this window is plotted using the red line. It is clear that this window has considerably less discontinuity at the two ends than that in the case of the original square window shown in Figure 4. 8-a.

The spectrum of this end matched data is shown in Figure 4. 21, it is clear that the energy leakage has reduced considerably compared to that of the original square window shown in Figure 4. 9.

It might seem strange given the generalized uncertainty principle to suggest that the reduction of the window length would also result in the reduction of the spectrum. This is true only since we are using a discrete spectrum to describe the wave's data. When changing the window length, the original spectrum sampling points are changed, since the spectrum is sampled at points

$$k_n = \frac{n2\pi}{L} \qquad n = 0,1,2\ldots\ldots \qquad and \qquad L = window\,length$$

The reduction of the energy leakage is due to the fact that end matching better reflects the convergence in the mean property of the Fourier series.

Prediction results using the end matched wave form for $t = (5,10,20,60)s$ are shown in Figure 4. 20-*b,c,d,e* respectively. The clear reduction in the ripples apparent in the original window prediction is a direct result of the reduction in the energy leakage.

There is also clearer improvement in the prediction results compared to that of the Hanning window shown in Figure 4. 16, this reflects the fact that unlike the classical windowing techniques, the end matching method improves the spectrum estimation without changing the spatial data which in turn proves to be very important in improving the wave prediction.

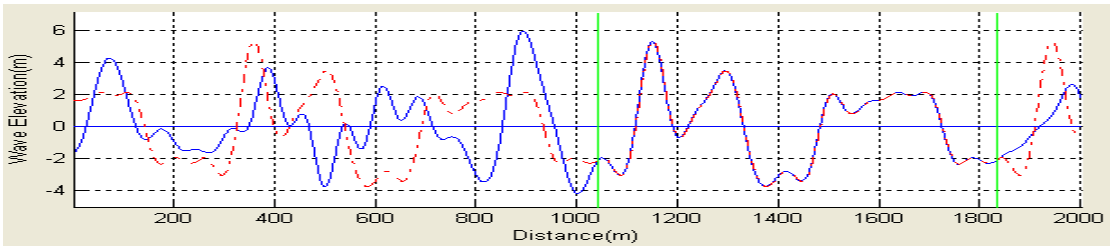

a)wave model and wave prediction model at t =0s

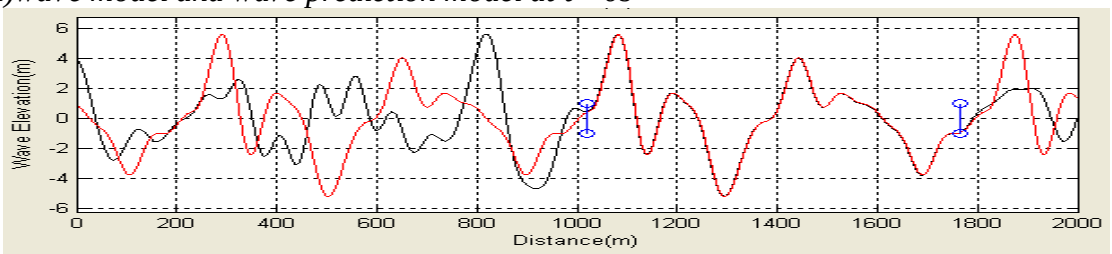

b)wave model and wave prediction model at t =5s

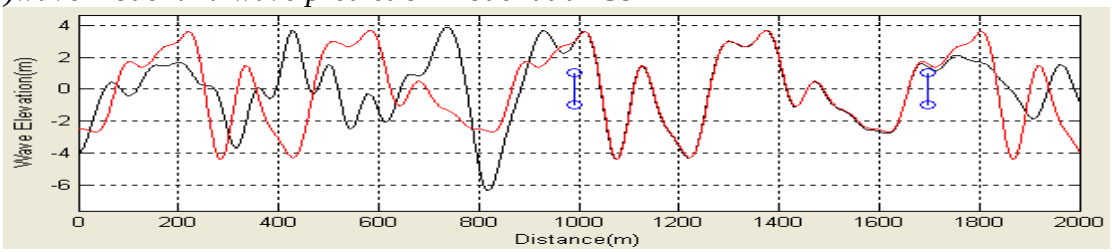

c)wave model and wave prediction model at t =10s

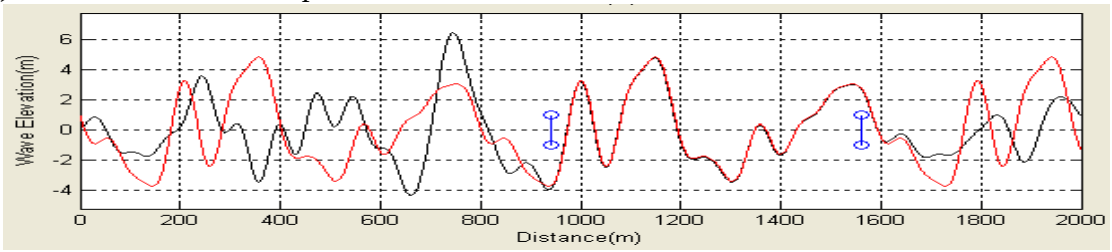

d)wave model and wave prediction model at t =20s

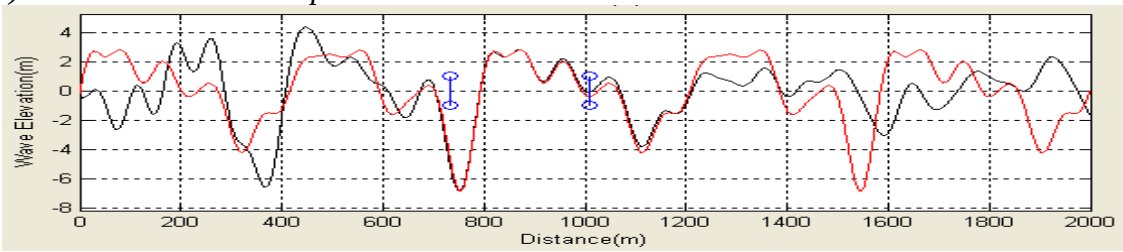

e)wave model and wave prediction model at t =60s

------ *Original wave* , ------- *Prediction wave model* , -------- *Prediction boundary*

Figure 4. 20: Wave prediction using and matching method

This method improves the prediction results compared to the original size window Figure 4. 8 and the Hanning window Figure 4. 16, however, it has the disadvantage of reducing the available data and in the some cases no matching can be found. The data reduction amount depends on two factors the scanning resolution and the wave's frequency content.

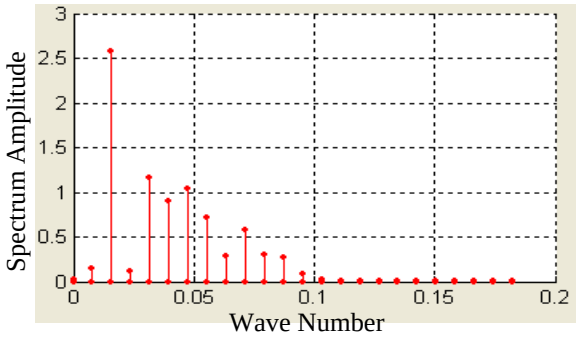

Figure 4. 21: Wave number spectrum using End- matching technique

4.5.1 Data record reduction associated with End-matching method

To study the reduction in the data record caused by the end matching method, the wave simulation described in *Section 2.7* was used to generate 1000 wave data records of length (1000m) and one metre resolution, for the Pierson Moskowitz wave model of (U=5,10,15,20)m/s. The window length reduction using the End-matching method was found for each wave model.

Figure 4. 22.*a* shows the probability distribution of the window reduction in metres. As expected the reduction in the measurement window length caused by end matching changes for different wind speed, where the case with the smallest dominant frequency (*U=20m/s)* suffers more reduction than that with larger dominant frequencies. The normalized lengths are obtained by dividing the reduction length of each example by it's dominant wave length given in *Table 2.1* . The distributions of the normalized window reduction of the different wave models are shown in Figure 4. 22 *b*. The End-matching technique caused an average data reduction around (40%) of the dominant wave length.

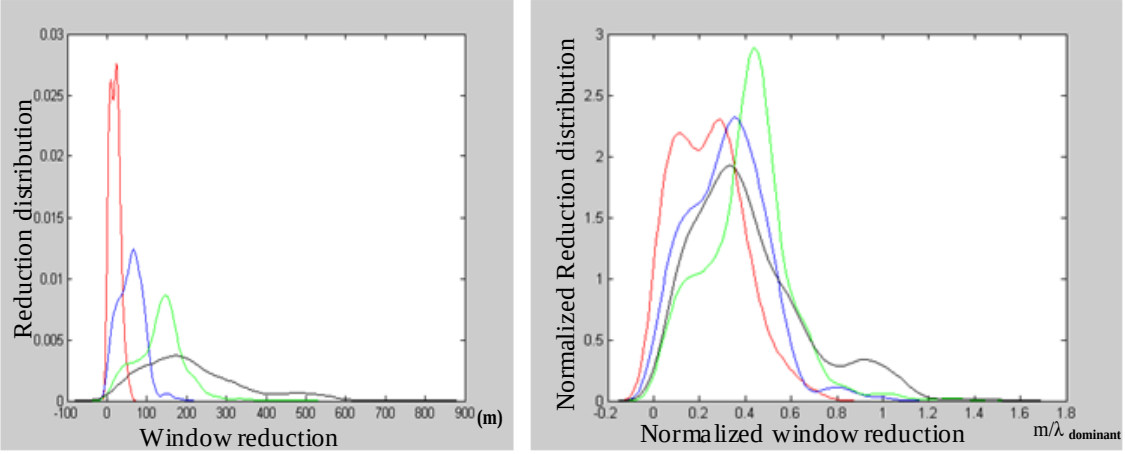

a) Window reduction distribution in metres *b) Normalized reduction distributions*
wind speed (---- $U=5ms^{-1}$, ---- $U=10ms^{-1}$, ---- $U=15ms^{-1}$, ---- $U=20ms^{-1}$)

Figure 4. 22: Window reduction using end matching method

4.5.2 Comparing the End-Matching method and the Hanning window

The window reduction associated with the End-Matching technique affects the prediction region length. On the other hand, the Hanning window deformation of the spatial information also results in a reduced prediction window. This test is set to compare the length of the prediction region of end matched waves with that of a Hanning weighted wave with the same length. The same simulation data described in the last section is used to compare these two methods. wave simulation described in *Section 2.7* was used to generate 1000 wave data records of length (1000m) and one meter resolution, for the Pierson Moskowitz wave model of (U=5,10,15,20)m/s.

First the wave is passed to the End-Matching algorithm. The result is then passed through a Hanning window. Then both wave models are passed through a propagation filter with $t_0 = (5,10,20)s$. The prediction length of the End-Matching prediction (p_{r1}) and that of the Hanning window prediction (p_{r2}) are estimated in this experiment by the region where the prediction error becomes larger than 10% of the significant wave height (SWH). The block diagram of this comparison is shown in *Figure 4. 23*.

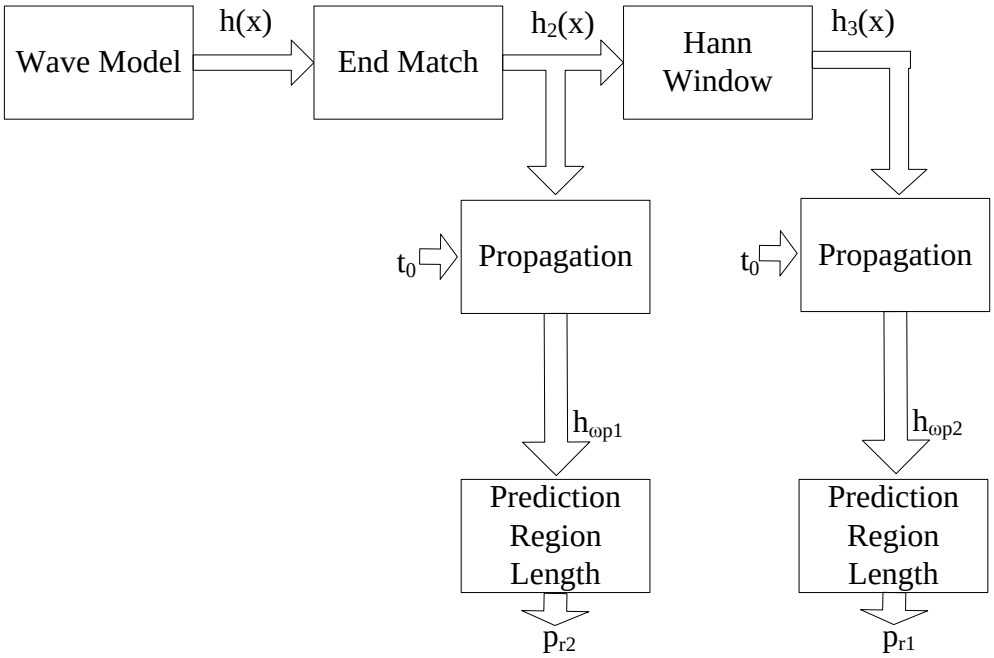

Figure 4. 23: Comparing End-Matching and Hanning window

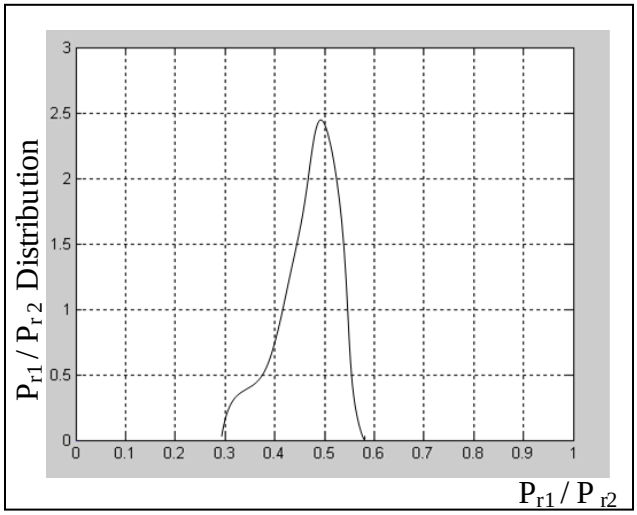

Figure 4. 24: Results of comparing End-matching and Hanning window P_{r1}/P_{r2} distribution

Figure 4. 24 illustrate the probability distribution of the factor ($\frac{P_{r2}}{P_{r1}}$), which represents the percentage of the prediction length obtained using the Hanning window of that resulting from the end matched wave. It is clear that the prediction region provided by a Hanning window is usually half of the prediction region provided by the rectangular window modified by the End-Matching.

This result is due to the fact that rectangular window have half the main lobe width of the Hanning window and hence the frequency resolution of the rectangular window is

double that of the hanning window. In practice the maximum reduction in the window size using End-matching should by half the window length, since the same result would be obtained using the Hanning window.

4.6 Window Expansion method

This new method tries to reduce the energy outside the wave system band without altering the spatial data as in the case of classical windowing techniques, and without reducing the window size as in the end-matching technique. The first step is to expand the data window by a certain length ($L_{\exp}$), secondly this expanded part is filled in with artificial data that results in a spectrum that is limited to the waves band width.

Two questions arise at this stage. First, what is the length of ($L_{\exp}$)?second, how to find the added data value that will limit the spectrum to the required band? We will require that the maximum extension is (L_D/2) where L_D is the dominant wave length.

$L_D = \frac{2\pi}{k_d}$ where k_d is the dominant wave number.

The value of the dominant wave lengths for different Pierson Moskowits sea are shown in *Table 2.1.* The extension length ($L_{\exp}$) used is the length of the dominant wave length weighted by the degree of leakage by:

$$L_{\exp} = \frac{L_D}{2} \cdot \frac{E_{out}}{E_T}$$

Where

E_{out} = Energy outside the spectrum band

E_T = Total energy of the spectrum

The Papoulis Gerchberg wave reconstruction technique introduced in *chapter 3*, is used to fill in the window extension so that the resulting wave spectrum is limited to the original spectrum. The same wave form shown in Figure 4. 8-*a* that was used to illustrate the prediction in previous section is used again to demonstrate the prediction results using window expansion method. Comparing the original measurement window dimensions (893,1832)*m* of that shown in Figure 4. 25.*a* by the two vertical green lines, window left edge is shifted to $(x = 781m)$, creating the expansion region between $(x = 781m)$ and $(x = 893m)$. This region is filled in with the artificial data using the Papoulis Gerchberg method.

Comparing the spectrum of this method - shown in *Figure 4. 26*- to the original square window spectrum - shown in Figure 4. 9- it is clear that the window expansion technique reduce the energy leakage without changing the data in the original window or reducing the size of the measurement window.

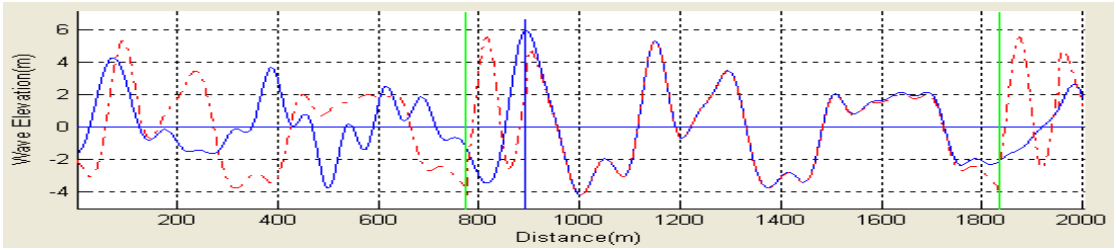

a) wave prediction at t =0s

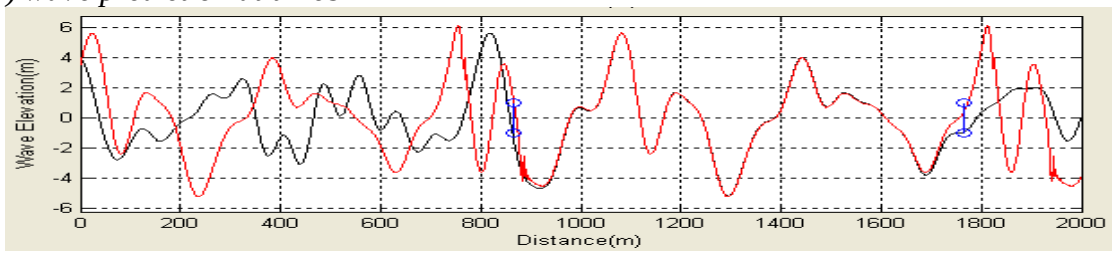

b) wave prediction at t =5s

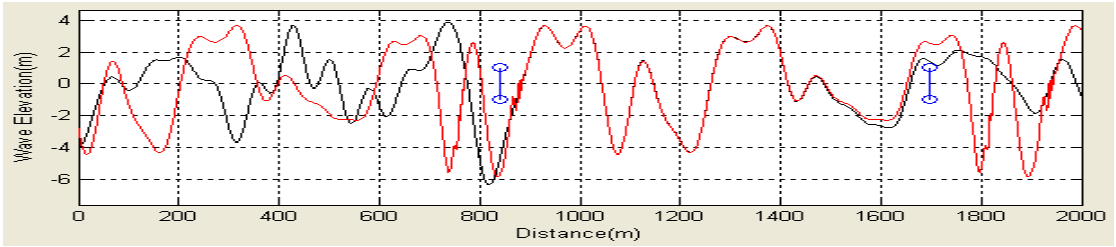

c) wave prediction at t =10s

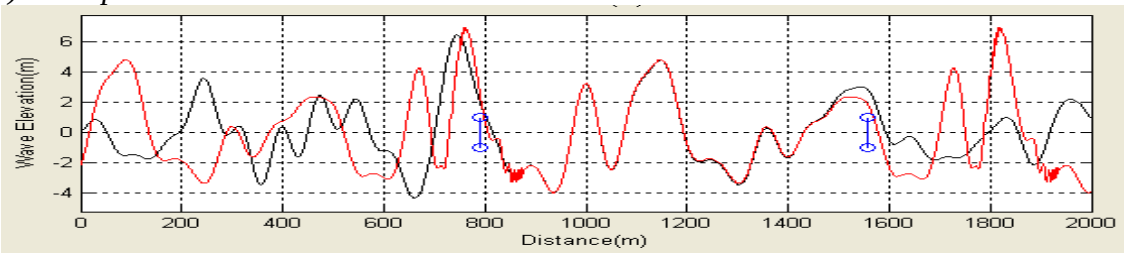

d) wave model and wave prediction model at t =20s

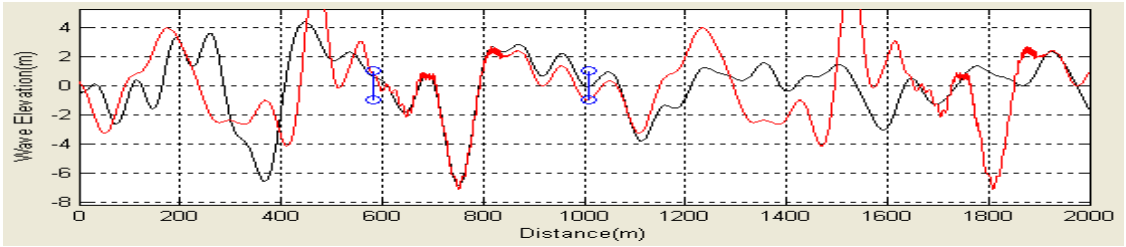

e) wave prediction at t =60s

----- *Original propagation wave* , ------ *Prediction wave,* ------ *Prediction boundary*

Figure 4. 25: Wave prediction using window expansion method

Since the Papoulis Gerchberg method is an iterative technique a balance is needed between reducing the energy leakage and the time spent generating the artificial data. For this application it was found that as low as 20 iterations are sufficient. The prediction results using the window expansion method are shown in Figure 4. 25-*b,c,d,e* for the prediction time $t = (5,10,20,60)$ respectively. Comparing these results to that of the previous methods it is clear that this technique provides the largest prediction region. The small ripples appearing in this prediction is a result of a small degree of discontinuity between the edges which appears as minor energy leakage in the spectrum.

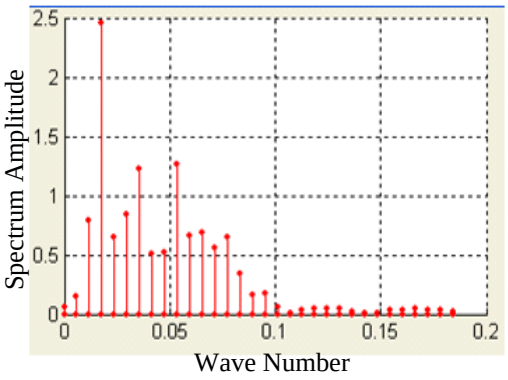

Figure 4. 26: wave number spectrum using Window expansion method

This Chapter displayed a single case to demonstrate the prediction error for each method, a more comprehensive comparison between these methods is given in the next chapter using the prediction error surface. Also a user panel shown in appendix (B-2) is designed to help simulate different wave measurements situation providing an important tool to compare more efficiently the different prediction methods discussed in this chapter. The main advantage of user interface panels is the flexibility in setting the measurement window size. After the measurement window is positioned on the required part of the wave, the spectrum based prediction algorithm is used to predict the wave at the given time delay.

Chapter 5

Prediction Region Examination

5.1 Introduction

One of the key questions associated with DSWP and its applications is "what controls how far ahead in time and space can waves be predicted". The second important issue is to understand what affects the prediction accuracy. There are essentially four aspects to these questions. The first is information based and is determined by the characteristics of the measurement processes, including its resolution and reliability. The second involves the detailed properties of the particular type of sea of interest. The third is concerned with the dynamics of wave propagation. The fourth is the specific properties of the prediction algorithms.

The prediction region boundaries were illustrated with a *(x,t)* plot in *Section 2.2.1* and *Section 2.2.2*, in this chapter the prediction accuracy distribution within the *(x,t)* plain is addressed, taking a close look in to the prediction region of DSWP for the fixed time mode, associated with different wave conditions.

5.2 Space/ Time Diagrams of Pierson-Moskowitz Seas

The boundaries of the region in which waves can be predicted from a given type of measurement mode is typically realized through the space/ time diagram, which doesn't hold any information about the accuracy of the prediction. *Figure 5. 1.* illustrates the (x,t) diagram of the Fixed Time mode. The sea surface is measured in one dimension along the x axis from point D_1 to point D_2 in a negligibly small time. The slope of

diagonal lines in the diagram corresponds to phase velocities of the component waves defined by the wave spectrum finite bandwidth hence, there will be a fastest and slowest phase velocity associated with the sea. Here the term bandwidth defines the upper and lower frequencies which contain a given fraction of the total energy in the wave system.

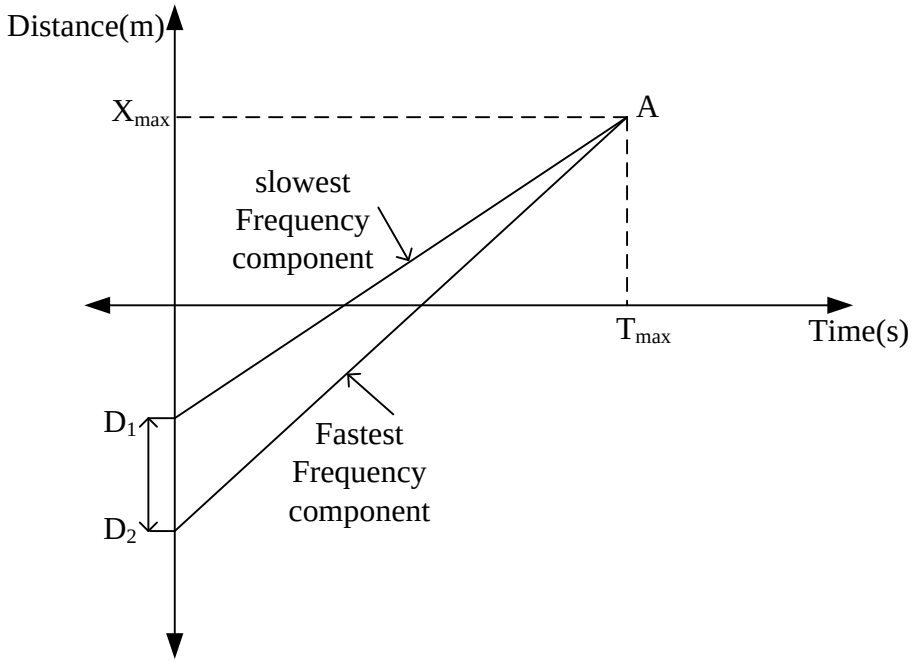

Figure 5. 1:Maximum time and distance for fixed time mode of DSWP

Figure 5. 1 also demonstrates two important parameters that characterize the prediction region:

T_{max}: The maximum time period from the measuring instance where prediction is possible.

X_{max}: The maximum distance from the beginning of the measuring region where prediction is possible.

These parameters have an important role in prediction region modelling as will be shown in *Section 5.6*. Using simple geometry it can be easily shown that the parameters T_{max} and X_{max} are defined as:

$$T_{max} = \frac{(D_1 - D_2)(\omega_2 \omega_1)}{g(\omega_2 - \omega_1)} \quad sec \qquad \textbf{5. 1}$$

$$X_{max} = \frac{(D_1 \omega_2) - (D_2 \omega_1)}{(\omega_2 - \omega_1)} \quad m \qquad \textbf{5. 2}$$

Where ω_1 wave spectrum lower limit. , ω_2 wave spectrum upper limit

This chapter investigates the properties of the fixed time mode prediction region of the Pierson Moskowitz seas, see *Section 1.3.3*.Given the above properties of space time diagrams it is clearly of interest to know the different extent to which various types of sea conditions affect prediction, i.e., asking the question what is the average prediction time available for a Pierson-Moskowitz power density spectrum for a given wind strength? Clearly given that each short group of waves has a different spectrum.

The prediction boundaries for this type of sea are defined by the spectrum band limits ω_1 given by Equation1. 9 and ω_2 given by Equation 1. 10. Substituting these values in Equation 5. 1 and Equation 5. 2 we get the parameters for the prediction region of the Pierson-Moskowitz seas defined as

$$T_{\max} = 0.93\left\{\frac{(D_2 - D_1)}{U\left(\left|\ln(r_1)\right|^{\frac{1}{4}} - \left|\ln(1-r_2)\right|^{\frac{1}{4}}\right)}\right\} \quad sec \qquad \textbf{5. 3}$$

$$X_{\max} = \frac{D_1\left|\ln(r_1)\right|^{\frac{1}{4}} - D_2\left|\ln(1-r_2)\right|^{\frac{1}{4}}}{\left|\ln(r_1)\right|^{\frac{1}{4}} - \left|\ln(1-r_2)\right|^{\frac{1}{4}}} \quad m \qquad \textbf{5. 4}$$

For the remaining of this chapter's experiments the measured part of the wave is over the range 0<x< 1000 *m* this gives the value ($X_{\max} = 566.7m$). While *Table 5.1* shows the value of T_{max} for different values of wind speed U.

Table 5.1: Maximum prediction time for different speed

Wind speed U (ms^{-1})	*5*	*10*	*15*	*20*	*25*
T_{max} (sec)	*221.5*	*110.8*	*73.8*	*55.4*	*44.3*

In the Pierson-Moskowitz case so far as prediction is concerned there are two competing processes operating as wind speed increases. The reduction in bandwidth increases prediction times while the move towards lower frequencies reduces it. Clearly, the inverse dependence of prediction time on wind speed given by *Equation 5. 3* shows that the shift to lower frequencies is dominant. It is interesting that for this type of spectrum the actual prediction distance scale is independent of wind speed. The above results are specific to the long fetch well developed seas described by the Pierson-

Moskowitz spectrum however it is a simple matter if required to repeat the above calculations for other types of parameterised model sea spectra such as the short fetch JONSWAP variant.

5.3 Prediction Error Surfaces

The error surface is a two dimensional function defining the prediction accuracy over the (x,t) plane. A numerical approach is adapted to construct the error surface of the prediction process. Assuming $\eta_1(x,t)$ is the wave elevation at point (x,t) evaluated using the simulation model described in *Section 2.7*.The wave $\eta_1(x,t)$ is measured at $t=0$ for the distance range $-L \le x \le 0 \ \ m$ where the measuring distance (L) is set to 1000m for all the experiments undertaken in this chapter.

The measured wave is used in the prediction model given in *Section 2.5.1* to estimate the wave elevation $\eta_2(x,t)$ over the (x,t) plane. The two dimensional grid over which the simulation is considered is shown in *Figure 5. 2*, the wave elevation and the predicted wave elevation being evaluated at each point on the grid $-L < x < 2X_{\max}$ $0 < t < 3T_{\max}$where *x* resolution is $(\Delta x = 1m)$. and *t* resolution is $(\Delta t = 1)sec.$

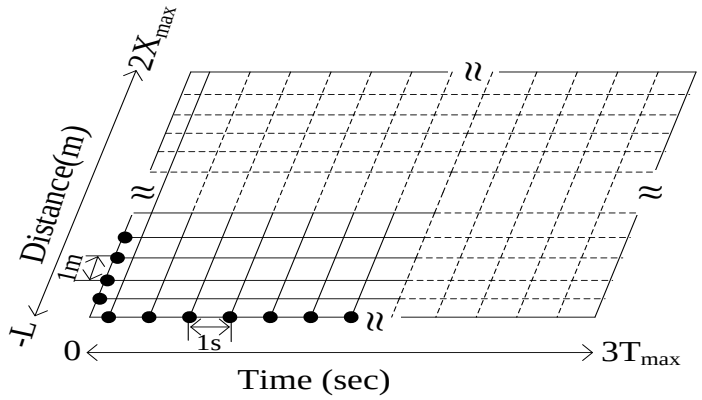

Figure 5. 2: Grid for prediction error surface estimation

The prediction error surface of a certain Pierson-Moskowitz sea model is evaluated numerically using 1000 wave sets generated from the particular model. The error function of one realization is calculated by:

$$e_i(m\Delta x, n\Delta t) = \left|\eta_1(m\Delta x, n\Delta t) - \eta_2(m\Delta x, n\Delta t)\right| \qquad \textbf{5. 5}$$

Where ($i = 1,2,3\ldots\ldots\ldots 1000$) is the wave model index.

The error surface was evaluated at each point in the space time plane by finding the maximum prediction error among the individual error function $e_i(m\Delta x, n\Delta t)$.

$$e(m\Delta x, n\Delta t) = Max(e_i(m\Delta x, n\Delta t)) \qquad i = 1,2,3,\ldots\ldots 1000 \qquad \textbf{5. 6}$$

The two dimensional grey level intensity image is used to display the prediction error function. Transforming to a grey scale is achieved via the relationship:

$$Pixel\_value = \left(1 - \frac{predcition\_error}{significant\_wave\_height}\right) \times 255 \qquad \textbf{5. 7}$$

Where black indicates zero error.

The grey level image in *Figure 5.3* display the prediction error surface of a Pierson-Moskowitz model with wind speed $15\, m \cdot s^{-1}$

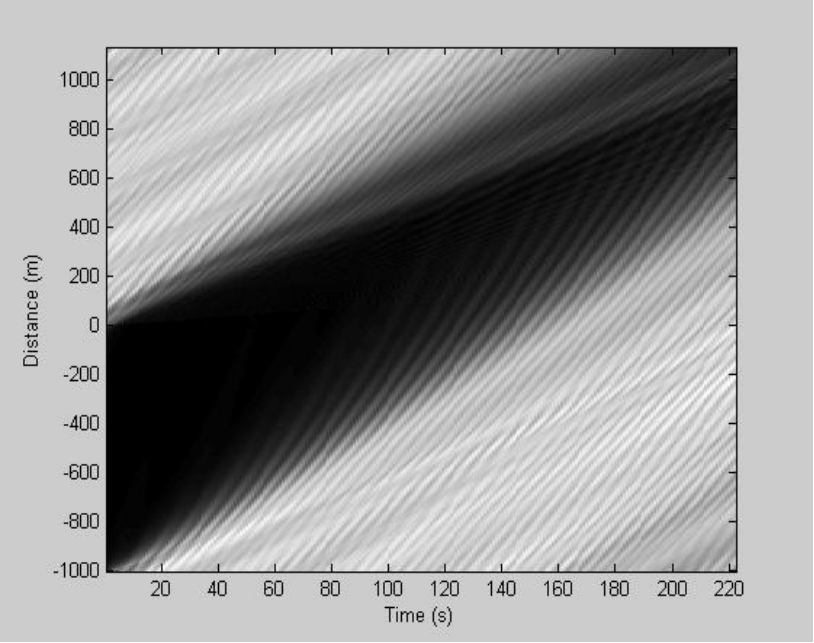

Figure 5. 3: Prediction error surface for Pierson Moskowitz sea model

The prediction error surface reveals the features expected from the space time diagram. However in a practical application of DSWP users will be mainly interested in the region where prediction error exceeds some critical value. Consequently a threshold is set and the information re-plotted to show the boundary separating the thresholded region. If the threshold value is set as *(thr)* the required region is defined by :

$$e_{thr}(n\Delta x, m\Delta t) = threshold(e(n\Delta x, m\Delta t) - Thr) \quad \textbf{5. 8}$$

where

$$threshold(r) = \begin{cases} 0 & r \geq 0 \\ 255 & r < 0 \end{cases}$$

Re-plotting of the data of Figure 5. 3 to show the regions where the prediction error doesn't exceeds a given maximum error is shown in Figure 5. 4. The two threshold values of $(5\%,10\%)\,SWH$ are used. It is clear that the error surface gives a more detailed view, since the prediction region is not set a predetermined boundary, but instead the accuracy required changes the boundaries of the region where prediction is possible, and in general the more accurate prediction is required, the smaller the prediction region becomes.

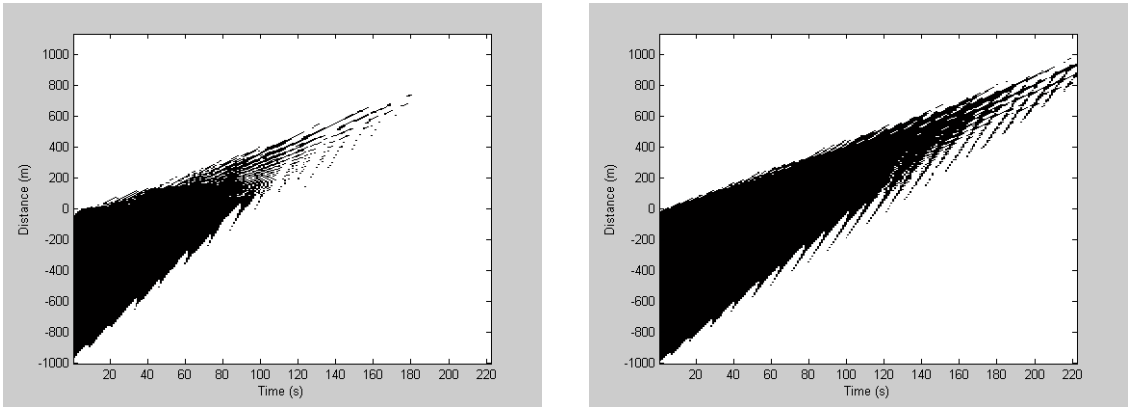

(a) *(b)*

Figure 5. 4: Prediction region with maximum error : a)5% SWH and b)10% SWH

5.4 Wind Speed Effect on Prediction Region of Pierson-Moskowitz Seas

In *Section 5.2* it was shown that for a Pierson-Moskowitz sea model T_{max} decreases with wind speed U. To explore this in detail the numerical experiment described in *Section 5.3* was repeated to generate the prediction region surface of a Pierson-Moskowitz sea model at various wind speeds (10, 15 ,20, 25) $m.s^{-1}$.The simulation grid for all four error surfaces in this experiment were fixed to the dimensions illustrated in the previous section for wind speed U=15 $m.s^{-1}$. Also the prediction algorithm used incorporated the window expansion method, *Section 4.6*. To compare the results more efficiently a threshold was used to display the region with better than 10%SWH error. The results are shown in *Figure 5. 5*.

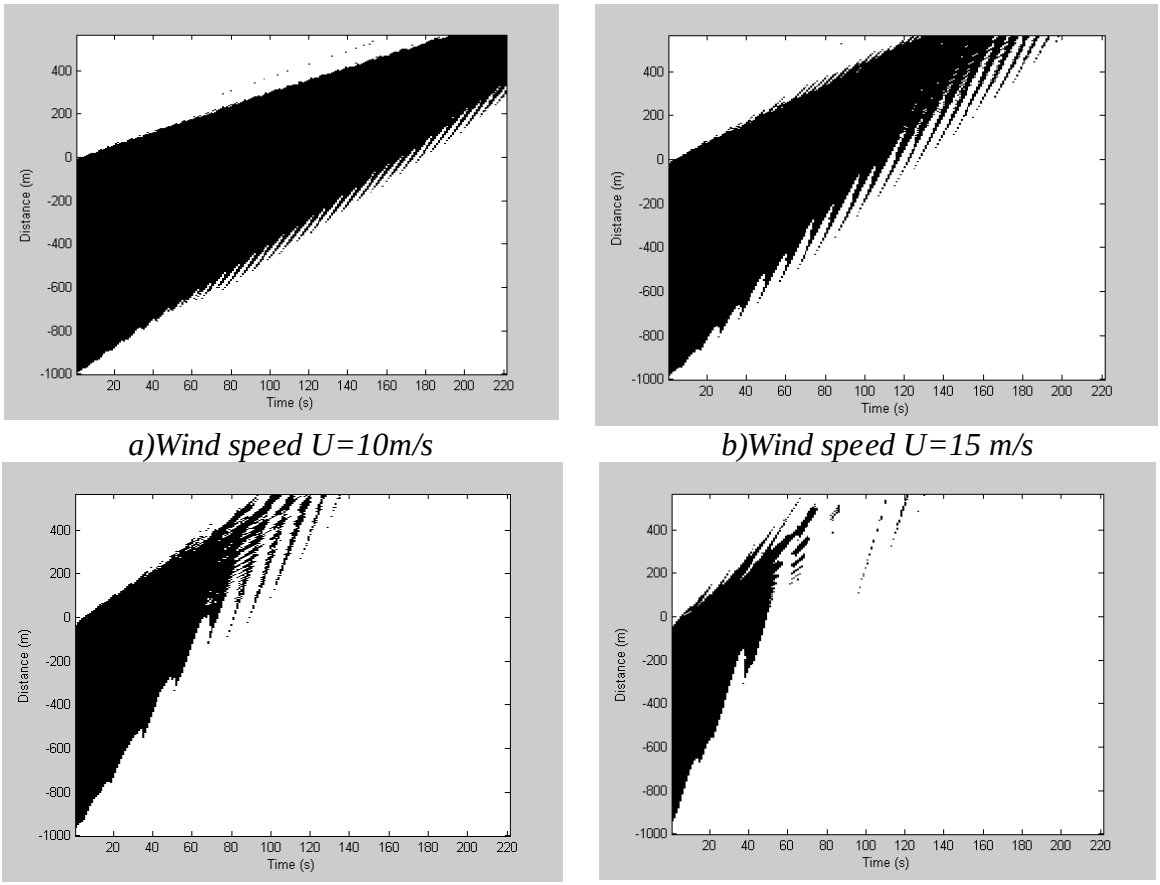

a)Wind speed U=10m/s *b)Wind speed U=15 m/s*

c)Wind speed U=20 m/s *d)Wind speed U=25 m/s*

Figure 5. 5: The effect of wind speed Pierson-Moskowitz sea prediction region of threshold 10% SWH

The results in *Figure 5. 5* bear out the findings from *Section 5.2* about the general nature of the effect of wind speed on the general prediction time and space scales. The effect of reduced prediction time at higher wind speed is very evident as is its cause, i.e, the trend for increasing phase velocities of the limiting wave components caused by down shifting of the whole spectrum.

5.5 Comparison of different Spectral Prediction Techniques

As indicated in Chapter 4 the End-matching and adaptive Window-Expansion techniques have been introduced to minimise spectral leakage effects without accompanying spatial distortion. The prediction error surface provides an effective tool to compare these two methods with each other and also against the use of raw data, which corresponds to a so called square window function, and with the Hanning window typically employed to improve spectral estimates.

Again the Pierson-Moskowitz based sea model demonstrated in *Section 2.7* with wind speed of U=15 ms^{-1} was used to generate 1000 different wave trains propagating in the positive x direction. The grid used in this experiment has the same spatial and time resolution as in the previous experiment. However the spatial range is $-L < x < X_{\max}$ and time range $0 < t < T_{\max}$.

When using End-Matching in this experiment a criteria were adaptively adjusted to produce a minimum data set length of 800m. A threshold of 10%SWH was used to find the region where the maximum prediction error does not exceed 10% of the maximum significant wave height.

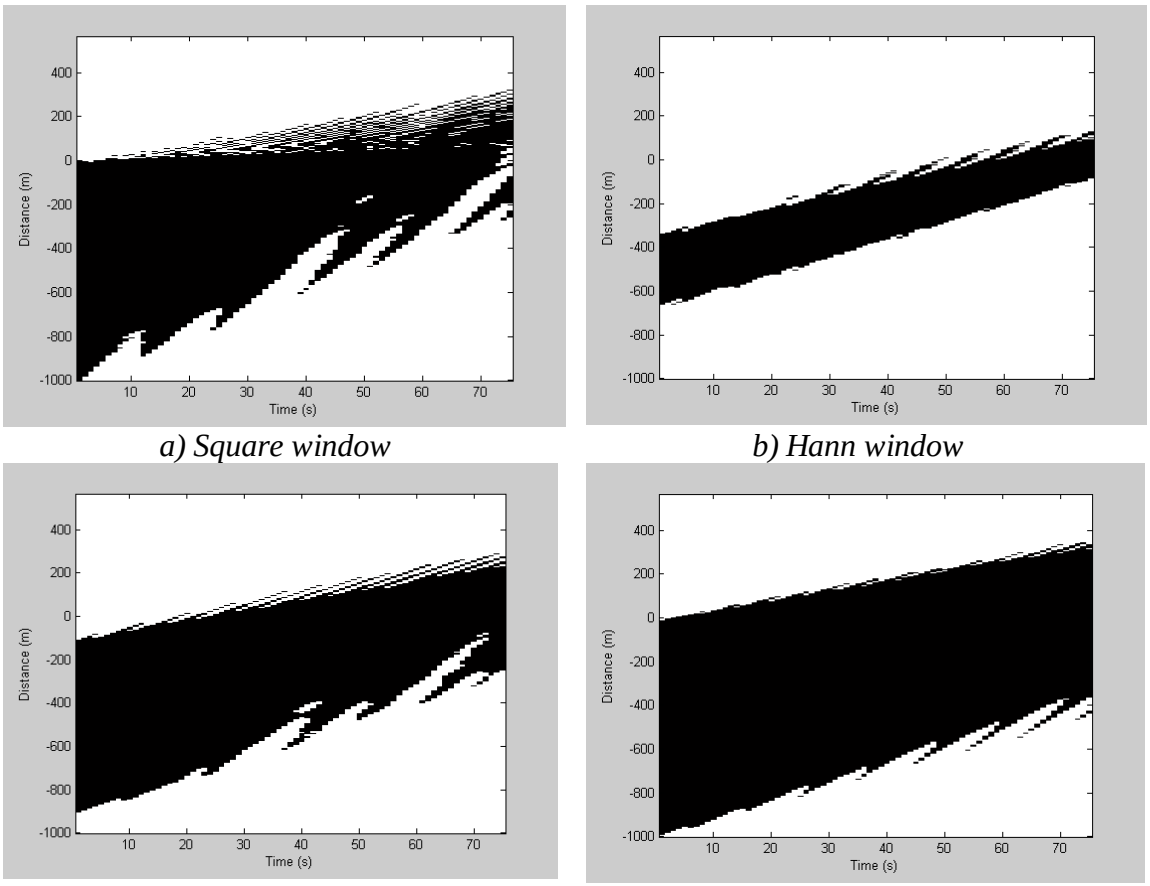

a) Square window *b) Hann window*

c)End-Matching method *d)Window-Expansion method*

Figure 5. 6: Prediction region of (10%SWH) error factor for different frequency domain prediction technique

It is clear from *Figure 5. 6-d* that the window expansion technique is significantly better than the other three, and hence this method is used for the rest of this chapter's experiments. As expected the Hanning window performed very badly, this is because the Hanning window introduces substantial distortion in the space domain in order to reduce the side lobe overlap between individual spectral components in the frequency domain, Ref [70] [71]. The price of this in the frequency domain is broadening of the

primary peak, which is normally acceptable, however the effects on prediction of such distortion are severe, as the Figure 5.6-b shows. Comparing the prediction error of the Hanning window case to that of the end matching method *Figure 5. 6*-c it is clear that in most region the prediction region of the first method is half of that of the latter method which agrees with the results of *Section 4.5.2*.

5.6 Prediction Region Modelling

Having established that the space/time prediction error surfaces provide a valuable method of comparing prediction under given circumstances it is sensible to parameterize these diagrams in some manner. Essentially this involves modelling the threshold boundary and given the oscillatory nature of this edge of these surfaces meant that some form of averaging must be implicit in the method used, otherwise an inconveniently large number of parameters would be involved. Two techniques were explored, one was to employ a low order spatial polynomial while the other exploited a form of edge detection used as part of feature detection in image analysis.

It was found that in order to develop a single model of the parameterized prediction error surfaces suitable for all Pierson-Moskowitz with different wind speed values, some kind normalization is required. Three quantities are non-dimensionalised, first the T_{max} is used to normalize the time variable, second the X_{max} is used to normalize the space variable, and third the prediction error value is scaled to the significant wave height. The new independent variables are:

$$\left.\begin{aligned} \tau &= \frac{t}{T_{\max}} \\ \alpha &= \frac{x}{X_{\max}} \\ \gamma &= \frac{e}{SWH} \end{aligned}\right\} \qquad \textbf{5. 9}$$

5.6.1 Spatial Polynomial Fitting

The goal is to model some characteristic aspects of predictions error surfaces. Instead of modelling the whole surface as a two dimensional function, the surface is disbanded in to successive one dimensional functions. These simple functions are modelled first, and then assemble to the original surface. The connection process between these simple functions is modelled also. For the polynomial fitting approach

the full prediction error (after non-dimensionalisation), are used, as opposed to the thresholded data.

Examination of sections taken along the spatial axis through the error surfaces indicated that over a wide range of conditions the sides of the "error valley" had very similar form. Thus these lower parts of the error surface were approximated by a quadratic function. The normalized error surface model $e_n(\alpha,\tau)$ at a given τ is approximated by :

$$e_n(\alpha,\tau) = a_2(\tau)\alpha^2 + a_1(\tau)\alpha + a_0 \qquad \textbf{5. 10}$$

The three coefficients $a_2(\tau), a_1(\tau)$ and $a_0(\tau)$ are a function of τ since the valley shaped part of the error surface shifts in position for different τ as shown in *Figure 5. 7*. The sections over the error values (0.5 ↔ 0.05) is used to evaluate the coefficient by fitting this part of the error surface with a quadratic function by least squares method. This process was then repeated for all points along the non-dimensionalised time axis (τ) each time producing three time dependent coefficients. This fitting process is illustrated in *Figure 5. 7* for non-dimensionalised times $\tau = 0.1$ and $\tau = 1.$ where the blue line represents the error function, while the green line represents the fitting quadratic function.

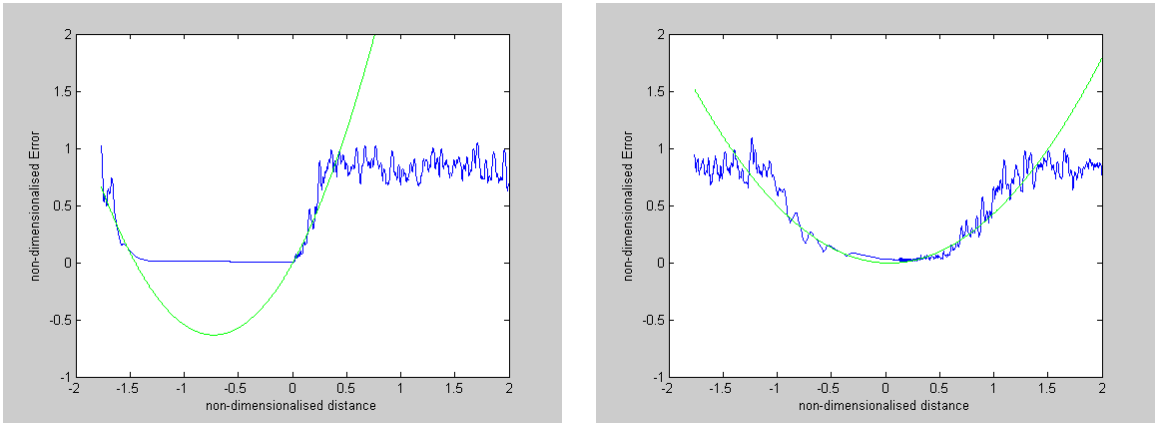

(a) *(b)*

----- *Non dimensionalised error surface* , ----- *One dimensional model*

Figure 5. 7:Modeling of slices through the prediction diagram ,a) τ = 0.1s . b) τ = 1s

The three time varying coefficients collected for different τ, were then individually least squares fitted to a suitable polynomial function non-dimentionalised time as given in *Equation* 5. 11 and shown in Figure 5. 8. The normalized error surface of wind speed of U=15 was used to find the model parameters, and the results were as follows:

$$\left.\begin{aligned} a_2 &= 0.187\tau^3 + 1.0953\tau^2 - 1.945\tau + 1.498 \\ a_1 &= 0.335\tau^3 + 1.793\tau^2 - 3.788\tau + 2.340 \\ a_0 &= 0.3265\tau^3 + 0.5214\tau + 0.133 \end{aligned}\right\} \quad \textbf{5. 11}$$

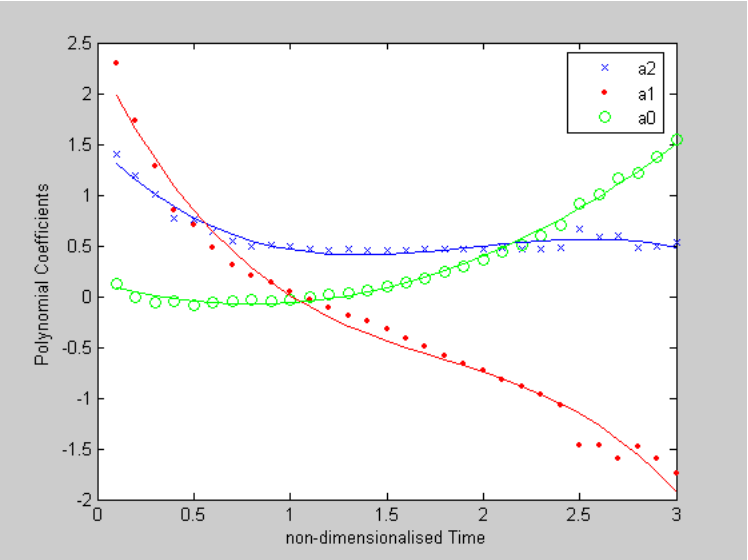

Figure 5. 8: Time dependence coefficients of the normalized error surface using the spatial polynomial fitting method

The normalized model built with the error surface of wind speed $U = 15ms^{-1}$ is used to simulate the prediction error surface of Pierson Moskowitz of different wind speeds. There are four steps to find the prediction error at a certain point (x,t)

1. Find normalized distance α and time τ from *Equation* 5. 9
2. Calculate the model coefficients $a_2(\tau), a_1(\tau)$ and $a_0(\tau)$.
3. Find the normalized prediction error value $e_n(\alpha,\tau)$ using *Equation 5. 10.*
4. The prediction error at point *(x,t)* is obtained by multiplying the normalized error by the SWH value.

To illustrate this process it is applied to the prediction error surfaces associated with the wind speed values U= 5,10,15 and 20 $m.\sec^{-1}$.

Figure 5. 9The smoothed boundary corresponding to the 10% error contour was then overlaid onto the thresholded prediction error surface produced using a 10% threshold value. The results are shown in

Figure 5. 9. *T*he blue and red lines correspond to the prediction region boundary as estimated by this model, while the black regions represent the actual prediction region of 10% SWH.

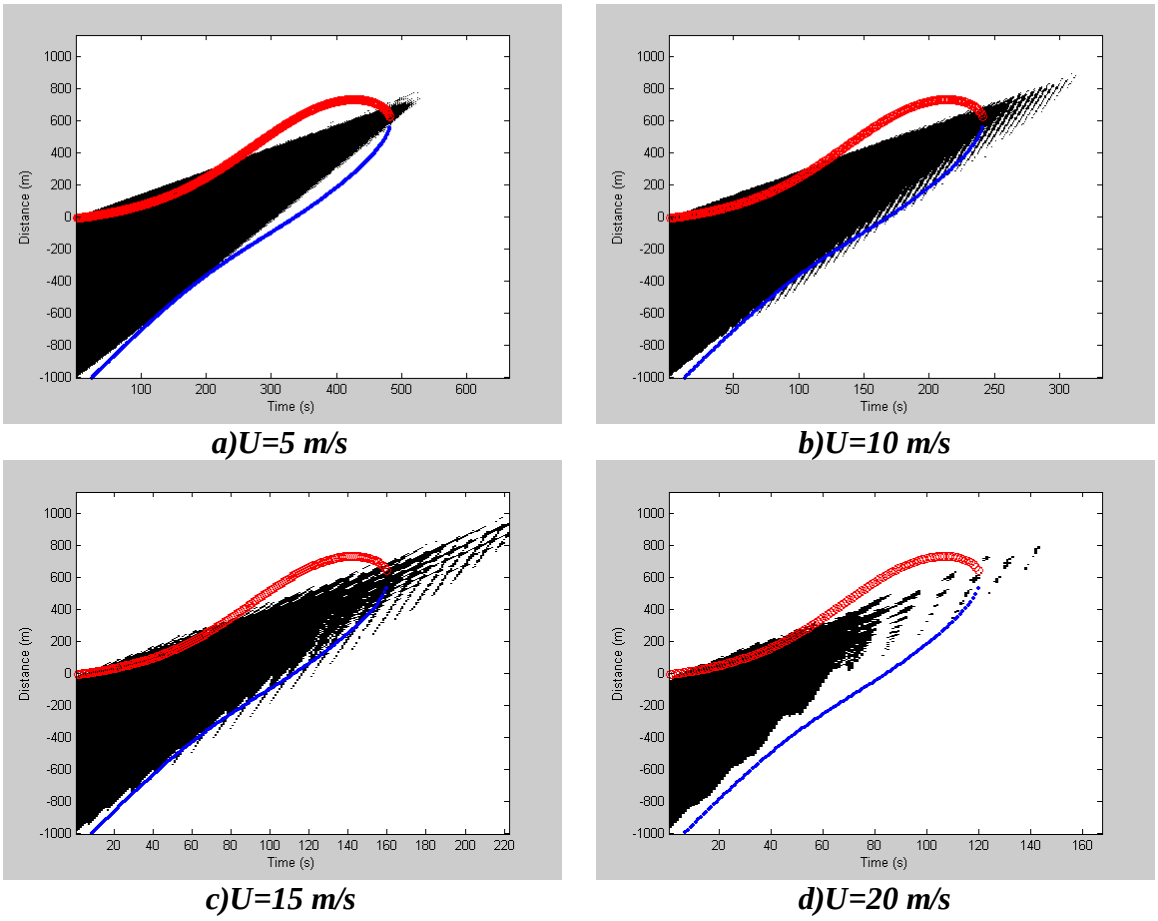

a)U=5 m/s ***b)U=10 m/s***

c)U=15 m/s ***d)U=20 m/s***

Figure 5. 9: Prediction region estimation for various wind speed using polynomial fitting model from the error surface of wind speed 15 ms^{-1}

It is clear that although the model was built using the prediction error surface of wind speed U=15ms^{-1}, the normalization procedure made it possible to use the same model to estimate the prediction region for different wind speed. The spatial polynomial fitting method described in this section manages to model the prediction error surface of the Pierson Moskowitz sea by using the eleven parameters of *Equation* 5. 11

5.6.2 An Image Processing Method

The second approach explores the parameterising of the prediction error surface boundary instead of the error surface itself. This is achieved by applying standard image processing based edge detection methods to the black & white images produced after thresholding. The first step was to find the edge of the prediction region using simple Sobel operators; this method finds edges using the Sobel approximation to the derivative, it returns edges at those points where the gradient is maximum. [73] The space time coordinates of the edge points were then least squares fitted by two straight

lines that represent a smoothed version of the threshold prediction region boundary for a certain threshold value, (Thr):

$$\left.\begin{aligned} X_1(Thr) &= a_1(Thr)\tau + a_0(Thr) \\ X_2(Thr) &= b_1(Thr)\tau + b_0(Thr) \end{aligned}\right\} \qquad \textbf{5. 12}$$

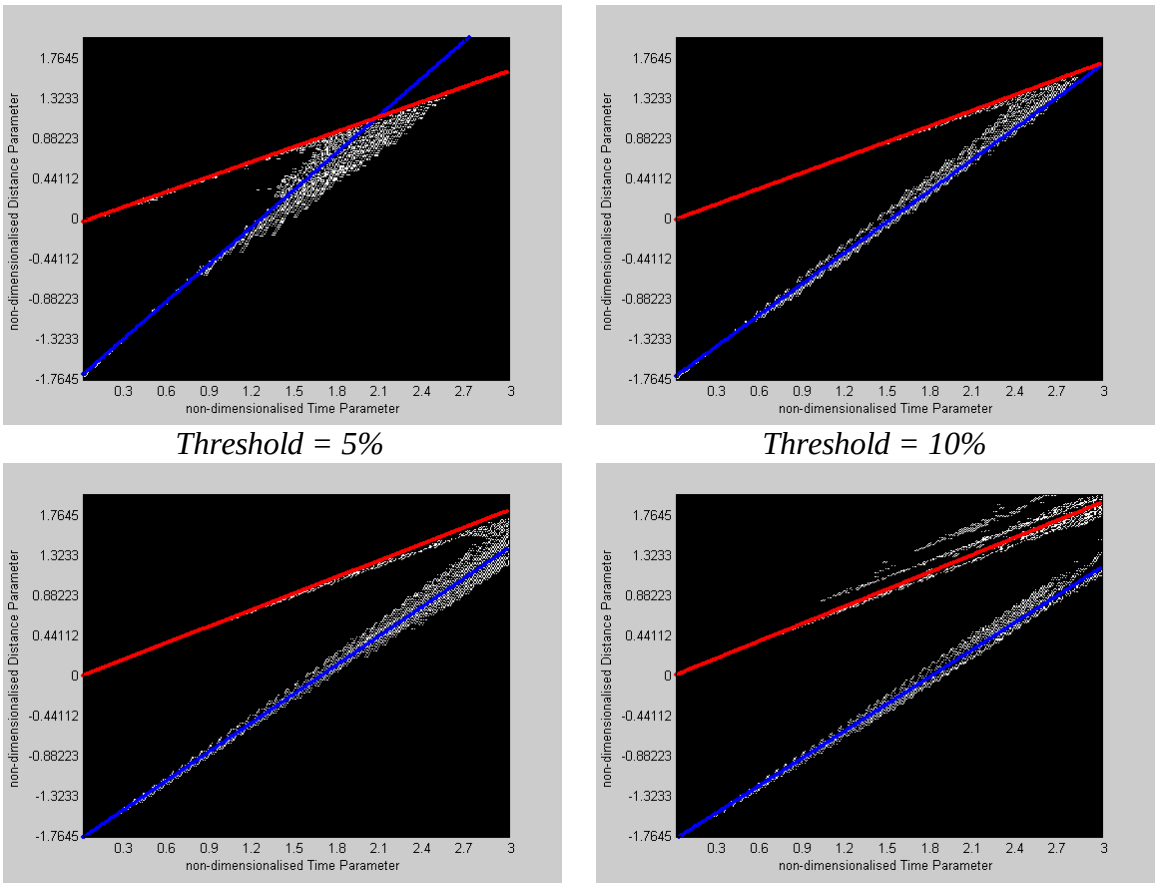

Threshold = 5% *Threshold = 10%*

Threshold = 20% *Threshold = 30%*

Figure 5. 10: Linear fitting of prediction region edge associated with different threshold values

Repeating this process for a set of threshold values produced the threshold dependencies of the coefficients which are illustrated in *Figure 5. 10*. As in the previous modelling method, the normalized error surface of wind speed U=15ms^{-1} is used to build this model. The four coefficients (a_1,a_0,b_1,b_0) are a function of the threshold value. The value of these coefficients were calculated over the range of threshold values (5%-50%) as indicated by the indivdual points in *Figure 5.11*, then the least squares method was used to fit to suitable polynomial as shown by the connected lines in *Figure 5.11* resulting in the four equations given by *Equation* 5. 13.

$$\left.\begin{aligned} b_1 &= 1.6thr^2 - 1.8thr + 1.4 \\ a_1 &= 0.6thr - 0.5 \\ a_0 &= 0.13thr - 0.3 \\ b_0 &= -0.16thr - 1.7 \end{aligned}\right\} \qquad \textbf{5. 13}$$

The threshold dependent coefficients can then be used to produce the equations for two straight lines which describe the boundary of the prediction error surface corresponding to any desired error threshold value using *Equation* 5. 12. The resulting four coefficients describing these two lines constitute the desired parameterisation of the prediction error surface.

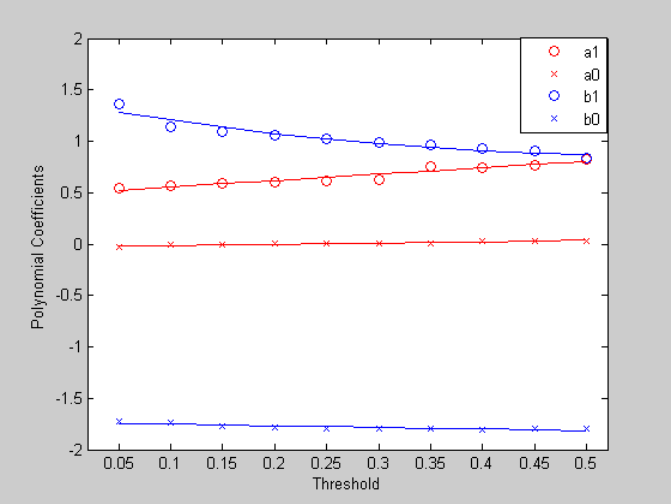

Figure 5. 11: The variation of the normalized prediction region boundary edge parameters as a function of the threshold value

The results of this process are illustrated for various threshold values at a wind speed of U=10 $m.\sec^{-1}$ in *Figure 5. 12.* Although the original model was built using the error surface of U=15ms^{-1}, still the obtained parameters describe the prediction region boundaries of the wind speed U=10ms^{-1}. This method produces a model with the nine parameters of *Equation* 5. 13 which follow the boundaries of the prediction region of the Pierson Moskowitz sea with any wind speed.

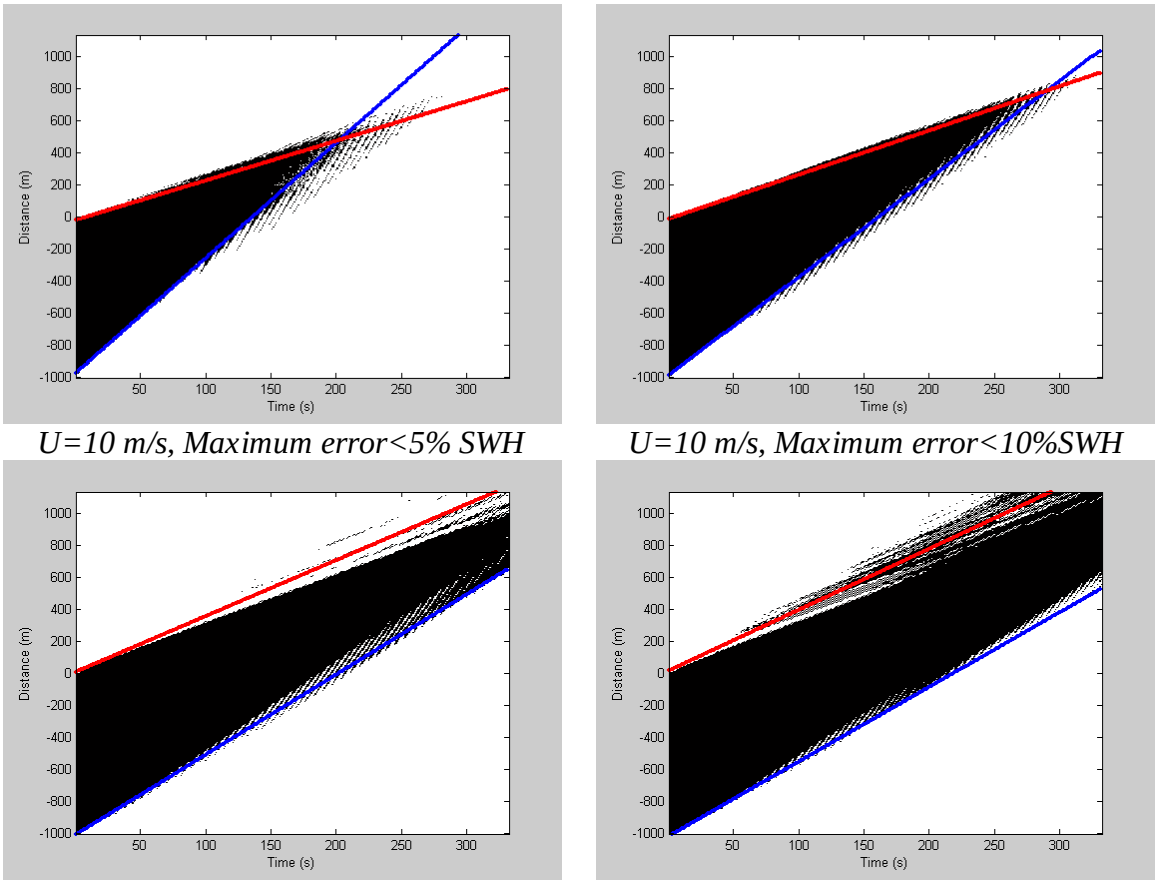

U=10 m/s, Maximum error<5% SWH *U=10 m/s, Maximum error<10%SWH*

U=10 m/s, Maximum error<30%SWH *U=10 m/s, Maximum error< 40%SWH*

Figure 5. 12: Error surface boundary models obtained using the image processing technique for a range of wind speeds

5.6.3 Comparison of the Two Boundary Parameterising Methods

The spatial polynomial fitting process and the image processing based method ere compared by assessing the fraction of erroneously prediction error points within the respectively enclose. For a given prediction error threshold the estimated boundary of the region will enclose total number of points, *A*, of which a number, *B*, will be erroneous points where the error actually exceeds the threshold. The fraction $\beta = \frac{B}{A}$ then constitutes the required quality metric. Clearly some points which lie within the threshold fall outside the boundary estimators but in practical applications of DSWP it was considered that this type of error only represented a missed opportunity to benefit from prediction. In contrast the error type identified could lead to potentially dangerous decisions and provided the important metric. The comparison of the two techniques over a range of wind speed is presented in *Figure 5. 13* and it is evident that the image processing technique is the superior method.

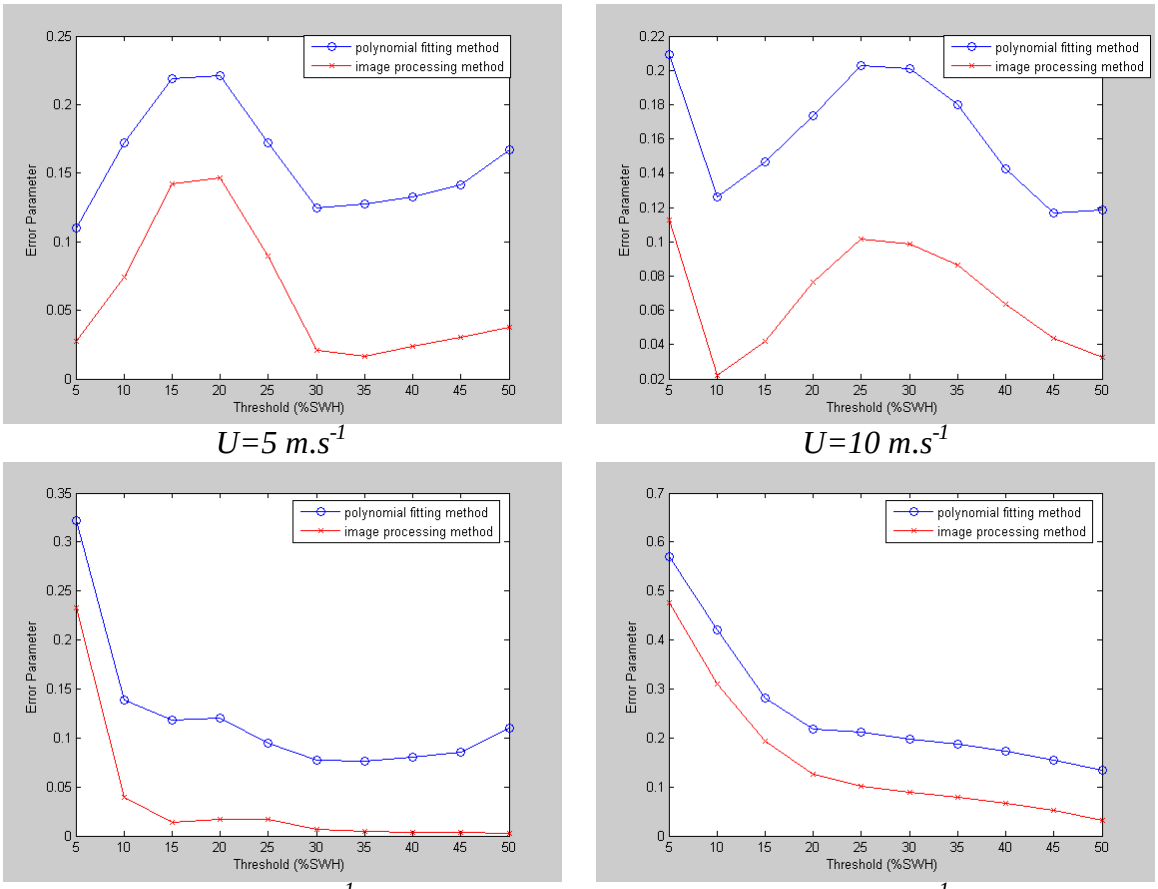

U=5 m.s^{-1} *U=10 m.s^{-1}*

U=15 m.s^{-1} *U=20 m.s^{-1}*

Figure 5. 13: Accuracy comparisons between the two boundary parameterisng methods

5.7 Summary

Space time wave propagation diagrams provide the basic scale parameters that describe prediction times and distances in DSWP. However they do not contain the quantitative information needed to explore the detailed aspects of prediction. This situation has been rectified by developing prediction error surfaces which occupy the same space time plane. These surfaces have been produced using an enhancement of the standard End-Matching spectral technique which uses a version of the Papoulis-Gerchberg iterative reconstruction technique for the purposes of window expansion.

The properties of the prediction error surfaces have been identified and a route to exploring the predictive properties of sea types has been illustrated. This has been applied to fully developed long fetch ocean wave systems as described by the Pierson-Moskowitz power density spectrum. Two techniques have been developed for parameterisng the prediction error threshold contour which defines the prediction regions where prediction accuracy exceeds a specified minimum. The normalized models are shown to give reasonable fit over a range wave conditions.

Chapter 6

Time/Space Domain Filter based Prediction

6.1 Introduction

The prediction process in the previous chapters of this work was based on the traditional frequency domain approach. This chapter considers the filtering process in the conjugate domain. The main purpose of finding an alternative description of the prediction filters in the time/space domain is to gain a better understanding of the prediction process. Adding more angles to this subject gives a broader field to develop methods with better prediction accuracy over wider prediction range.

In this chapter propagation filters are represented by their impulse responses and prediction is achieved by convolution with the time records and space snapshots. As described in *Section 2.4* the prediction process is represented as a unity gain all-pass filter with the dispersion relation describing the filter's behaviour. The transfer function of the Fixed Point prediction filter *H(ω)* is given by *Equation* 6. 1 and shown in Figure 6. 1.a

$$H(\omega) = e^{i\left(-sign(\omega)\left(\frac{\omega^2}{g}\Delta x\right)\right)} \qquad \textbf{6. 1}$$

Also the transfer function of the Fixed Time prediction filter *F(k)* is given by *Equation* 6. 2and shown in Figure 6. 1.b

$$F(k) = e^{i\left(-sign(k)\cdot\sqrt{|k|g}\Delta t\right)} \qquad \textbf{6. 2}$$

The impulse responses of the two propagation filters given in *Equation* 6. 1 and *Equation* 6. 2 have unbounded first derivatives at large *x* and *t [44]*, the next section addresses this issue.

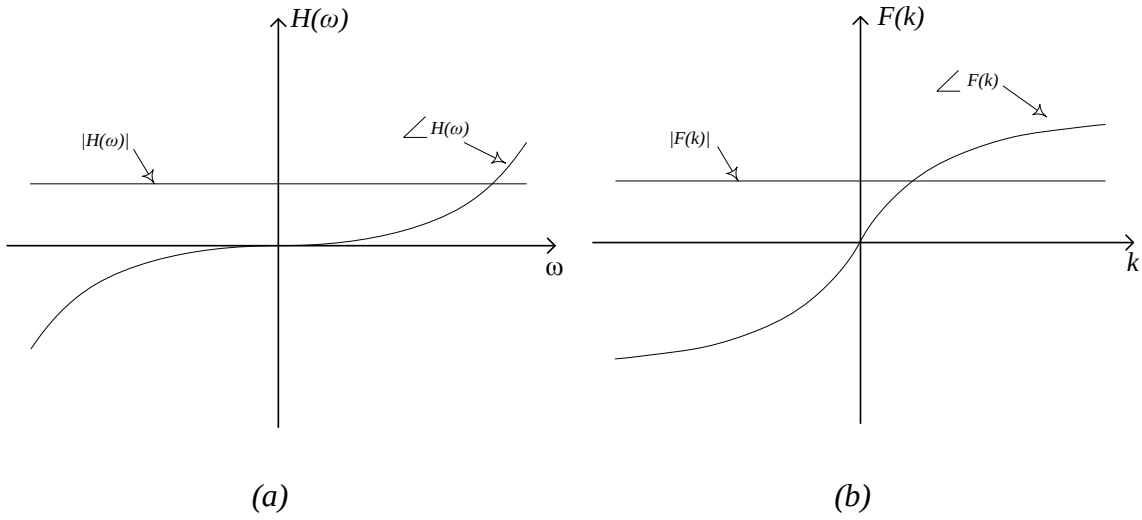

(a) *(b)*

Figure 6. 1: a) Fixed Point prediction filter H(ω). b) Fixed Time prediction filter F(k)

6.2 Prediction using time domain /space domain filters

Time / space domain representations of the propagation filters are discussed in [44]. Describing the filters in the conjugate domain requires determining the filter's impulse response. In *Section 4.1.1* the convolution form of the prediction process was determined from the analysis of the two dimensional spectrum of the infinite time record and the infinite snapshot. The impulse response of the Fixed Point filter and the Fixed Time filter are given by *Equation* 4. 18 and *Equation* 4.31 respectively.

To evaluate the response of the prediction filters we modify their limits to the limits of the propagation wave spectrum. This is possible because both the measured wave $\eta(x,t_o)$ and the predicted wave $\eta(x,t_p)$ have the same finite band width $\omega_{\min} < \omega < \omega_{\max}$. Following a similar argument the Fixed Time case is truncated to the wave's band $k_{\min} < k < k_{\max}$. This results in the modified Fixed Point filter *H(ω)* defined as in *Equation* 6. 3 and shown in *Figure 6. 2.a* and the modified Fixed Time filter *F(k)* defined as in *Equation* 6. 4 and shown in *Figure 6. 2.b*.

$$H(\omega)=\begin{cases} e^{\left(-i\cdot\frac{\omega^2}{g}(\Delta x)\right)} & \omega_{\min}<\omega<\omega_{\max} \\ e^{\left(i\cdot\frac{\omega^2}{g}(\Delta x)\right)} & -\omega_{\max}<\omega<-\omega_{\min} \\ 0 & \textit{Otherwise} \end{cases} \qquad \textbf{6. 3}$$

And

$$F(k)=\begin{cases} e^{\left(-i\cdot\sqrt{k\cdot g}(\Delta t)\right)} & k_{\min}<k<k_{\max} \\ e^{\left(i\cdot\sqrt{-k\cdot g}(\Delta t)\right)} & -k_{\max}<k<-k_{\min} \\ 0 & \textit{Otherwise} \end{cases} \qquad \textbf{6. 4}$$

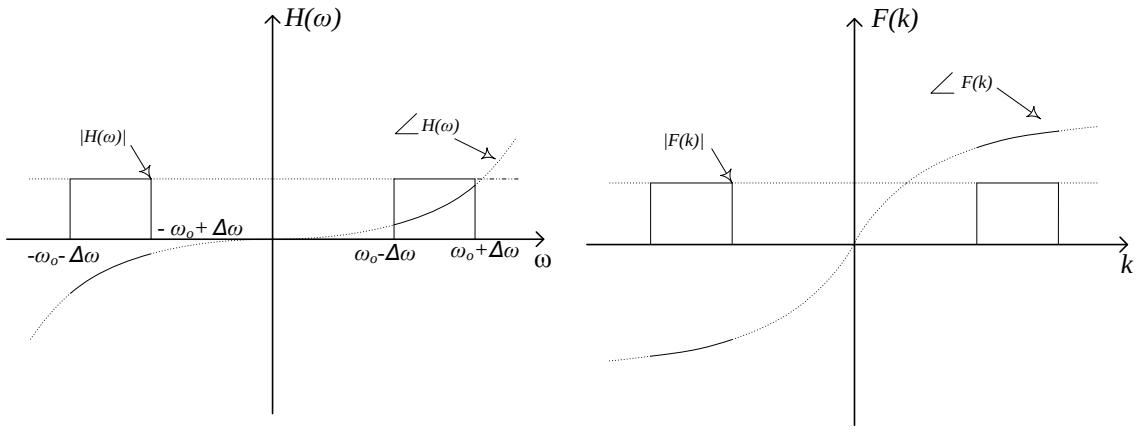

(a) *(b)*

Figure 6. 2: Finite bandwidth prediction filters a)Fixed point prediction filter H(ω). b)Fixed time prediction filter F(k)

The impulse responses are directly evaluated from these finite bandwidth prediction filters. The Fixed Point impulse response λ(t,Δx) derived from *Equation* 6. 3 is given by:

$$\lambda(t,\Delta x)=\sqrt{\frac{2\pi g}{\Delta x}}\left\{cos\left(\frac{g}{4\Delta x}t^2\right)\left[C(z_2)-C(z_1)\right]+sin\left(\frac{g}{4\Delta x}t^2\right)\left[S(z_2)-S(z_1)\right]\right\} \qquad \textbf{6. 5}$$

Where

$$z_1(t)=\sqrt{\frac{2}{\pi}}\left(\sqrt{\frac{\Delta x}{g}}(\omega_o-\Delta\omega)-\frac{t}{2}\sqrt{\frac{g}{\Delta x}}\right)$$

$$z_2(t)=\sqrt{\frac{2}{\pi}}\left(\sqrt{\frac{\Delta x}{g}}(\omega_o+\Delta\omega)-\frac{t}{2}\sqrt{\frac{g}{\Delta x}}\right)$$

Using direct evaluation of *Equation* 6. 4 the Fixed Time impulse response $\zeta(\Delta t, x)$ is given by:

$$\zeta(\Delta t, x) = \frac{1}{x}\left\{sin\left(k_{max}x - \sqrt{k_{\max} g}\,\Delta t\right) - sin\left(k_{min}x - \sqrt{k_{\min} g}\,\Delta t\right)\right\}$$
$$+ \frac{\sqrt{g\pi}}{2}\frac{1}{x^{3/2}}\left\{\Delta t \cdot cos\left(\frac{g}{4x}\Delta t^2\right)\left[C(z_3) - C(z_4)\right] + \Delta t \cdot sin\left(\frac{g}{4x}\Delta t^2\right)\left[S(z_3) - S(z_4)\right]\right\} \qquad \textbf{6. 6}$$

Where

$$z_3(x) = \sqrt{\frac{2}{\pi}}\left(\frac{-2x\sqrt{k_o + \Delta k} + \sqrt{g}\,\Delta t}{2\sqrt{x}}\right)$$

$$z_4(x) = \sqrt{\frac{2}{\pi}}\left(\frac{-2x\sqrt{k_o - \Delta k} + \sqrt{g}\,\Delta t}{2\sqrt{x}}\right)$$

In which C( )and S( ) are the Fresnel integral, see Appendix (C). More information on these integrals is found in [74] .Throughout this work the improved method for computing Fresnel integrals described in[75] is used in impulse response simulation.

In practice the time record *η(t,xo)* and snap shot *η (to,x)* are only defined on the measured regions *(x_1,x_2)* and (t_1, t_2) respectively. Prediction errors *e(t,x)* given by *Equation* 6. 7 and *Equation* 6. 8 for the Fixed Point and the Fixed Time respectively are caused by finite sized data segments.

$$e(t,x) = \int_{-\infty}^{t_1} \eta(\tau, x_o)\cdot\lambda(t-\tau, x-x_o)d\tau + \int_{t_2}^{\infty} \eta(\tau, x_o)\cdot\lambda(t-\tau, x-x_o)d\tau \qquad \textbf{6. 7}$$

$$e(t,x) = \int_{-\infty}^{x1} \eta(t_o, \gamma)\cdot\zeta(t-t_o, x-\gamma)d\gamma + \int_{x2}^{\infty} \eta(t_o, \gamma)\cdot\zeta(t-t_o, x-\gamma)d\gamma \qquad \textbf{6. 8}$$

Over short time intervals for which the sea is statistically stationary it can be presumed that the sea spectrum doesn't change over the time and distance frame scales used for prediction. The above errors are clearly related to the distribution of the energy within the impulse response (its magnitude squared). If this is concentrated in a small region (less than the measured region length) then small errors are possible for certain point in the (x,t) plane.

6.3 Energy concentration regions in prediction filters

An important practical issue with both time and space impulse response $\lambda(t,\Delta x)$and $\zeta(\Delta t,x)$ given by the last two *Equation* 6. 5 and *Equation* 6. 6, *is* whether or not they describe a non-causal filter. In the Fixed Time mode non-causality is not a problem, since it affects the response location and there aren't any physical difficulties in this response being in front or behind measurement region, on the other hand, in the Fixed Point mode causality is essential, since in the non-causal case an impulse at a given instant evokes a respond in the future.

From inspection of plotted examples of the band limited form of the two time/space impulse response $\lambda(t,\Delta x)$and $\zeta(\Delta t,x)$ it was clear that the energy is concentrated within a limited region, giving the response the appearance of localized wave packets. More importantly, the region containing most of the energy is in the causal part of the filter reducing the practical effects of the non causal part. This will be more apparent in the next section where we attempt to evaluate the prediction filter's impulse response properties.

The filter response is described by two properties, first is the response duration (λ_D,ζ_D) which is the length of the region in time (or space) that includes the majority of the waves energy. The second property is the response shift from the origin $(\lambda_{shift},\zeta_{shift})$ which can be viewed as the mean value of the response.

Since the original propagation filters are all-pass filters the response duration due to the zero phase part is negligible. The impulse response duration of interest is related to the phase diversions from linearity. The relation between signal duration and spectrum is discussed in [76] [77].

The signal duration is defined as the signal variance. If a signal *g(t)* with zero mean has the Fourier transform *G(ω)* where :

$g(t) \Leftrightarrow |G(\omega)|\, e^{j\theta(\omega)}$

Then its duration $\Delta^2 g$ is defined as:

$$\Delta^2 g = \int_{-\infty}^{\infty} \left(\frac{d}{d\omega}|G(\omega)|\right)^2 d\omega + \frac{1}{2\pi}\int_{-\infty}^{\infty}|G(\omega)|^2\left(\frac{d}{d\omega}\theta(\omega)\right)d\omega \qquad \textbf{6. 9}$$

Using the variance definition of signal duration to estimate the Fixed Point propagation filters duration (λ_D) we get:

$$\lambda_D = \frac{1}{2\pi}\int_{\omega_0-\Delta\omega}^{\omega_0+\Delta\omega}\left(\frac{d}{d\omega}\left(\frac{\omega^2}{g}\Delta x\right)\right)d\omega = \frac{4\Delta x}{g}(\Delta\omega) \qquad \textbf{6. 10}$$

In the Fixed Time case the propagation filter's duration ζ_D are estimated as:

$$\zeta_D = \frac{1}{2\pi}\int_{k_0-\Delta k}^{k_0+\Delta k}\left(\frac{d}{dk}\left(\sqrt{gk}\Delta t\right)\right)dk = \frac{\Delta t\sqrt{g}}{2}\left(\frac{1}{\sqrt{k_0-\Delta k}} - \frac{1}{\sqrt{k_0+\Delta k}}\right) \qquad \textbf{6. 11}$$

To check the properties of these filters the response is plotted for different parameters. In the Fixed Point filters the responses are plotted over the range *-10<t<100 sec* with a resolution of (0.1) sec .The effect of varying the displacement Δx, mid frequency ω_0 and the filter's band width $\Delta\omega$, on the impulse response duration and position (λ_D, λ_{shift}) is illustrated in *Figure 6. 3*, *Figure 6. 4*, and *Figure 6. 5*, respectively

Case 1: $\Delta\omega$=0.406 rad s^{-1} ω_0=0.87 rad s^{-1} Δx=(50,150,200) m

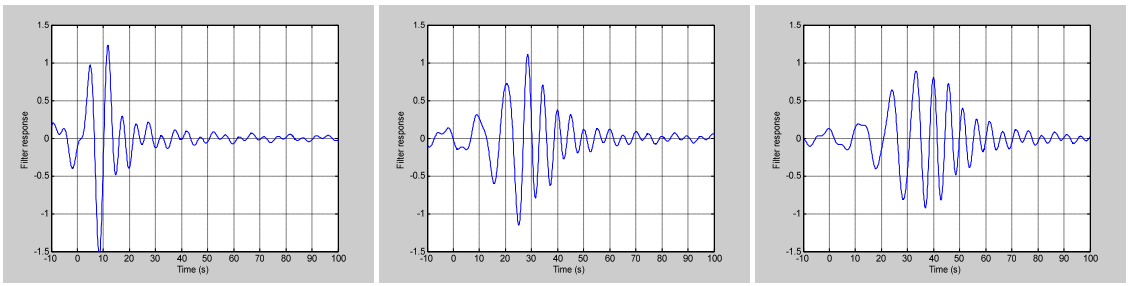

(a) *(b)* *(c)*

Figure 6. 3: Effect of change in Δx on Fixed Point filter Δω=0.406 rad s^{-1},ω_0=0.87 rad s^{-1} a)Δx=50m, b) Δx=150m, c) Δx=200m

The increase in Δx results in an increase in the response's duration. The change in Δx also affects the response's location. Hence the larger the displacement Δx the response both broadens and shifts in position. This property of the propagation filter is the cause of the triangular shaped prediction region discussed previously.

Case 2: $\Delta\omega$=0.406 rad s^{-1} Δx=100 m ω_0= (0.87,1.07, 1.27) rad s^{-1}

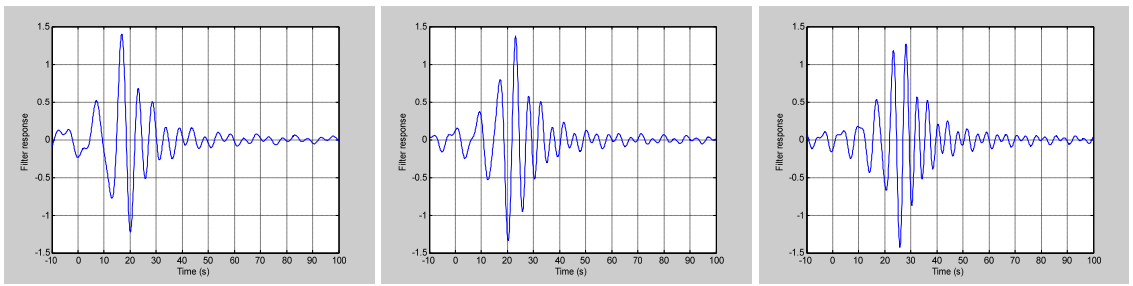

(a) *(b)* *(c)*

Figure 6. 4: Effect of change in ω_0 on Fixed Point filter Δω=0.406 rad s^{-1}, Δx =100m a) ω_0 =0.87 rad s^{-1}, b) ω_0 =1.07 rad s^{-1}, c) ω_0 =1.27 rad s^{-1}

The illustrated examples show the mid frequency to have an effect on the response location, but do not appear to have an obvious effect on the response duration.

Case 3: $\omega_0 = 0.87$ rad s^{-1} $\Delta x = 200$ m $\Delta\omega = (0.24, 0.406, 0.64)$ rad s^{-1}

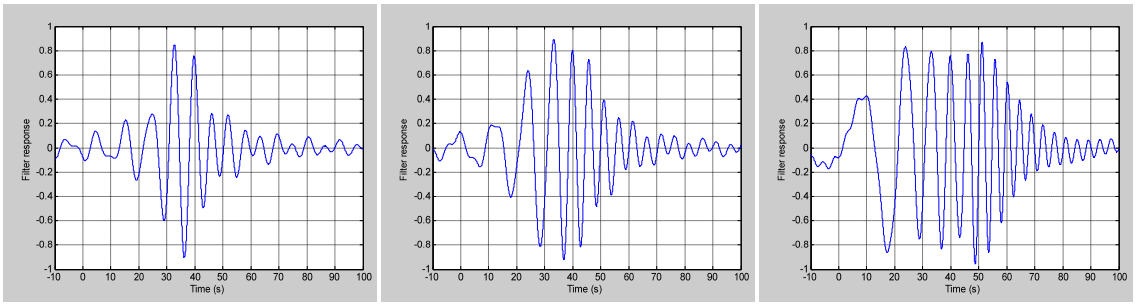

(a) *(b)* *(c)*

Figure 6. 5: Effect of change in Δω on Fixed Point filter ω_0 =0.87 rad s^{-1}, Δx =200m a) Δω =0.24 rad s^{-1}, b) Δω =0.406 rad s^{-1}, c) Δω =0.64 rad s^{-1}

The increase in the band width results in a clear increase in the duration. However, the location of the response seems to be unaffected by the change. The results in the three cases agree with the definition of the response duration given by *Equation* 6. 10

6.4 Approximating the filters properties

Using the variance definition of signal duration, an expression was found to estimate the impulse response duration of the Fixed Time mode *Equation* 6. 11 and the duration of the Fixed Point filter *Equation* 6. 10 . However, these expressions do not give any indication on the location of the energy concentration region of these filters along the time/space dimension.

Two different approaches are employed to estimate the filters' duration and shift from the origin. The Polygonal Approximation method [76] is used to define the impulse response boundaries directly from the filters' phase distortion. On the other hand the unsymmetrical system analysis method [76]attempts to estimate the response envelope, since the response's boundaries are defined by its envelope's properties.

6.4.1 Fixed point mode (Polygonal Approximation)

The Polygonal Approximation method [76] is a classical technique for determining the response of filters with arbitrary phase distortion which in this sense means a departure from linear phase characteristics. As it is the case that the prediction filters in both fixed time and fixed point mode have a nonlinear phase distortion, the Polygonal

Approximation method is an appropriate tool. As the name suggest, the method employs a polygonal approximation of the phase to estimate the filter's impulse response. However the main aim is not to approximate the response itself, but to use the approximation properties to estimate the filters response boundaries.

The first step in this method is to divide the pass band ***n*** intervals (ω_i, ω_{i+1}) where (*i*) is the interval's index, for simplicity these are chosen to have the same length. As illustrated in *Figure 6. 6* the Fixed Point filter's phase ($\theta(\omega) = \frac{\omega^2}{g}\Delta x$) in each interval is approximated by a straight line

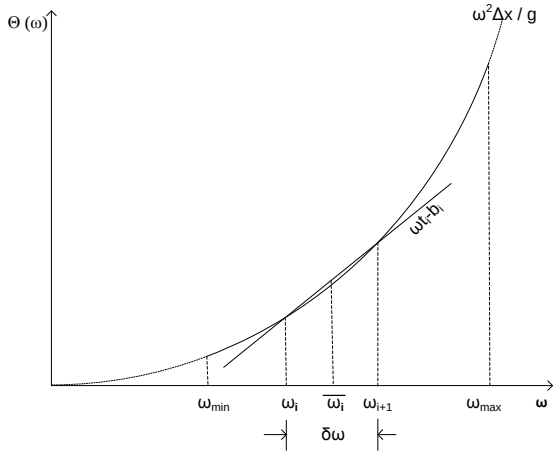

Figure 6. 6: Polygonal Approximation of the Fixed Time mode filter

$$\theta(\omega) \approx \omega t_i - b_i \qquad for \qquad \omega_i < \omega < \omega_{i+1} \qquad \textbf{6. 12}$$

For the uniform segmentation the length of the interval is defined by $\delta\omega = \frac{\omega_{\max} - \omega_{\min}}{n}$, and the beginning of each interval is defined as $\omega_i = \omega_{\min} + (i-1)\delta\omega_{i-1}$, while the mid frequency $\overline{\omega_i} = \frac{\omega_i + \omega_{i+1}}{2}$, using these definitions the coefficients of linear approximation are given by :

$$\left.\begin{aligned} t_i &= \frac{2\Delta x \cdot \overline{\omega_i}}{g} \\ b_i &= \frac{\Delta x}{g}\omega_i \cdot \omega_{i+1} \end{aligned}\right\} \qquad \textbf{6. 13}$$

Replacing the phase in the impulse response of the Fixed point mode given in *Equation*4. 18 by the polygonal approximation, produces:

$$\lambda(t, \Delta x) = 2 \cdot \int_{\omega_o - \Delta\omega}^{\omega_o + \Delta\omega} \cos\left(\omega t - \frac{\omega^2}{g}(\Delta x)\right) d\omega \approx 2\sum_{i=1}^{n-1} \int_{\omega_i}^{\omega_i + 1} \cos(\omega t - \omega t_i - b_i)\, d\omega$$

$$= 2\sum_{i=1}^{n-1} \frac{\sin\frac{\delta\omega}{2}(t - t_i)}{t - t_i} \sin\left(\overline{\omega_i}(t - t_i) - b_i\right)$$

$$= \delta\omega \sum_{i=1}^{n-1} sinc\left(\frac{\delta\omega}{2}(t - t_i) \right) \cdot sin(\overline{\omega}_i(t - t_i) - b_i) \qquad \textbf{6. 14}$$

$$\lambda(t, \Delta x) = \sum_{i=1}^{n-1} \lambda_i(t, \Delta x) \qquad \textbf{6. 15}$$

The impulse response is represented by a series of simpler functions λ_i. Assuming $\overline{\omega}_i >> \delta\omega$ the *sinc( )* function in *Equation* 6. 14 *a*cts as an envelope to each individual function λ_i, each envelope is shifted from the previous one by the factor $(t_i - t_{i-1})$, which is the difference between the slope of the individual lines representing the phase's segments.

Since the property of the impulse response of interest is caused by the phase divergence from linearity, the boundaries of the response (τ_1,τ_2) are determined by the first and the last envelopes (λ_1 ,λ_n). For large values of n these are given by :

$$\left.\begin{aligned} \tau_1 &= limit_{n\to\infty}(t_1) = \frac{2\Delta x \omega_{\min}}{g} \\ \tau_2 &= limit_{n\to\infty}(t_n) = \frac{2\Delta x \omega_{\max}}{g} \end{aligned}\right\} \qquad \textbf{6. 16}$$

The impulse response duration λ_D is the distance between the first and the last envelope, witch is the difference of the phase curve slopes at the band ends, defined as:

$$\lambda_D = \tau_2 - \tau_2 = \frac{4\Delta x}{g}(\Delta\omega) \qquad \textbf{6. 17}$$

The impulse response shift λ_{shift} is approximated by the average shift of all envelopes as $n \to \infty$.

$$\lambda_{shift} = \frac{2\Delta x}{3\ g} \frac{\int_{\omega\min}^{\omega\max} t_i \cdot \omega d\omega}{\int_{\omega\min}^{\omega\max} t_i d\omega} = \frac{4\Delta x}{3\ g} \cdot \frac{(\omega_{\max}^3 - \omega_{\min}^3)}{(\omega_{\max}^2 - \omega_{\min}^2)} \qquad \textbf{6. 18}$$

The response duration obtained by this method is the same as that of the variance definition given in *Equation* 6. 10. This gives more credibility to the two region boundaries *(τ_1,τ_2)* and the region mean point λ_{shift} defined by the Polygonal Approximation method

Figure 6. 7. shows the impulse response for different conditions, the effective area of the impulse response is defined by the Polygonal Approximation method for the

Fixed Point mode. Also appearing in the figure is the λ_{shift} which identifies the central energy point.

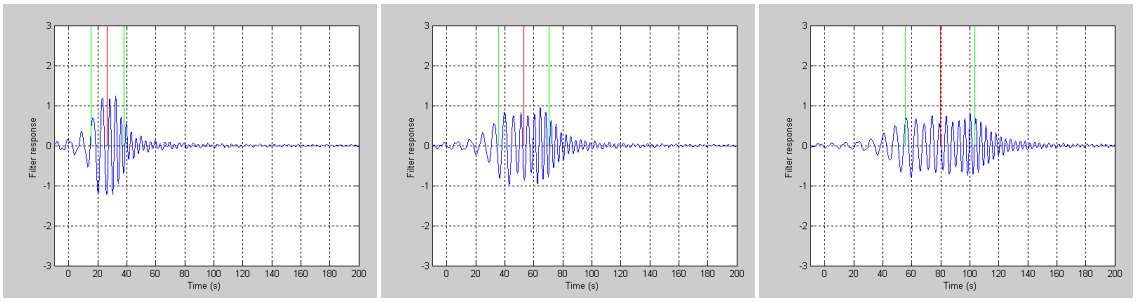

(a) *(b)* *(c)*

------ *Filter's impulse response* ------ *Filter's boundaries* (τ_1,τ_2) ------- λ_{shift}

Figure 6. 7: Fixed Point impulse response boundaries estimation using Polygonal Approximation(ω_0=1.3 rad s-1 $\Delta\omega$ =0.61 rad s-1) a) Δx =100m b) Δx =200m c) Δx =300m

6.4.2 Fixed point mode (Unsymmetrical system analysis)

In this section an impulse response representation is developed of the propagation filter based on unsymmetrical system analysis [76]. Although the impulse response of the unsymmetrical system is both amplitude and phase modulated, these features are not always clear from the direct representation as given in *Equation* 6. 5. This method provides the envelope of the response, which defines the properties of the filter's impulse response. The first step in the unsymmetrical system analysis is to separate the filter's transfer function in two parts, this is done by putting the propagation filter $H(\omega)$ given by *Equation*6. 3. in the form :

$$H(\omega)= H_1(\omega)+ H_2(\omega)$$

Where

$$H_1(\omega) = e^{\left(-i\cdot\frac{\omega^2}{g}(\Delta x)\right)}\cdot\left[u\left(\omega-\left(\omega_o-\Delta\omega\right)\right)-u\left(\omega-\left(\omega_o+\Delta\omega\right)\right)\right] \quad \textbf{6. 19}$$

And

$$H_2(\omega) = e^{\left(i\cdot\frac{\omega^2}{g}(\Delta x)\right)}\cdot\left[u\left(\omega+\left(\omega_o+\Delta\omega\right)\right)-u\left(\omega+\left(\omega_o-\Delta\omega\right)\right)\right] \quad \textbf{6. 20}$$

$u(\omega)$ is unit Heaviside step functions.

The second step in this analysis is to obtain the low pass filter equivalents of the two parts of the original filter. This is done by shifting the left hand side part to the right by ω_o, which results in the low pass filter $H_{l1}(\omega)$. In contrast the right hand side is shifted to the left by ω_o giving the low pass filter $H_{l2}(\omega)$. The two low pass filters are given by *Equation* 6. 21 and *Equation* 6. 22 see *Figure 6. 8.*

$$H_{l1}(\omega) = H_1(\omega + \omega_o) = e^{\left(-i\cdot\frac{(\omega+\omega_o)^2}{g}(\Delta x)\right)} \cdot [u(\omega + \Delta\omega) - u(\omega - \Delta\omega)] \qquad \textbf{6. 21}$$

And

$$H_{l2}(\omega) = H_2(\omega - \omega_o) = e^{\left(i\cdot\frac{(\omega-\omega_o)^2}{g}(\Delta x)\right)} \cdot [u(\omega + \Delta\omega) - u(\omega - \Delta\omega)] \qquad \textbf{6. 22}$$

The Fixed Point filter $H(\omega)$ is an unsymmetrical band pass filter since there is no mid frequency ω_o that will give $H_1(\omega)$ and $H_2(\omega)$ that fulfill the symmetrical condition, where $H_{l2}(\omega) \neq H_{l1}(\omega)$

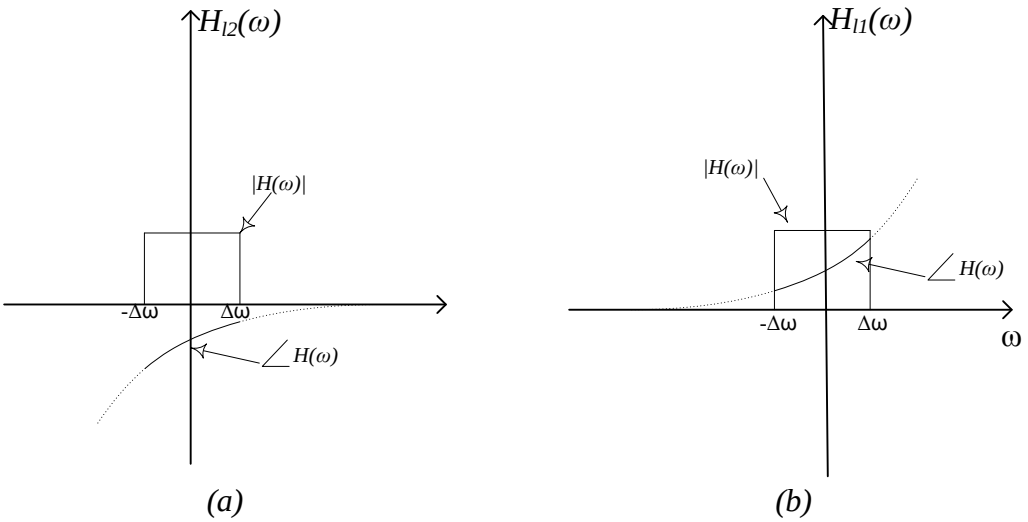

Figure 6. 8: The low pass filters equivalent of the Fixed Point mode filter's sides. a)Right band side equivalent , b)Left band side equivalent

The third step is to find the (*in-phase* H_p) system functions which are defined as:

$$H_p(\omega) = \frac{1}{2}\cdot(H_{l2}(\omega) + H_{l1}(\omega))$$

$$H_p(\omega) = \frac{1}{2}\cdot\left(e^{\left(i\cdot\frac{(\omega-\omega_o)^2}{g}(\Delta x)\right)} + e^{\left(-i\cdot\frac{(\omega+\omega_o)^2}{g}(\Delta x)\right)}\right)\cdot[u(\omega + \Delta\omega) - u(\omega - \Delta\omega)] \qquad \textbf{6. 23}$$

and *(quadrature H_q)* system functions which are defined as:

$$H_q(\omega) = \frac{1}{2i} \cdot \left(H_{l2}(\omega) - H_{l1}(\omega)\right)$$

$$H_q(\omega) = \frac{1}{2i} \cdot \left(e^{\left(i \cdot \frac{(\omega-\omega_o)^2}{g}(\Delta x) \right)} - e^{\left(-i \cdot \frac{(\omega+\omega_o)^2}{g}(\Delta x) \right)} \right) \cdot \left[u(\omega+\Delta\omega) - u(\omega-\Delta\omega)\right] \quad \textbf{6. 24}$$

The fourth step in this analysis is to find (h_p) and (h_q) which are the impulse responses of the (*in-phase)* and the *(quadrature)* systems respectively. These are found to be given as :

$$h_p(t) = \frac{1}{4}\sqrt{\frac{2g}{\Delta x \cdot \pi}} \cdot \left[cos\left(t\omega_o - \frac{t^2 g}{4\Delta x} \right) \cdot \left\{ C(z_2(t)) - C(z_1(t)) \right\} - sin\left(t\omega_o - \frac{t^2 g}{4\Delta x} \right) \left\{ S(z_2(t)) - S(z_1(t)) \right\} \right] \quad \textbf{6. 25}$$

$$h_q(t) = \frac{1}{4}\sqrt{\frac{2g}{\Delta x \cdot \pi}} \cdot \left[cos\left(t\omega_o - \frac{t^2 g}{4\Delta x} \right) . \left\{ S(z_2(t)) - S(z_1(t)) \right\} + sin\left(t\omega_o - \frac{t^2 g}{4\Delta x} \right) \cdot \left\{ C(z_2(t)) - C(z_1(t)) \right\} \right] \quad \textbf{6. 26}$$

Where $z_1(t)$, $z_2(t)$ are defined in *Equation* 6. 5

The fifth and final step is to define the impulse response of our original unsymmetrical system $\lambda(t,\Delta x)$ in terms of the (*in-phase hp(t)*) and the *(quadrature hq(t))*systems.

$$\lambda(t,\Delta x) = 2 \cdot \sqrt{h_p^2(t) + h_q^2(t)} \cos\left[\omega_o - \tan^{-1} \frac{h_q(t)}{h_p(t)} \right] \quad \textbf{6. 27}$$

The impulse response of the unsymmetrical system is both amplitude and phase modulated. Appendix(D) demonstrates the full mathematical manipulations required to obtain the simplified representations of the response envelope and phase term which are given below.

$$\sqrt{h_p^2(t)+h_q^2(t)}=\frac{1}{4\pi}\sqrt{\frac{2\pi g}{\Delta x}}\cdot\left[\left\{C(z_1(t))-C(z_2(t))\right\}^2+\left\{S(z_1(t))-S(z_2(t))\right\}^2\right]^{\frac{1}{2}} \quad \textbf{6. 28}$$

$$\phi(t)=\arctan\left(\frac{h_q(t)}{h_p(t)}\right)=\tan^{-1}\left(\frac{cos\left(t\omega_o-\frac{t^2g}{4\Delta x}\right)\cdot[S(z_1)-S(z_2)]+sin\left(t\omega_o-\frac{t^2g}{4\Delta x}\right)[C(z_1)-C(z_2)]}{cos\left(t\omega_o-\frac{t^2g}{4\Delta x}\right)\cdot[C(z_1)-C(z_2)]-sin\left(t\omega_o-\frac{t^2g}{4\Delta x}\right)[S(z_1)-S(z_2)]}\right) \quad \textbf{6. 29}$$

Where

$$z_1(t)=\sqrt{\frac{2}{\pi}}\left(\sqrt{\frac{\Delta x}{g}}(\omega_o-\Delta\omega)-\frac{t}{2}\sqrt{\frac{g}{\Delta x}}\right)$$

$$z_2(t)=\sqrt{\frac{2}{\pi}}\left(\sqrt{\frac{\Delta x}{g}}(\omega_o+\Delta\omega)-\frac{t}{2}\sqrt{\frac{g}{\Delta x}}\right)$$

The impulse response properties (shift & duration) are defined by the properties of the response envelop which in turn is defined by the two terms $\left\{C(z_1(t))-C(z_2(t))\right\}^2$ and $\left\{S(z_1(t))-S(z_2(t))\right\}^2$.

As explained in appendix(C) these terms represent time windows with the window edges defined by the Fresnel function's coefficients ($z_1(t)$ and $z_2(t)$) shown in *Figure 6. 9*. The outer window edges are defined by the two points (τ_3 and τ_4) given by

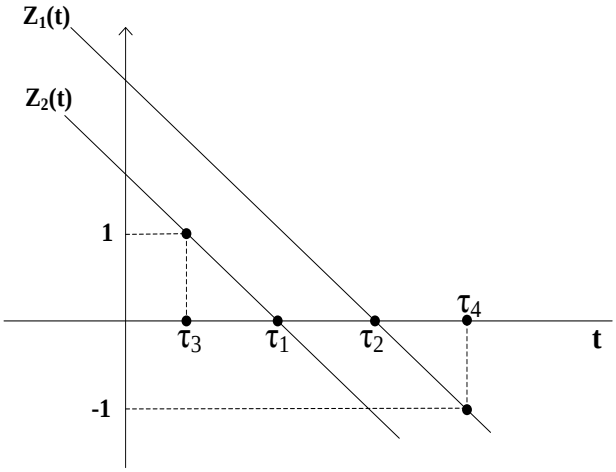

Figure 6. 9: Edge points of the Fresnel window defining the Fixed Point filter envelope

$$\left.\begin{aligned} z_1(\tau_3)=1 \quad &\longrightarrow \quad \tau_3=\frac{2\Delta x}{g}\omega_{\min}-\pi\sqrt{\frac{2\Delta x}{g}} \\ z_2(\tau_4)=-1 \quad &\longrightarrow \quad \tau_4=\frac{2\Delta x}{g}\omega_{\max}+\pi\sqrt{\frac{2\Delta x}{g}} \end{aligned}\right\} \quad \textbf{6. 30}$$

While the two points (τ_1 and τ_2) defining the mid height window edges are given by:

$$\left.\begin{aligned} z_1(\tau_1)=0 \quad &\longrightarrow \quad \tau_1=\frac{2\Delta x}{g}\omega_{\min} \\ z_2(\tau_2)=0 \quad &\longrightarrow \quad \tau_2=\frac{2\Delta x}{g}\omega_{\max} \end{aligned}\right\} \quad \textbf{6. 31}$$

Figure 6. 10 shows the impulse response of the propagation filters in the Fixed Point mode for different prediction conditions and the filters boundaries as approximated by this method. Also included in the plot is the envelope defined by *Equation* 6. 28. It is obvious that the impulse response properties (duration and shift) are totally defined by the properties of its envelop. The two pairs of envelope edge points are also shown.

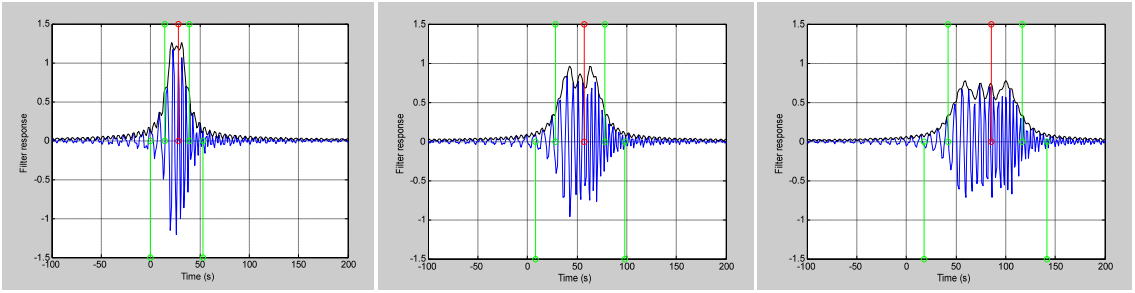

(a) Δx=100m *(b) Δx=200 m* *(c) Δx=300 m*

----- *Impulse response,* ----- *Envelope ,* ----- λ_{shift} , ----- $\tau_1,\tau_2,\tau_3,\tau_4$

Figure 6. 10: Fixed Point mode impulse response boundaries estimated using Polygonal Approximation. ω_0=1.3 $\Delta\omega$=0.61 rad/sec

Notice that the mid height window edges (τ_1 and τ_2) are exactly the same as the impulse response boundaries defined by the Polygonal Approximation method. However the outer edge points (τ_3 and τ_4) include more of the impulse response energy, with the expense of a larger impulse response dimension which in turn reduces the prediction region as will be shown in the next section.

If we define τ_3 as the beginning of the impulse response energy concentration region, and τ_4 as the end of the impulse response energy concentration region, we find the response duration as

$$\lambda_D = \tau_4 - \tau_3 = \frac{4\Delta x}{g}\Delta\omega + 2\cdot\pi\sqrt{\frac{2\Delta x}{g}} \qquad \textbf{6. 32}$$

When compared to the result of λ_D obtained by using (τ_1 and τ_2) *Equation* 6. 10 the response duration λ_D has an additional term ($2\cdot\pi\sqrt{\frac{2\Delta x}{g}}$) which makes the duration determined by these boundaries longer than that in the previous method.

6.4.3 Fixed Time mode (Polygonal Approximation)

In this and the next section the Fixed Time mode filter is considered. As with the Fixed Point mode two methods are introduced to estimate the filters response properties (duration and shift). In view of the fact that the Fixed Time mode filter also has a nonlinear phase, the polygonal approximation method is suitable for determining the response properties of the filter. The analysis is carried out by dividing the pass band into ***n*** intervals (k_i, k_{i+1}) and approximating the phase segments by straight lines, as shown in *Figure 6. 11*.

This method approximates the phase of the Fixed Time filter's phase as

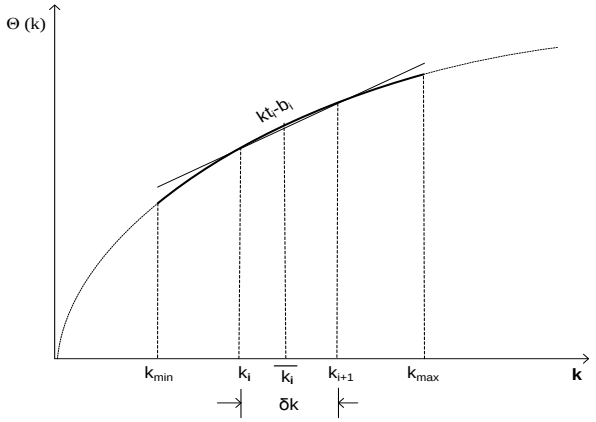

Figure 6. 11: Polygonal Approximation of the Fixed Time mode filter

$$\phi(k) = \sqrt{g \cdot k} \cdot \Delta t \approx k x_i - a_i \qquad for \qquad k_i < k < k_{i+1} \qquad \textbf{6. 33}$$

Where

$$x_i = \frac{\sqrt{g}\Delta t}{\left(\sqrt{k_i} + \sqrt{k_{i+1}}\right)} \qquad a_i = \frac{\Delta t \cdot \sqrt{g} \cdot \sqrt{k_i}\sqrt{k_{i+1}}}{\left(\sqrt{k_i} + \sqrt{k_{i+1}}\right)}$$

Using this approximation, the impulse response $\zeta(x,\Delta t)$ of the finite Fixed Time mode filter given in *Equation* 4.31 of the dispersion filter is represented by the summation of n simpler functions ζ_i.

$$\zeta(x,\Delta t) = 2 \cdot \int_{k_o-\Delta k}^{k_o+\Delta k} cos\left(k \cdot x - \sqrt{g \cdot k}(\Delta t)\right) dk$$

$$\zeta(x,\Delta t) \approx 2\sum_{i=1}^{n-1} \int_{k_i}^{k_{i+1}} cos(k \cdot x - k \cdot x_i - a_i) dk$$

$$= 2\sum_{i=1}^{n-1} sinc\left(\frac{\delta k}{2}(x - x_i)\right) \cdot sin\left(\bar{k}_i \cdot (x - x_i) - a_i\right) \qquad \textbf{6. 34}$$

$$\zeta(x,\Delta t) \approx 2\sum_{i=1}^{n-1} \zeta_i(x,\Delta t) \qquad \textbf{6. 35}$$

Where the length of the interval $\delta k = \frac{k_{\max} - k_{\min}}{n}$ and the mid wave number given by $\bar{k}_i = \frac{k_i + k_{i+1}}{2}$

The shift of the first *sinc* ( ) function for $n \to \infty$ is used to define the beginning of the impulse response(γ_1) , while the end of the response is defined by the shift of the n[th] *sinc* function for $n \to \infty$.

$$\left.\begin{aligned} \gamma_1 &= \lim_{n\to\infty}(x_1) = \frac{\Delta t\sqrt{g}}{2}\left(\frac{1}{\sqrt{k_{\max}}}\right) \\ \gamma_2 &= \lim_{n\to\infty}(x_n) = \frac{\Delta t\sqrt{g}}{2}\left(\frac{1}{\sqrt{k_{\min}}}\right) \end{aligned}\right\} \qquad \textbf{6. 36}$$

The response duration ζ_D is approximated by :

$$\zeta_D = \gamma_1 - \gamma_2 = \frac{\Delta t\sqrt{g}}{2}\left(\frac{1}{\sqrt{k_{\min}}} - \frac{1}{\sqrt{k_{\max}}}\right) \qquad \textbf{6. 37}$$

While the response position ζ_{shift} is defined by the average shift of all the envelops as $n\to\infty$..

$$\zeta_{shift} = \frac{\Delta t\sqrt{g}}{2}\left(\frac{\int_{k\min}^{k\max} x_i \cdot k\,dk}{\int_{k\min}^{k\max} x_i\,dk}\right)^{(-1/2)} = \frac{\Delta t\sqrt{3\cdot g}}{2}\cdot\left(\frac{(k_{\max}^{1/2} - k_{\min}^{1/2})}{(k_{\max}^{3/2} - k_{\min}^{3/2})}\right)^{1/2} \qquad \textbf{6. 38}$$

As was the case with the Fixed Point mode, the duration estimated with this method for the Fixed Time mode is consistent with that of the variance definition of duration given in *Equation* 6. 11 which also gives more credibility to the two boundaries (γ_1,γ_2) .

Figure 6. 12 shows the impulse response for different conditions and the impulse response affective area defined by the Polygonal Approximation method for the fixed time mode. Also appearing in the figure is the ζ_{shift} which identifies the central energy point. The central point of the response in the case of the Fixed Time mode is shifted to one of the sides much more obvious than in the case of the Fixed Point mode that appeared almost in the centre of the region.

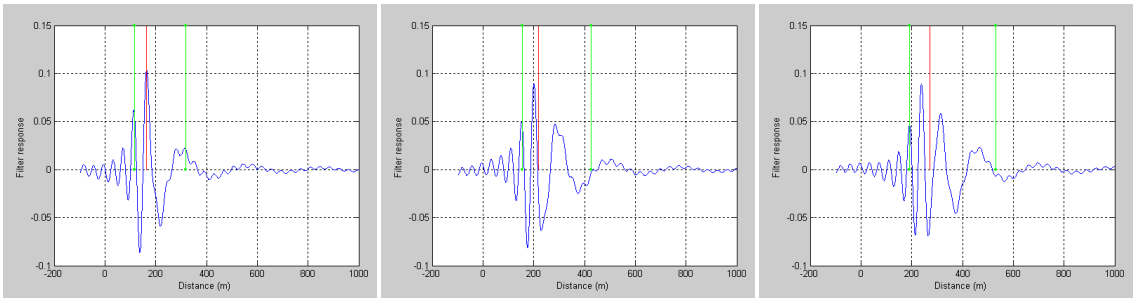

(a) Δt =30 s *(b) Δt =40 s* *(c)) Δt =50 s*

------ *Filter's impulse response* ------ *Filter's boundaries* (γ_1,γ_2) ------ ζ_{shirt0}

Figure 6. 12: Fixed Time impulse response boundaries estimation using Polygonal Approximation(k_0=0.1 Δk =0.07)

6.4.4 Fixed Time mode (Unsymmetrical system analysis)

Same as in the case of the Fixed Point mode, the unsymmetrical system analysis method is used to develop an impulse response representation in the Fixed Time mode. The Fixed Time mode filter is an unsymmetrical band pass filter as given by *Equation*6. 4 and shown in *Figure 6. 2.b*. The low pass filters equivalent of the Fixed Time mode filter's sides. are shown in *Figure 6. 13*.

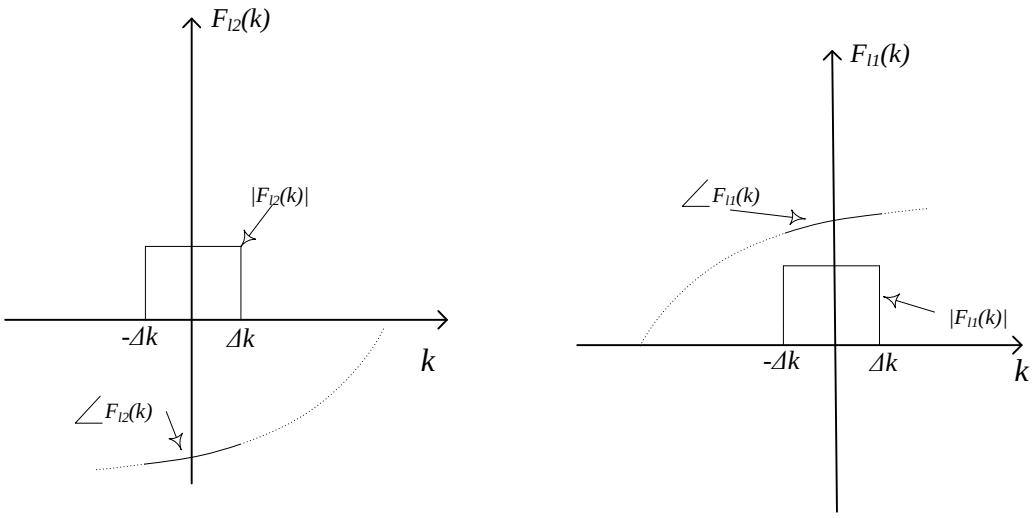

Figure 6. 13: The low pass filters equivalent of the Fixed Time mode filter's sides. a)Right band side equivalent , b)Left band side equivalent

Following the same four steps explained in *Section 6.4.2* produces the impulse response of the (*in-phase* f_p) and *(quadrature* f_q*)* systems, given by *Equation 6. 39* and *Equation* 6. 40.The full mathematical manipulations are shown in Appendix (C)

$$f_p(x)=\frac{1}{8\pi x\sqrt{x}}\left[4\sqrt{x}\left(sin\left(\sqrt{g}\Delta t\sqrt{k_o-\Delta k}+x\Delta k\right)-sin\left(\sqrt{g}\Delta t\sqrt{k_o+\Delta k}-x\Delta k\right)\right)+ 2\sqrt{2}\sqrt{\pi g}\Delta t\left(\cos\left(\frac{x^2k_o+g\Delta^2t}{4x}\right)\left(C(z_4)-C(z3)\right)+sin\left(\frac{x^2k_o+g\Delta^2t}{4x}\right)\left(S(z_4)-S(z_3)\right)\right)\right]$$

6. 39

$$f_q(x)=\frac{1}{8\pi x\sqrt{x}}\left[4\sqrt{x}\left(cos\left(\sqrt{g}\Delta t\sqrt{k_o+\Delta k}-x\Delta k\right)-cos\left(\sqrt{g}\Delta t\sqrt{k_o-\Delta k}+x\Delta k\right)\right)+ 2\sqrt{2}\sqrt{\pi g}\Delta t\left(\sin\left(\frac{x^2k_o+g\Delta^2t}{4x}\right)\left(C(z_4)-C(z_3)\right)-cos\left(\frac{x^2k_o+g\Delta^2t}{4x}\right)\left(S(z_4)-S(z_3)\right)\right)\right]$$

6. 40

Where

$$z_3(x)=\sqrt{\frac{2}{\pi}}\left(\frac{-2x\sqrt{k_o+\Delta k}+\sqrt{g}\Delta t}{2\sqrt{x}}\right)$$

$$z_4(x)=\sqrt{\frac{2}{\pi}}\left(\frac{-2x\sqrt{k_o-\Delta k}+\sqrt{g}\Delta t}{2\sqrt{x}}\right)$$

The (*in-phase* f_p) and *(quadrature* f_q*)* systems are in turn used to define the filter's envelop given by the relation:

$$filter's\ envelp=2\cdot\sqrt{f_p^2(x)+f_q^2(x)}$$

6. 41

The impulse response properties (shift & duration) are defined by the properties of the response envelop as in the case of the Fixed Point mode, the envelop properties are defined by the two terms $\{C(z_4(x))-C(z_3(x))\}$ and $\{S(z_4(x))-S(z_3(x))\}$.

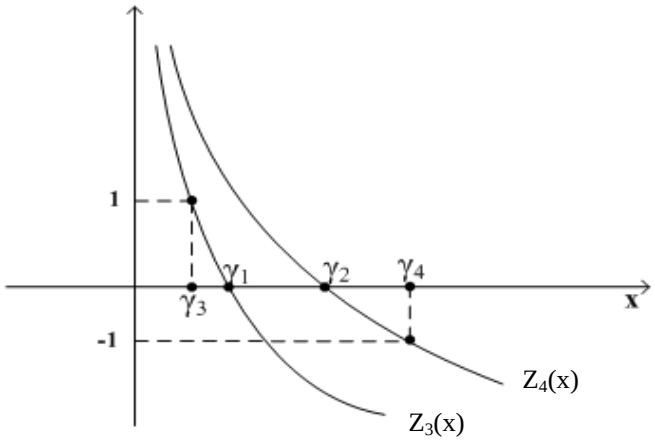

Figure 6. 14: Edge point of Fresnel window defining the Fixed Time filter envelope

The Fresnel function's coefficients ($z_3(x)$ and $z_4(x)$) are shown in Figure 6. 14 The outer window edges are defined by the two points (γ_3 and γ_4) given by:

$$z_3(\gamma_3)=1 \quad \longrightarrow \quad \gamma_3=\frac{\Delta t\sqrt{g}}{2\sqrt{k_{\max}}}+\pi\left(\frac{1-\sqrt{1+\frac{4\sqrt{g\,k_{\max}}\Delta t}{\pi}}}{4k_{\max}}\right) \qquad \textbf{6. 42}$$

$$z_4(\gamma_4)=1 \quad \longrightarrow \quad \gamma_4=\frac{\Delta t\sqrt{g}}{2\sqrt{k_{\min}}}+\pi\left(\frac{1+\sqrt{1+\frac{4\sqrt{g\,k_{\min}}\Delta t}{\pi}}}{4k_{\min}}\right) \qquad \textbf{6. 43}$$

While the two points (γ_1 and γ_2) defining the mid height window edges are given by:

$$z_3(\gamma_1)=0 \quad \longrightarrow \quad \gamma_1=\frac{\Delta t\sqrt{g}}{2\sqrt{k_{\max}}} \qquad \textbf{6. 44}$$

$$z_4(\gamma_2)=0 \quad \longrightarrow \quad \gamma_2=\frac{\Delta t\sqrt{g}}{2\sqrt{k_{\min}}} \qquad \textbf{6. 45}$$

Figure 6. 15a-b-c shows the impulse response of the propagation filters in the Fixed Time mode and their envelopes given by the *Equation 6. 39*. It is obvious that the envelope represent the impulse response properties (duration and shift) between the two outer edge points (γ_3 and γ_4). If we define γ_3 as the beginning of the impulse response energy concentration region, and γ_4 as the end of the impulse response energy concentration region, we find the response duration as

$$\zeta_D=\gamma_4-\gamma_3 \qquad \textbf{6. 46}$$

$$\zeta_D=\frac{\Delta t\sqrt{g}}{2}\left(\frac{1}{\sqrt{k_{\min}}}-\frac{1}{\sqrt{k_{\max}}}\right)+\left(\frac{\pi(k_{\max}-k_{\min})+\pi\,k_{\max}\sqrt{1+\frac{4\sqrt{k_{\min}}\Delta t\sqrt{g}}{\pi}}+\pi\,k_{\min}\sqrt{1+\frac{4\sqrt{k_{\max}}\Delta t\sqrt{g}}{\pi}}}{4k_{\min}k_{\max}}\right) \qquad \textbf{6. 47}$$

As in the case of the Fixed Point mode the two mid height points (γ_1 , γ_2) are the same as the response boundaries defined by the polygonal approximation method. Using these boundaries gives a smaller duration.

Figure 6. 15 shows a closer view to illustrate the impulse response's affective areas defined by this method.

An interesting feature of the envelop behaviour for $x < \gamma_3$, the plotted examples indicate that the impulse response is a locally zero mean function which oscillates with increasing speed. Putting in mind that for the prediction purposes these are multiplied by $\eta(t_o,x)$ which is band limited, the oscillation results in cancellation of the contribution made in these regions, limiting the impulse response effective part to the region defined by(γ_3 , γ_4). The extremely high oscillation leads to increasingly more complete cancellation of the contribution made to the convolution integration. On the other hand the regions x > γ_4 are very diminutive also resulting in an insignificant contribution in the convolution integral. This leaves the impulse region as being defined between (γ_3, γ_4).

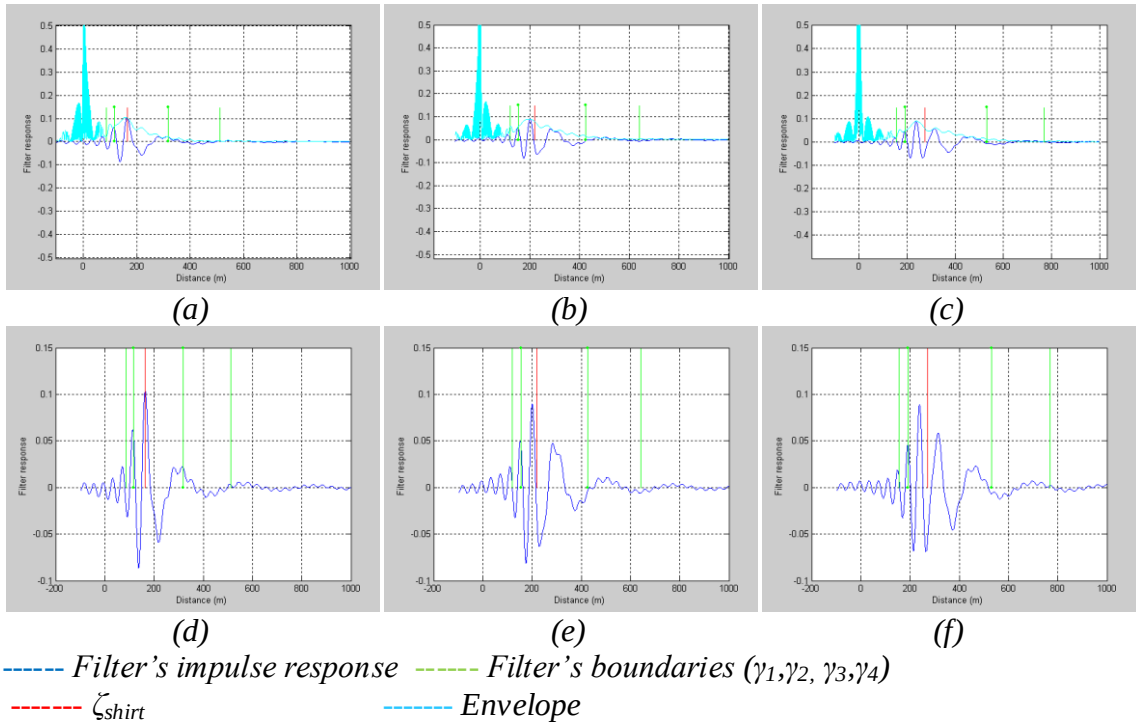

Figure 6. 15: Fixed Time impulse response boundaries estimated using unsymmetrical system analysis k_0=0.1 Δk =0.07 (a)(d) Δt =30 s (b)(e) Δt =40 s (c)(f) Δt =50 s

6.5 Prediction region estimation using impulse response properties

In the previous section different methods were used to estimate the properties of the propagation filters. The first method provided a pair of boundaries of the energy concentration region while the second method provided two pairs, one of which is the same as the first method. These pairs are chosen as a building block of the more general definition of the impulse response boundaries In the Fixed Point mode the boundaries (τ_1,τ_2) are extended to the more general boundaries (τ_{r1},τ_{r2}) by using the parameter r >0 as shown in the following relation

$$\left.\begin{aligned}\tau_{r1}(\Delta x) &= \lambda_{shift}(\Delta x) - r\left(\lambda_{shift}(\Delta x) - \tau_1(\Delta x)\right)\\ \tau_{r2}(\Delta x) &= \lambda_{shift}(\Delta x) + r\left(\tau_2(\Delta x) - \lambda_{shift}(\Delta x)\right)\end{aligned}\right\} \quad \textbf{6. 48}$$

A similar extension is used in the Fixed Time mode, the two boundaries $(\gamma_1\ ,\ \gamma_2)$ derived in the previous section are extended to the general form $(\gamma_{r1}\ ,\ \gamma_{r2})$.

$$\left.\begin{aligned}\gamma_{r1}(\Delta t) &= \zeta_{shift}(\Delta t) - r\left(\zeta_{shift}(\Delta t) - \gamma_1(\Delta t)\right)\\ \gamma_{r2}(\Delta t) &= \zeta_{shift}(\Delta t) + r\left(\gamma_2(\Delta t) - \zeta_{shift}(\Delta t)\right)\end{aligned}\right\} \quad \textbf{6. 49}$$

Where the value of r determines the size of the response duration, and hence determines the percentage of the total filter energy which is being considered. When (τ_r,γ_r) are used to determine the filters impulse response duration, the percentage energy associated with a particular r determines the prediction error. Since the energy of the filter is concentrated in $(\tau_{r1},\ \tau_{r2})$ in the Fixed Point mode and in the region $(\gamma_{r1},\ \gamma_{r2})$ for the Fixed Time mode, the energy outside this regions is neglected, this results in the integration in the prediction convolution relation given by *Equation 4.18* and *Equation 4.31* being limited to the impulse response's affective region, giving the predicted wave estimated as :

$$\eta_r(t, x_p) = \int_{t-\tau_{r2}}^{t-\tau_{r1}} \eta(\tau, x_o)\cdot\lambda(t-\tau, x_p - x_o)\,d\tau \quad \textbf{6. 50}$$

$$\eta_r(t_p, x) = \int_{x-\gamma_{r2}}^{x-\gamma_{r1}} \eta(t_o, \gamma)\cdot\zeta(t_p - t_o, x-\gamma)\,d\gamma \quad \textbf{6. 51}$$

Furthermore, since the wave is measured over a limited period of time (t_1,t_2)in the Fixed Point mode and a limited region in space (x_1,x_2) in the Fixed Time mode, this is represented by multiplying the original wave with a suitable window in time or space

$$\eta_{Wt}(t,x_o)=W_t\cdot\eta(t,x_o) \qquad \textit{where} \qquad W_t=\begin{cases}1 & t_1<t<t_2\\ 0 & \textit{otherwize}\end{cases} \qquad \textbf{6. 52}$$

$$\eta_{Wx}(t_o,x)=W_x\cdot\eta(t_o,x) \qquad \textit{where} \qquad \textbf{6. 53}$$

$$W_x=\begin{cases}1 & x_1<x<x_2\\ 0 & \textit{otherwize}\end{cases}$$

Convolving this windowed wave with the impulse response of the propagation filter results in $\eta_w(t,x_p)$ given by *Equation* 6. 55. This process is demonstrated in *Figure 6. 16*

$$\eta_w(t,x_p)=\int_{t-\tau_{r2}}^{t-\tau_{r1}}W_t(\tau)\cdot\eta(\tau,x_o)\cdot\lambda(t-\tau,x_p-x_o)d\tau \qquad \textbf{6. 54}$$

$$\eta_w(t,x_p)=\begin{cases}0 & -\infty<t<t_1+\tau_{r1}\\ \int_{t_1}^{t-\tau_{r1}}\eta(\tau,x_o)\cdot\lambda(t-\tau,x_p-x_o)\,d\tau & t_1+\tau_{r1}<t<t_1+\tau_{r2}\\ \int_{t-\tau_{r2}}^{t-\tau_{r1}}\eta(\tau,x_o)\cdot\lambda(t-\tau,x_p-x_o)\,d\tau & t_1+\tau_{r2}<t<t_2+\tau_{r1}\\ \int_{t-\tau_{r2}}^{t_2}\eta(\tau,x_o)\cdot\lambda(t-\tau,x_p-x_o)\,d\tau & t_2+\tau_{r1}<t<t_2+\tau_{r2}\\ 0 & t_2+\tau_{r2}<t<\infty\end{cases} \qquad \textbf{6. 55}$$

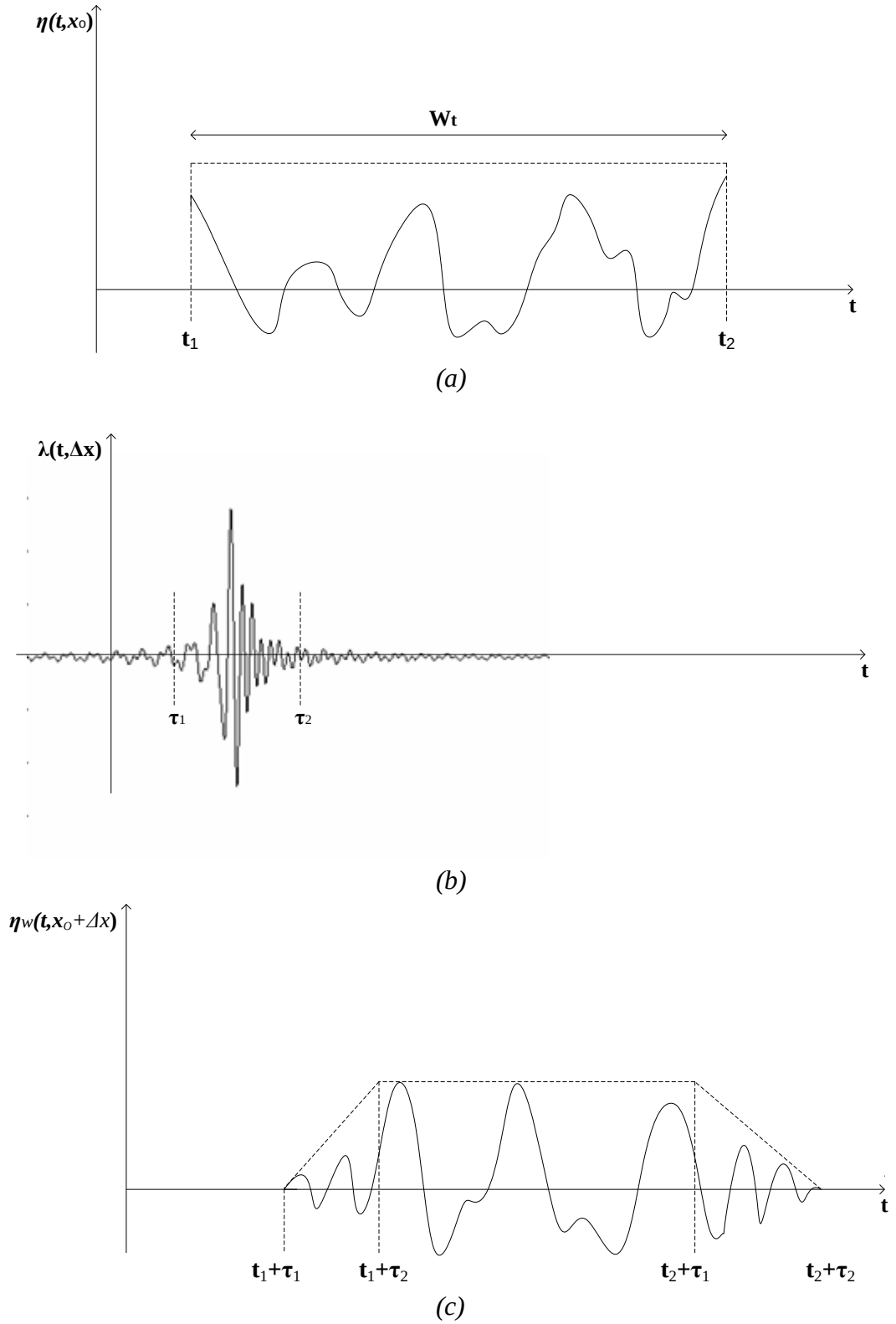

Figure 6. 16: Prediction region estimation using impulse response properties. a) Windowed wave form, b)Fixed Point mode filter's response, c)Different sections of predicted wave.

Comparing $\eta_w(t,x_p)$ in *Equation* 6. 55. and $\eta(t,x_p)$ in *Equation* 6. 50 results in*:*

$$\eta_w(t,x_p) = \eta_r(t,x_p) \qquad for \qquad t_1+\tau_{r2} < t < t_2+\tau_{r1} \qquad \textbf{6. 56}$$

This relation is of most importance in the DSWP. This suggests that a certain length of the time record of a wave at a certain point in space (x_p) is determined by the limited time record at a remote location (x_o). The limits of *Equation 6. 56* provide a straight forward method of determining the prediction region. The prediction duration and position is defined by the duration and the position of the filters impulse response, (τ_{r1}, τ_{r2}) and the measured length (t_1,t_2).

Using a similar argument in the Fixed Time mode, the wave is measured over the distance $x_1 < x < x_2$, and the filters boundaries defined by $(\gamma_{r1}, \gamma_{r2})$. We can find the relation between the predicted wave $(\eta_w(t_p,x))$ and the wave elevation at the instance (t_p), $\eta(t_p,x)$ where

$$\eta_w(t_p,x) = \int_{x-\gamma_{r2}}^{x-\gamma_{r1}} W_x(\gamma)\cdot\eta(t_o,x)\cdot\zeta(t_p-t_o,x-\gamma)d\gamma \qquad \textbf{6. 57}$$

$$\eta_w(t_p,x) = \begin{cases} 0 & -\infty < x < x_1+\gamma_{r1} \\ \int_{x_1}^{x-\gamma_{r1}} \eta(\tau,x_o)\cdot\zeta(t_p-t_o,x-\gamma)d\gamma & x_1+\gamma_{r1} < x < x_1+\gamma_{r2} \\ \int_{x-\gamma_{r2}}^{x-\gamma_{r1}} \eta(\tau,x_o)\cdot\zeta(t_p-t_o,x-\gamma)d\gamma & x_1+\gamma_{r2} < x < x_2+\gamma_{r1} \\ \int_{x-\gamma_{r2}}^{x_2} \eta(\tau,x_o)\cdot\zeta(t_p-t_o,x-\gamma)d\gamma & x_2+\gamma_{r1} < x < x_2+\gamma_{r2} \\ 0 & x_2+\gamma_{r2} < x < \infty \end{cases} \qquad \textbf{6. 58}$$

This states that in the Fixed Time mode a limited snap shot in space at time (t_o) is adequate to predict the wave at $t = t_p$ in the region defined by the original measurement location and impulse response properties. The predicted wave equals the waves elevation in the region defined by $x_1+\gamma_{r2} < x < x_2+\gamma_{r1}$, and hence these are considered the prediction region boundaries.

The prediction region boundaries in the Fixed Point mode are defined by the two lines:

$$\begin{aligned} &\text{line 1} \quad : t = t_1+\tau_{r2}(\Delta x) \\ &\text{line 2} \quad : t = t_2+\tau_{r1}(\Delta x) \end{aligned} \qquad \textbf{6. 59}$$

While the prediction region boundaries in the Fixed Time mode are defined by the two lines:

$$\begin{aligned} &\text{line 1} \quad : x = x_1+\gamma_{r2}(\Delta t) \\ &\text{line 2} \quad : x = x_2+\gamma_{r1}(\Delta t) \end{aligned} \qquad \textbf{6. 60}$$

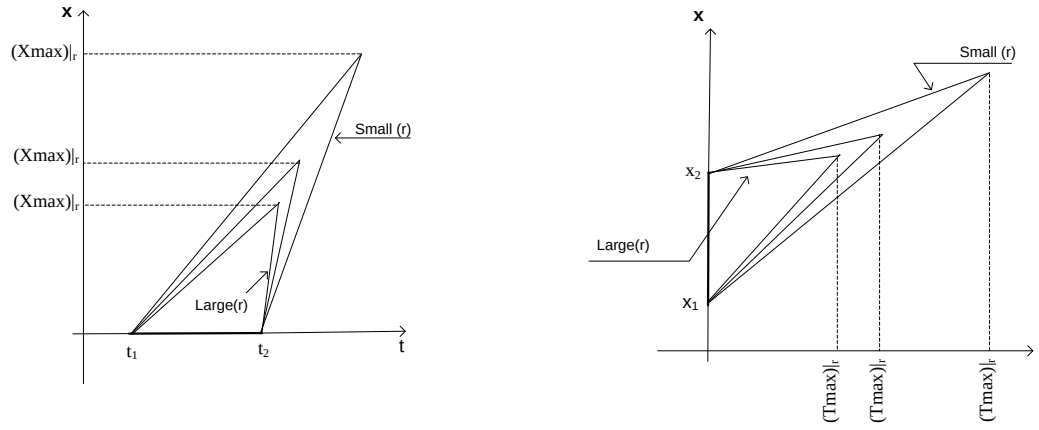

(a) *(b)*

Figure 6. 17: Prediction region diagram for different values of (r) . a)Fixed Point mode ,b) Fixed Time mode

With this definition of the prediction region we notice that the prediction region dimensions depend on the variable (r), where the larger the impulse response we use for the prediction the smaller the region becomes. On the other hand the more energy we consider the more accurate prediction we expect. *Figure 6. 17* demonstrates the prediction regions for a different r values for both the Fixed Time and Fixed Point mode. Also the prediction region parameters T_{max} X_{max} vary with the choice of (r), for the remaining of this chapter that maximum prediction distance defined for the value r is denoted as $X_{max}|_r$, while the maximum prediction time defined for the value r is denoted as $T_{max}|_r$. For the Fixed Point mode $X_{max}|_r$ the maximum prediction distance can be defined as the point in space where $t_1 + \tau_{r2} = t_2 + \tau_{r1}$. In this case the impulse response λ_D is equal to the measured length.

$$\lambda_D = \tau_{r2} - \tau_{r1} = t_2 - t_1 \qquad \textbf{6. 61}$$

Substituting *Equation*6. 61 In *Equation* 6. 10 the maximum prediction distances Xmax for a given r value is estimated by:

$$X_{\max}|_r = \frac{(t_2 - t_1)\cdot g}{4r\Delta\omega} \qquad \textbf{6. 62}$$

This shows the expected reverse relation between the factor (r) and X_{max} where a larger window length results in a smaller prediction region. On the other hand for Fixed Time mode the maximum prediction time occurs when the two prediction region boundaries are equal($x_1 + \gamma_{r2} = x_2 + \gamma_{r1}$),in this case the impulse response duration ζ_D equals the length of the measured wave

$$\zeta_D = \gamma_{r2} - \gamma_{r1} = x_2 - x_1$$

Using the above value of the response duration the maximum time is evaluated from *Equation* 6. 11as:.

$$T_{\max}|_r = \frac{2(x_2 - x_1)}{r\sqrt{g}}\left(\frac{\sqrt{k_{\max}k_{\min}}}{\sqrt{k_{\max}} - \sqrt{k_{\min}}}\right) \quad \textbf{6. 63}$$

6.6 Numerical estimation of truncated impulse response energy

The factor r was introduced in the previous section to build the general impulse response boundaries from the original boundaries (τ_1,τ_2) and (γ_1,γ_2). The general boundaries (τ_{r1},τ_{r2}) and $(\gamma_{r1},\gamma_{r2})$ given by *Equation* 6. 48 *a*nd *Equation* 6. 49 are used to truncate the impulse response with different duration depending on the value of r. In this section a numerical approach is used to estimate the energy of truncated part as percentage of the total energy. In the Fixed Point mode, the energy of the impulse response truncated using the factor r is estimated by

$$E_r = \sum_i \lambda^2(t_i, \Delta x)$$

Where $\tau_{r1}(\Delta x) < t_i < \tau_{r2}(\Delta x)$ with a time step of 0.1 sec.

The value $r = 100$ is used to generate a large window that is used as the total energy of the impulse response, where the percentage energy is calculated by:

$$percentage\ energy\% = \frac{E_r}{E_{100}} \times 100 \quad \textbf{6. 64}$$

To cover a wide range of different conditions the percentage energy was calculated for $\Delta x = (0.2X_{max}, 0.5X_{max}, 0.7X_{max})$ and the mid frequency and band width of the Pierson Moskwitz with wind speed $U=(10,15,20)\ ms^{-1}$ used, giving us the nine curves plotted in *Figure 6. 18.*

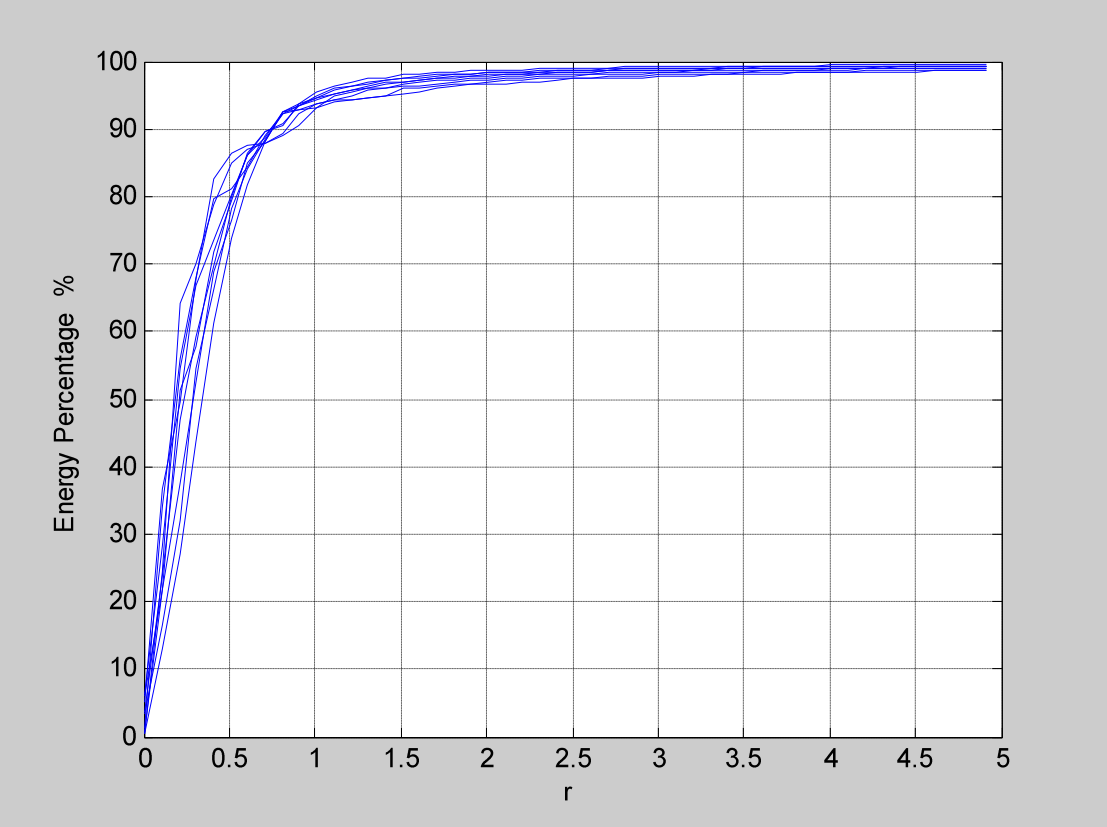

Figure 6. 18: Fixed point mode Truncated impulse response energy percentage for different values of Δx=(0.2 X_{max}, 0.5 X_{max}, 0.7 X_{max}) and U=(10,15,20) ms^{-1}

A similar numerical experiment is carried out for the Fixed Time case. The truncated energy is calculated using

$$E_r = \sum_i \zeta^2(x_i, \Delta t)$$

Where $\gamma_{r1}(\Delta t) < x_i < \gamma_{r2}(\Delta t)$ and a spatial step size 0.1 m is used.

The percentage energy in this case also uses the relation *Equation* 6. 64, the evaluation was carried out using different $\Delta t = (0.2T_{max}, 0.5T_{max}, 0.7T_{max})$ and wave number upper and lower band values of Pierson Moskowitz spectrum with wind speed *U=(10,15,20) ms^{-1}*. The nine plots are shown in *Figure 6. 19.* Also shown plotted using the red line is the average relation whish is used in the next section to define the prediction region with a given maximum error.

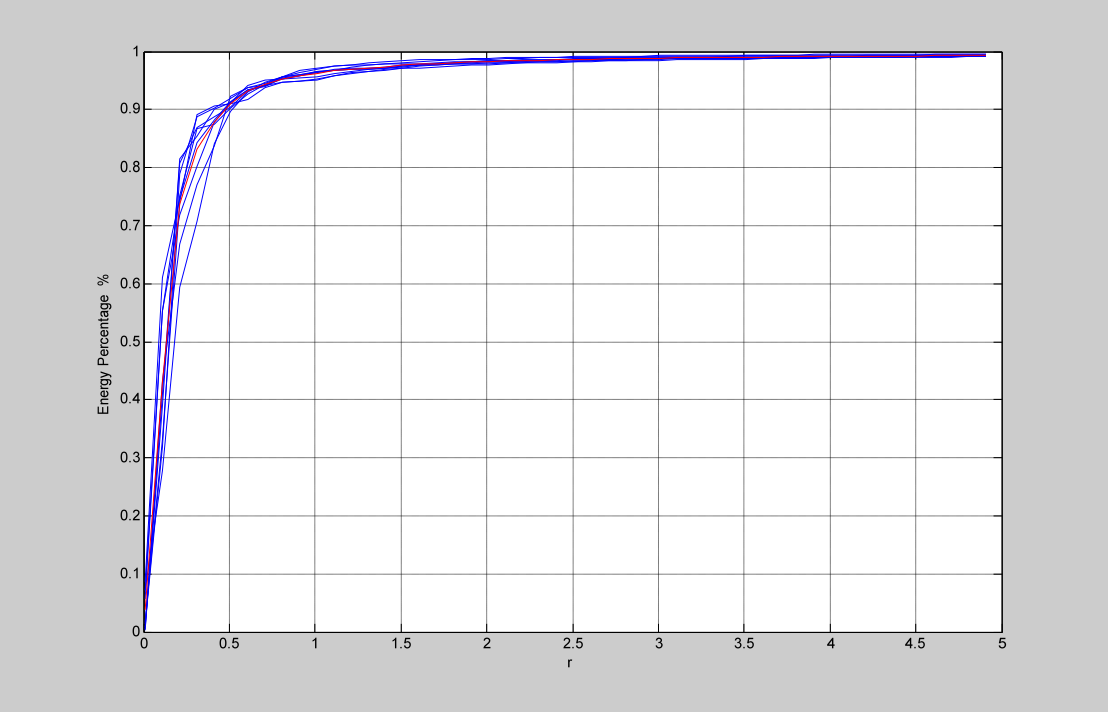

Figure 6. 19: Truncated impulse response energy percentage in Fixed Time mode percentage for different values of Δt=(0.2 T_{max}, 0.5 T_{max}, 0.7 T_{max}) and U=(10,15,20) ms^{-1}

Considering the results of that both the Point mode and the Fixed Time mode it is clear that there is a direct relationship between r and the percentage energy of the impulse response region defined by (τ_{r1},τ_{r2}) in the Fixed Point mode and $(\gamma_{r1}, \gamma_{r2})$ in the Fixed Time mode. More importantly this relationship is almost the same for different conditions of the time/space displacement and the filters band.

6.7 Prediction region estimation using prediction filter's properties

A general prediction region model was generated in *Section 5.4* by using a normalization process. It was shown that the error surface of predicting any Pierson Moskowitz sea follows a single model that is normalized using X_{max} for the space dimension and T_{max} for the time dimension. The normalization process was tested and shown to give reasonable results for different wave conditions. This section introduces an analytical explanation for this process and represents a normalized prediction region model using the prediction filter's properties.

The slopes of prediction region borders giving in *Equation* 6. 60 are given by :

$$\left.\begin{aligned}\frac{dl_1}{dt} &= \frac{\gamma_{2r}}{\Delta t}\\ \frac{dl_2}{dt} &= \frac{\gamma_{1r}}{\Delta t}\end{aligned}\right\} \qquad \textbf{6. 65}$$

By substituting *Equations* 6. 36, *Equations* 6. 38 *and Equations* 6. 49 *in Equations* 6. 65 we obtain

$$\frac{dl_1}{dt} = \frac{\gamma_{2r}}{\Delta t} = \frac{\sqrt{3g}\Delta t}{2\sqrt{k_{\max} + k_{\max}^{1/2}k_{\min}^{1/2} + k_{\min}}} + r\left[\frac{\sqrt{g}}{2\sqrt{k_{\min}}} - \frac{\sqrt{3g}}{2\sqrt{k_{\max} + k_{\max}^{1/2}k_{\min}^{1/2} + k_{\min}}}\right]$$

$$\frac{dl_2}{dt} = \frac{\gamma_{1r}}{\Delta t} = \frac{\sqrt{3g}}{2\sqrt{k_{\max} + k_{\max}^{1/2}k_{\min}^{1/2} + k_{\min}}} - r\left[\frac{\sqrt{3g}}{2\sqrt{k_{\max} + k_{\max}^{1/2}k_{\min}^{1/2} + k_{\min}}} - \frac{\sqrt{g}}{2\sqrt{k_{\max}}}\right] \qquad \textbf{6. 66}$$

Using the same normalizing factor $X_{max,}$ T_{max} defined in *Equation 5.3 Equation 5.4* to normalize the spatial and time dimensions results in the two normalized slops for the Fixed Time mode Boundaries for the Pierson Moskowitz seas given by

$$Normalized\ \frac{dl_1}{dt} = \frac{\gamma_{2r}}{\Delta t}\cdot\frac{T_{\max}}{X_{\max}} = 0.7108 + 0.6753\ r$$

$$Normalized\ \frac{dl_2}{dt} = \frac{\gamma_{1r}}{\Delta t}\cdot\frac{T_{\max}}{X_{\max}} = 0.7108 - 0.2094\ r \qquad \textbf{6. 67}$$

This result shows that the Pierson Moskowits seas have a normalized prediction boundaries, where the value of *r* and hence the amount of energy in the particular chosen length of the impulse determine the slope of the boundaries lines, and in turn define the size of the prediction region of that particular *r*. Having the normalized region boundaries that don't depend on the wind speed (model parameter) indicates that a common representation for the prediction accuracy through the (x,t) plane can be found. This agrees with the findings of *Chapter 5*.

Using the normalized line slope the prediction region of any Pierson-Moskowitz ocean can be estimated. This is done in four steps

- Find *(r)* for the required threshold from the average plot in *Figure 6. 19* Where (energy =1- threshold). For example in the *r* value of the thresholds (5%, 10%,25%,35%) are r=(0.75,0.5,0.25,0.2) respectively.
- Determine the normalized slopes of the boundary lines from *Equation* 6. 67.
- Multiply by the factor ($X_{max,}/ T_{max)}$ to get the prediction boundary slopes.

To test this method the same prediction error surfaces obtained in *Chapter 5* are used. The threshold error surface of error (5%,10%,25%,30%) for the Pierson-

Moskowitz waves at wind speed U=10m/s are shown in *Figure 6. 20*. Also showing in the figure are the upper and lower boundaries described above. Although there error surface was developed using the spectrum method, the normalized line slope resulting from the impulse response filter show reasonable tracking of the prediction region.

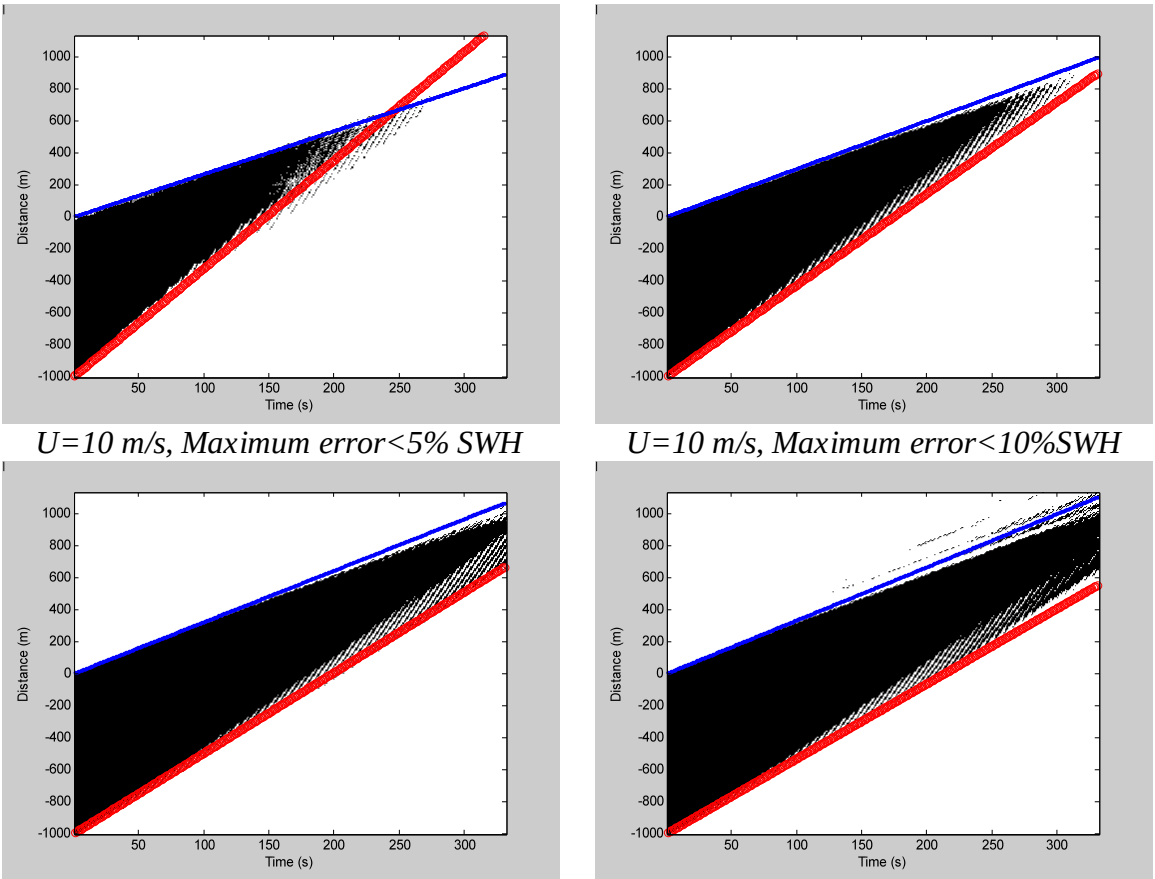

U=10 m/s, Maximum error<5% SWH *U=10 m/s, Maximum error<10%SWH*

U=10 m/s, Maximum error<25%SWH *U=10 m/s, Maximum error< 30%SWH*

------ *Lower boundary* -------- *Upper boundary*

Figure 6. 20: Prediction region estimation using Fixed Time mode filter's properties

6.8 Prediction using terminated impulse response

The main goal of considering the impulse response of the prediction filter was to introduce an alternative prediction method and to improve the prediction quality obtained from the frequency domain prediction technique. This section shows the findings of prediction in the conjugate domain. The implementation algorithms used for prediction purposes were derived by direct discretisation of the continuous analytic forms.

The convolution form of the prediction algorithms given by *Equation* 6. 54 for the Fixed Point mode and *Equation* 6. 57 for the Fixed Time mode, are transformed to their discrete form by substituting the integration with a summation and using a time step of *0.1sec* and a spatial step of *0.1m*. The prediction was carried out using different length of the impulse response, by using *r =(2,1,0.5)*.

6.8.1 Fixed Point mode

This section illustrates the results of prediction using terminated impulse response in the Fixed Point mode. The diagram in Figure 6. 21 illustrates the prediction region of the different wave models U=(10 $m.sec^{-1}$, 15 $m.sec^{-1}$, 20 $m.sec^{-1}$)for various values of r (2,1,0.5) , this diagram also illustrates the colour code scheme used to simplify illustrating the results in the next figures (black r=2) (red r=1) (green r=0.5).

This prediction method is tested over different conditions. The successive steps for implementing these tests are as follows:

1. The first step is to define the prediction point Δx , these are given in Table 6. 1

Table 6. 1:Prediction point for different wave models

Δx =	$0.25(Xmax)_{r=2}$	$0.5(Xmax)_{r=2}$	$0.75(Xmax)_{r=2}$
Wind speed U=10	*50.2m*	*100.5m*	*150.7m*
Wind speed U=15	*75.37m*	*150.7.5m*	*226m*
Wind speed U=20	*100.5m*	*200.9m*	*301.5m*

2. Given the prediction point Δx find the filters parameters (τ_1, τ_2) , Table 6. 2 gives these values for the three prediction distance Δx= ($0.25(Xmax)_{r=2}$, $0.5(Xmax)_{r=2}$, $0.75(Xmax)_{r=2}$). It is interesting that the same values are found for the different wave models.

Table 6. 2: Filters parameter (τ_1 , τ_2) for different prediction distances

Δx =	$0.25(X_{max})_{r=2}$	$0.5(X_{max})_{r=2}$	$0.75(X_{max})_{r=2}$
τ_1 (s)	*7.0847*	*14.1656*	*21.2437*
τ_2 (s)	*19.5853*	*39.1602*	*58.7273*

3. Calculate the general filter's boundaries (τ_{1r}, τ_{2r}) for the three values *r=(.05, 1,2)*. These values are shown in Table 6.3.

Table 6. 3 :General filter's boundaries (τ_{1r}, τ_{2r}) for different prediction points

	Δx =	$0.25(X_{max})_{r=2}$	$0.5(X_{max})_{r=2}$	$0.75(X_{max})_{r=2}$
(r =2)	τ_{1r}	*-0.1422*	*-0.2843*	*-0.4263*
	τ_{2r}	*24.8591*	*49.7049*	*74.5409*
(r =1)	τ_{1r}	*7.0847*	*14.1656*	*21.2437*
	τ_{2r}	*19.5853*	*39.1602*	*58.7273*
(r =0.5)	τ_{1r}	*10.6981*	*21.3905*	*32.0787*
	τ_{2r}	*16.9484*	*33.8878*	*50.8205*

4. From the given measurement region (t_1= 0 , t_2= 100 sec), find the inner and outer prediction region boundaries. The inner boundaries represent the prediction region while the outer boundaries represent the region where only partial information of the wave is present, where the prediction fades away. These values are given in Table 6.4., and the inner boundaries are illustrated in the diagram in Figure 6. 21. Although the prediction distance value is different for different wave models these boundaries are the same as illustrated with the colour coded vertical lines.

Table 6. 4: Inner and outer boundaries for different prediction points

	Δx		$0.25(Xmax)_{r=2}$	$0.5(Xmax)_{r=2}$	$0.75(Xmax)_{r=2}$
r=2	*Inner boundaries*	$t_{1+}\ \tau_{2r}$	*24.8591*	*49.7049*	*74.5409*
		$t_{2+}\ \tau_{1r}$	*99.8578*	*99.7157*	*99.5737*
	Outer boundaries	$t_{1+}\ \tau_{1r}$	*-0.1422*	*-0.2843*	*-0.4263*
		$t_{2+}\ \tau_{2r}$	*124.8591*	*149.7049*	*174.5409*
r=1	*Inner boundaries*	$t_{1+}\ \tau_{2r}$	*19.5853*	*39.1602*	*58.7273*
		$t_{2+}\ \tau_{1r}$	*107.0847*	*114.1656*	*121.2437*
	Outer boundaries	$t_{1+}\ \tau_{1r}$	*7.0847*	*14.1656*	*21.2437*
		$t_{2+}\ \tau_{2r}$	*119.5853*	*139.1602*	*158.7273*
r=0.5	*Inner boundaries*	$t_{1+}\ \tau_{2r}$	*16.9484*	*33.8878*	*50.8205*
		$t_{2+}\ \tau_{1r}$	*110.6981*	*121.3905*	*132.0787*
	Outer boundaries	$t_{1+}\ \tau_{1r}$	*10.6981*	*21.3905*	*32.0787*
		$t_{2+}\ \tau_{2r}$	*116.9484*	*133.8878*	*150.8205*

5. Truncate the impulse response to the general boundaries given in Table 6.3

$$\lambda^r(t,\Delta x) = \begin{cases} \lambda(t,\Delta x) & \tau_{1r} < t < \tau_{2r} \\ 0 & otherwize \end{cases}$$

6. The wave prediction is given by:

$$\eta^r(k\delta t,\Delta x) = \sum_i \eta(i\delta t,0)\lambda^r\big((k-i)\delta t,\Delta x\big)$$

Where $\left[\frac{t_1}{\delta t}\right] < i < \left[\frac{t_2}{\delta t}\right]$

The [ ] represent the nearest integer function. And δt is the time step.

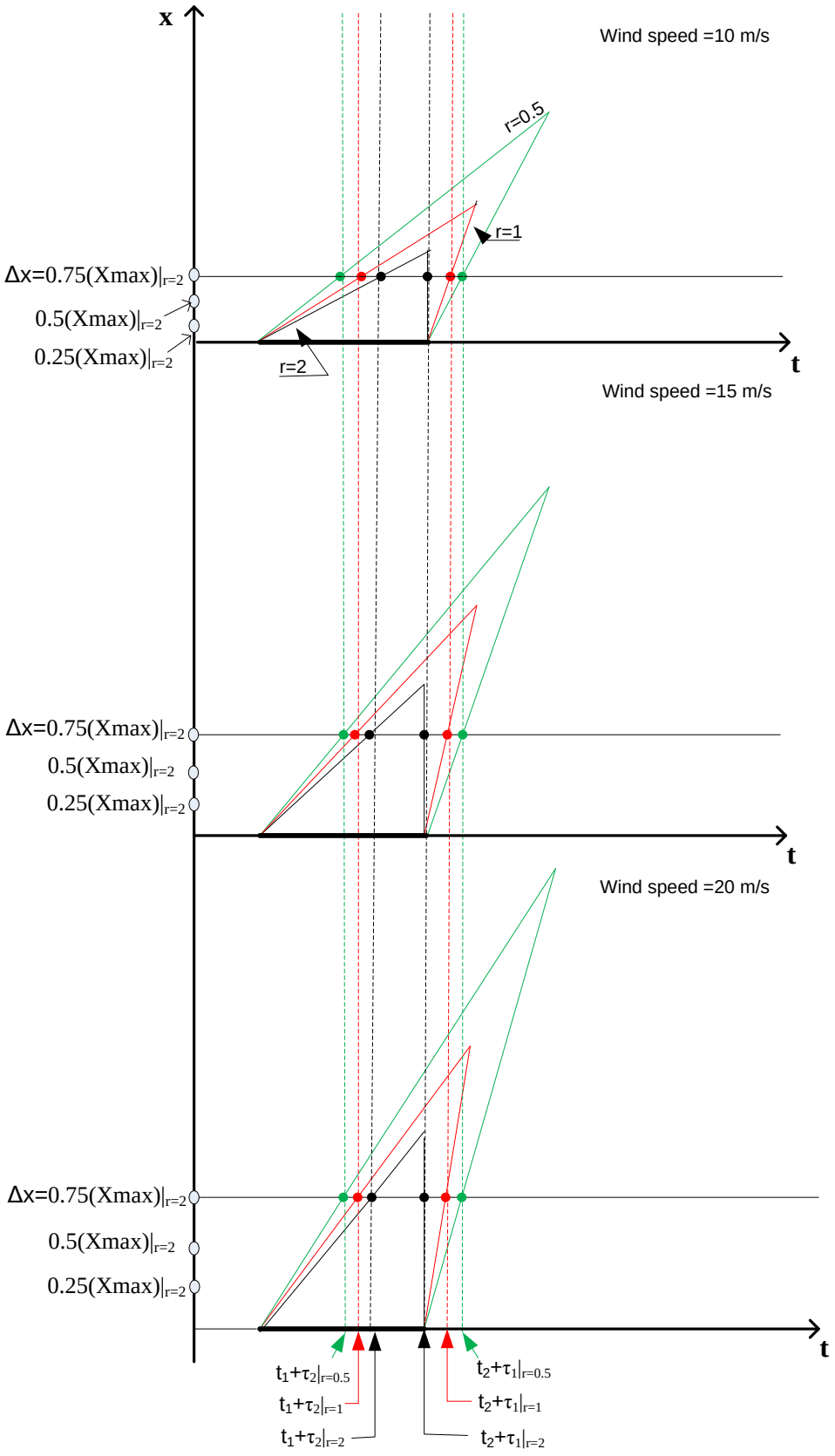

Figure 6. 21: Diagram of prediction results using truncated Fixed Point mode impulse response

An example of the prediction using this method is given in Figure 6. 22. In this case the wave is a Pierson Moskowitz wave with wind speed U=15 $m.s^{-1}$. The prediction results of using different lengths of the impulse response are show colour coded as explained above. The prediction results of using the larger value of *r* -the black plots in the first column- gave as expected the more accurate prediction. The inner and outer boundaries given in Table 6.4 are illustrated as vertical lines, the inner boundaries are shown in the lower part of the plot, and the outer boundaries are shown in the upper part of the plot. The prediction region defined by the two lower vertical lines increases in length for smaller values of *r*. Also clear in the given example the relation between the prediction region and the prediction point. For a given *r* value the further away from the measuring point, the smaller the region becomes.

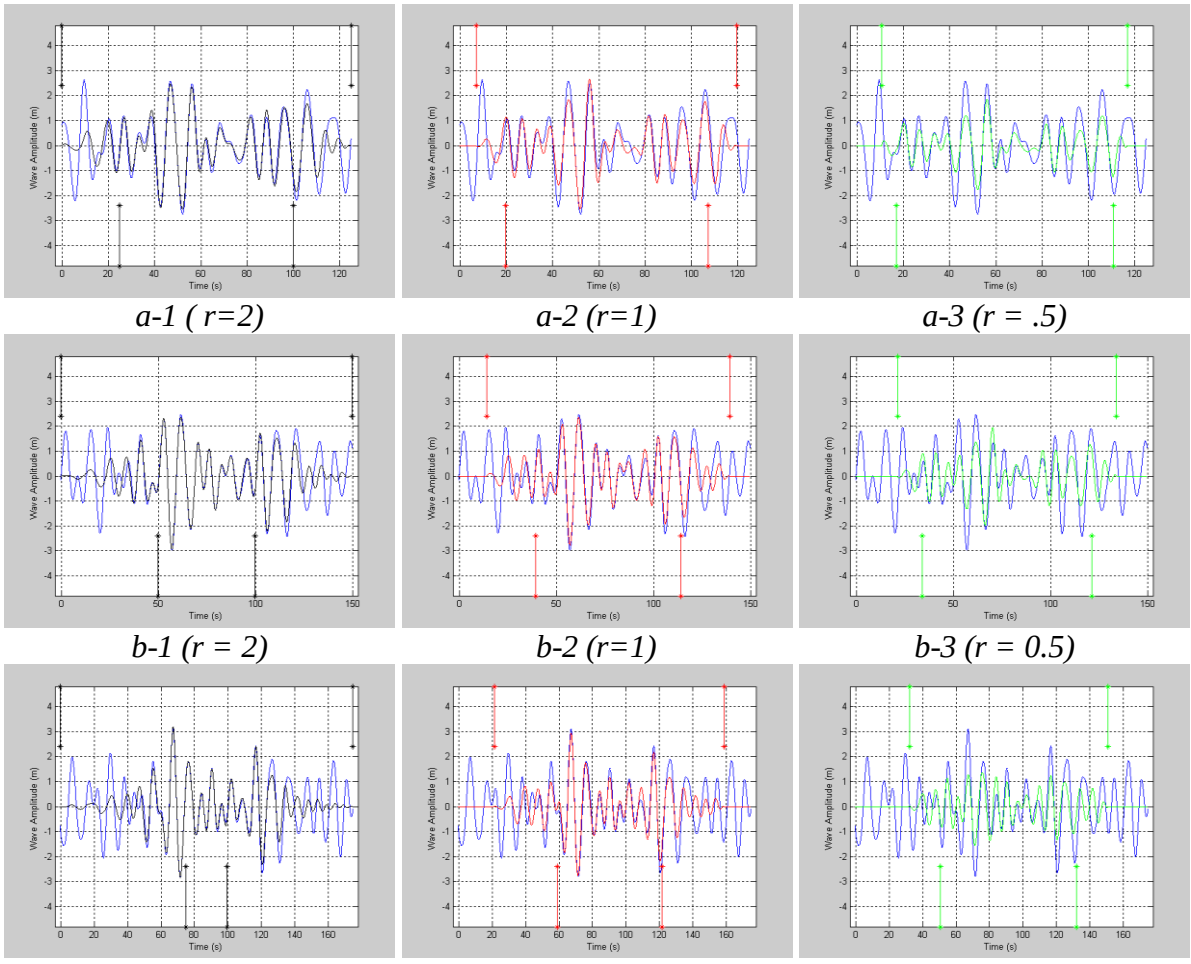

a-1 (r=2) *a-2 (r=1)* *a-3 (r = .5)*

b-1 (r = 2) *b-2 (r=1)* *b-3 (r = 0.5)*

c-1 (r=2) *c-2 (r=1)* *c-3 (r=0.5)*

------- *wave model* , ------- *wave prediction using r=2* , ------- *wave prediction using r=1* , ------ *wave prediction using r=0.5* ,

Upper vertical lines $(t_1+\tau_{r1})$ $(t_2+\tau_{r2})$, *Lower vertical lines(prediction region)* $(t_1+\tau_{r2})$ $(t_2+\tau_{r1})$

Figure 6. 22: Fixed Point wave model and wave prediction for Pierson Moskowitz of wind speed U=15 ms^{-1} using different length truncated impulse response a)$\Delta x=0.25(Xmax)_{r=2}$=75.4(m), b) $\Delta x=0.5(Xmax)_{r=2}$= 150.7 (m), c) $\Delta x=0.75(Xmax)_{r=2}$= 226 (m)

For a more comprehensive testing of this prediction method the maximum prediction error of is found for (1000) runs. This is repeated for different impulse response length (r = 2,1,0.5), different prediction positions Δx=(0.25(Xmax)r=2, 0.5(Xmax)r=2, 0.75(Xmax)r=2), and different wave conditions U=(10 m.sec^{-1} , 15 m.sec^{-1} , 20 m.sec^{-1}). These error surface cross sections are shown in *Figure 6. 23* using the same colour scheme used previously. As expected, in all the given cases the errors associated with the larger value of r is smaller than that of the smaller value of r. Also it is interesting that these error values hold for the duration defined by their respective prediction boundaries show on the plot as the vertical lines colour coded to match. Also noticeable is the gradual increase in the prediction error between the inner and outer

boundaries. However the value of the error surface associated with a particular value r changes for different prediction point position. The relation between the percentage energy and the value of the factor r was discussed in *Section 6.6*, and was found to be very close for different prediction conditions. If the prediction error is associated with the percentage of the total energy within the truncated impulse response, then it would be expected that the prediction error surface of a particular r reflects the same value for different prediction conditions, however this was not the case in the given case.

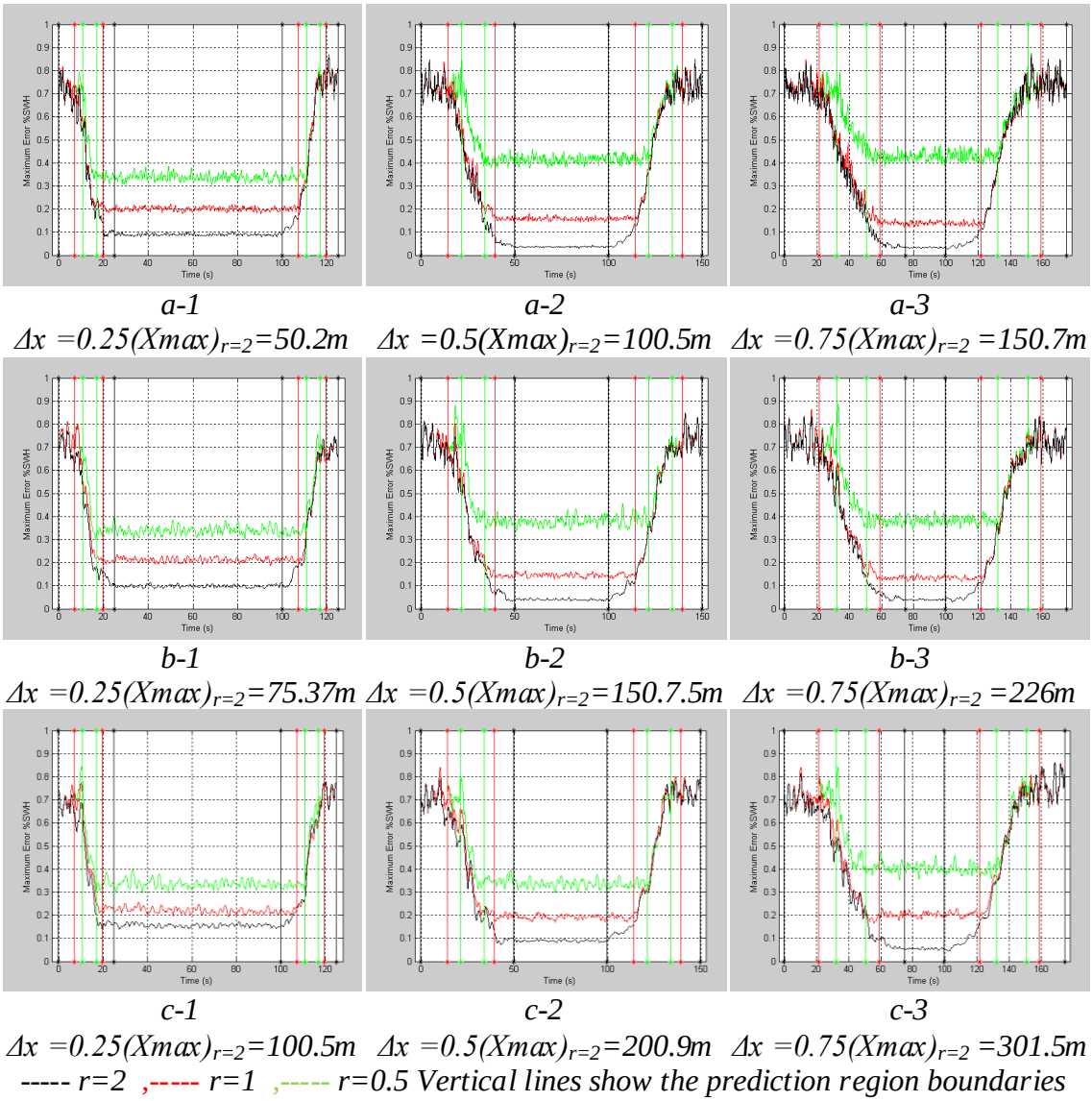

a-1 *a-2* *a-3*

$\Delta x = 0.25(Xmax)_{r=2} = 50.2m$ $\Delta x = 0.5(Xmax)_{r=2} = 100.5m$ $\Delta x = 0.75(Xmax)_{r=2} = 150.7m$

b-1 *b-2* *b-3*

$\Delta x = 0.25(Xmax)_{r=2} = 75.37m$ $\Delta x = 0.5(Xmax)_{r=2} = 150.7.5m$ $\Delta x = 0.75(Xmax)_{r=2} = 226m$

c-1 *c-2* *c-3*

$\Delta x = 0.25(Xmax)_{r=2} = 100.5m$ $\Delta x = 0.5(Xmax)_{r=2} = 200.9m$ $\Delta x = 0.75(Xmax)_{r=2} = 301.5m$

----- *r=2* ,----- *r=1* ,----- *r=0.5 Vertical lines show the prediction region boundaries*

Figure 6. 23: Prediction error surface cross section for Pierson-Mosskowitz sea with a)Wind speed U=10ms^{-1} ,b) Wind speed U=15ms^{-1} ,c) Wind speed U=20ms^{-1}

6.8.2 Fixed time mode

This section illustrates the results of prediction using terminated impulse response in the Fixed Time mode. The diagram in Figure 6.24 illustrates the prediction region of the different wave models U=(10 m.sec^{-1} , 15 m.sec^{-1} , 20 m.sec^{-1}), for various values of r (2,1,0.5), this diagram also illustrates the colour code scheme used to simplify illustrating the results in the next figures (black r=2) (red r=1) (green r=0.5).

This prediction method is tested over different conditions. The successive steps for implementing these tests are given:

1. The first step is to define the prediction time Δt for the different wave models. These are givin in Table 6.5

Table 6. 5: Prediction time Δt for different wave models

Δt =	$0.25(T_{max})_{r=2}$	$0.5(T_{max})_{r=2}$	$0.75(T_{max})_{r=2}$
Wind speed U=10	*27.6(s)*	*55.2(s)*	*82.8(s)*
Wind speed U=15	*18.4 (s)*	*36.8 (s)*	*55.2(s)*
Wind speed U=20	*13.8(s)*	*27.6(s)*	*41.4 (s)*

2. Given the prediction point Δt find the filters parameters (γ_1, γ_2) , Table 6. 6 gives these values for the three prediction instances ($0.25(T_{max})_{r=2}$,$0.5(T_{max})_{r=2}$, $0.75(T_{max})_{r=2}$).

Table 6. 6: Fixed Time Filters parameter (γ_1 , γ_2) for different prediction distances

Δt =	$0.25(T_{max})_{r=2}$	$0.5(T_{max})_{r=2}$	$0.75(T_{max})_{r=2}$
γ_1	*70.8086*	*141.6173*	*212.4259*
γ_2	*195.7478*	*391.4956*	*587.2434*

3. Calculate the general filter's boundaries (γ_{1r}, γ_{2r}) for the three values *r=(.05, 1,2).* These values are given in Table 6. 7

Table 6. 7 :General filter's boundaries (γ_{1r}, γ_{2r}) for different prediction points

	Δt =	$0.25(T_{max})_{r=2}$	$0.5(T_{max})_{r=2}$	$0.75(T_{max})_{r=2}$
(r =2)	γ_{1r}	*41.2303*	*82.4607*	*123.6910*
	γ_{2r}	*291.1087*	*582.2173*	*873.3260*
(r =1)	γ_{1r}	*70.8086*	*141.6173*	*212.4259*
	γ_{2r}	*195.7478*	*391.4956*	*587.2434*
(r =0.5)	γ_{1r}	*85.5978*	*171.1956*	*256.7934*
	γ_{2r}	*148.0674*	*296.1348*	*444.2022*

4. From the given measurement region , find the inner and outer prediction region boundaries. The inner boundaries represent the prediction region while the outer

boundaries represent the region where only partial information of the wave is present, where the prediction fades away.

Table 6. 8: Inner and outer boundaries of the prediction region

	Δt		*0.25(Tmax)r=2*	*0.5(Tmax)r=2*	*0.75(Tmax)r=2*
r=2	*Inner boundaries*	*x1+ γ2r*	*-708.8913*	*-417.7827*	*-126.6740*
		x2+ γ1r	*41.2303*	*82.4607*	*123.6910*
	Outer boundaries	*x1+ γ1r*	*-958.7697*	*-917.5393*	*-876.3090*
		x2+ γ2r	*291.1087*	*582.2173*	*873.3260*
r=1	*Inner boundaries*	*x1+ γ2r*	*-804.2522*	*-608.5044*	*-412.7566*
		x2+ γ1r	*70.8086*	*141.6173*	*212.4259*
	Outer boundaries	*x1+ γ1r*	*-929.1914*	*-858.3827*	*-787.5741*
		x2+ γ2r	*195.7478*	*391.4956*	*587.2434*
r=0.5	*Inner boundaries*	*x1+ γ2r*	*-851.9326*	*-703.8652*	*-555.7978*
		x2+ γ1r	*85.5978*	*171.1956*	*256.7934*
	Outer boundaries	*x1+ γ1r*	*-914.4022*	*-828.8044*	*-743.2066*
		x2+ γ2r	*148.0674*	*296.1348*	*444.2022*

These boundaries are illustrated as vertical lines in the diagram of Figure 6. 24

5. Truncate the impulse response to the general boundaries given in Table 6. 7

$$\zeta_r(x,\Delta t) = \begin{cases} \zeta(t,\Delta x) & \gamma_{1r} < x < \gamma_{2r} \\ 0 & otherwize \end{cases}$$

6. The wave prediction is given by:

$$\eta'(kx,\Delta t) = \sum_i \eta(i\delta x,\Delta t)\ \zeta_r\big((k-i)\delta x,\Delta t\big)$$

Where $\left[\frac{x_1}{\delta x}\right] < i < \left[\frac{x_2}{\delta x}\right]$

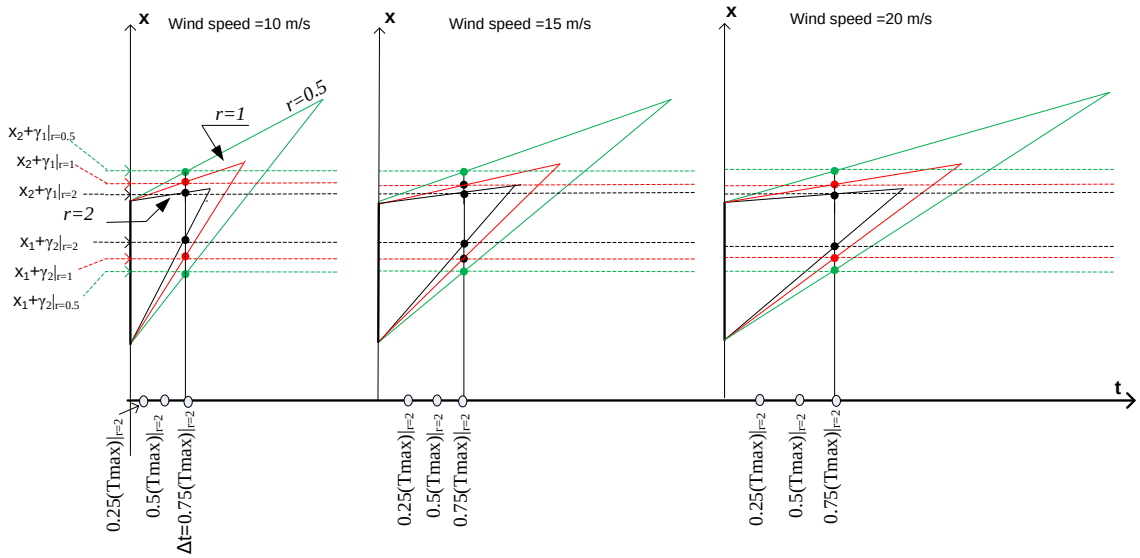

Figure 6. 24: Diagram of prediction results using truncation impulse response-Fixed Time mode

An example of the prediction using this method is given in Figure 6. 25. In this case the wave is a Pierson Moskowitz wave with wind speed U=15. m.s^{-1} The prediction results of using different lengths of the impulse response are show colour coded as explained above. The prediction results of using the larger value of *r* -the black plots in the first column- gave as expected the more accurate prediction. The inner and outer boundaries given in Table 6. 8 are illustrated as vertical lines, the inner boundaries are shown in the lower part of the plot, and the outer boundaries are shown in the upper part of the plot. The prediction region defined by the two lower vertical lines increases in length for smaller values of *r*. Also clear in the given example the relation between the prediction region and the prediction point. For a given *r* value the further away from the measuring point, the smaller the region becomes.

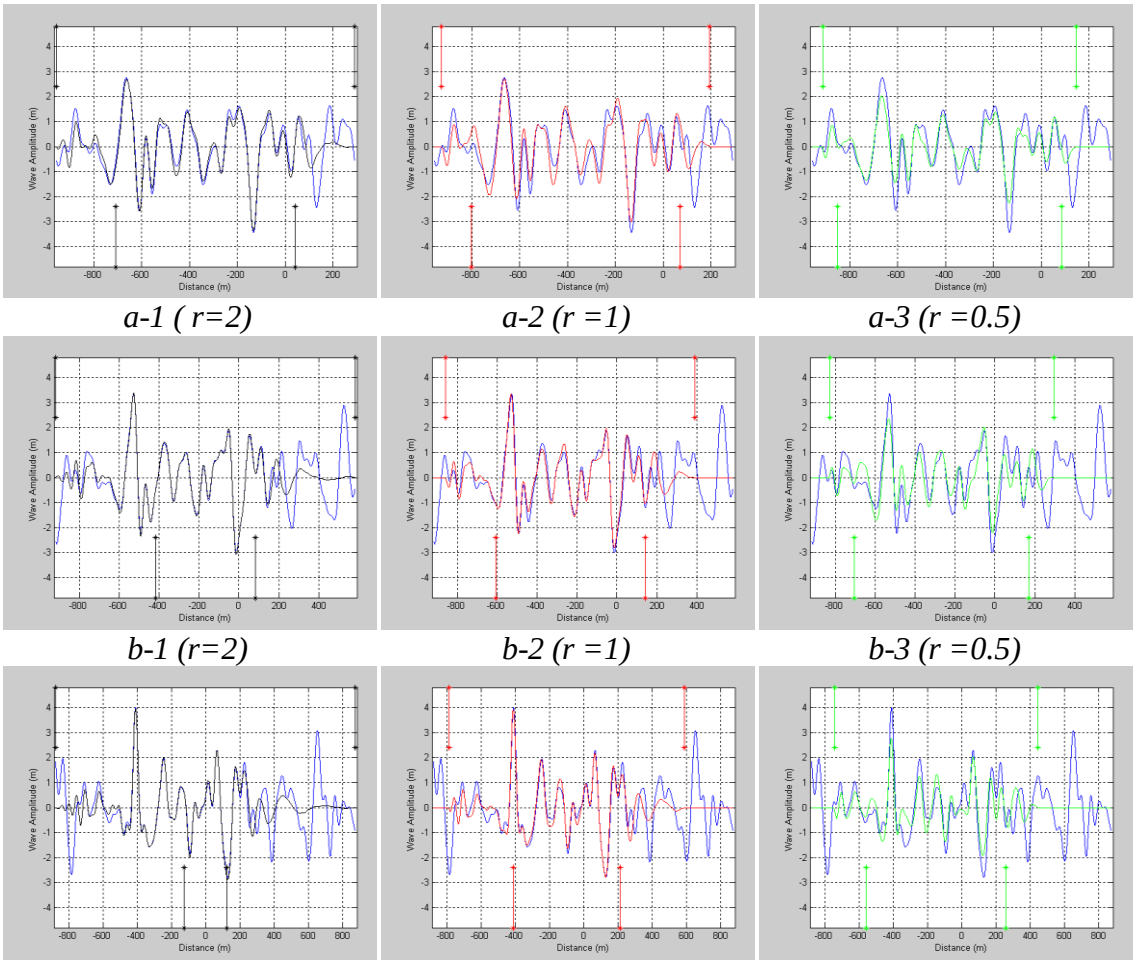

a-1 (r=2) *a-2 (r =1)* *a-3 (r =0.5)*

b-1 (r=2) *b-2 (r =1)* *b-3 (r =0.5)*

c-1 (r=2) *c-2 (r =1)* *c-3 (r = 0.5)*

------- *wave model ,* ------- *wave prediction using r=2 ,*
------- *wave prediction using r=1 ,* ------- *wave prediction using r=0.5*
Upper vertical lines$(t_1+\tau_{r1})(t_2+\tau_{r2})$*,Lower vertical lines* $(t_1+\tau_{r2})$ $(t_2+\tau_{r1})$

Figure 6. 25: Fixed Time wave model and wave prediction for Pierson Moskowitz of wind speed U=15 ms^{-1} using different length truncated impulse response
a) $\Delta t=0.25(Tmax)_{r=2}=18.4$ *(s)b)* $\Delta t=0.5(Tmax)_{r=2}=36.8$ *(s) (m),*
c) $\Delta t=0.75(Tmax)_{r=2}=55.2$ *(s)*

As was in the case of the Fixed Point mode, also in this mode a comprehensive testing of this prediction method is carried out. The maximum prediction error is found for (1000) runs for different impulse response length (r = 2,1,0.5), different prediction positions Δx=(0.25(Xmax)r=2, 0.5(Xmax)r=2, 0.75(Xmax)r=2), and different wave conditions U=(10 m.sec^{-1} , 15 m.sec^{-1} , 20 m.sec^{-1}). These error surface cross sections are shown in Figure 6. 26 using the same colour scheme used previously. As expected, in all the given cases the errors associated with the larger value of r is smaller than that of the smaller value of r. These error values also hold for the duration defined by their respective prediction boundaries show on the plot as the vertical lines colour coded to match. The gradual increase in the prediction error between the inner and outer boundaries is expected. However the value of the error surface associated with a particular value r changes for different prediction conditions.

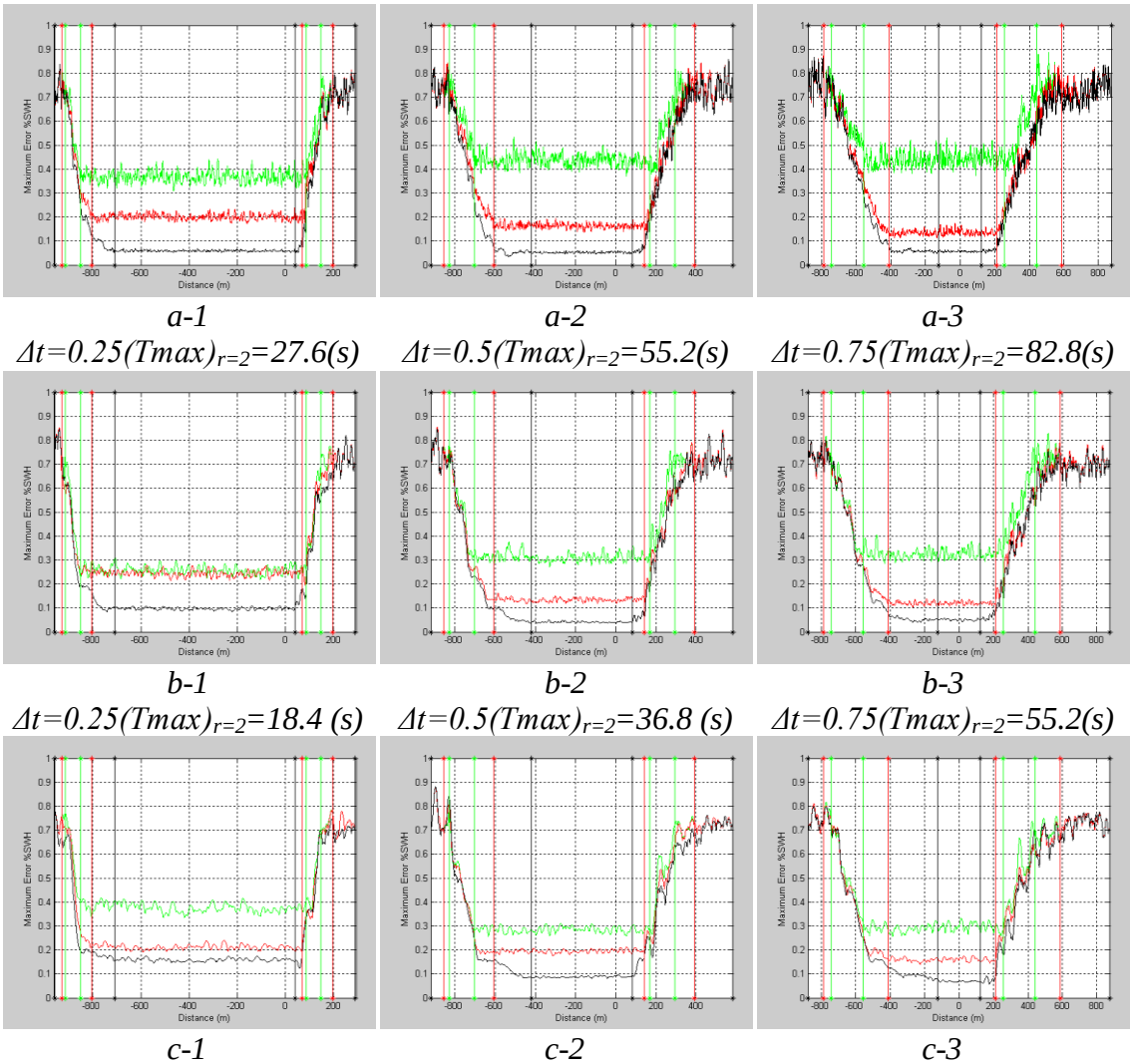

a-1 *a-2* *a-3*

$\Delta t=0.25(Tmax)_{r=2}=27.6(s)$ $\Delta t=0.5(Tmax)_{r=2}=55.2(s)$ $\Delta t=0.75(Tmax)_{r=2}=82.8(s)$

b-1 *b-2* *b-3*

$\Delta t=0.25(Tmax)_{r=2}=18.4\ (s)$ $\Delta t=0.5(Tmax)_{r=2}=36.8\ (s)$ $\Delta t=0.75(Tmax)_{r=2}=55.2(s)$

c-1 *c-2* *c-3*

$\Delta t=0.25(Tmax)_{r=2}=13.8(s)$ $\Delta t=0.5(Tmax)_{r=2}=27.6(s)$ $\Delta t=0.5(Tmax)_{r=2}=41.4\ (s)$

----- *r=2* ,----- *r=1* ,----- *r=0.5 Vertical lines show the prediction region boundaries*

Figure 6. 26: Prediction error surface cross section for Pierson-Mosskowitz sea with a)Wind speed U=10ms^{-1} ,b) Wind speed U=15ms^{-1} ,c) Wind speed U=20ms^{-1}

Chapter 7

Conclusion and future work

In this thesis different aspects of DSWP have been studied. Both pre-prediction and prediction procedures were explored. A range of new methods were developed and tested to improve the quality of deterministic wave prediction. The research objectives of this work were stated as:

- To investigate problem associated with shallow angle LIDAR data specially the shadow region and non-uniformity.
- To examine the performance of different spectrum domain prediction methods.
- To explore the time/space domain approach of wave.

The work described in this thesis has addressed each of the research objectives. Chapter 3 has investigated the characteristics of wave data acquired by the shallow angle LIDAR system. The shadow region properties for different wave conditions were shown to depend mainly on the laser position. This interesting empirical finding was also true for the average reconstruction error associated with varying wave conditions.

Another part of this investigation considers the problem of reconstructing the wave from nonuniform samples. Unsatisfactory reconstruction results were obtained using the nonlinear filtering method also known as (Time-Varying method). This is mainly due to large gaps in the data set resulting from wave shadowing. On the other hand, more promising wave construction was achieved via iterative methods.

Different versions of the alternating domain method were designed to include additional information specified by the problem in hand. It was shown that adding the

laser height reconstruction and the propagation dynamic information improved the reconstruction error considerably. The work in this chapter introduces an important base to design the operating scheme of shallow angle LIDAR based DSWP system.

Both *Chapter 4* and *Chapter 5* describe the work toward the second research objective stated above. The spectral domain point of view was introduced and a prediction algorithm for mixed data type wave developed based on the two dimensional spectrum concept. Carrying on the spectral analysis of the DSWP, the relation between the energy leakage introduced by data record limitation and the prediction accuracy was investigated. An improved prediction algorithm based on window expansion was introduced and tested. Comparing this new method with the existing windowing techniques showed it to improve the prediction result considerably. This is because this method reduces the energy leakage without deforming the wave form as in the case of typical window functions. Another advantage of the window expansion method is that the reduction of the energy leakage is not associated with the reduction of the data set as in the case of end matching technique usually used to improve the wave prediction accuracy.

The final part in investigating the spectral domain prediction, defined the different prediction regions of the (Fixed Time mode) for Pierson Moskwitz seas. Two models of the prediction error surface were introduced and compared. These simple surface descriptions were suggested to reduce the parameters required to describe the prediction error region boundaries associated with a certain required accuracy. The image processing method gave an average (30)% better results in estimating the prediction region than these of polynomial fitting method. Identifying the prediction region is an important pre-processing step for the design of a practical DSWP system. The work shown in Chapter 5 produced a simple method for determining the boundaries of the prediction region for the Fixed Time mode. Although these regions were estimated based on numerical methods using Pierson Moskwitz seas, the same methodology can be used for different sea models.

The final research objective of this work was addressed in Chapter 6. The prediction filters' impulse response were studied and prediction in the Time/Spatial domain was explored. Two parameters were identified to help describe the impulse response characteristics. Both the Polygonal Approximation and the Non-symmetric System Analysis were implemented to qualify the response parameters.

A new technique associating the prediction region accuracy with prediction filter's properties was introduced. This technique was tested using prediction error surfaces of the window expansion frequency domain method, and it was shown to have on average (0.1)% error factor in defining the prediction regions.

The prediction results using truncated impulse responses were examined. Although the prediction results obtained by using Time/Spatial domain filtering method were worse than the results of the typical spectral domain methods, nevertheless the work described in Chapter 6 gave a serious insight into the prediction processes for both the Fixed Point mode and the Fixed Time mode. Introducing the prediction process from the conjugate domain provides a wider field for developing new prediction algorithms and improving the prediction accuracy.

7.1 List of contributions

- Extending the Papoulis and Gerchberg method to include both the laser height restriction on the maximum wave elevation and dynamic wave propagation information. These modified versions of the iterative method have been shown to provide very useful data recovery techniques in wave shadowing situations.

- The basic spectral domain prediction method has been shown to be capable of significant improvement using the iterative window expansion method.

- Significant progress has been made in linking the simple space-time prediction region diagrams to the actual prediction accuracy estimations. It has been shown that the prediction region increases with the reduction of the maximum prediction accuracy requirement. A normalized model of the boundaries of the prediction region for a Pierson Moskowitz sea has been developed.

- The prediction filter's Time/Spatial domain impulse responses have been successfully introduced. Certain filter's properties were identified using both the Polygonal Approximation method and the Unsymmetrical system analysis. The relation between the filters' properties and the prediction region boundaries have been quantified for both the Fixed Point and Fixed Time modes.

- A better understanding of the prediction process from both the spectral domain and the Time /Spatial domain has been represented; this gives a greater opportunity for the development of new algorithms better suited for the prediction problem.

- Overall DSWP has been moved significantly closer to becoming a practically viable methodology, this is due to: the ability to sensibly identify the quantitative predictions that are possible for given sea conditions, and secondly the development of new and improved algorithms that consider the problems associated with different aspects of the DSWP process.

7.2 Future work

The work presented in this thesis considers deep water swells, which are characterized by linear unidirectional waves. The obvious extension of this work is to cover more types of waves, to include different depth conditions, and to address the multi directional case.

Many of the algorithms developed in this work such as the Window Extension method -in Chapter 3- and the prediction region boundaries modelling-in Chapter 5- are rather ad hoc. Further analysis work is required to justify experimental results.

The following part of this section addresses some suggestions for future work and potential directions:

- Multi directional sea

The discussion presented in this thesis involved only unidirectional waves. This covers the one remote storm case, or when there is a clear dominant storm direction that other smaller waves are ignored. However in the multi storm case of a more complicated representation of the sea is required.

Usually there are few dominant wave directions that represent remote storms, as shown in the Figure 7.1. If these directions are determined then the wave at any location can be presented as the combination of a number of unidirectional waves.

The linear nature of the problem means that all equations might be extended to matrix form. However the spatial matrices are expected to be Vandermonde matrices and thus rapidly become ill-conditioned as the dimension of the problem increases.

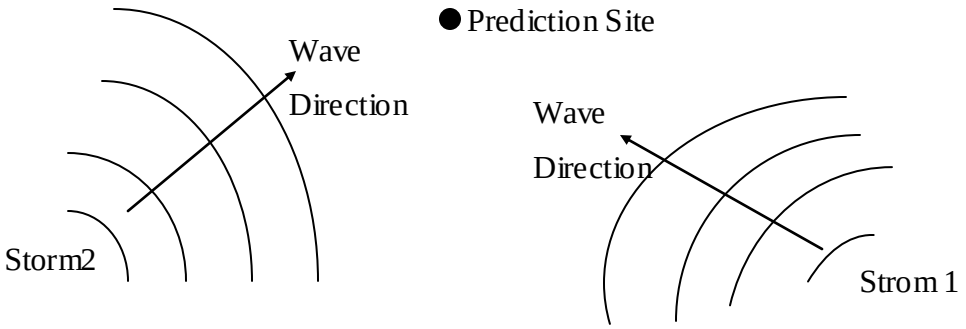

Figure 7.1 Multi Strom Sea

- Shadow region reconstruction

Reconstructing the shadow regions of the sea wave from shallow angle LIDAR data was addressed in Chapter 3. New algorithms were developed to tackle this problem, which involve including the laser beam height as a constraint to the wave height, and adding the wave propagation dynamic information into the reconstructing methods. Integrating these two algorithms into one seems to be a sensible direction to improve the reconstruction performance.

Another direction to improve these algorithms is to extend to use multi snapshots, this is a step further than the two snapshot algorethem presented in Section 3.6.2. However a balance needs to be found between the number of snap-shots used and the time required to reconstruct the wave.

- Non –stationary sea

Another assumption made throughout this work is that the prediction window in both time and space is small enough to assume the sea to be stationary. Finding new methods that improves the prediction quality by including the non-stationary case is another angle where this future work might turn.

There may be some advantages in representing the raw data using the empirical decomposition method. These representations are well suited to non-stationary data which is the case with sea waves.

- Prediction using Mixed data

The optimum operating mode for the shallow angle LIDAR system is with a fixed scan angle, however the data acquired by this mode is mixed space- time data. Unfortunately, it is very complicated to implement the prediction process with such data type.

In Section 4.1.3 the prediction algorithm for a certain type of mixed data was developed, a linear relation between the location of the wave samples and the sampling time was assumed. General case of mixed space- time prediction method still needs developing.

Appendix A : Shadow region parameters distributions

A.1. Shadow region parameters distribution for **Pierson Moskowitz spectrum** with wind speed U=5 m/s

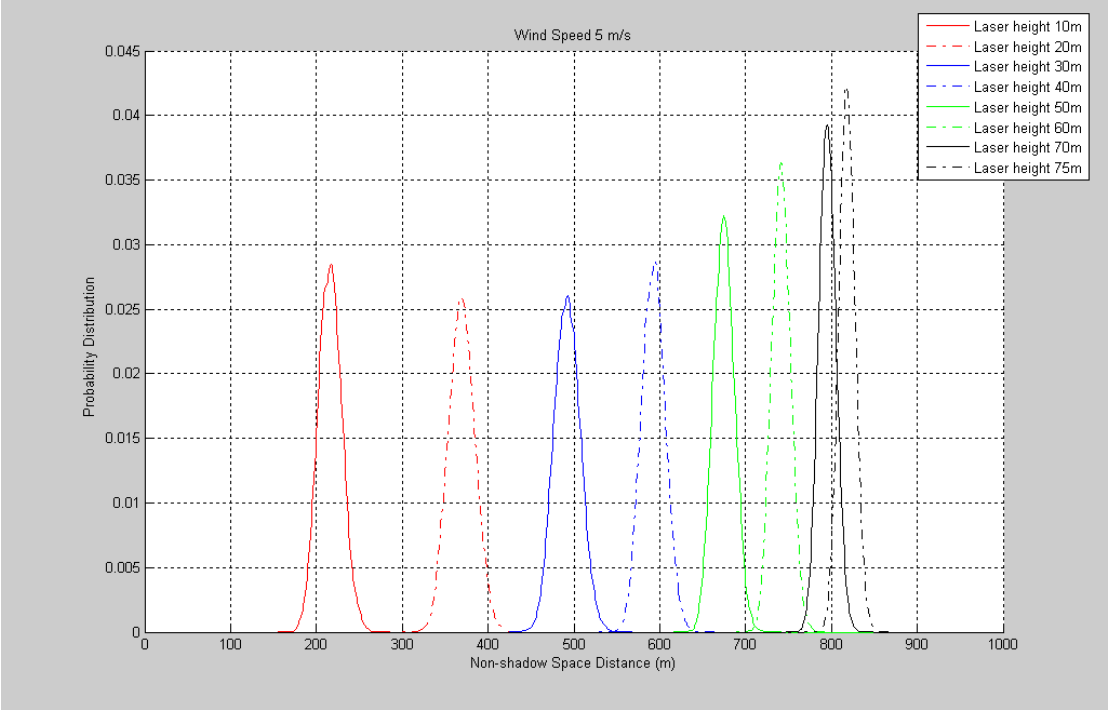

Fig(A.1.a) Non-shadow Space Distance Distribution

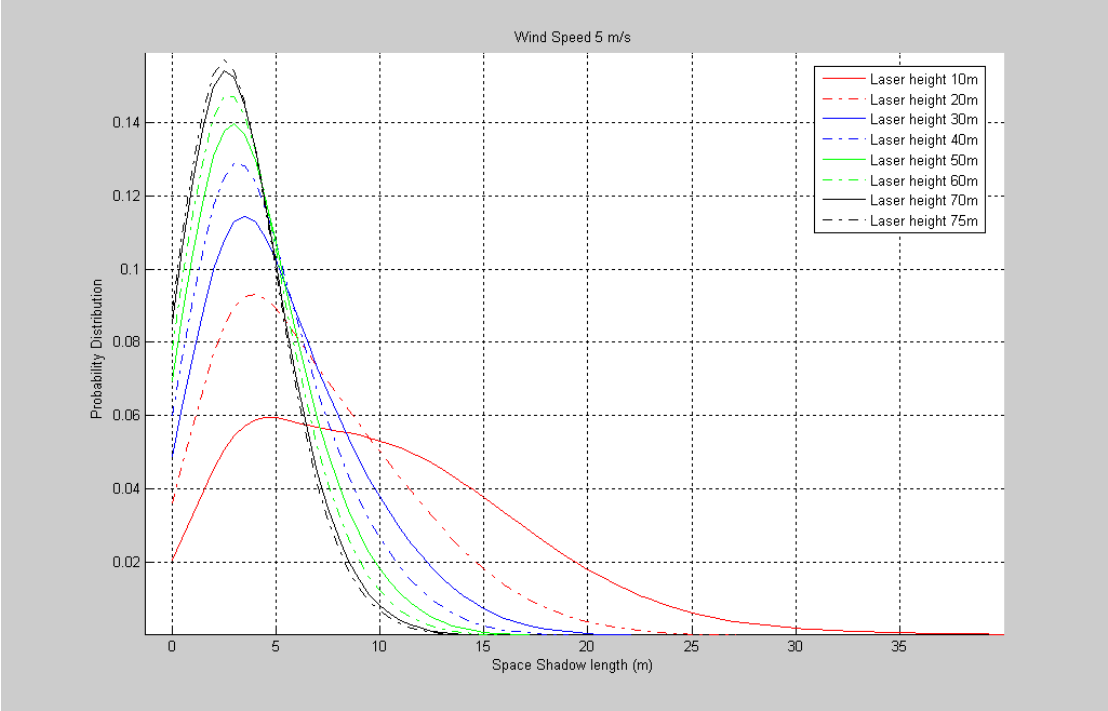

Fig(A.1.b) Space Shadow Length Distribution

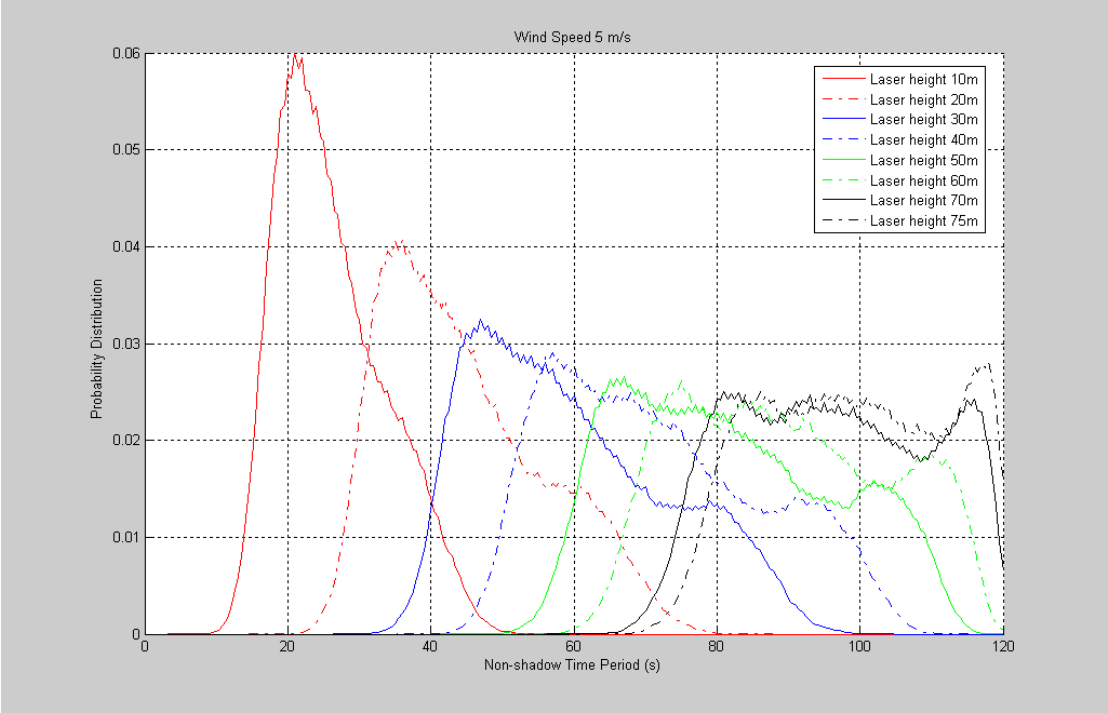

Fig(A.1.c) Non-shadow Time Period Distribution

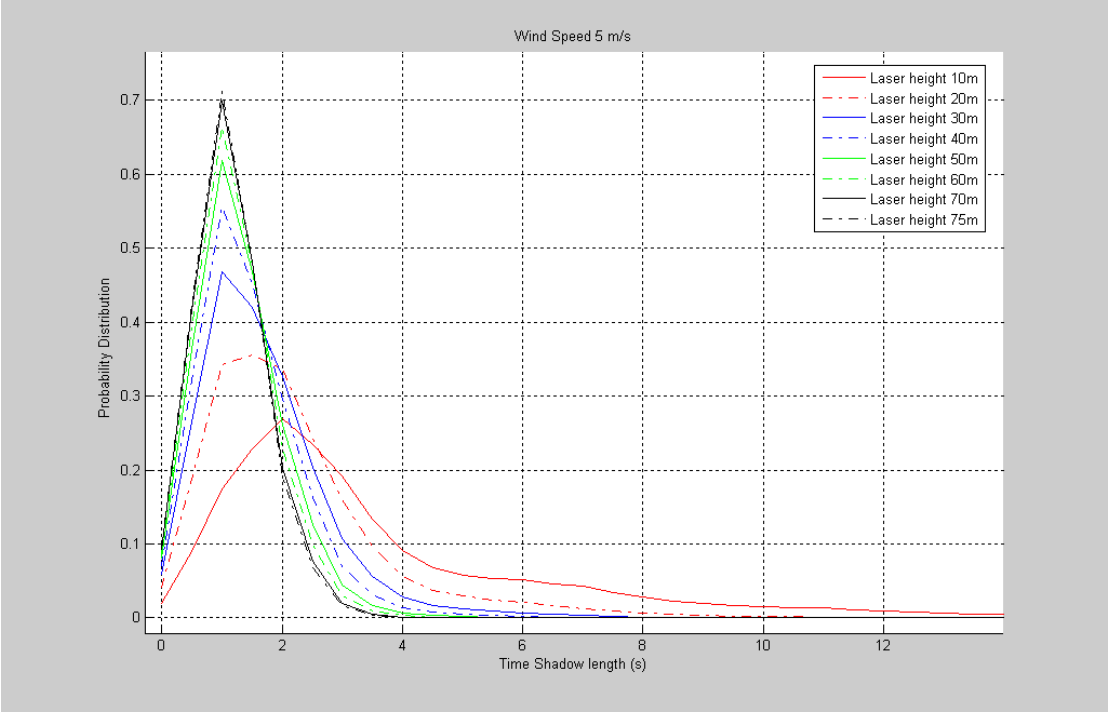

Fig(A.1.d) Time Shadow Length Distribution

A.2. Shadow region parameters distribution for **Pierson Moskowich spectrum** with wind speed U=10 m/s

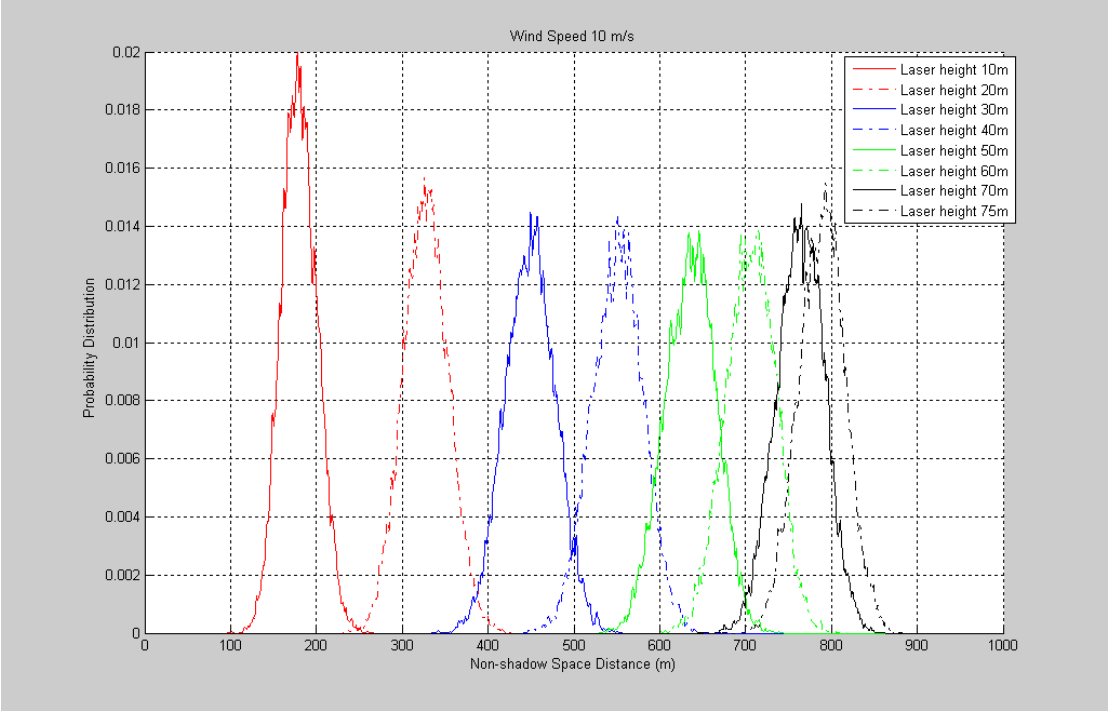

Fig(A.2.a) Non-shadow Space Distance Distribution

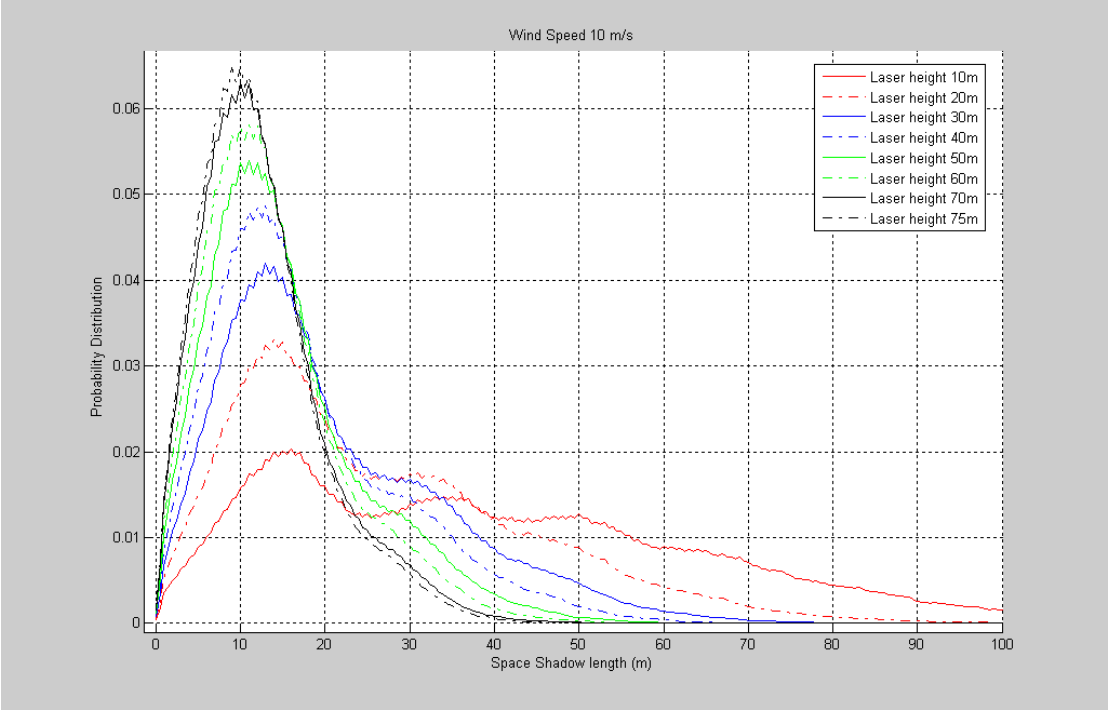

Fig(A.2.b) Space Shadow Length Distribution

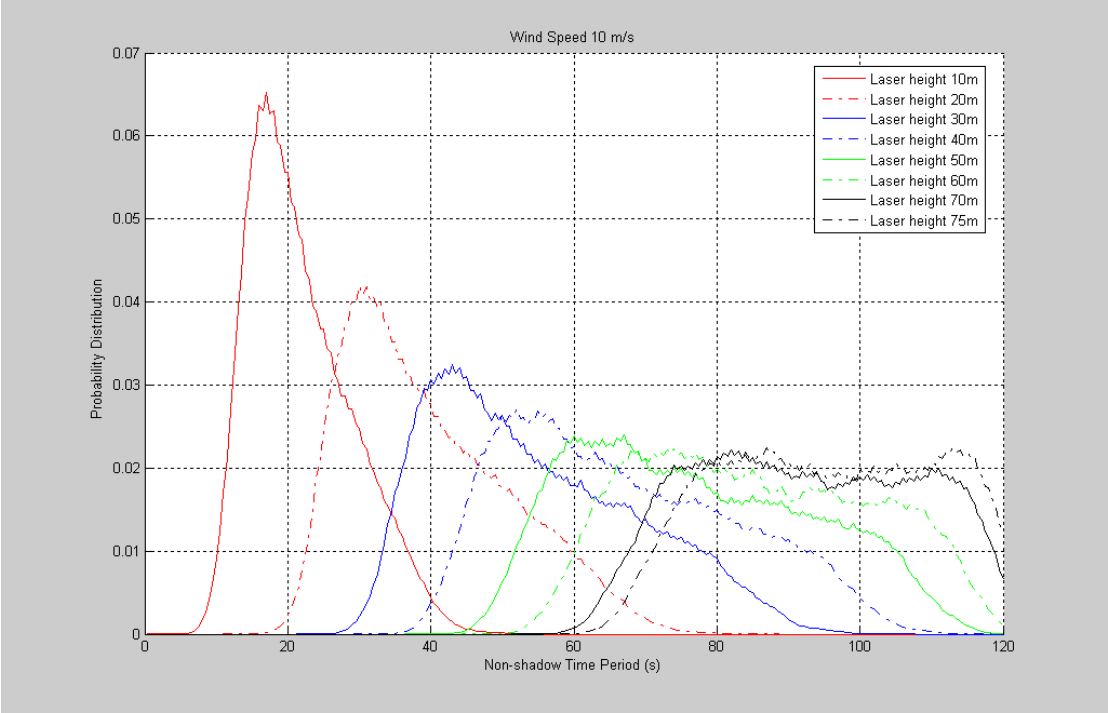

Fig(A.2.c) Non-shadow Time Period Distribution

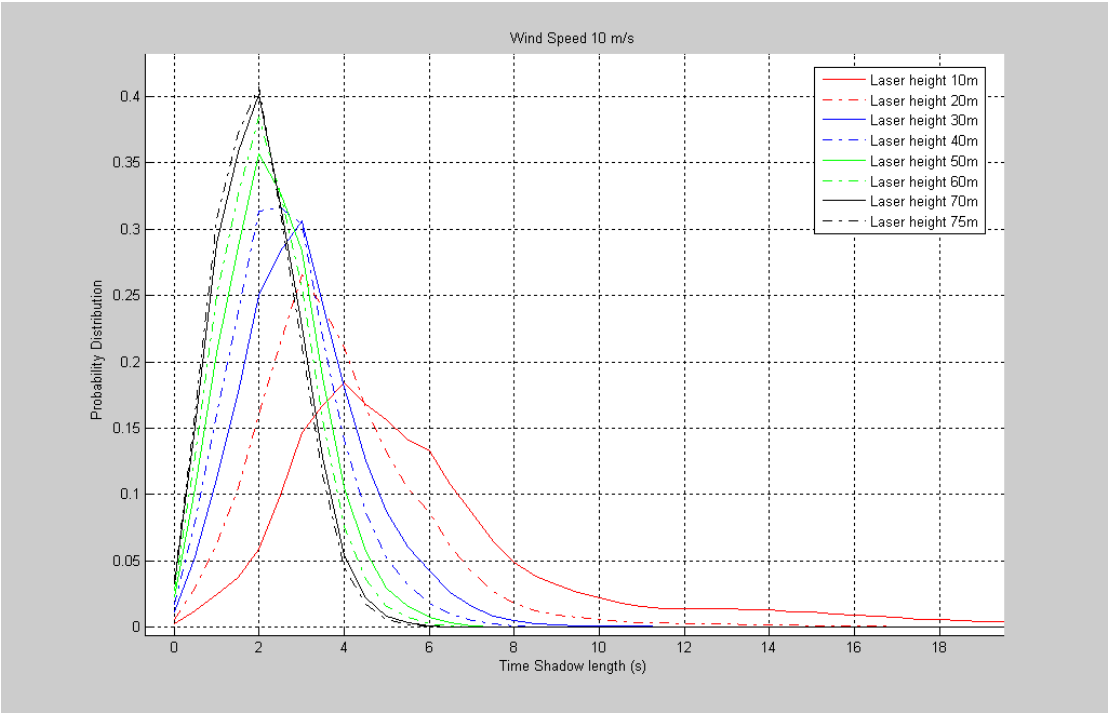

Fig(A.2.d) Time Shadow Length Distribution

A.3. Shadow region p arameters distribution for **Pierson Moskowich spectrum** with wind speed U=15 m/s

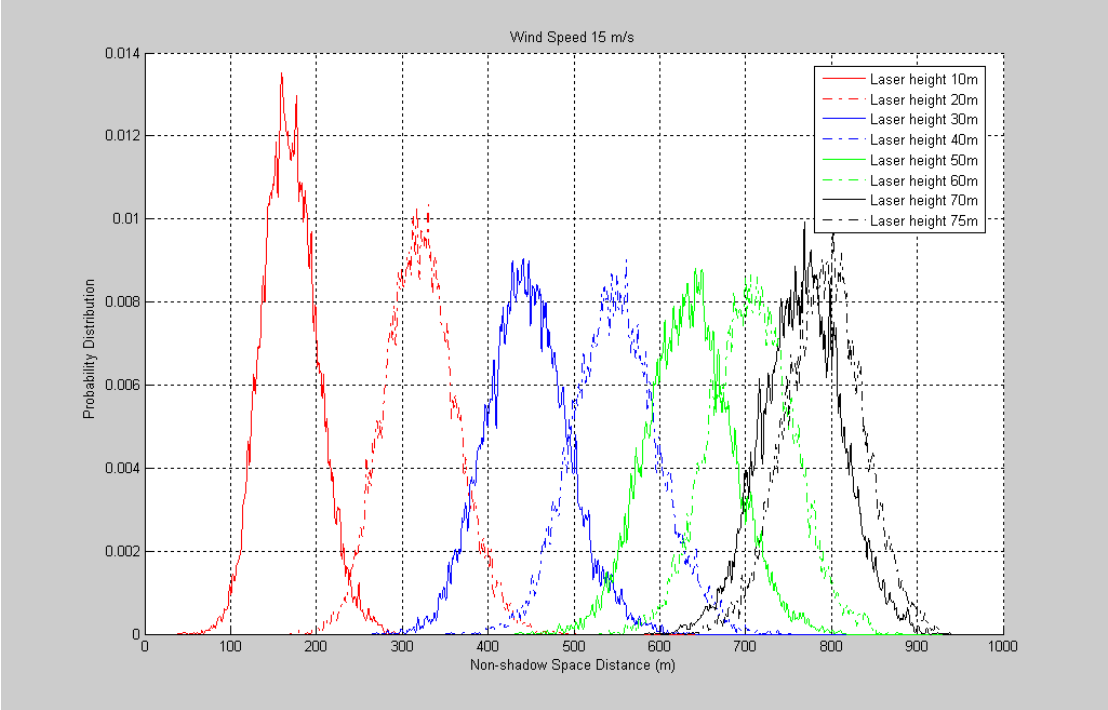

Fig(A.3.a) Non-shadow Space Distance Distribution

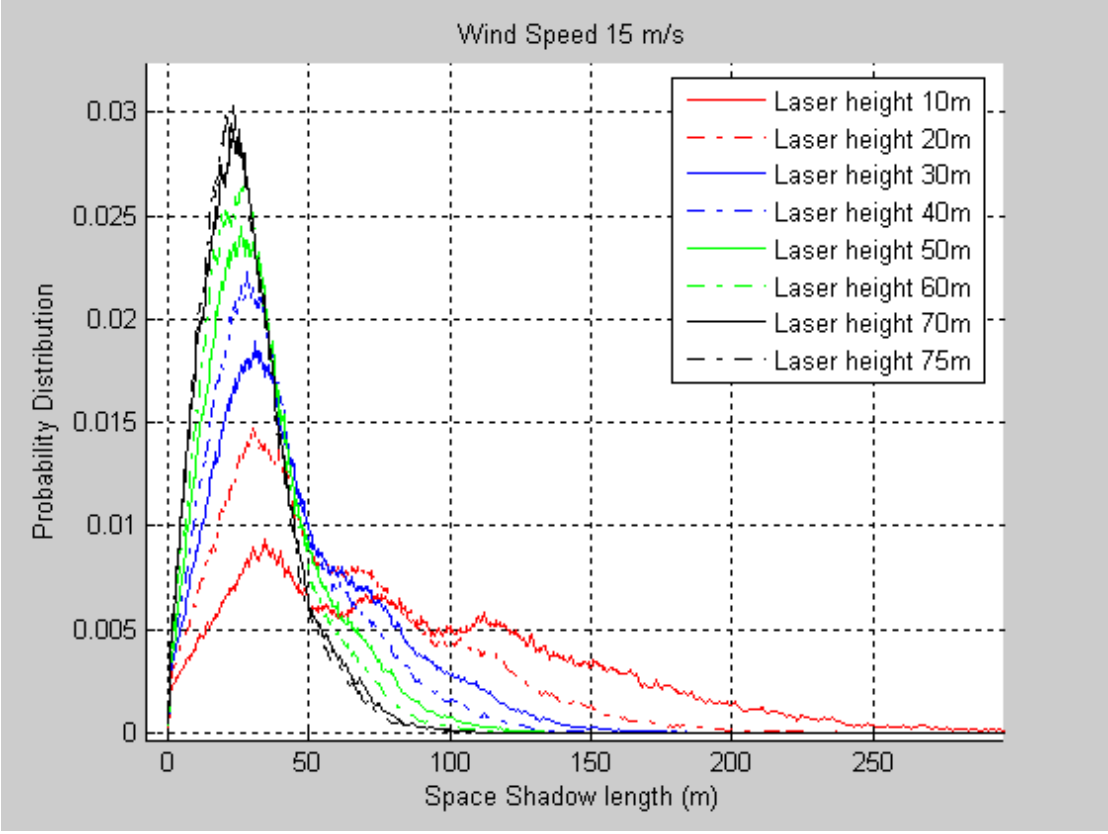

Fig(A.3.b) Space Shadow Length Distribution

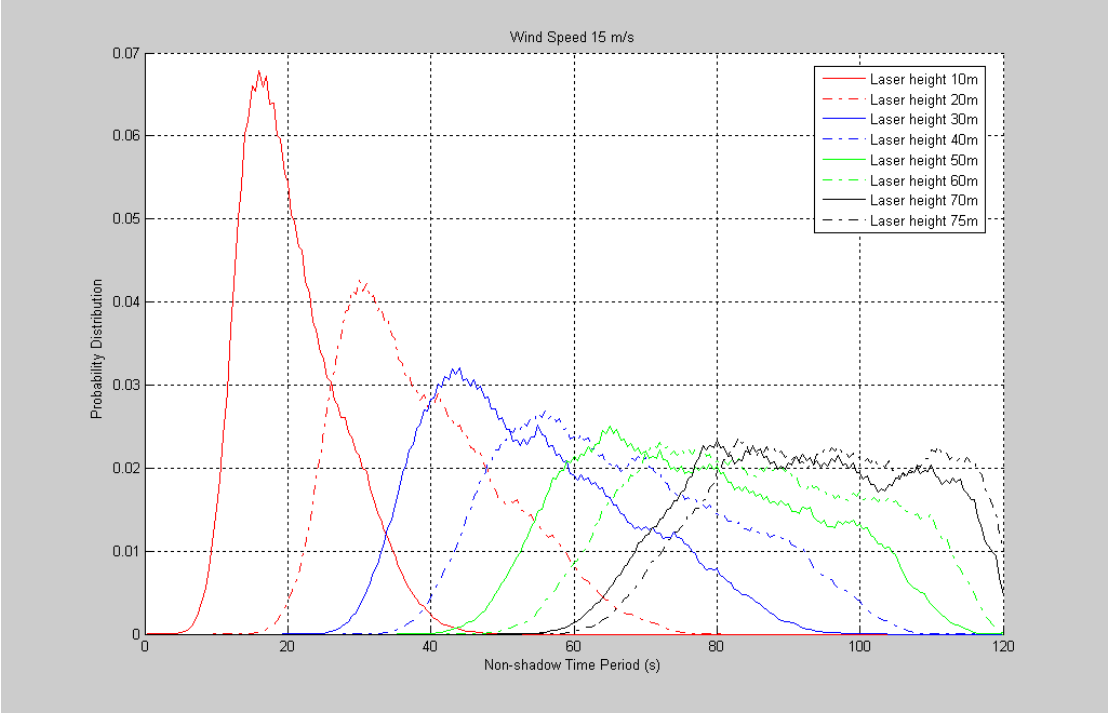

Fig(A.3.c) Non-shadow Time Period Distribution

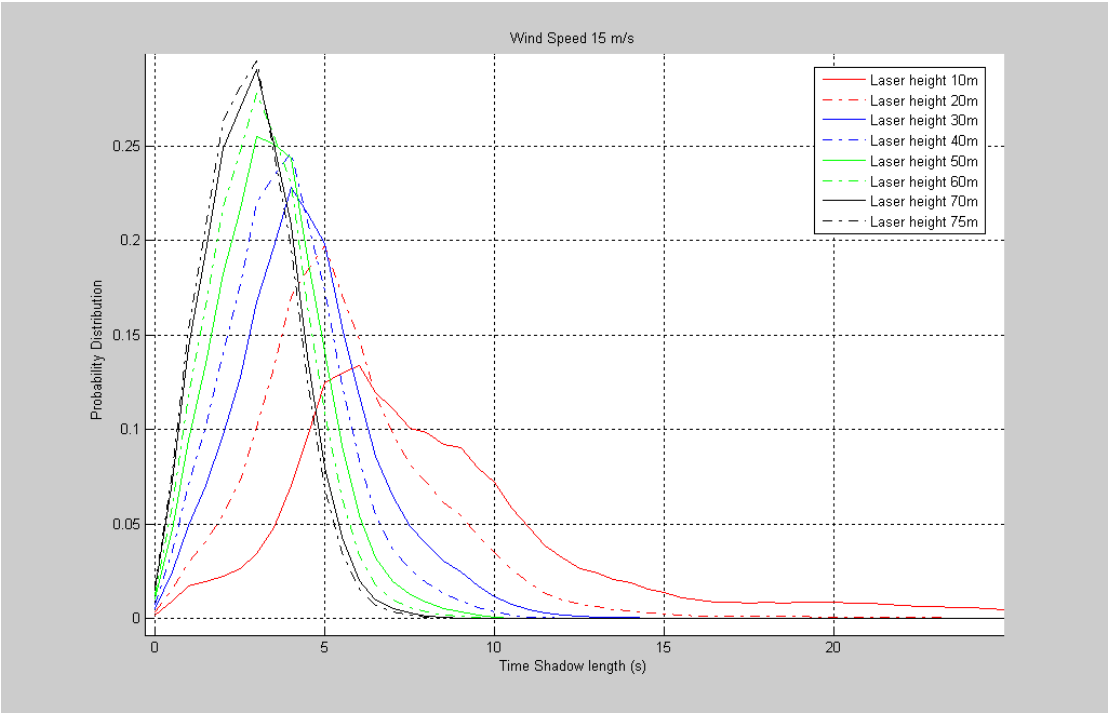

Fig(A.3.d) Time Shadow Length Distribution

A.4. Shadow region parameters distribution for **Pierson Moskowich spectrum** with wind speed U=20 m/s

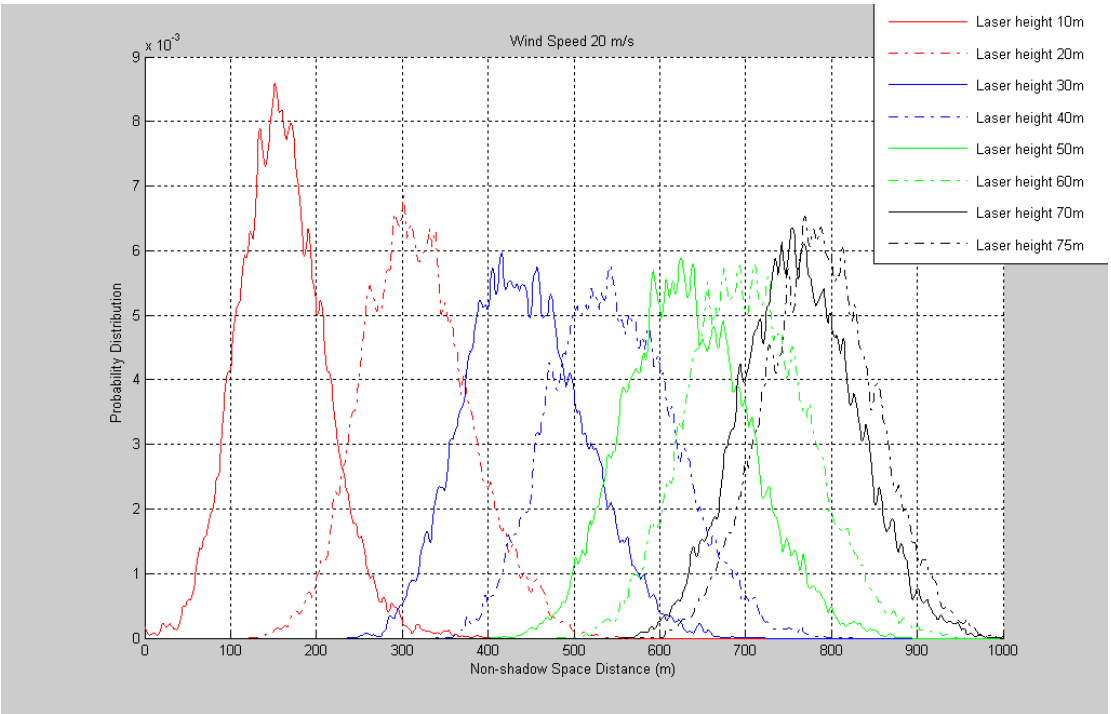

Fig(A.4.a) Non-shadow Space Distance Distribution

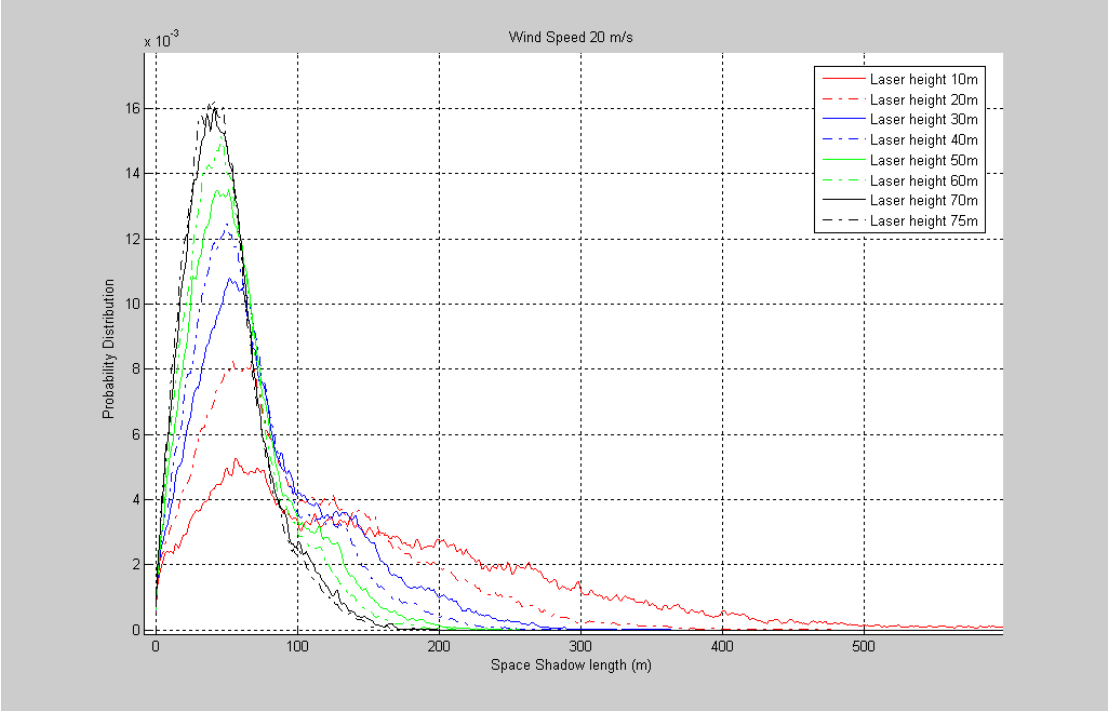

Fig(A.4.b) Space Shadow Length Distribution

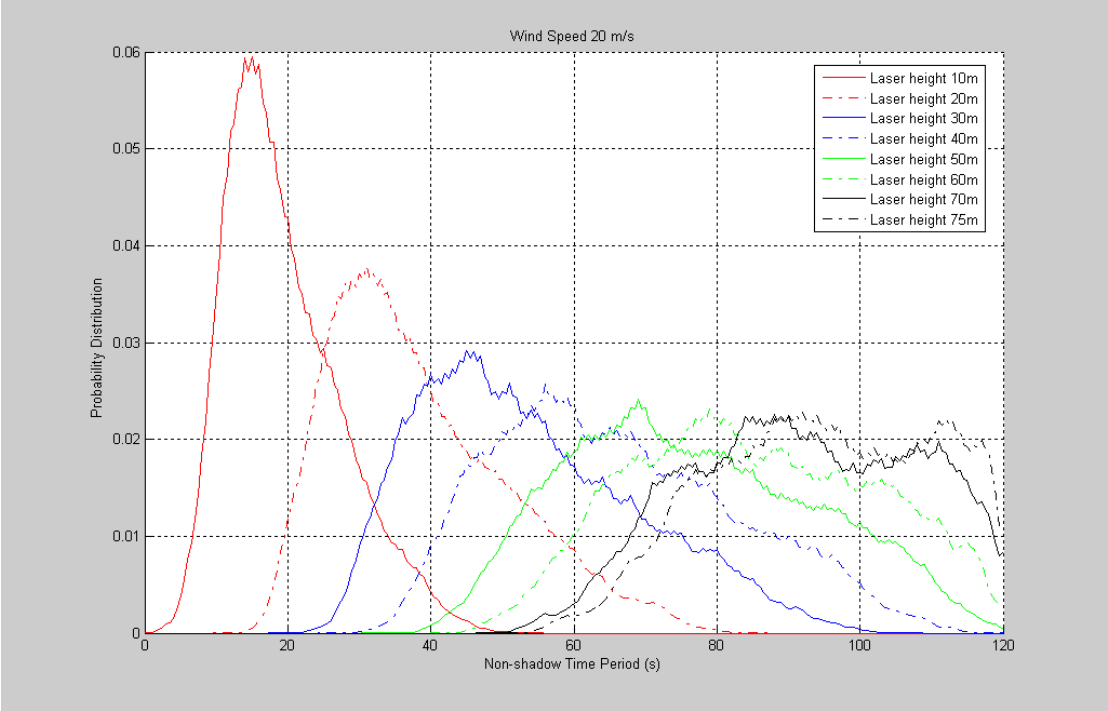

Fig(A.4.c) Non-shadow Time Period Distribution

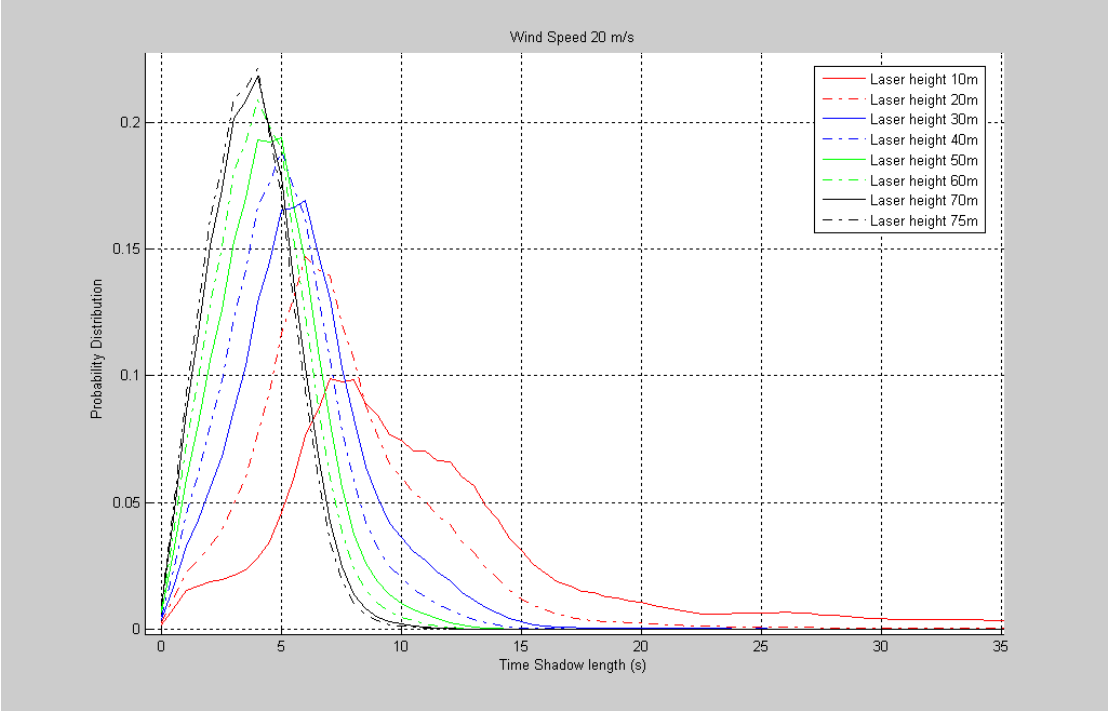

Fig(A.4.d) Time Shadow Length Distribution

A.5. Shadow region parameters distribution for **Pierson Moskowitz spectrum** with wind speed U=25 m/s

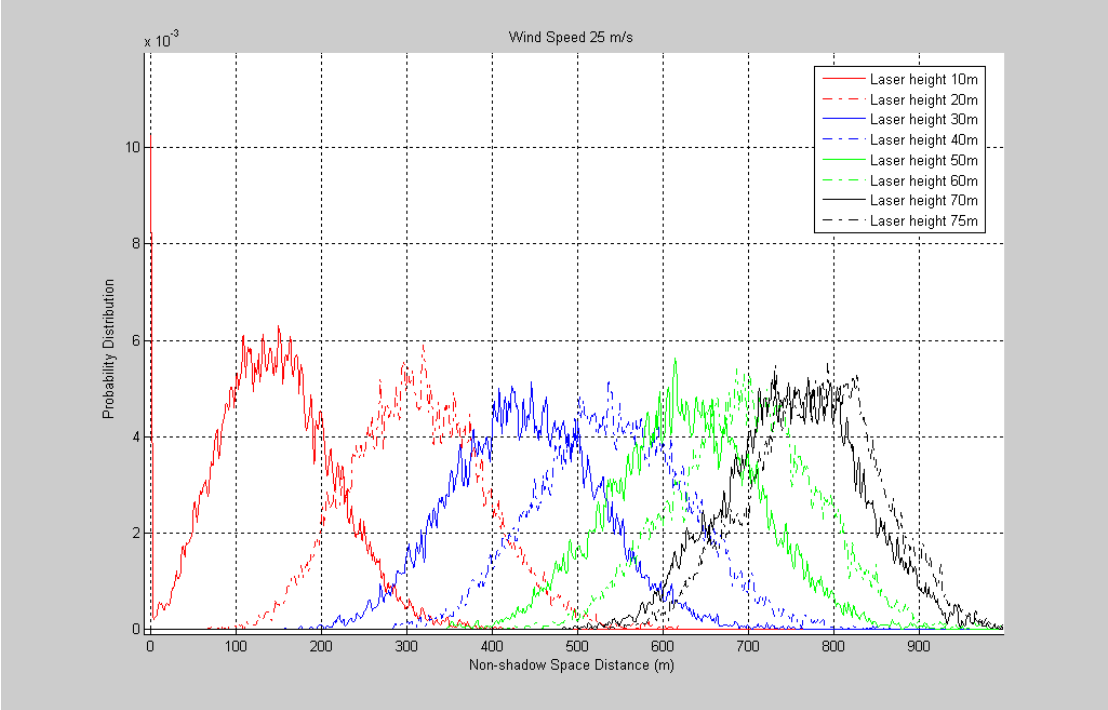

Fig(A.5.a) Non-shadow Space Distance Distribution

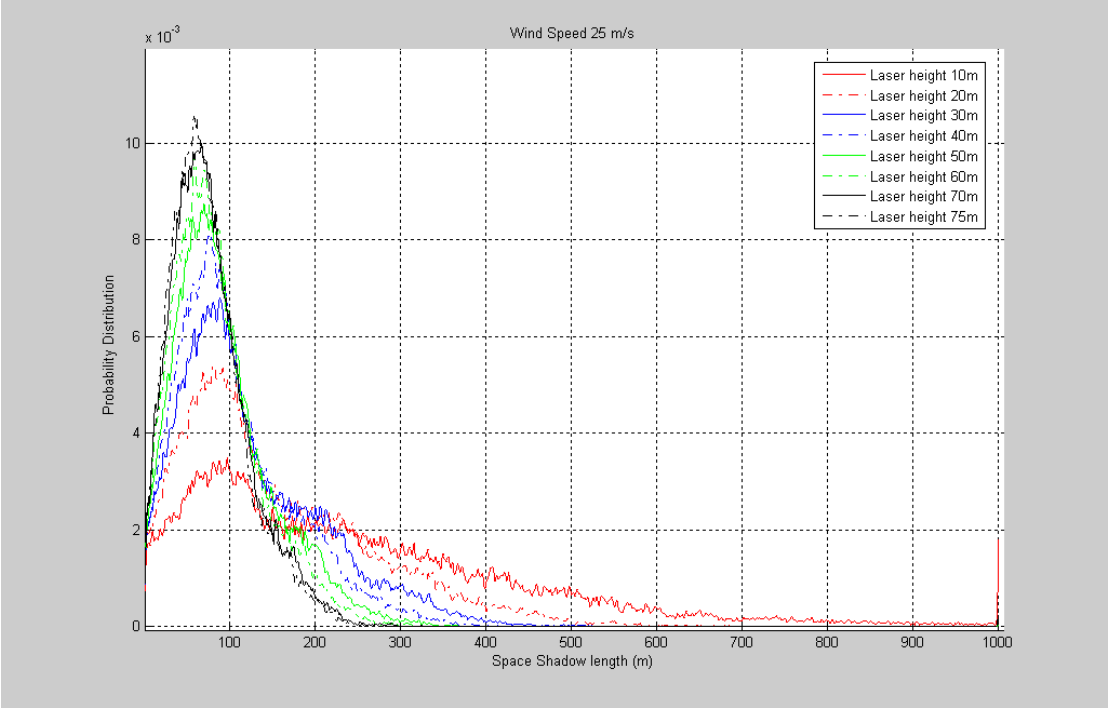

Fig(A.5.b) Space Shadow Length Distribution

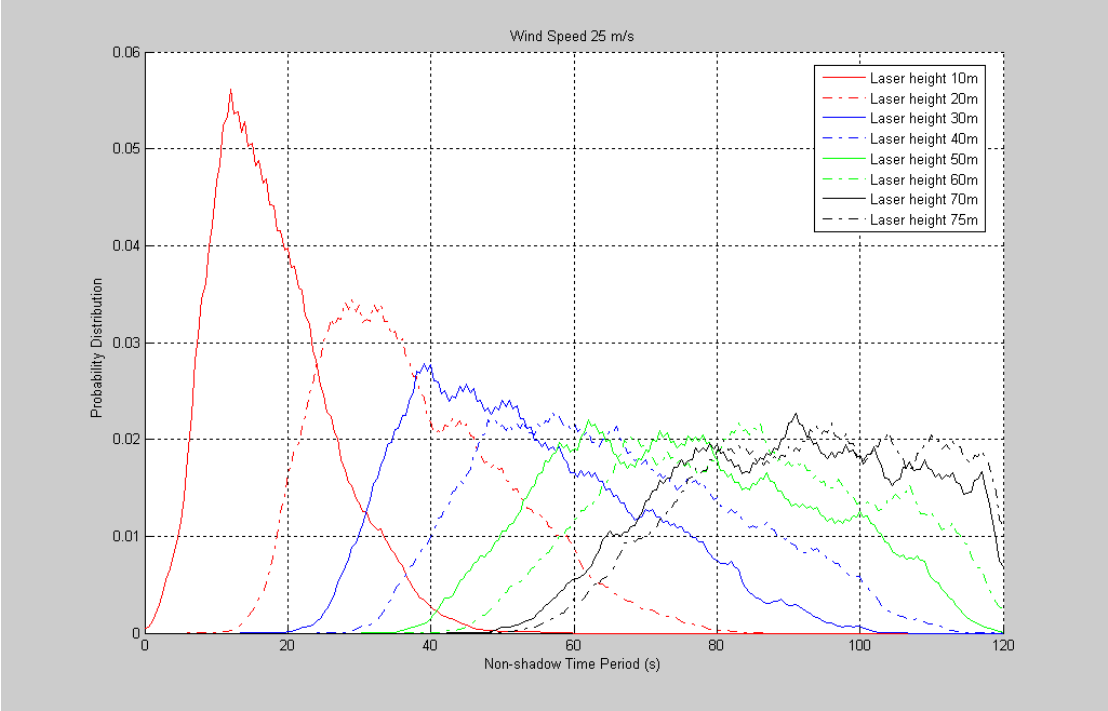

Fig(A.5.c) Non-shadow Time Period Distribution

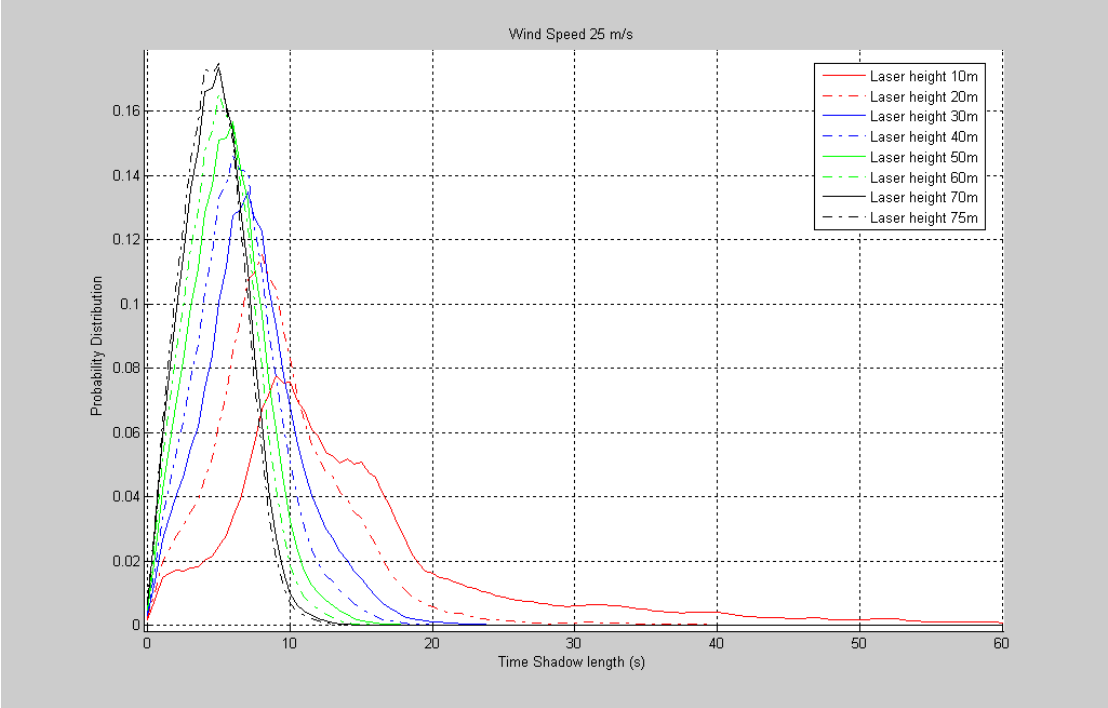

Fig(A.5.d) Time Shadow Length Distribution

A.6. Shadow region parameters distribution for **Pierson Moskowitz spectrum** with wind speed U=35 m/s

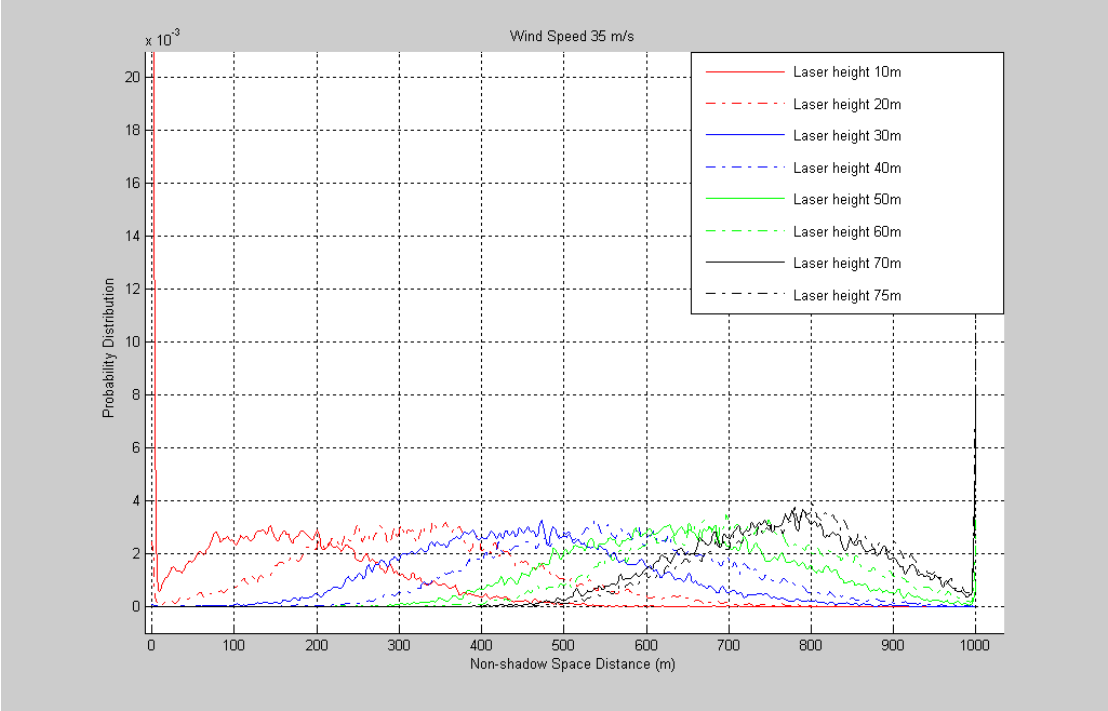

Fig(A.6.a) Non-shadow Space Distance Distribution

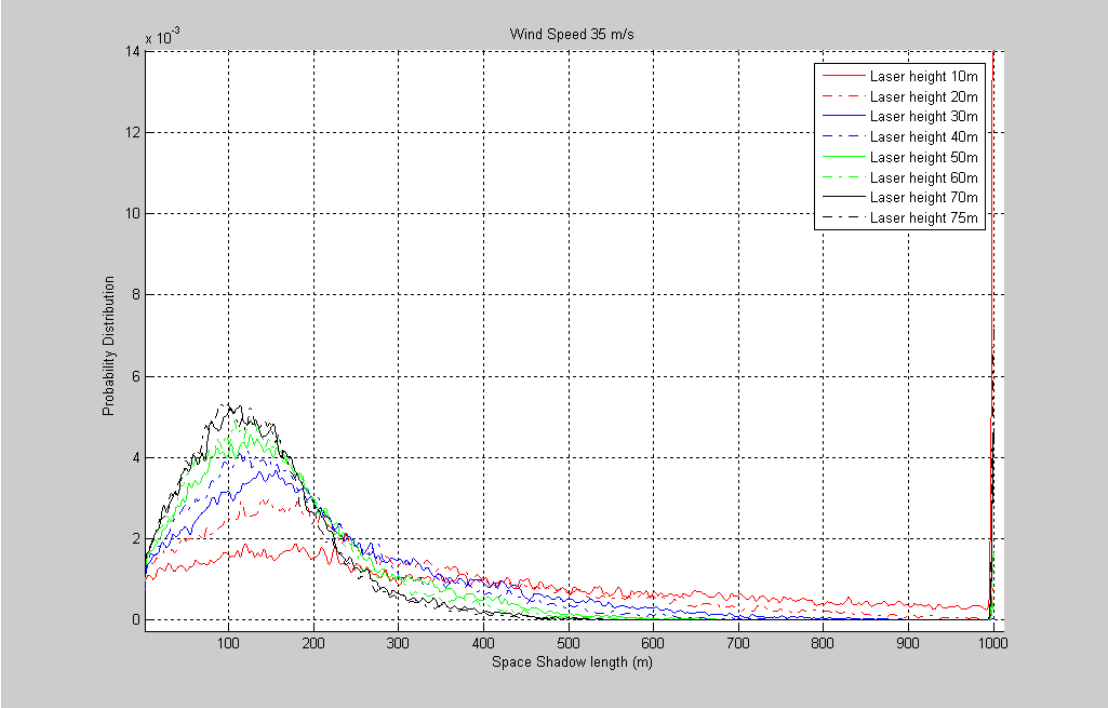

Fig(A.6.b) Space Shadow Length Distribution

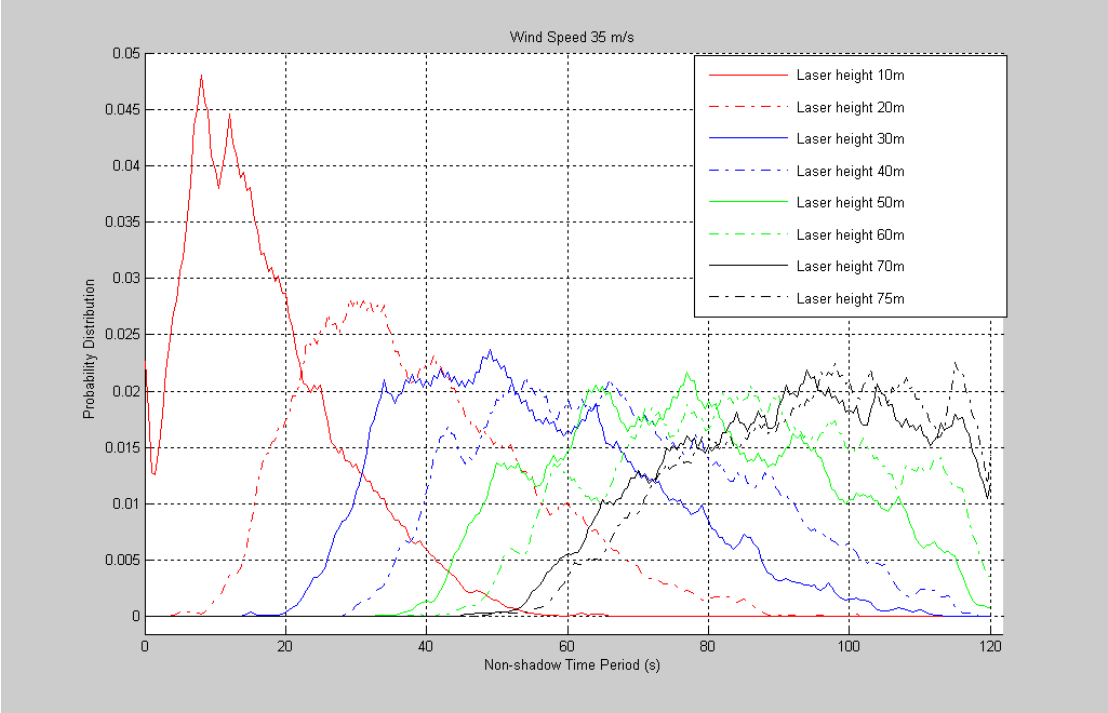

Fig(A.6.c) Non-shadow Time Period Distribution

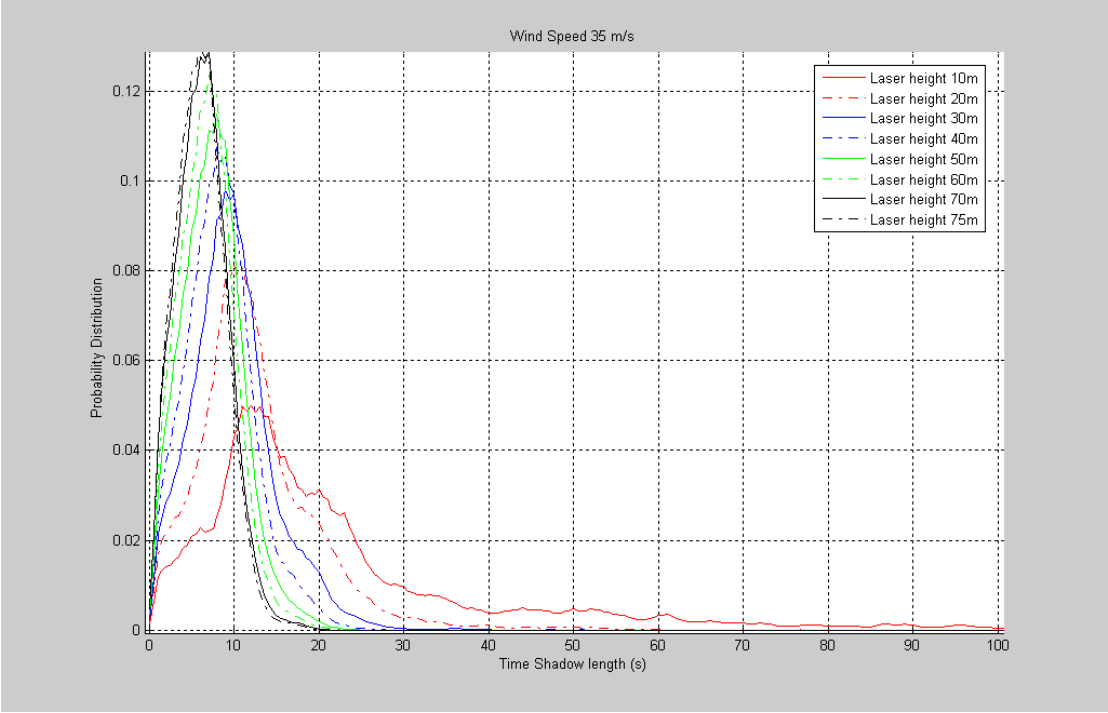

Fig(A.6.d) Time Shadow Length Distribution

Appendix B : User interface Panels

B-1 Shadow region and wave reconstruction

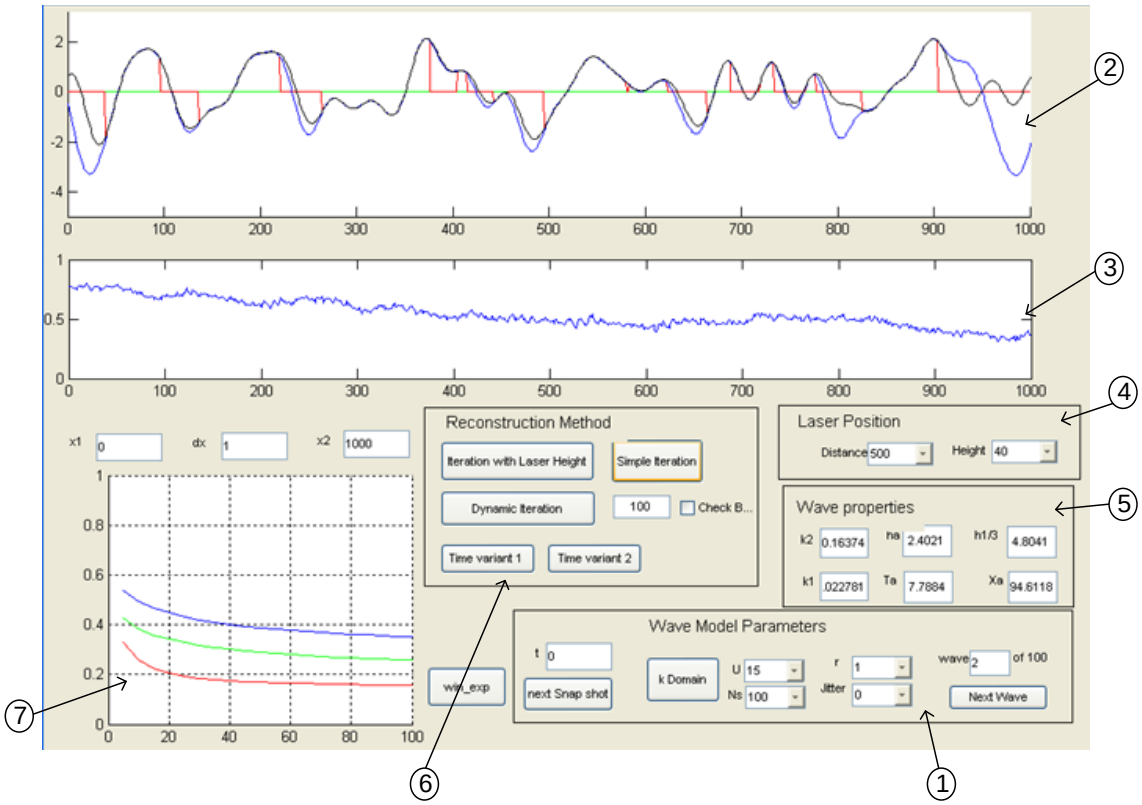

1- Wave Model Parameters
   1- U: Wind speed.
   2- Ns Number of spectrum points
   3- r Random Phase.
   4- Jitter Percentage of Jetter in spectrum samples.
2- Measurement Window
   ---- original Wave Model
   ---- Scanned Region.
   ---- Reconstructed Wave
3- Percentage of Time Availability.
4- Laser Position

Distance: Laser distance from the beginning of measureing region.

Height: Laser height.

5- Wave Properties

K_1: Sceptical lower boundary.

K_2: Sceptical upper boundary.

H_a: Average Wave Height.

$H_{1/3}$: Maximum Wave Height.

T_a: Average Wave Time Period.

X_a: Average Wave length.

6- Reconstruction Method

Sample Iteration: Iteration with Laser Height restriction Iteration with dynamic information.

Check Box: reduce the number of sampling points to given value.

Time Variant: reconstruct wave using Time Variant method with points from all the wave form.

7- Reconstruction Error

---- Sample Iteration.

---- Iteration with Laser height reconstruction.

---- Iteration with dynamic information.

B-2 Wave Predection (Fixed Time mode)

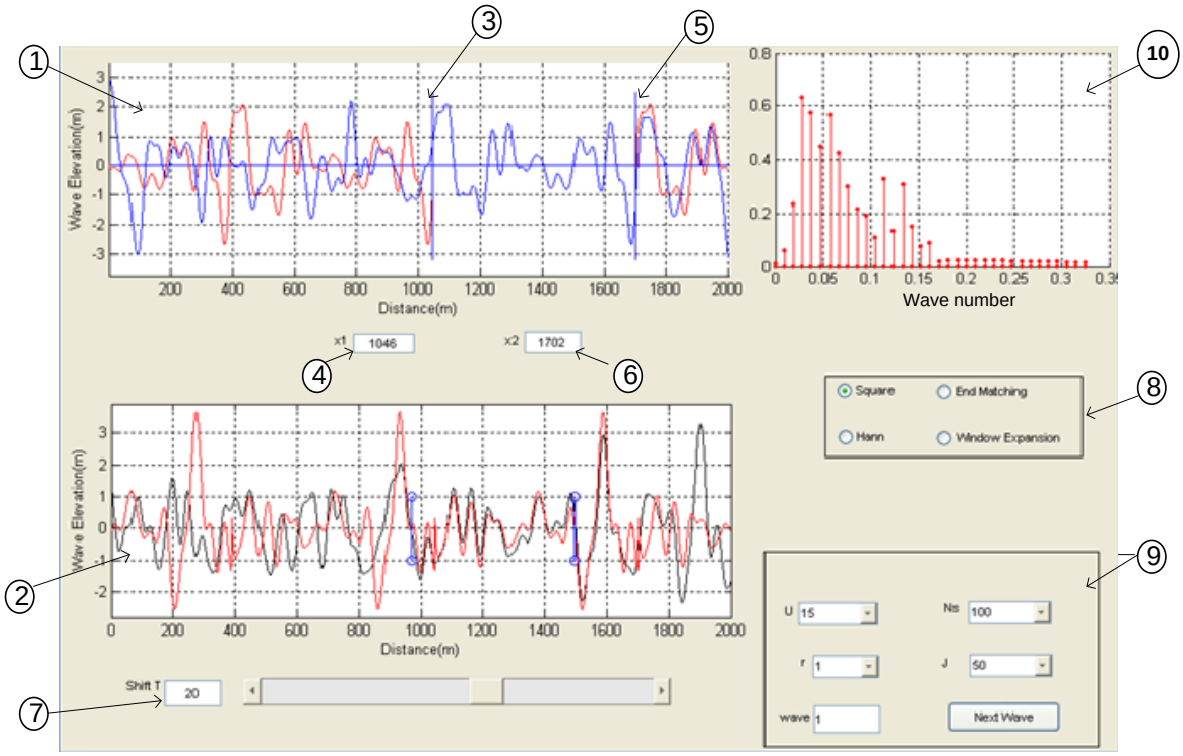

1- Wave Measurement Window
   ---- Original Wave Snapshot
   ---- Prediction Wave Model
2- Wave Propagation Window
   ---- original propagated wave
   ---- Predicted Wave
   ---- Prediction Window
3- Beginning of measurement region.
4- Beginning of measurement region.
5- End of measurement region.
6- End of measurement region.
7- Propagation Time.
8- Windowing Method.
9- Original Wave Model Parameter
   1- Wind speed.
   2- Ns Number of spectrum points
   3- r Random Phase.
   4- J Percentage of Jetter in spectrum points.
10- Prediction Wave Spectrum Model.

Appendix C :Fresnel Integrals

$$S(x) = \int_0^x \sin(t^2)\,dt, \quad C(x) = \int_0^x \cos(t^2)\,dt.$$

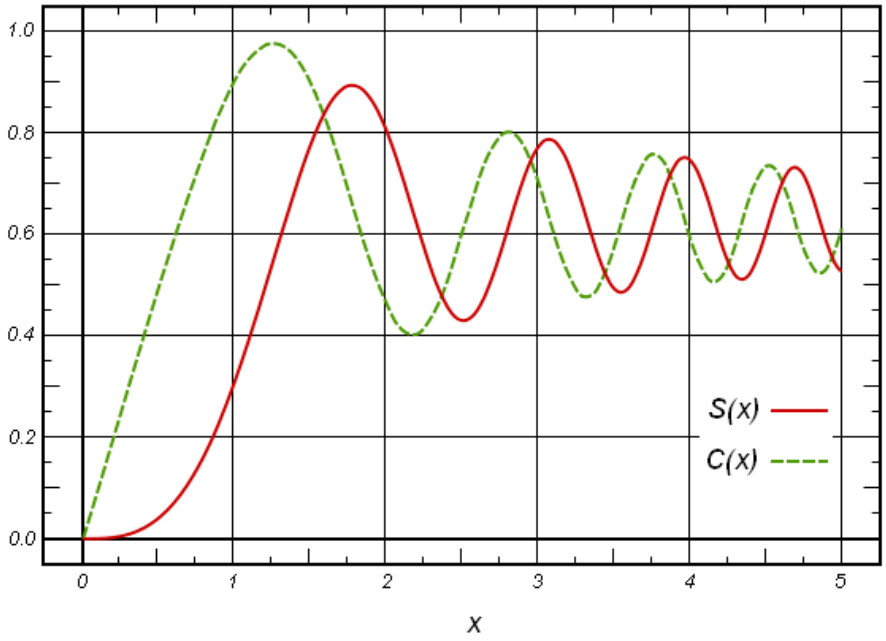

The Fresnel integrals power series expansion converge for all x:

$$S(x) = \int_0^x \sin(t^2)\,dt = \sum_{n=0}^{\infty} (-1)^n \frac{x^{4n+3}}{(4n+3)(2n+1)!},$$
$$C(x) = \int_0^x \cos(t^2)\,dt = \sum_{n=0}^{\infty} (-1)^n \frac{x^{4n+1}}{(4n+1)(2n)!}.$$

Properties

$$S(x) = \frac{\sqrt{\pi}}{4}\left(\sqrt{i}\,\operatorname{erf}(\sqrt{i}\,x) + \sqrt{-i}\,\operatorname{erf}(\sqrt{-i}\,x)\right)$$
$$C(x) = \frac{\sqrt{\pi}}{4}\left(\sqrt{-i}\,\operatorname{erf}(\sqrt{i}\,x) + \sqrt{i}\,\operatorname{erf}(\sqrt{-i}\,x)\right).$$

Appendix D

D-1Unsymmetrical System Fixed Point mode

$$H_a(\omega) = e^{\left(-i \cdot sign(\omega) \cdot \frac{\omega^2}{g}(\Delta x)\right)}$$

Since h_1 has a band width $\omega_o - \Delta\omega < \omega < \omega_o + \Delta\omega$

We can introduce an additional filter H_b

$$H_b = \begin{cases} 1 & \omega_o - \Delta\omega < \omega < \omega_o + \Delta\omega \\ 0 & Otherwize \end{cases}$$

$$H = \begin{cases} e^{\left(-i \cdot \frac{\omega^2}{g}(\Delta x)\right)} & \omega_o - \Delta\omega < \omega < \omega_o + \Delta\omega \\ e^{\left(i \cdot \frac{\omega^2}{g}(\Delta x)\right)} & -\omega_o - \Delta\omega < \omega < -\omega_o + \Delta\omega \\ 0 & Otherwize \end{cases}$$

this is an unsymmetrical band pass filter. we can write $H(\omega)$ as the sum

$H(\omega) = H_1(\omega) + H_2(\omega)$

where

$$H_1(\omega) = e^{\left(-i \cdot \frac{\omega^2}{g}(\Delta x)\right)} \cdot \left[u\left(\omega - \left(\omega_o - \Delta\omega\right)\right) - u\left(\omega - \left(\omega_o + \Delta\omega\right)\right)\right]$$

And

$$H_2(\omega) = e^{\left(i \cdot \frac{\omega^2}{g}(\Delta x)\right)} \cdot \left[u\left(\omega + \left(\omega_o + \Delta\omega\right)\right) - u\left(\omega + \left(\omega_o - \Delta\omega\right)\right)\right]$$

Shifting the two parts

$H_{l1}(\omega) = H_1(\omega + \omega_o)$

$$H_{l1}(\omega) = e^{\left(-i \cdot \frac{(\omega+\omega_o)^2}{g}(\Delta x)\right)} \cdot \left[u\left(\omega + \Delta\omega\right) - u\left(\omega - \Delta\omega\right)\right]$$

And

$H_{l2}(\omega) = H_2(\omega - \omega_o)$

$$H_{l2}(\omega) = e^{\left(i \cdot \frac{(\omega-\omega_o)^2}{g}(\Delta x)\right)} \cdot \left[u\left(\omega + \Delta\omega\right) - u\left(\omega - \Delta\omega\right)\right]$$

The in-pase and quadrature system functions

$$H_p(\omega)=\frac{1}{2}\cdot\left(H_{l2}(\omega)+H_{l1}(\omega)\right)$$

$$H_p(\omega)=\frac{1}{2}\cdot\left(e^{\left(i\cdot\frac{(\omega-\omega_o)^2}{g}(\Delta x)\right)}+e^{\left(-i\cdot\frac{(\omega+\omega_o)^2}{g}(\Delta x)\right)}\right)\cdot\left[u(\omega+\Delta\omega)-u(\omega-\Delta\omega)\right]$$

$$H_q(\omega)=\frac{1}{2i}\cdot\left(H_{l2}(\omega)-H_{l1}(\omega)\right)$$

$$H_q(\omega)=\frac{1}{2i}\cdot\left(e^{\left(i\cdot\frac{(\omega-\omega_o)^2}{g}(\Delta x)\right)}-e^{\left(-i\cdot\frac{(\omega+\omega_o)^2}{g}(\Delta x)\right)}\right)\cdot\left[u(\omega+\Delta\omega)-u(\omega-\Delta\omega)\right]$$

the impulse response

$$h_p(t)=\frac{1}{4\pi}\cdot\int_{-\Delta\omega}^{\Delta\omega}\left(e^{\left(i\cdot\frac{(\omega-\omega_o)^2}{g}(\Delta x)\right)}+e^{\left(-i\cdot\frac{(\omega+\omega_o)^2}{g}(\Delta x)\right)}\right)\cdot e^{i\omega t}d\omega$$

$$h_p(t)=\sqrt{2}\cdot\frac{1}{4\pi}\sqrt{\frac{\pi g}{\Delta x}}\cdot\left[cos\left(t\omega_o-\frac{t^2 g}{4\Delta x}\right)\cdot\left\{C\left(\sqrt{\frac{2}{\pi}}z_1\right)-C\left(\sqrt{\frac{2}{\pi}}z_2\right)\right\}\right.$$

$$\left.-sin\left(t\omega_o-\frac{t^2 g}{4\Delta x}\right)\left\{S\left(\sqrt{\frac{2}{\pi}}z_1\right)-S\left(\sqrt{\frac{2}{\pi}}z_2\right)\right\}\right]$$

and

$$h_q(t)=\sqrt{2}\cdot\frac{1}{4\pi}\sqrt{\frac{\pi g}{\Delta x}}\cdot\left[cos\left(t\omega_o-\frac{t^2 g}{4\Delta x}\right)\cdot\left\{S\left(\sqrt{\frac{2}{\pi}}z_1\right)-S\left(\sqrt{\frac{2}{\pi}}z_2\right)\right\}\right.$$

$$\left.+sin\left(t\omega_o-\frac{t^2 g}{4\Delta x}\right)\left\{C\left(\sqrt{\frac{2}{\pi}}z_1\right)-C\left(\sqrt{\frac{2}{\pi}}z_2\right)\right\}\right]$$

where

$$z_1=\sqrt{\frac{\Delta x}{g}}(\omega_o+\Delta\omega)-\frac{t}{2}\sqrt{\frac{g}{\Delta x}}$$

$$z_2=\sqrt{\frac{\Delta x}{g}}(\omega_o-\Delta\omega)-\frac{t}{2}\sqrt{\frac{g}{\Delta x}}$$

$$envelope(t)=\sqrt{h_p^2(t)+h_q^2(t)}$$

$$= \frac{1}{4\pi}\sqrt{\frac{2\pi g}{\Delta x}}\cdot\left[\left\{C\left(\sqrt{\frac{2}{\pi}}z_1\right)-C\left(\sqrt{\frac{2}{\pi}}z_2\right)\right\}^2+\left\{S\left(\sqrt{\frac{2}{\pi}}z_1\right)-S\left(\sqrt{\frac{2}{\pi}}z_2\right)\right\}^2\right]^{\frac{1}{2}}$$

$$\phi(t)=\arctan\left(\frac{h_q(t)}{h_p(t)}\right)$$

$$=\arctan\left(\frac{cos\left(t\omega_o-\frac{t^2 g}{4\Delta x}\right)\cdot\left(S\left(\sqrt{\frac{2}{\pi}}z_1\right)-S\left(\sqrt{\frac{2}{\pi}}z_2\right)\right)+sin\left(t\omega_o-\frac{t^2 g}{4\Delta x}\right)\left(C\left(\sqrt{\frac{2}{\pi}}z_1\right)-C\left(\sqrt{\frac{2}{\pi}}z_2\right)\right)}{cos\left(t\omega_o-\frac{t^2 g}{4\Delta x}\right)\cdot\left(C\left(\sqrt{\frac{2}{\pi}}z_1\right)-C\left(\sqrt{\frac{2}{\pi}}z_2\right)\right)-sin\left(t\omega_o-\frac{t^2 g}{4\Delta x}\right)\left(S\left(\sqrt{\frac{2}{\pi}}z_1\right)-S\left(\sqrt{\frac{2}{\pi}}z_2\right)\right)}\right)$$

$$h_p(t)=\frac{1}{4\pi}\cdot\int_{-\Delta\omega}^{\Delta\omega}\left(e^{-\left(-i\cdot\frac{\Delta x}{g}\omega^2+2i\left(\frac{\Delta x\omega_o}{g}-\frac{t}{2}\right)\cdot\omega-i\cdot\frac{(\Delta x)}{g}\omega_o^2\right)}+e^{-\left(i\cdot\frac{\Delta x}{g}\omega^2+2i\left(\frac{\Delta x\omega_o}{g}-\frac{t1}{2}\right)\cdot\omega+i\cdot\frac{(\Delta x)}{g}\omega_o^2\right)}\right)d\omega$$

using the integration

$$\int e^{-(ax^2+2bx+c)}dx=\frac{1}{2}\sqrt{\frac{\pi}{a}}e^{\frac{b^2-ac}{a}}erf\left(\sqrt{a}x+\frac{b}{\sqrt{a}}\right)$$

$$h_p(t)=\frac{1}{4\pi}\cdot\left[\frac{1}{2}\sqrt{\frac{\pi g}{\Delta x}}\sqrt{\frac{1}{-i}}e^{\left(\left(\frac{\Delta x^2\omega_o^2}{g^2}-\left(\frac{\Delta x\omega_o}{g}-\frac{t}{2}\right)^2\right)\frac{g}{-i\Delta x}\right)}\cdot erf\left(\sqrt{-i}\sqrt{\frac{\Delta x}{g}}(\Delta\omega)+\frac{i\left(\frac{\Delta x\omega_o}{g}-\frac{t}{2}\right)}{\sqrt{-i}\sqrt{\frac{\Delta x}{g}}}\right)\right.$$

$$-\frac{1}{2}\sqrt{\frac{\pi g}{\Delta x}}\sqrt{\frac{1}{-i}}e^{\left(\left(\frac{\Delta x^2\omega_o^2}{g^2}-\left(\frac{\Delta x\omega_o}{g}-\frac{t}{2}\right)^2\right)\frac{g}{-i\Delta x}\right)}\cdot erf\left(\sqrt{-i}\sqrt{\frac{\Delta x}{g}}(-\Delta\omega)+\frac{i\left(\frac{\Delta x\omega_o}{g}-\frac{t}{2}\right)}{\sqrt{-i}\sqrt{\frac{\Delta x}{g}}}\right)$$

$$+\frac{1}{2}\sqrt{\frac{\pi g}{\Delta x}}\sqrt{\frac{1}{i}}e^{\left(\left(\frac{\Delta x^2\omega_o^2}{g^2}-\left(\frac{\Delta x\omega_o}{g}-\frac{t}{2}\right)^2\right)\frac{g}{i\Delta x}\right)}\cdot erf\left(\sqrt{i}\sqrt{\frac{\Delta x}{g}}(\Delta\omega)+\frac{i\left(\frac{\Delta x\omega_o}{g}-\frac{t}{2}\right)}{\sqrt{i}\sqrt{\frac{\Delta x}{g}}}\right)$$

$$\left.-\frac{1}{2}\sqrt{\frac{\pi g}{\Delta x}}\sqrt{\frac{1}{i}}e^{\left(\left(\frac{\Delta x^2\omega_o^2}{g^2}-\left(\frac{\Delta x\omega_o}{g}-\frac{t}{2}\right)^2\right)\frac{g}{i\Delta x}\right)}\cdot erf\left(\sqrt{i}\sqrt{\frac{\Delta x}{g}}(-\Delta\omega)+\frac{i\left(\frac{\Delta x\omega_o}{g}-\frac{t}{2}\right)}{\sqrt{-i}\sqrt{\frac{\Delta x}{g}}}\right)\right]$$

$$A = \frac{g}{\Delta x}\left(\frac{\Delta x^2 \omega_o^2}{g^2} - \left(\frac{\Delta x \omega_o}{g} - \frac{t}{2}\right)^2\right) = t\omega_o - \frac{t^2 g}{4\Delta x}$$

$$B = \frac{1}{8\pi}\sqrt{\frac{\pi g}{\Delta x}}$$

$$D = \sqrt{\frac{\Delta x}{g}}(\Delta\omega) + \frac{\left(\frac{\Delta x \omega_o}{g} - \frac{t}{2}\right)}{\sqrt{\frac{\Delta x}{g}}} = \sqrt{\frac{\Delta x}{g}}(\omega_o + \Delta\omega) - \frac{t}{2}\sqrt{\frac{g}{\Delta x}}$$

$$E = \sqrt{\frac{\Delta x}{g}}(-\Delta\omega) + \frac{\left(\frac{\Delta x \omega_o}{g} - \frac{t}{2}\right)}{\sqrt{\frac{\Delta x}{g}}} = \sqrt{\frac{\Delta x}{g}}(\omega_o - \Delta\omega) - \frac{t}{2}\sqrt{\frac{g}{\Delta x}}$$

$$h_p(t) = B\left[\sqrt{\frac{1}{-i}}\, e^{iA} \cdot erf\left(-\sqrt{-iE}\right) - \sqrt{\frac{1}{-i}}\, e^{iA} \cdot erf\left(-\sqrt{-iD}\right) + \sqrt{\frac{1}{i}}\, e^{-iA} \cdot erf\left(\sqrt{iD}\right) - \sqrt{\frac{1}{i}}\, e^{iA} \cdot erf\left(\sqrt{iE}\right)\right]$$

using the (*erf*)function properties

$$erf(-z) = -erf(z) \qquad erf(-z^*) = -erf(z)^*$$

and notice that $G = \sqrt{\frac{1}{-i}} = \sqrt{i}$ $\qquad$ $G^* = \sqrt{\frac{1}{i}} = \sqrt{-i}$

$$h_p(t) = B\left[-\sqrt{\frac{1}{-i}}\, e^{iA} \cdot erf\left(\sqrt{-iE}\right) + \sqrt{\frac{1}{-i}}\, e^{iA} \cdot erf\left(-\sqrt{-iD}\right) + \sqrt{\frac{1}{i}}\, e^{-iA} \cdot erf^*\left(\sqrt{-iD}\right) - \sqrt{\frac{1}{i}}\, e^{-iA} \cdot erf^*\left(\sqrt{iE}\right)^*\right]$$

$$h_p(t) = B\left[2 \cdot Real\left(\sqrt{\frac{1}{-i}}\, e^{iA} \cdot erf\left(-\sqrt{-iD}\right)\right) - 2 \cdot Real\left(\sqrt{\frac{1}{-i}}\, e^{iA} \cdot erf\left(\sqrt{iE}\right)\right)\right]$$

using the relation ship

$$C(z) + iS(z) = \frac{1+i}{2} erf\left(\frac{\sqrt{\pi}}{2}(1-i)z\right)$$

$$h_p(t) = 2B \cdot Real\left[e^{iA} \cdot \left(\frac{1+i}{2} \cdot \sqrt{2} \cdot erf\left(\frac{1-i}{2} \cdot \sqrt{2D}\right) + \frac{1+i}{2} \cdot \sqrt{2} \cdot erf\left(-\frac{1-i}{2} \cdot \sqrt{2E}\right)\right)\right]$$

$$z_1 = \frac{\sqrt{2}}{\sqrt{\pi}} \cdot D \qquad z_2 = \frac{\sqrt{2}}{\sqrt{\pi}} \cdot E$$

$$h_p(t) = 2\sqrt{2} \cdot B \cdot Real\left[e^{iA} \cdot \left(\frac{1+i}{2} \cdot erf\left(\frac{\sqrt{\pi}}{2}(1-i)z_1 \right) - \frac{1+i}{2} \cdot erf\left(\frac{\sqrt{\pi}}{2}(1-i)z_2 \right) \right) \right]$$

$$h_p(t) = 2\sqrt{2} \cdot B \cdot Real\left[e^{iA} \cdot \left(C(z_1) + iS(z_1) - C(z_2) - iS(z_2) \right) \right]$$

$$h_p(t) = 2\sqrt{2} \cdot B \cdot \left[cos(A) \cdot \left(C(z_1) - C(z_2) \right) - \sin(A) \cdot \left(S(z_1) - S(z_2) \right) \right]$$

$$h_p(t) = \sqrt{2}\,\frac{1}{4\pi}\sqrt{\frac{\pi g}{\Delta x}} \cdot \left[cos\left(t\omega_o - \frac{t^2 g}{4\Delta x} \right) \cdot \right.$$

$$\left\{ C\left(\frac{\sqrt{2}}{\pi}\left(\sqrt{\frac{\Delta x}{g}}(\omega_o + \Delta\omega) - \frac{t}{2}\sqrt{\frac{g}{\Delta x}} \right) \right) - C\left(\frac{\sqrt{2}}{\pi}\left(\sqrt{\frac{\Delta x}{g}}(\omega_o - \Delta\omega) - \frac{t}{2}\sqrt{\frac{g}{\Delta x}} \right) \right) \right\}$$

$$- sin\left(t\omega_o - \frac{t^2 g}{4\Delta x} \right)$$

$$\left. \left\{ S\left(\frac{\sqrt{2}}{\pi}\left(\sqrt{\frac{\Delta x}{g}}(\omega_o + \Delta\omega) - \frac{t}{2}\sqrt{\frac{g}{\Delta x}} \right) \right) - S\left(\frac{\sqrt{2}}{\pi}\left(\sqrt{\frac{\Delta x}{g}}(\omega_o - \Delta\omega) - \frac{t}{2}\sqrt{\frac{g}{\Delta x}} \right) \right) \right\} \right]$$

$$h_q(t) = \frac{1}{4i\pi} \cdot \int_{-\Delta\omega}^{\Delta\omega} \left(e^{\left(i \cdot \frac{(\omega-\omega_o)^2}{g}(\Delta x) \right)} - e^{\left(-i \cdot \frac{(\omega+\omega_o)^2}{g}(\Delta x) \right)} \right) \cdot e^{i\omega t} d\omega$$

derivation

$$h_q(t) = \frac{1}{4i\pi} \cdot \int_{-\Delta\omega}^{\Delta\omega} \left(e^{-\left(-i \cdot \frac{\Delta x}{g}\omega^2 + 2i\left(\frac{\Delta x \omega_o}{g} - \frac{t}{2} \right) \cdot \omega - i \cdot \frac{(\Delta x)}{g}\omega_o^2 \right)} - e^{-\left(i \cdot \frac{\Delta x}{g}\omega^2 + 2i\left(\frac{\Delta x \omega_o}{g} - \frac{t}{2} \right) \cdot \omega + i \cdot \frac{(\Delta x)}{g}\omega_o^2 \right)} \right) d\omega$$

$$h_q(t) = \frac{1}{4\pi} \cdot \left[\frac{1}{2}\sqrt{\frac{\pi g}{\Delta x}}\sqrt{\frac{1}{-i}}\, e^{\left(\left(\frac{\Delta x^2 \omega_o^2}{g^2} - \left(\frac{\Delta x \omega_o}{g} - \frac{t}{2} \right)^2 \right) \frac{g}{-i\Delta x} \right)} \cdot erf\left(\sqrt{-i}\sqrt{\frac{\Delta x}{g}}(\Delta\omega) + \frac{i\left(\frac{\Delta x \omega_o}{g} - \frac{t}{2} \right)}{\sqrt{-i}\sqrt{\frac{\Delta x}{g}}} \right) \right.$$

$$\left. - \frac{1}{2}\sqrt{\frac{\pi g}{\Delta x}}\sqrt{\frac{1}{-i}}\, e^{\left(\left(\frac{\Delta x^2 \omega_o^2}{g^2} - \left(\frac{\Delta x \omega_o}{g} - \frac{t}{2} \right)^2 \right) \frac{g}{-i\Delta x} \right)} \cdot erf\left(\sqrt{-i}\sqrt{\frac{\Delta x}{g}}(-\Delta\omega) + \frac{i\left(\frac{\Delta x \omega_o}{g} - \frac{t}{2} \right)}{\sqrt{-i}\sqrt{\frac{\Delta x}{g}}} \right) \right]$$

$$-\frac{1}{2}\sqrt{\frac{\pi g}{\Delta x}}\sqrt{\frac{1}{i}}\,e^{\left(\left(\frac{\Delta x^2\omega_o^2}{g^2}-\left(\frac{\Delta x\omega_o}{g}-\frac{t}{2}\right)^2\right)\frac{g}{i\Delta x}\right)}\cdot erf\left(\sqrt{i}\sqrt{\frac{\Delta x}{g}}(\Delta\omega)+\frac{i\left(\frac{\Delta x\omega_o}{g}-\frac{t}{2}\right)}{\sqrt{i}\sqrt{\frac{\Delta x}{g}}}\right)$$

$$+\frac{1}{2}\sqrt{\frac{\pi g}{\Delta x}}\sqrt{\frac{1}{i}}\,e^{\left(\left(\frac{\Delta x^2\omega_o^2}{g^2}-\left(\frac{\Delta x\omega_o}{g}-\frac{t}{2}\right)^2\right)\frac{g}{i\Delta x}\right)}\cdot erf\left(\sqrt{i}\sqrt{\frac{\Delta x}{g}}(-\Delta\omega)+\frac{i\left(\frac{\Delta x\omega_o}{g}-\frac{t}{2}\right)}{\sqrt{i}\sqrt{\frac{\Delta x}{g}}}\right)$$

using the same as in h_p derivation

$$h_q(t)=B(-i)\left[\sqrt{\frac{1}{-i}}\,e^{iA}\cdot erf\left(-\sqrt{-i}E\right)-\sqrt{\frac{1}{-i}}\,e^{iA}\cdot erf\left(-\sqrt{-i}D\right)\right.$$

$$\left.-\sqrt{\frac{1}{i}}\,e^{-iA}\cdot erf\left(\sqrt{i}D\right)+\sqrt{\frac{1}{i}}\,e^{iA}\cdot erf\left(\sqrt{i}E\right)\right]$$

$$h_q(t)=B(-i)\left[-\sqrt{\frac{1}{-i}}\,e^{iA}\cdot erf\left(-\sqrt{-i}E\right)+\sqrt{\frac{1}{-i}}\,e^{iA}\cdot erf\left(\sqrt{-i}D\right)\right.$$

$$\left.-\sqrt{\frac{1}{i}}\,e^{-iA}\cdot erf*\left(\sqrt{-i}D\right)+\sqrt{\frac{1}{i}}\,e^{-iA}\cdot erf*\left(\sqrt{-i}E\right)*\right]$$

$$h_q(t)=B\left[2\cdot Imag\left(\sqrt{\frac{1}{-i}}\,e^{iA}\cdot erf\left(\sqrt{-i}D\right)\right)-2\cdot Imag\left(\sqrt{\frac{1}{-i}}\,e^{iA}\cdot erf\left(\sqrt{i}E\right)\right)\right]$$

$$h_q(t)=2B\cdot Imag\left[e^{iA}\cdot\left(\frac{1+i}{2}\cdot\sqrt{2}\cdot erf\left(\frac{1-i}{2}\cdot\sqrt{2}D\right)+\frac{1+i}{2}\cdot\sqrt{2}\cdot erf\left(-\frac{1-i}{2}\cdot\sqrt{2}E\right)\right)\right]$$

$$z_1=\frac{\sqrt{2}}{\sqrt{\pi}}\cdot D\qquad z_2=\frac{\sqrt{2}}{\sqrt{\pi}}\cdot E$$

$$h_q(t)=2\sqrt{2}\cdot B\cdot Imag\left[e^{iA}\cdot\left(\frac{1+i}{2}\cdot erf\left(\frac{\sqrt{\pi}}{2}(1-i)z_1\right)-\frac{1+i}{2}\cdot erf\left(\frac{\sqrt{\pi}}{2}(1-i)z_2\right)\right)\right]$$

$$h_q(t)=2\sqrt{2}\cdot B\cdot Imag\left[e^{iA}\cdot\left(C(z_1)+iS(z_1)-C(z_2)-iS(z_2)\right)\right]$$

$$h_q(t)=2\sqrt{2}\cdot B\cdot\left[\cos(A)\cdot\left(S(z_1)-S(z_2)\right)+\sin(A)\cdot\left(C(z_1)-C(z_2)\right)\right]$$

$$h_q(t)=\sqrt{2}\,\frac{1}{4\pi}\sqrt{\frac{\pi g}{\Delta x}}\cdot\left[\cos\left(t\omega_o-\frac{t^2 g}{4\Delta x}\right)\cdot\right.$$

$$\left\{S\left(\frac{\sqrt{2}}{\pi}\left(\sqrt{\frac{\Delta x}{g}}(\omega_o+\Delta\omega)-\frac{t}{2}\sqrt{\frac{g}{\Delta x}}\right)\right)-S\left(\frac{\sqrt{2}}{\pi}\left(\sqrt{\frac{\Delta x}{g}}(\omega_o-\Delta\omega)-\frac{t}{2}\sqrt{\frac{g}{\Delta x}}\right)\right)\right\}$$

$$+sin\left(t\omega_o-\frac{t^2 g}{4\Delta x}\right)$$

$$\left\{C\left(\frac{\sqrt{2}}{\pi}\left(\sqrt{\frac{\Delta x}{g}}(\omega_o+\Delta\omega)-\frac{t}{2}\sqrt{\frac{g}{\Delta x}}\right)\right)-C\left(\frac{\sqrt{2}}{\pi}\left(\sqrt{\frac{\Delta x}{g}}(\omega_o-\Delta\omega)-\frac{t}{2}\sqrt{\frac{g}{\Delta x}}\right)\right)\right\}\Bigg]$$

$$M=\left\{C\left(\frac{\sqrt{2}}{\pi}\left(\sqrt{\frac{\Delta x}{g}}(\omega_o+\Delta\omega)-\frac{t}{2}\sqrt{\frac{g}{\Delta x}}\right)\right)-C\left(\frac{\sqrt{2}}{\pi}\left(\sqrt{\frac{\Delta x}{g}}(\omega_o-\Delta\omega)-\frac{t}{2}\sqrt{\frac{g}{\Delta x}}\right)\right)\right\}$$

$$N=\left\{S\left(\frac{\sqrt{2}}{\pi}\left(\sqrt{\frac{\Delta x}{g}}(\omega_o+\Delta\omega)-\frac{t}{2}\sqrt{\frac{g}{\Delta x}}\right)\right)-S\left(\frac{\sqrt{2}}{\pi}\left(\sqrt{\frac{\Delta x}{g}}(\omega_o-\Delta\omega)-\frac{t}{2}\sqrt{\frac{g}{\Delta x}}\right)\right)\right\}\Bigg]$$

$$\sqrt{h_p^2+h_q^2}=\sqrt{2}\,\frac{1}{4\pi}\sqrt{\frac{\pi g}{\Delta x}}\Big[(cos(A)\cdot M+sin(A)\cdot N)^2+(cos(A)\cdot N+sin(A)\cdot M)^2\Big]^{\frac{1}{2}}$$

$$=\sqrt{2}\,\frac{1}{4\pi}\sqrt{\frac{\pi g}{\Delta x}}\Big[cos(A)^2\cdot M^2+sin(A)^2\cdot N^2+cos(A)^2\cdot N^2+sin(A)^2\cdot M^2\Big]^{\frac{1}{2}}$$

$$=\sqrt{2}\,\frac{1}{4\pi}\sqrt{\frac{\pi g}{\Delta x}}\Big[\left(cos(A)^2+sin(A)^2\right)\cdot\left(M^2+N^2\right)\Big]^{\frac{1}{2}}$$

$$=\sqrt{2}\,\frac{1}{4\pi}\sqrt{\frac{\pi g}{\Delta x}}\left[\left\{C\left(\frac{\sqrt{2}}{\pi}\cdot D\right)-C\left(\frac{\sqrt{2}}{\pi}E\right)\right\}^2+\left\{S\left(\frac{\sqrt{2}}{\pi}\cdot D\right)-S\left(\frac{\sqrt{2}}{\pi}E\right)\right\}^2\right]^{\frac{1}{2}}$$

$$\arctan\left(\frac{h_q}{h_p}\right)=\arctan\left(\frac{cos(A)\cdot(S(z_1)-S(z_2))+sin(A)(C(z_1)-C(z_2))}{cos(A)\cdot(C(z_1)-C(z_2))-sin(A)(S(z_1)-S(z_2))}\right)$$

D-2 Unsymmetrical System Fixed Time mode

$$F_a(k)=e^{\left(-i\cdot sign(k)\cdot\sqrt{sign(k)k\cdot g}(\Delta t)\right)}$$

Since f_1 has a band width $k_o-\Delta k<k<k_o+\Delta k$

We can introduce an additional filter F_b

$$F_b = \begin{cases} 1 & k_o - \Delta k < k < k_o + \Delta k \\ 0 & Otherwize \end{cases}$$

$$F = \begin{cases} e^{\left(-i\cdot\sqrt{k\cdot g}(\Delta t)\right)} & k_o - \Delta k < k < k_o + \Delta k \\ e^{\left(i\cdot\sqrt{-k\cdot g}(\Delta t)\right)} & -k_o - \Delta k < k < -k_o + \Delta k \\ 0 & Otherwize \end{cases}$$

This is an unsymmetrical band pass filter. we can write $F(k)$ as the sum $F(\omega)= F_1(\omega)+ F_2(\omega)$

where

$$F_1(k)= e^{\left(-i\cdot\sqrt{k\cdot g}(\Delta t)\right)}\cdot\left[u\left(k-\left(k_o-\Delta k\right)\right)-u\left(k-\left(k_o+\Delta k\right)\right)\right]$$

And

$$F_2(k) = e^{\left(i\cdot\sqrt{k\cdot g}(\Delta t)\right)}\cdot\left[u\left(k+\left(k_o+\Delta k\right)\right)-u\left(k+\left(k_o-\Delta k\right)\right)\right]$$

Shifting the two parts

$$F_{l1}(\omega) = F_1(k+ k_o)$$

$$F_{l1}(k) = e^{\left(-i\cdot\sqrt{(k+k_o)\cdot g}(\Delta t)\right)}\cdot\left[u\left(k+\Delta k\right)-u\left(k-\Delta k\right)\right]$$

And

$$F_{l2}(k) = F_2(k - k_o)$$

$$F_{l2}(k) = e^{\left(i\cdot\sqrt{(k-k_o)\cdot g}(\Delta t)\right)}\cdot\left[u\left(k+\Delta k\right)-u\left(k-\Delta k\right)\right]$$

The in-pase and quadrature system functions

$$F_p(k)=\frac{1}{2}\cdot\left(F_{l2}(k)+F_{l1}(k)\right)$$

$$F_p(k)=\frac{1}{2}\cdot\left(e^{\left(i\cdot\sqrt{(k-k_o)\cdot g}(\Delta t)\right)}+e^{\left(-i\cdot\sqrt{(k+k_o)\cdot g}(\Delta t)\right)}\right)\cdot\left[u\left(k+\Delta k\right)-u\left(k-\Delta k\right)\right]$$

$$F_q(k)=\frac{1}{2i}\cdot\left(F_{l2}(k)-F_{l1}(k)\right)$$

$$F_q(k)=\frac{1}{2i}\cdot\left(e^{\left(i\cdot\sqrt{(k-k_o)\cdot g}(\Delta t)\right)}-e^{\left(-i\cdot\sqrt{(k+k_o)\cdot g}(\Delta t)\right)}\right)\cdot\left[u\left(k+\Delta k\right)-u\left(k-\Delta k\right)\right]$$

the impulse response

$$f_p(x)=\frac{1}{4\pi}\cdot\int_{-\Delta k}^{\Delta k}\left(e^{\left(i\cdot\sqrt{(k-k_o)\cdot g}(\Delta t)\right)}+e^{\left(-i\cdot\sqrt{(k+k_o)\cdot g}(\Delta t)\right)}\right)\cdot e^{i\cdot kx}dk$$

$$f_q(x)=\frac{1}{4\pi i}\cdot\int_{-\Delta k}^{\Delta k}e^{i\left(\sqrt{g}\cdot\Delta t\sqrt{(k_o-k)}+kx\right)}dk-e^{-i\left(\sqrt{g}\cdot\Delta t\sqrt{(k_o+k)}-kx\right)}dk$$

$$f_q(x)=\frac{-i}{8\pi x\sqrt{x}\sqrt{i}}\left[-2i\sqrt{i}\sqrt{x}e^{i\left(\sqrt{g}\cdot\Delta t\sqrt{(k_o-k)}+x\Delta k\right)}+2i\sqrt{i}\sqrt{x}e^{i\left(\sqrt{g}\cdot\Delta t\sqrt{(k_o+k)}-x\Delta k\right)}\right.$$

$$+\sqrt{\pi g}\Delta t\,e^{i\frac{4x^2k_o+g\Delta^2t}{4x}}erf\left(\sqrt{i}\,\frac{-2x\sqrt{k_o-\Delta k}+\sqrt{g}\Delta t}{2\sqrt{x}}\right)$$

$$-\sqrt{\pi g}\Delta t\,e^{i\frac{4x^2k_o+g\Delta^2t}{4x}}erf\left(\sqrt{i}\,\frac{-2x\sqrt{k_o+\Delta k}+\sqrt{g}\Delta t}{2\sqrt{x}}\right)$$

$$-\frac{i}{8\pi x\sqrt{x}\sqrt{-i}}\left[2i\sqrt{-i}\sqrt{x}e^{-i\left(\sqrt{g}\cdot\Delta t\sqrt{(k_o+k)}-x\Delta k\right)}-2i\sqrt{-i}\sqrt{x}e^{-i\left(\sqrt{g}\cdot\Delta t\sqrt{(k_o-k)}+x\Delta k\right)}\right.$$

$$-\sqrt{\pi g}\Delta t\,e^{-i\frac{4x^2k_o+g\Delta^2t}{4x}}erf\left(-\sqrt{-i}\,\frac{-2x\sqrt{k_o+\Delta k}+\sqrt{g}\Delta t}{2\sqrt{x}}\right)$$

$$\left.+\sqrt{\pi g}\Delta t\,e^{-i\frac{4x^2k_o+g\Delta^2t}{4x}}erf\left(-\sqrt{-i}\,\frac{-2x\sqrt{k_o-\Delta k}+\sqrt{g}\Delta t}{2\sqrt{x}}\right)\right]$$

$$f_q(x)=A\left[2i\sqrt{x}\left(-e^{iB_2}+e^{iB_1}+e^{-iB_1}-e^{-iB_2}\right)-i\sqrt{\pi g}\Delta t\left\{\sqrt{-i}e^{iJ}erf\left(\sqrt{i}D_1\right)\right.\right.$$

$$\left.\left.-\sqrt{-i}e^{iJ}erf\left(\sqrt{i}D_2\right)-\sqrt{i}e^{-iJ}erf\left(-\sqrt{-i}D_2\right)+\sqrt{i}e^{-iJ}erf\left(-\sqrt{-i}D_1\right)\right\}\right]$$

$$f_q(x)=A\left[4\sqrt{x}\left(\cos(B_1)-\cos(B_2)\right)-i\sqrt{\pi g}\Delta t\left\{\sqrt{-i}e^{iJ}erf*\left(\sqrt{-i}D_1\right)\right.\right.$$

$$\left.\left.-\sqrt{-i}e^{iJ}erf*\left(\sqrt{-i}D_2\right)+\sqrt{i}e^{-iJ}erf\left(\sqrt{-i}D_2\right)-\sqrt{i}e^{-iJ}erf\left(\sqrt{-i}D_1\right)\right\}\right]$$

$$f_q(x)=A\left[4\sqrt{x}\left(\cos(B_1)-\cos(B_2)\right)+2\sqrt{\pi g}\Delta t\cdot Imag\left(e^{-iJ}\left(\sqrt{i}erf\left(\sqrt{-i}D_2\right)-\sqrt{i}erf\left(\sqrt{-i}D_1\right)\right)\right)\right]$$

$$z_3=\sqrt{\frac{2}{\pi}}D_1\qquad z_4=\sqrt{\frac{2}{\pi}}D_2$$

$$f_q(x)=A\left[4\sqrt{x}\left(\cos(B_1)-\cos(B_2)\right)\right.$$

$$\left.+2\sqrt{\pi g}\Delta t\cdot Imag\left(e^{-iJ}\left(\frac{1+i}{2}\cdot\sqrt{2}erf\left(\frac{1-i}{2}\cdot\sqrt{2}\cdot D_2\right)-\frac{1+i}{2}\cdot\sqrt{2}erf\left(\frac{1-i}{2}\cdot\sqrt{2}\cdot D_1\right)\right)\right)\right]$$

$$f_q(x)=A\left[4\sqrt{x}\left(\cos(B_1)-\cos(B_2)\right)+2\sqrt{2}\sqrt{\pi g}\Delta t\cdot Imag\left(e^{-iJ}\left(C(z_2)+iS(z_1)-C(z_2)-iS(z_2)\right)\right)\right]$$

$$f_q(x)=A\left[4\sqrt{x}\left(\cos(B_1)-\cos(B_2)\right)+2\sqrt{2}\sqrt{\pi g}\Delta t\left(\sin(J)\left(C(z_2)-C(z_1)\right)-\cos(J)\left(S(z_2)-S(z_1)\right)\right)\right]$$

$$envelope=\sqrt{f_p^2(x)+f_q^2(x)}$$

$$= \frac{\sin^2\left(\frac{D_2^2 - D_1^2}{2}\right)}{\pi^2 x^2} + \frac{g\Delta^2 t}{8\pi x^2}\left[\left(c(z_2) - c(z_1)\right)^2 + \left(S(z_2) - S(z_1)\right)^2\right]$$
$$+ \left[\frac{\Delta t\sqrt{2\pi g x}}{2\pi x^3}\right] sin\left(\frac{D_2^2 - D_1^2}{2}\right) \cdot$$
$$\left[\left(C(z_2) - C(z_1)\right) \cdot cos\left(\frac{D_2{}^2 + D_1{}^2}{2}\right) + \left(S(z_2) - S(z_1)\right) \cdot sin\left(\frac{D_2{}^2 + D_1{}^2}{2}\right)\right]$$

References

1. Pierson Jr., W.J., E. Neumann, and R.W. James, *Practical Methods of Observing and Forecasting Ocean Waves by Means of Wave Spectra and Statistics.* 1955, U.S. Navy Hydrographic Office.
2. Edgar, D.R., Horwood, J. M. K.,Thurley, R. W. F.,Belmont, M. R., *The effects of parameters on the maximum prediction time possible in short term forecasting of sea surface shape.* Int. Shipbuilding Progress, 2000, 47(451):p. 287-301
3. Morris, E.L., H.K. Zienkiewicz, and M.R. Belmont, *Short-Term Forecasting of Sea Surface Shape.* Int. Shipbuilding Progress, 1998. 45,no. 444 pp. 383-400.
4. Morris, E.L., H.K. Zienkiewicz, and M.R. Belmont, *short-term forecasting of the sea-state* Intern.Shipbuilding Progress, 1998. 45(444): p. 383-400.
5. Belmont, M.R.S., W. Gill, P., *30 Seconds Ahead.* Offshore Focus, June 1995.
6. M R Belmont, E L Morris, J M K Horwood and R W T Thurley. *Deterministic Wave Prediction Linked to Wave Energy Absorbers*. *3rd European Conf*. 1998. Patras, Greece, pp. 153-161..
7. World Meteorological Organization, *Guide to wave analysis and forecasting*. 2nd ed. 1998, Secretariat of the World Meteorological Organization, Geneva, Switzerland: WMO No. 702.
8. Tucker, M.J., *Waves in Ocean Engineering: Measurement, Analysis, Interpretation*. 1992 Ellis Horwood.
9. Kinsman, B., *Wind Waves*. 1965: Dover Inc.,.
10. M.J.Tucker and E.G.Pitt, *Waves in Ocean Engineering*, eds. R.Bhattacharyya *and M.E.McCormick*. *Vol. 5. 2001: Elsevier Ocean Engineering Book Series London.*
11. Airy, G.B., *Tides and Waves,* . Encyc. Metrop., 1845. **192**: p. 241-396.
12. Crapper, G.D., *Introduction to water waves.* Publ. Ellis Harwood., 1984.
13. Longuet-Higgins, M., *Resonant interactions between two trains of gravity waves.* Fluid Mechanics,, 1962. **12**(3): p. 321-332.
14. CEM, *The Coastal Engineering Manual Part II* Corps of Engineers,WES CERC Vicksburg, 2000
15. Cote L.J., D.J.O., Marks W., McGough R.J., E.Mehr, Pierson Jr. W.J., Ropek J.F., Stephenson G., and Vetter R.C.,, *The directional spectrum of a wind generated sea as obtained from data obtained by the Stereo Wave Observation Project*. *Meteorol.* . Vol. 2(6). 1960 Papers, N.Y.U., Coll. of Eng. . 88pp.
16. Belmont M.R., Morris E.L., Zienkiewicz H.K. ,Pourzanjani M.M.A., Flower J.O., *Sea surface prediction*. 1991, S.E.R.C. Contract No. GR/F 32165 (SHP 54)
17. Belmont, M.R., Pourzanjani,M.M.A. ,Zienkiewicz , H.K.,Morris, E.L., *Application of a sea-surface estimator in predictive ship control.* 2nd Int.Conf.on Maneuvering and Control of Marine Craft,, July1992: p. 547-571.
18. Morris, E.L., Zienkiewicz, H.K. ,Flower, J.O., Belmont, M. R., *Techniques for sea-state prediction.* 2nd Int.Conf.on Maneuvering and Control of Marine Craft,, July 1992: p. 547-571.

19. Zienkiewicz, H.K., Belmont, M. R.,Morris, E.L., Pourzanjani, M.M.A.,Flower, J.O., *The correlation between width and maximum power for north atlantic wave spectra.* Intern. Shipbuilding Progress, 1993. **40**: p. 217-225.
20. Belmont, M.R. and E.L. Morris, *Adaptive measurement and signal processing strategies associated with deterministic sea wave prediction.* IEE Proc. Conf.on Electronic Engineering in Oceanography, July 1994: p. 181-185.
21. Belmont, M.R., Morris, E.L., Maskell, S.J., Horwood, J. M. K., Thurley, R. W.F. , *Sea surface shape prediction and its applications*, S.I. Shipping, B. Marine, and B.M. Technology, Editors. 1995.
22. A.J.Pugh, W.H., P.R.Shepherd, S.R.Pennock, M.R.Belmont,, *An Adaptive Phase Measuring System for Surface Profile Measurement*. I.E.E. Proc., 2003. **150**: p. 113-118.
23. J.M.K.Horwood, M.R. Belmont , and R.W.F.Thurley, *A novel design for surface following buoys for oceanography and wave prediction.* Meas. Cont., 2002. **35**: p. 176-180.
24. Barrick, D.E. *30 Years of CMTC and CODAR, Current Measurement Technology*. in *CMTC 2008. IEEE/OES 9th Working Conference* 2008.
25. M.R.Belmont, Thurley, R. W. F.,Horwood, J. M. K.,Baker, J., *Shallow Angle Wave profiling LIDAR.* Journal of Atmospheric and Oceanic Technology, Oct 2004.
26. Belmont, M.R., Horwood,J.M.K.,Baker,R.W.F.,Baker,J., *Shallow Angle Wave profiling LIDAR.* Journal of Atmosperic and Oceanic Technology, June 2007. **24**(6): p. 1150-1156.
27. Belmont, M.R., Horwood,J.M.K.,Baker,R.W.F.,Baker,J., et al., *Shallow angle wave profiling LIDAR.* J. Physical Oceanography, July 2004.
28. Steinvall, O., Koppari, K., and Karlsson, U., *Experimental Evaluation of an Airborne Depth-Sounding Lidar*. Optical Engineering, 1993. **32 (6)**: p. 1307-1321.
29. Nairn, R.R., *Royal Australian Navy Laser Airborne Depth Sounder, The First Year of Operations.* The International Hydrographic Review, 1994. **134**: p. 109-119.
30. West, G.R., T. Graham, K.Smith, J.Spittal,. *Improving the efficiency, safety and economy of the New Zealand National Charting Programme through the integrated use of Lidar in a multi-sensor surveys*. in *U.S. Hydrographic Conference*. 1999. Mobile, Alabama. p. 26-29.
31. Steinvall, O., Koppari, K., Lejdebrink, U., Winell, J., Nilsson, M., Ellsen, R., and Gjellan, E. *Depth Sounding Lidar-Performance and Models.* in *Laser Radar Technology and applications*. 1996. Orlando, SPIE Vol. 2748, p. 18-38
32. Casey, M.J., O'Neil, R.A., Conrad, P.,*The Advent of Larsen*. in *Canadian Hydrographic Conference*. 1985. Halifax, N.S., p. 7-12
33. Guenther, G.C., Eisler, T.J., Riley, J.L., Perez, S.W. *Obstruction Detection and Data Decimation for Airborne Laser Hydrography*. in *Canadian Hydrographic Conference*. June 1996. Halifax, Nova Scotia, Canada.
34. Guenther, G.C., Thomas, R.W.L., and LaRocque, P.E., *Design considerations for Achieving High Accuracy with the SHOALS Bathymetric Lidar System. SPIE: Laser Remote Sensing of Natural Waters From Theory to Practice, .* 1996. **2964**: p. 54-71.
35. Ivanov A.P., C., A.P., Khutko I.S., Vorobey N.P., *Investigation of Backreflection Coefficient of Optical Radiation from a Sea Surface for Grazing Incidence. Izvestiya, Oceanic and Atmospheric Physics*. 7 ed. Vol. 22 1986. 579-584. .

36. Duck T.J., S.D.P., Salah J.E. and Meriwether J.W.,. *Monostatic liadr at f/200: A new instrument at Millstone Hill/MIT Haystack Observatory. In Advances in Laser Remote Sensing ISBN 2-7302-0798-8*. in *20th Int., Laser Radar Conf.* 2000 Ecole Polytechnique, France: published in Proc 10-14 July, Vichy, Franc.
37. Maslov D.V., F.V.V., and Lyashenko A. *A Shore-Based LIDAR for Coastal Sea Water Monitoring*. in *On line proceedings of the 4th EARSeL Workshop on Lidar Remote Sensing of Land and Sea*. . 2000. Dresden.
38. Belmont, M.R., Abusedra, L.,Horwood, J. M. K.,Thurley, R. W. F.,Baker, J., Challenor, P.G, *The Special Features of Wave and General Profile Measurements Produced by Shallow Angle LIDAR.* Awaiting publication.
39. Belmont, M.R., Abusedra, L.,Horwood, J. M. K.,Thurley, R. W. F., *The Special Features of Wave Elevation Data as Measured by :Shallow Angle Lidar.* Awaiting publication.
40. Belmont, M.R. and J.M.K. Horwood, *The effect of frequancy distribution in sea model spectra on simulations of deterministic sea wave prediction.* Intern.Shipbuilding Progress, 1998. **46**(447): p. 265-276.
41. Zhang, J., Prislin, I.,Yang, J.,Wen, J., *Deterministic wave model for short-crested ocean waves: Part II. Comparison with laboratory and field measurements.* Applied Ocean Research, 1999. **21**(4): p. 189-206.
42. Zhang, J., Yang, J.,Wen, J.,Prislin, I.,Hong, K., *Deterministic wave model for short-crested ocean waves: Part I. Theory and numerical scheme.* Applied Ocean Research, 1999. **21**(4): p. 167-188.
43. Prislin, I. and J. Zhang, *Deterministic decomposition of deep water short-crested irregular gravity waves.* J.Geophys. Research, 1997. **102**: p. 677-688.
44. Belmont, M.R., Horwood, J. M. K.,Thurley, R. W. F.,Baker, J., *Filters for linear sea-wave prediction.* Ocean Engineering, 2006. **33**(17-18): p. 2332-2351.
45. Nonweiler T.R.F., Tanner P.H., Wilkinson P., *Moving-weight ship stabilizers.* Third Ship Control Systems Symposium, Univ., Bath, 1972.
46. Corduneau, C., *Almost Periodic Functions.* Wiley Interscience, 1968, New York.
47. Bohr, H., *Almost Periodic Functions*. 1947, New York, Chelsea
48. Morooka, C.K. and I.H. Yokoo, *Numerical Simulation and Spectral Analysis of Irregular Sea Waves.* International Journal of Offshore and Polar Engineering, 1997. **7**(3): p. 82-89.
49. M.J.Tucker, P. G. Challenor, and D. J. T. Carter, *Numerical simulation of a random sea: a common error and its effect upon wave group statistics.* Applied Ocean Research, 1984. **6**: p. 118-122.
50. Belmont, M.R., *Application of non-uniform to uniform data mapping to: Shallow angle LIDAR with the introduction of independent variable techniques.* Signal Processing, 2007. **87**(10): p. 2461-2472.
51. Belmont, M.R. and L. Abusedra, *Non-uniform to Uniform Data Mapping and its Application to Shallow Angle Lidar Data.* Awaiting publication.
52. Belmont, M.R., *Nonuniform sampling specially for finite length data.* IEEE Proc. F, 1993. **140**: p. 55-62.
53. Bowman, A.W, Azzalini, A., *Applied Smoothing Techniques for Data Analysis*. 1997: Oxford University Press.
54. Chen, K.H., *Non-uniform sampling and n-dimensional sampling.* Lecture notes in pure and applied mathematics, 1977. **28**: p. 105-109.
55. Benedetto, J.J. and P.J.S.G. Ferreira., *Modern Sampling Theory: Mathematics and Applications* Applied and Numerical Harmonic Analysis 2001: Birkhauser Boston.

56. Belmont, M.R., *An extension to Nyquist's theorem for nonuniformly sampled finite length data.* Intern .J.of Adaptive Control and Signal Processing, 1995. **9**: p. 163-181.
57. Farokh A.Marvasti, *A Unified Approach to Zero-Crossings and Nonuniform Sampling: Of Single and Multidimensional Signals and Systems* 1987
58. Marvasti F. A, *Nonuniform Sampling: Theory and Practice*. 2001: Pbl. Plenum.
59. Mohanty N.C. and K. L.O. *Spectrum estimation of nonuniform sampled data.* in *Proc. I.E.E.E. Int. Conf., on Acoustics, Speech and signal Processing*. 1978.
60. Marziliano, P. and M. Vetterli. *Irregular sampling with unknown locations.* in *Proceedings of the Acoustics, Speech, and Signal Processing IEEE International Conference* 1999: IEEE Computer Society.
61. Martin, R.J., *Irregularly Sampled Signals:Theories and Techniques for Analysis*, Ph.D.thesis, January 1998, University College London.
62. Marziliano, P. and M. Vetterli, *Reconstruction of irregularly sampled discrete-time bandlimited signals with unknown sampling locations.* IEEE Signal Processing Society, 2000. **48**(12): p. 3462- 3471.
63. Marvasti, F.A., *Spectrum of nonuniform samples.* Electron, Lett., 1984. **20**: p. 896-897.
64. E. Plotkin, L.R., and M.Swamy,, *Reconstruction of nonuniformly sampled band limited signal and jitter error reduction.* Signal Processing, 1984. **7**: p. 151-160.
65. Marvasti, F.A.C., P.M. Dokic, M.V. Goenchanart, U. Liu, C. , *Reconstruction of speech signals with lost samples.* IEEE Transactions on Signal Processing, 1992. **40**(12): p. 2897-2903.
66. A.Papoulis, *A New Algorithm in Spectral Analysis and Band-Limited Extrapolation.* IEEE Trans. Circuits Syst., 1975. **22**(1): p. 735-742.
67. R.W.Gerchberg., *Super-Resolution Through Error Energy Reduction.* Optica Acta, 1974. **21**(9): p. 709-720.
68. Strohmer, T., *Efficient Methods for Digital Signal and Image Reconstruction from Nonuniform Samples*. Ph.D.thesis, 1993, University of Vienna.
69. H.G. Feichtinger and K. Gröechenig., *Itterative reconstruction of multi-variate band-limited functions from irregular sampling values.* . SIAM J. Math, 1992. **231**(1): p. 244-261.
70. Brigham, E.O., *The Fast Fourier Transform FFT and Its Applications*. 1988, Englewood Cliffs, New Jersey: Prentice Hall,Inc.
71. Nuttall, A.H., *Some Windows with Very Good Sidelobe Behavior.* IEEE Transactions on Acoustics, Speech, and Signal Processing, February 1981. ASSP-29(1):p 84–91.
72. Harris, F.J., *On the use of Windows for Harmonic Analysis with the Discrete Fourier Transform*. Proceedings of the IEEE January 1978. **66**(1): p. pp 51–83.
73. Rafael C. Gonzalez , R.E.W., *Digital Image Processing*. 3rd ed. 2007: Prentice hall.
74. Milton Abramowitz , eds, Stegun, I.A., *Handbook of Mathematical Functions with Formulas, Graphs, and Mathematical Tables*. 1972: New York: Dover.
75. Mielenz, K.D., *Computation of Fresnel Integrals. II.* J. Res. Natl. Inst. Stand. Technol., 2000. **105**(589): p 589-590.
76. Papoulis, A., *The Fourier Integral and its Applications*. 1987: McGraw-Hill,Inc.
77. Pohling, S.C., *Signal duration and the Fourier transform.* Proceedings of the IEEE, May 1980. 68(5): p 629 - 630